Design and development of a synthetic acoustic antenna for highly directional sound measurements.
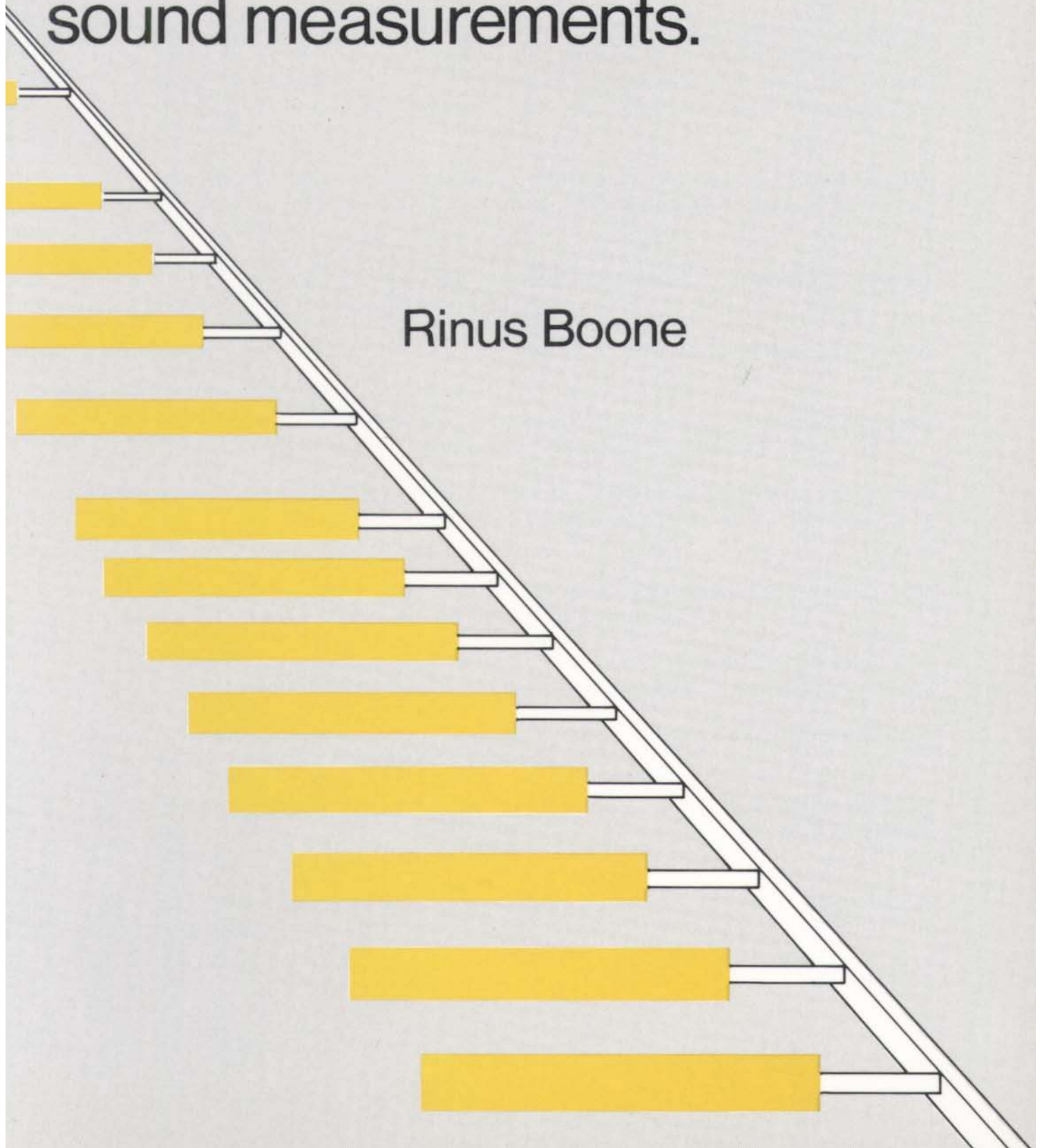
Rinus Boone

Design and development of a synthetic acoustic antenna
for highly directional sound measurements

DESIGN AND DEVELOPMENT
OF A SYNTHETIC ACOUSTIC ANTENNA
FOR HIGHLY DIRECTIONAL SOUND
MEASUREMENTS

MARINUS MARIAS BOONE

geboren te Kortgene
natuurkundig ingenieur

Dit proefschrift is goedgekeurd door de promotor
prof.dr.ir. A.J. Berkhout

Ter nagedachtenis
aan mijn ouders

PREFACE

The idea of developing an acoustic antenna for industrial sound immission measurements goes back to 1978, when the Group of Acoustics of Delft University of Technology was asked by the TPD ("Technisch Physische Dienst", TNO Institute of Applied Physics) to look into the problem of sound immission measurements that could distinguish between the contributions of the various sources. The problem was regarded by our Group as a challenge. The project started with a feasibility study, conducted by my colleague ir. G. Faber and with full support of my promoter, prof.dr.ir. A.J. Berkhout and the late prof.ir. D.W. van Wulfften Palthe. Since 1979 I have been in charge of the project which has resulted in the development of SYNTACAN.

The project involved considerable investments, an important part of which was provided by the Delft University Fund "de Beleidsruimte". In a critical stage of the project, the TPD enabled us to complete the system. I also wish to acknowledge the financial support of the Dutch Ministry of Housing, Physical Planning and Environment for an evaluation study of the applicability of SYNTACAN.

I sincerely thank my promoter prof. Berkhout, for his ever stimulating criticism that encouraged me to improve the manuscript of my thesis again and again. I appreciate his patience in teaching me to bring my writing in accord with his high standards. Many thanks are also due to my colleagues at the Delft University and the TPD for their cordial support, and to the students who were involved in the SYNTACAN project for their helpful contributions.

May SYNTACAN be a valuable tool in many applications.

CONTENTS

CHAPTER 3
OUTDOOR SOUND PROPAGATION

CHAPTER 4
SYSTEM DESIGN AND DEVELOPMENT

CHAPTER 5
TEST RESULTS

CHAPTER 6
PRACTICAL RESULTS

CHAPTER 7
ANTENNA SIGNAL PROCESSING TECHNIQUES IN RELATED DISCIPLINES

CHAPTER 1

INTRODUCTION

1.1 REASONS FOR DIRECTIONAL SOUND MEASUREMENTS

This thesis describes the development of a high resolution synthetic acoustic antenna system, named SYNTACAN. The system has been developed in answer to the urgent practical need for a highly directional microphone that could be used for noise control measurements around large industrial areas.

In the Netherlands noise pollution from industry is legislated in Chapters IV and V of the "Noise Abatement Act" [1], which prescribes the licensing and zoning around industries and the cleaning up of existing, inadmissible situations. The legislation is based on the 50 dB(A) contour. This contour is a separation between the industrial zone, where high noise immission levels are allowed, and the dwelling areas, where the immission should not exceed the 50 dB(A) limit. These immission levels are based on the measured or calculated levels at a height of 5 m, with adjustments for meteorological conditions and time of the day.

After a certain noise zone has been agreed on, it forms the basis for:

- the licensing policy for noise emission by existing and new industries;
- the licensing policy for new dwellings.

Notice that the zoning acts two ways. On the one hand it protects the community against severe noise levels due to industry; on the other hand it provides industry enough space to function without severe complaints from the surroundings. Particularly in existing situations, the immission levels in the dwelling areas can exceed the 50 dB(A) limit. If it remains below 55 dB(A), a dispensation can be given in some cases. Otherwise special measures have to be taken ("sanitation").

Meeting of these regulations is possible only after the appropriate sound measurements and calculations have been carried out. For zoning itself it is sufficient to measure or calculate the total noise immission from each industrial area. If, in addition, the emission levels from the individual noise sources are to be evaluated, a more diagnostic approach is required.

In our country the government has provided rules for these measurements and calculations, which are described in the "Guide for measuring and calculating industrial noise" (Handleiding meten en rekenen industrielawaai) [2]. The standard measurement methods which are described in this guide, make use of single, *omni-directional* microphones, as a part of simple sound level meters or more complicated spectral and statistical analyzers. These measurement methods can roughly be divided into two groups, i.e. emission and immission measurements.

Emission measurements are performed to find the acoustical power of the individual noise sources. If the individual sources are geometrically concentrated and if they behave like monopoles — giving a uniform radiation in all directions — the acoustic power can easily be calculated by measuring the sound pressure in the near field of the noise sources. However, these measurements can be difficult or even impossible if the noise sources have large dimensions and radiate with some directional characteristic. In addition, the emission measurements will be disturbed by the emitted sound of surrounding noise sources. After the emission powers have been determined, the immission noise levels are calculated by using a model of the sound transfer from the equivalent point sources to the immission sites of interest. Such a model will always deviate from the real transfer function by simplifications and/or inaccuracies due to ground absorption and screening. Furthermore, noise sources cannot always be modeled as monopoles.

Many of these problems can be overcome with immission measurements. In this case models of the noise sources and transfer functions are superfluous. However, in practice these measurements are often not feasible due to the influence of noise sources from other industrial areas or from traffic. For these reasons, most immission measurements are performed at closer sites. The results can then be extrapolated to the area of interest with a relatively simple transfer model. In many instances this method leads to good results, but the individual contributions of the different noise sources are not determined. For that reason it is often decided to perform the time consuming emission measurements as well, especially in those cases where the immission levels are too high, and expensive measures have to be taken to diminish the annoyance.

By now it will be clear that many measurement problems can be met by using a highly directional microphone at some well selected immission places. This gives the possibility to determine the immission from the different noise sources of interest *separately*, thereby avoiding the need for emission measurements — if possible at all — and yet giving the possibility to quantify the effect of the individual noise sources. To be useful in practical situations, such a microphone must have a high degree of directivity (at most a few degrees), in order to obtain a good separation between the noise sources under investigation. Of course, a directional microphone cannot distinguish between sources which lie behind each other. Therefore, the selection of the measurement sites must be done with care.

1.2 TYPES OF DIRECTIONAL SOUND MEASUREMENTS

Directional sound measurement techniques can be divided into the following groups:

a. Sound pressure-gradient techniques

The pressure-gradient can be measured with a microphone that responds to the difference in pressure at two closely spaced points. So, strictly speaking, this type of microphone does not measure the pressure-gradient ∇p, but its projection in one direction $\partial p/\partial n = \nabla p \cdot \mathbf{n}$. The directivity characteristic of such a microphone is given in figure 1.1a.
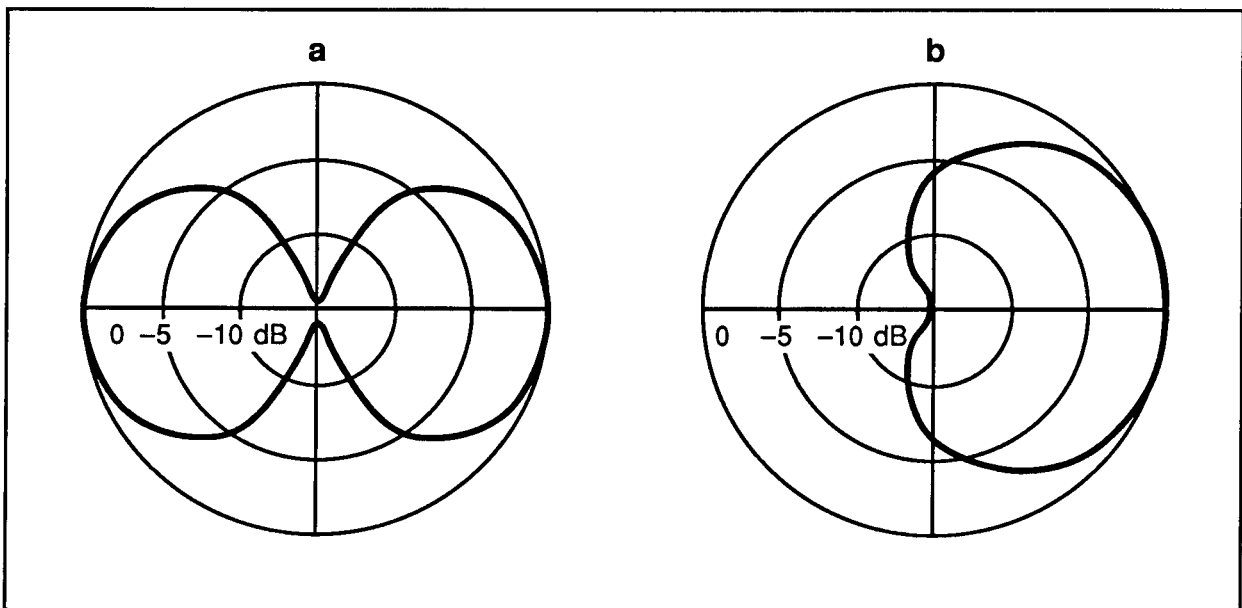
Figure 1.1: Directivity characteristics of a pressure-gradient microphone (a) and a combination pressure and pressure-gradient microphone (b).

A classical way of constructing a pressure-gradient microphone is by using a diaphragm of which both sides are exposed to the sound field (see for instance Beranek [3]). By using acoustic damping materials, it is possible to obtain a combined pressure and pressure-gradient sensitivity with a cardioid directivity characteristic (fig. 1.1b). This kind of microphone is widely used in sound reproduction and public address systems. Although these microphones can give a reasonable suppression of unwanted sound from certain directions, their directivity is poor. In conclusion it can be stated that a single directional microphone is not suitable for our purpose.

b. Sound intensity techniques

This measurement technique is based on the simultaneous measurement of the sound pressure $p(t)$ and the particle velocity $v(t)$, from which the intensity I_{av} can be estimated from the relation

$$I_{av} = E\{p(t) \cdot v(t)\} \quad . \tag{1.1}$$

In recent years the measurement of sound intensity has become very popular [4], especially for the determination of the sound power of individual noise sources by emission measurements. For directional immission measurements, the method might be applicable, because of the directional behavior of the intensity. At large distances, the soundfield can be described as a number of plane waves. The intensity of a plane wave is given by (see § 2.4.4):

$$I_{av} = \frac{p_{eff}^2}{\rho_0 c_0} n_i \tag{1.2a}$$

where p_{eff} is a measure for the immission level and n_i gives the direction of a particular plane wave. Here the same applies as for the pressure-gradient technique, that not I_{av} itself is measured, but its projection in the probe direction n, leading to:

$$I_{av} = \frac{p_{eff}^2}{\rho_0 c_0} n_i \cdot n \quad . \tag{1.2b}$$

Hence, the directivity of this method is essentially the same as shown in figure 1a; it is insufficient for our purposes.

c. Source-receiver correlations

If the positions of the noise sources are known, and if a signal can be obtained that is representative of the source signal, for instance with a microphone in the direct field of the source, then the coherent immission spectrum of that source can be found by measuring the auto- and cross-spectra of the source and receiver signals. For a description of the theory, the reader is referred to Bendat and Piersol [5]. Such a measurement technique looks promising, as it requires only two microphones, a signal delay line (to compensate for the acoustic wave travel time from source to receiver) and a two-channel spectrum (FFT) analyzer.

The performance of the source-receiver correlation technique was tested amongst others by Verhulst [6]. He found that this method does not give reliable results for source-receiver distances of more than 100 m. This is caused primarily by the fact that outdoor wave propagation is strongly influenced by meteorological factors like wind and temperature, especially near to the ground, leading to decorrelation of source and receiver signals (see also Chapter 3). Another fundamental difficulty with this method is to find a fully correlated source signal in case of distributed noise sources.

d. Source imaging techniques

These methods obtain their directivity from the measurement of the soundfield over an aperture which is large in relation to the wavelength of the sound field. All make use of constructive signal addition for a preferred distance and direction — thereby amplifying the output for a sound source at that position — and destructive interference for other source positions. The constructive signal addition is obtained by applying an appropriate time-shift to the received signals at each point of the aperture. This principle is illustrated in figure 1.2.
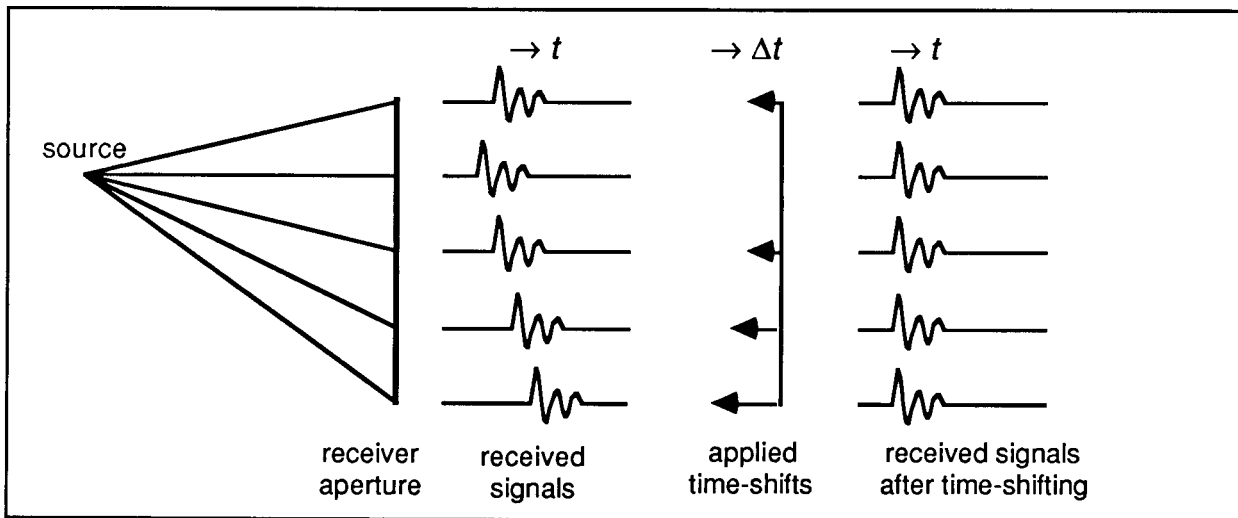
Figure 1.2: Illustration of the application of time-shifts to the receiver signals from a single source.

If we confine ourselves to plane receiver apertures, we can distinguish between three situations:

a. The general case where the source is at a finite or infinite distance and the medium is inhomogeneous. The inhomogeneities may give rise to a complicated time-shift pattern, caused by the spatial differences in the sound propagation speed of the medium.

b. The source is at a finite distance and the medium is considered to be homogeneous. In this case the wave field is spherical and the time-shifts are hyperbolic along the aperture.

c. The source is at infinity and the medium is homogeneous, leading to a plane wave with linear time-shifts along the aperture. In practice this situation occurs if the source is at such a large distance from the receiver that the incident spherical wave field can be approximated as a plane wave along the antenna (the Fraunhofer approximation).

In outdoor sound propagation the inhomogeneities are mainly caused by wind and temperature differences. This leads to only small variations in the time-shifts, compared with the hyperbolic or linear time-shifts which occur in a homogeneous medium. As a consequence, the inhomogeneities can be neglected here in first approximation.
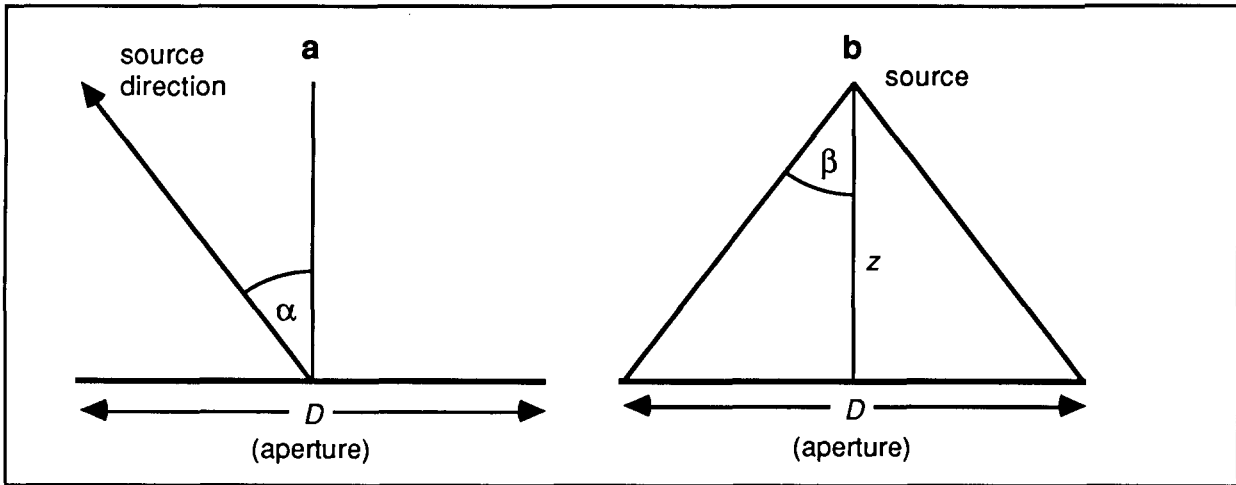
Figure 1.3: a. Definition of the source direction α in the far field; b. Definition of the illumination angle β in the near field.

For sound sources at large distances the lateral resolving power of the source imaging techniques is generally defined by:

$$B = \lambda / (D \cos \alpha) \qquad (1.3)$$

where B is a measure for the resolving power or resolution in radians, defined as the minimum detectable separation angle between the radiating sources (see Chapter 2), λ is the wavelength of the radiation, D is the aperture of the antenna system and α is the angle between the source direction and the plane normal to the aperture, as indicated in figure 1.3a.

In the near field the lateral resolving power for frontal incidence is given by (see Berkhout [7]):

$$B = \lambda / (2z \sin \beta) \qquad (1.4)$$

where β is the maximum aperture angle as indicated in figure 1.3b. At large distances $\sin \beta \approx$ $1/2 \, D/z$ so that Eq. (1.4) approximates Eq. (1.3) for frontal incidence.

Eq. (1.3) and (1.4) describe general physical laws that are valid in all wave field oriented disciplines like optics, radio astronomy, acoustics and seismology.

We mention two classical examples of antenna techniques in acoustics. One is the parabolic reflector with a pressure-sensitive microphone in the focal point. Here the maximum sensitivity is in the direction $\alpha = 0$. Such a configuration is called *broad-side*. The other example is the interference microphone, which makes use of a leaky wave conducting tube. Its maximum sensitivity is in the direction $\alpha = 90°$. This is called an *end-fire* configuration.

An often used approach to source imaging is the synthetic antenna principle. Given a one- or two-dimensional array of transducers, the output signal of each transducer is electrically or numerically (after sampling) time shifted and weighted, and all signals are then summed in such a way that a maximum output is obtained for one source direction and a smaller output for other

directions. The synthetic antenna principle is well known in underwater acoustics, where it finds its application in passive sonar systems, and in radio astronomy where even radio waves collected by telescopes which are thousands of kilometers apart are recorded simultaneously and subsequently added together [8], giving a resolving power of 0.0001 arc-second. For our purposes a one-dimensional horizontal array is sufficient, because resolution is only required in the horizontal plane.With some array techniques it is possible to get an even higher resolution than given by Eq. (1.3) and (1.4). These *super resolution techniques* require additional information about the sources and their transfer functions (see Chapter 7).

1.3   THE CHOICE OF OUR MEASUREMENT SYSTEM

As discussed in the preceding section, there are several ways to perform directional sound measurements. Here we will discuss the applicability of these measurement techniques for directional acoustic noise immission measurements.

The most important physical factors which have to be taken into account are:

- **Resolving power of the system.** In order to separate the contributions of different noise sources, the resolving power of the system must be as high as possible, preferably a few degrees at the most.

- **Frequency range and spectral resolution.** The standard immission measurement procedures prescribe the use of octave bands with midband frequencies ranging from 31.5 Hz to 8000 Hz. In many practical situations a more restricted frequency range is permitted, dependent on source spectrum, screening, atmospheric damping and A-weighting. Concerning the spectral resolution it must be mentioned that for more precise calculations, measurements in $1/3$-octave bands give sufficient resolution in most practical situations.

- **Calibration.** The system must not only be able to find the directions of the noise sources (in many cases the source positions are known in advance) and their relative strengths; it must also be possible to measure the correct immission levels of the individual sources. The calibration must be feasible under well defined conditions, preferably in an anechoic chamber.

In addition some practical requirements need to be considered:

- **Investments and maintenance costs.** In this regard we also have to take into account the availability of equipment and the necessity of manufacturing certain parts of the system in house.

- **Mobility.** The system should be transportable and manageable in the field.

In the design of our measurement system the resolving power plays a major role. As discussed in Section 1.2, a high directionality cannot be expected from small transducer systems such as the pressure gradient microphone and the intensity probe. We also mentioned that the

applicability of the correlation technique is limited severely by the source-receiver decorrelation and by the fundamental difficulty of measuring a fully correlated source signal when noise sources are distributed.

Let us now take a closer look at the source imaging techniques. As shown in Eq. (1.3), the resolving power of an antenna in the far field is given by the ratio λ/D, assuming that the source direction $\alpha \approx 0°$. This means that for a resolving power of 2°, or 0.035 rad, an aperture of $D = \lambda/0.035 = c/(0.035\ f) \approx 10000/f$ is needed. Here c is the sound velocity (340 m/s) and f is the frequency in Hz. This leads to an aperture or antenna length of 100 m at a frequency of 100 Hz, or even longer for still lower frequencies. It will be clear that these apertures can only be realized with synthetic antennas and not with acoustic reflectors or interference tubes.

The concept of synthetic antenna techniques is not new to acoustic noise measurements. Two systems were developed specially for noise source localization of jet engines. The first is the Acoustic Telescope of Billingsley et al. [9], where use is made of a linear microphone array and numerical beam steering. A disadvantage of a linear array is that, in order to avoid multiple main lobes due to *spatial aliasing* (see Chapter 2), a large number of microphones has to be used. The second system is the Polar Correlation Technique used by Fisher et al. [10], which measures the spatial correlation function on a polar arc around the expected noise region. If the measurements are performed with a full (polar) array, this method also needs a large number of microphones. It is however possible to measure the spatial correlation functions with a smaller number of microphones. In that case some microphones have to be repositioned during the measurements, and the spatial correlation functions are measured sequentially. This procedure can be carried out with as few as two microphones. A disadvantage of this approach is that the noise sources need to be stationary in time and place during the measurements.

Another possibility to reduce the number of microphones considerably is obtained by using a special signal processing technique, known as sparsed array processing. This technique — which is also based on the measurement of the spatial correlation functions — has been applied successfully in radio astronomy (a well-known example is the radio interferometer of the Westerbork Observatory), but also for industrial noise source identification. In a research program, supported by the French government, the outdoor sound propagation was studied by Escudié et al. [11] and a synthetic acoustic antenna (based on sparsed array processing) was developed by them with a resolving power of 5° to 10° [12]. This antenna was demonstrated during a conference on noise source identification [13]. It clearly showed the possibility of constructing a synthetic antenna that is mobile and operated easily in the field.

An advantage of sparsed array processing is that the array can be constructed in such a way that all signals that have to be correlated can be measured simultaneously, which makes this technique not critically dependent on the stationarity of the sound field.

From a theoretical viewpoint the concept of a synthetic acoustic antenna looks most promising, although one has to pay attention to the fact that the resolving power given in Eq. (1.3) is a theoretical expectation for an ideal, undisturbed field. As in the case of the source-receiver correlations, the atmospheric turbulence will again reduce the correlation of the wave field along the aperture. This phenomenon is called the *mutual* or *transverse coherence loss*. It was measured by Ningre [14] as a part of the research for the synthetic acoustic antenna of Escudié et al. [12]. From his results we concluded that a much better resolution could be obtained than the resolving power of 5° to 10° of their antenna, although it had to be considered that Ningre carried out his measurements over the surface of the sea, and that the transverse coherence loss might be worse over land. For that reason we investigated the transverse coherence loss over grassland in studies reported by Bergsma [15] and Hoyer [16]. The results were used in computer simulations of a high-resolution sparsed array antenna. These simulations showed that a resolving power of a few degrees was attainable under practical meteorological conditions, even for source distances of more than 1 kilometer.

We finally decided to base our antenna system SYNTACAN on one-dimensional sparsed synthetic array processing, because of the following reasons:

a. Resolution is only required in the horizontal plane;

b. Synthetic array processing gives the possibility of an integrated system approach in which hardware and software can be combined optimally, and new features can easily be added to the system at a later stage;

c. Sparsed array processing is possible with a relatively small number of microphones. It also gives the possibility to measure all signals that have to be correlated simultaneously, so that the method is not critically dependent on the stationarity of the sound field. As we will see in Chapter 2 there are some drawbacks for correlated noise sources, but usually this is not a serious problem with industrial noise sources at large distances;

d. From our simulations based on measurements of the transverse coherence loss, the high resolution of 1 to 2 degrees could be expected under proper meteorological conditions (within the so-called "meteorological window"), which was sufficient for the applications we had in mind, and was considerably better than the resolution of existing systems;

e. Theoretical and experimental studies did show that our antenna system is also well suited for resolution enhancement techniques, like beampattern deconvolution and parametric model inversion. By making use of a-priori information about the source positions, these techniques can lead to so-called super-resolution (see Chapter 7).

During the development of SYNTACAN a number of problems had to be solved:

a. Optimization of the resolving power for a broad frequency range with a minimal number of microphones. This problem was solved by the design of a synthetic antenna in which redundant microphone positions are eliminated by a very efficient sparsing scheme, and by separate data processing for each octave band.

b. Mechanical and electronic construction of the antenna system. This included the selection, design and development of the microphones, the installation material such as tripods and cables, preamplifiers, and the data acquisition and computer system.

c. Software development. Because of the dedicated system design, most of the application software had to be developed specially. Great attention was given to the user interface, to obtain a system that is easy to use and is reliable, and to the post-processing of the results. The results are obtained in a standardized format which is compatible with conventional immission measurements.

Many of these problems could only be solved adequately after we had gained practical experience with the system in a proto-type form. In addition some features were installed for special applications for which the system was not developed originally. The most important of these applications are the noise source characterization of windturbines and the source height localization of passing vehicles. For the latter application the antenna has to be installed vertically.

In its present form, SYNTACAN has as main characteristics:

* array length: horizontally max. 76.65 m with 32 microphones, vertically max. 9.45 m with 20 microphones;
* frequency range: 89 to 1413 Hz in 4 octave bands of 125, 250, 500 and 1000 Hz;
* spectral resolution: $^1/_{12}$ octave band;
* angular range: $-30°$ to $+30°$ with regard to the main direction of the antenna (broad-side);
* resolving power: $1.5° \pm 0.5°$;
* triggering on external events;
* time windowing to get sharp images of moving noise sources;
* automatic canceling of measurements when overload conditions occur;
* automatic logging of environmental information such as the moment of time of measurement, meteorological conditions, omni-directional immission levels and operator comments;
* post-processing with focussing on the source distance and presentation of the results in various formats, like polar diagrams per octave, spectral diagrams for any direction and integrated over an arbitrary angular range.

CHAPTER 2

THEORY

2.1 INTRODUCTION

Since the propagation of sound through the outdoor environment is strongly influenced by meteorological factors such as wind and temperature, it is not easy to describe this propagation in a closed mathematical form. For computational purposes, however, it is convenient to divide the propagation into three parts:

a. a deterministic part, based on the linear wave equation for a homogeneous medium without flow and temperature gradients;

b. a deterministic part, due to a stationary[1] wind flow and stationary temperature gradients;

c. a statistical part, due to random air movements caused by wind turbulence and random variations in temperature.

In this chapter we will first derive the wave equation under various conditions and present solutions for plane waves and point sources (monopoles). Special attention will be given to the important situation of a stationary and uniform wind flow. We will then continue with the antenna theory, based on spatial correlation functions of the wavefield in a homogeneous flowless medium. This forms the basis of our antenna design.

For a discussion of the effects of wind and temperature on the antenna performance, the reader is referred to Chapter 3.

---

[1]stationary is used for time independence

2.2   THE WAVE EQUATION OF A HOMOGENEOUS, STATIONARY MEDIUM

For the derivation of the wave equation we will use as symbols:

p = acoustic pressure;

p_0 = static pressure;

p_t = total pressure: $p_t = p_0 + p$

and similarly for the density of the air:

$\rho_t = \rho_0 + \rho$

and for the velocity of the air particles:

$\mathbf{v}_t = \mathbf{v}_0 + \mathbf{v}$.

In a homogeneous and flow-less medium p_0 and ρ_0 are constant and $\mathbf{v}_0 = \mathbf{0}$. In this case the loss-free, linear wave equation is easily derived from the basic physical relations which apply to an arbitrary small volume of air, assuming no external forces:

a. Conservation of momentum (shear forces and viscosity are neglected):

$$-\nabla p = \rho_0 \frac{\partial \mathbf{v}}{\partial t} \quad . \tag{2.1}$$

b. Conservation of mass:

$$-\nabla \cdot \mathbf{v} = \frac{1}{\rho_0} \frac{\partial \rho}{\partial t} \quad . \tag{2.2}$$

c. The adiabatic equation of state:

$$p_t \rho_t^{-\kappa} = \text{constant} \tag{2.3}$$

with κ = the ratio between the specific heats c_p and c_v.

From Eq. (2.3) it can be found after linearization that

$$\frac{\partial \rho}{\partial t} = \frac{\rho_0}{\kappa p_0} \frac{\partial p}{\partial t} \quad . \tag{2.4}$$

Combination of Eq. (2.2) and (2.4) gives:

$$-\nabla \cdot \mathbf{v} = \frac{1}{\kappa p_0} \frac{\partial p}{\partial t} = \frac{1}{K} \frac{\partial p}{\partial t} \quad , \tag{2.5}$$

where K is the compression modulus. Eq. (2.5) is known as Hooke's law.

By taking the divergence of Eq. (2.1) and after substitution of the time derivative of Eq. (2.5), the wave equation of the acoustic pressure is obtained:

$$\nabla^2 p = \frac{1}{c^2} \frac{\partial^2 p}{\partial t^2} \tag{2.6a}$$

with

$$c^2 = \kappa p_0 / \rho_0 \quad . \tag{2.6b}$$

The quantity c is called the sound velocity.

In the case of an ideal gas, the ratio of static pressure and density is given by

$$p_0 / \rho_0 = RT/M \quad , \tag{2.7}$$

with R = gasconstant, T = temperature in K and M = molecular weight. Substitution of Eq. (2.7) in (2.6b) gives

$$c = \sqrt{\kappa RT/M} \quad . \tag{2.8}$$

So, for a particular ideal gas, the sound velocity is only dependent on temperature. If we apply this result to air, by approximating it as an ideal gas with molecular weight M = 29, and if we also substitute the numerical values κ = 1.4 and R = 8.28×10^3, then Eq. (2.8) reduces to

$$c = 20 \sqrt{T} = 20 \sqrt{273 + T_c} \quad , \tag{2.9}$$

with T_c = temperature in °C (For T_c = 20 °C we find c = 342 m/s).

We now give some well known solutions of the wave equation:

a. A plane wave travelling in the $+x$-direction

In this case the acoustic pressure is only a function of time and the x-coordinate, which simplifies Eq. (2.6a) to the one-dimensional wave equation:

$$\frac{\partial^2 p}{\partial x^2} = \frac{1}{c^2} \frac{\partial^2 p}{\partial t^2} \tag{2.10}$$

with the solution:

$$p(x, t) = p(t - x/c) \quad . \tag{2.11}$$

b. A plane wave travelling in the x-y plane

For an arbitrary plane wave in the x-y plane the solution can be obtained from Eq. (2.11) by rotation of the coordinate system (see fig. 2.1) which gives:

$$p(x, y, t) = p(t - x/c_x + y/c_y) \tag{2.12}$$

with $c_x = c/\sin \alpha$ and $c_y = c/\cos \alpha$, for a plane wave travelling in the (+x,−y) direction.
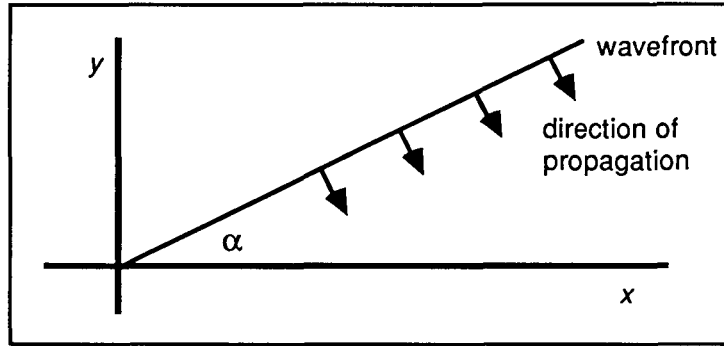
Figure 2.1: A plane wave travelling in the x-y plane.

c. The spherical wave of a pointsource (monopole)

Here the acoustic pressure is only a function of time and the distance r to the pointsource. In polar coordinates the wave equation is:

$$\frac{\partial^2 p}{\partial r^2} + \frac{2}{r} \frac{\partial p}{\partial r} = \frac{1}{c^2} \frac{\partial^2 p}{\partial t^2} \tag{2.13}$$

with the solution of the waves travelling away from the monopole:

$$p(r, t) = \frac{s(t - r/c)}{r} \quad , \tag{2.14}$$

where $s(t)$ is called the source function of the monopole. If the source distance is large, the wave front can locally be approximated as a plane wave. This is called the Fraunhofer approximation.

2.3 THE WAVE EQUATION IN A MEDIUM WITH NON-UNIFORM FLOW AND TEMPERATURE

As a first order approximation, wave propagation outdoors can be described with the linear, homogeneous wave equation of Eq. (2.6a). The propagation will, however, be disturbed by two meteorological factors, viz. wind and temperature, which both can be a function of time and space.

2.3.1 The influence of wind

In a moving medium the wave equation is governed by the same basic physical relations as for a stationary medium, but now the time derivative $\partial/\partial t$ has to be replaced by $\partial/\partial t + (v_t \cdot \nabla)$. The term $(v_t \cdot \nabla)$ is usually neglected in a flow-free medium, which is permitted under linear acoustic conditions: when $|v_t/c| \ll 1$. In a moving medium this simplification is not allowed. The equation for the conservation of momentum is now given by

$$-\nabla p = \rho_0 \frac{\partial v_t}{\partial t} + \rho_0 (v_t \cdot \nabla) v_t \tag{2.15}$$

and Eq. (2.5) is replaced by

$$-\nabla \cdot v_t = \frac{1}{K} \left[\frac{\partial p}{\partial t} + (v_t \cdot \nabla) p \right] . \tag{2.16}$$

Combination of Eq. (2.15) and (2.16) gives the general wave equation

$$\rho_0 \nabla \cdot (\frac{1}{\rho_0} \nabla p) - \frac{1}{c^2} \left[\frac{\partial^2 p}{\partial t^2} + \frac{\partial}{\partial t} (v_t \cdot \nabla) p \right] + \rho_0 \nabla \cdot (v_t \cdot \nabla) v_t = 0 . \tag{2.17}$$

The equation is very general as it allows for unrestricted variations of v_t as a function of time and space. However, it is difficult to solve. We will show that under certain conditions Eq. (2.17) can be simplified considerably. The last term of Eq. (2.17) can be worked out to give

$$\rho_0 \nabla \cdot (v_t \cdot \nabla) v_t = \rho_0 (v_t \cdot \nabla) \nabla \cdot v_t + \rho_0 s \tag{2.18a}$$

with

$$s = (\frac{\partial v_t}{\partial x} \cdot \nabla) v_{tx} + (\frac{\partial v_t}{\partial y} \cdot \nabla) v_{ty} + (\frac{\partial v_t}{\partial z} \cdot \nabla) v_{tz} . \tag{2.18b}$$

Here v_{tx}, v_{ty} and v_{tz} are the components of v_t in the directions x, y and z resp.
Substitution of Eq. (2.18) in (2.17), making use of (2.16) gives

$$\rho_0 \nabla \cdot (\frac{1}{\rho_0} \nabla p) - \frac{1}{c^2}\left[\frac{\partial^2 p}{\partial t^2} + \frac{\partial}{\partial t}(v_t \cdot \nabla)p + (v_t \cdot \nabla)\frac{\partial p}{\partial t} + (v_t \cdot \nabla)(v_t \cdot \nabla)p \right] = -\rho_0 s \quad . \tag{2.19}$$

Although Eq. (2.17) and (2.19) are of similar complexity, the latter is better suited for further simplifications that will be introduced now.

a. Linear acoustics

We recall that $v_t = v_0 + v$, where v_0 is the wind velocity and v is the acoustic particle velocity. Under the conditions of linear acoustics, $|v/c| \ll 1$. This condition is fulfilled under most practical circumstances For instance, for a plane wave with $L_p = 100$ dB (re 20 μPa), $v = 0.0045$ m/s. Under this assumption, Eq. (2.19) reduces to:

$$\rho_0 \nabla \cdot (\frac{1}{\rho_0} \nabla p) - \frac{1}{c^2}\left[\frac{\partial^2 p}{\partial t^2} + \frac{\partial}{\partial t}(v_0 \cdot \nabla)p + (v_0 \cdot \nabla)\frac{\partial p}{\partial t} + (v_0 \cdot \nabla)(v_0 \cdot \nabla)p \right] = -\rho_0 s \tag{2.20}$$

with s given by Eq. (2.18b). Note that the expression for s cannot be simplified yet, as no assumptions have been made about the spatial derivatives of v_0.

b. Stationary windspeed

When there are no temporal changes in the windspeed, Eq. (2.20) reduces to:

$$\rho_0 \nabla \cdot (\frac{1}{\rho_0} \nabla p) - \frac{1}{c^2}\left[\frac{\partial^2 p}{\partial t^2} + 2(v_0 \cdot \nabla)\frac{\partial p}{\partial t} + (v_0 \cdot \nabla)(v_0 \cdot \nabla)p \right] = -\rho_0 s \quad , \tag{2.21}$$

with s still given by Eq. (2.18b).

Note that under these conditions (linear acoustics + stationary windspeed), the equation of motion, Eq. (2.15) can be written as:

$$-\nabla p = \rho_0 \frac{\partial v}{\partial t} + \rho_0 (v_0 \cdot \nabla)v \quad , \tag{2.22}$$

a result that will be used later.

c. Stratified medium with stationary windspeed

The expression for s, as given by Eq. (2.18b) can be simplified considerably in a stratified medium, where the windspeed $v_0 = (v_{0x}, v_{0y}, v_{0z})$ is zero in the vertical direction: $v_{0z} = 0$, and where the spatial derivatives of v_0 are only a function of the height z, so $\partial v_0/\partial x = 0$ and $\partial v_0/\partial y = 0$.

Under these conditions we find:

$$\left(\frac{\partial \mathbf{v_t}}{\partial x}\cdot\nabla\right)v_{tx} = \left(\frac{\partial \mathbf{v_0}}{\partial x}\cdot\nabla\right)v_{0x} + \left(\frac{\partial \mathbf{v_0}}{\partial x}\cdot\nabla\right)v_{x} + \left(\frac{\partial \mathbf{v}}{\partial x}\cdot\nabla\right)v_{0x} + \left(\frac{\partial \mathbf{v}}{\partial x}\cdot\nabla\right)v_{x} \quad .$$

$$(2.23a)$$

In this expression $\partial v_0/\partial x = 0$ because of the stratification. The term $(\partial v/\partial x\cdot\nabla)v_x$ is a convection term that may be neglected under the condition of linear acoustics, so Eq. (2.23.a) becomes:

$$\left(\frac{\partial \mathbf{v_t}}{\partial x}\cdot\nabla\right)v_{tx} = \left(\frac{\partial \mathbf{v}}{\partial x}\cdot\nabla\right)v_{0x} = \frac{\partial v_z}{\partial x}\frac{\partial v_{0x}}{\partial z} \quad ,$$

$$(2.23b)$$

due to the stratification. In the same way we find

$$\left(\frac{\partial \mathbf{v_t}}{\partial y}\cdot\nabla\right)v_{ty} = \frac{\partial v_z}{\partial y}\frac{\partial v_{0y}}{\partial z}$$

$$(2.23c)$$

and

$$\left(\frac{\partial \mathbf{v_t}}{\partial z}\cdot\nabla\right)v_{tz} = \left(\frac{\partial \mathbf{v_0}}{\partial z}\cdot\nabla\right)v_{tz} = \frac{\partial v_{0x}}{\partial z}\frac{\partial v_z}{\partial x} + \frac{\partial v_{0y}}{\partial z}\frac{\partial v_z}{\partial y} \quad .$$

$$(2.23d)$$

Substitution of these results in Eq. (2.21) gives:

$$\rho_0\nabla\cdot\left(\frac{1}{\rho_0}\nabla p\right) - \frac{1}{c^2}\left[\frac{\partial^2 p}{\partial t^2} + 2(\mathbf{v_0}\cdot\nabla)\frac{\partial p}{\partial t} + (\mathbf{v_0}\cdot\nabla)(\mathbf{v_0}\cdot\nabla)p\right] =$$

$$- 2\rho_0\left[\frac{\partial v_{0x}}{\partial z}\frac{\partial v_z}{\partial x} + \frac{\partial v_{0y}}{\partial z}\frac{\partial v_z}{\partial y}\right] \quad .$$

$$(2.24)$$

d. Stationary and uniform windspeed

Under these conditions, Eq. (2.21) is valid with $s = 0$:

$$\rho_0\nabla\cdot\left(\frac{1}{\rho_0}\nabla p\right) - \frac{1}{c^2}\left[\frac{\partial^2 p}{\partial t^2} + 2(\mathbf{v_0}\cdot\nabla)\frac{\partial p}{\partial t} + (\mathbf{v_0}\cdot\nabla)(\mathbf{v_0}\cdot\nabla)p\right] = 0 \quad .$$

$$(2.25)$$

2.3.2 The influence of temperature

The influence of temperature fluctuations can be easily quantified by realizing that temporal and spatial variations of the temperature will give rise to temporal and spatial variations of the static pressure p_0 and density ρ_0, leading to variations in the sound velocity c. If the sound velocity is c_0 at the average temperature T_0 of the medium, then it follows from Eq. (2.8) that, when we approximate the air as an ideal gas and define $\Delta T = T - T_0$:

$$c = c_0(1 + \Delta T/T_0)^{1/2} \quad .$$

$$(2.26)$$

For a general description of the temperature effects on the sound propagation, Eq. (2.19) has to be used, where ρ_0 and c are functions of the temperature. Notice that the difference in temperature will in general involve pressure differences, leading to a dynamic behavior of the convection v_0. Such a situation usually can not be described analytically, and use has to be made of statistical methods (see Section 3.3). In a stable temperature distribution, with only small temperature changes, the spatial dependence of ρ_0 and c will be very gradual. In such a situation, if we also assume a constant and uniform windspeed, combination of Eq. (2.25) and (2.26) will give as a first order approximation:

$$\nabla^2 p = \frac{1}{c_0^2}(1 - \Delta T/T_0)\left[\frac{\partial^2 p}{\partial t^2} + 2(\mathbf{v}_0 \cdot \nabla)\frac{\partial p}{\partial t} + (\mathbf{v}_0 \cdot \nabla)(\mathbf{v}_0 \cdot \nabla)p\right] . \tag{2.27}$$

If the temperature is uniform, we get the important wave equation for a homogeneous medium with a stationary and uniform windspeed:

$$\nabla^2 p = \frac{1}{c_0^2}\left[\frac{\partial^2 p}{\partial t^2} + 2(\mathbf{v}_0 \cdot \nabla)\frac{\partial p}{\partial t} + (\mathbf{v}_0 \cdot \nabla)(\mathbf{v}_0 \cdot \nabla)p\right] . \tag{2.28}$$

2.4 SOUND PROPAGATION IN A MEDIUM WITH STATIONARY AND UNIFORM FLOW

As we will see in Section 3.2, the windspeed can give rise to an error in the observation of the source directions with the antenna. The description of propagation through a moving medium has led to many discussions in the literature and also to wrong conclusions. For that reason the subject will be treated here with great care.

2.4.1 Solutions of the wave equation for a medium with stationary and uniform flow

If $p(\mathbf{r}, t)$ is a solution of the wave equation of a homogeneous and flow-less medium:

$$\nabla^2 p = \frac{1}{c_0^2}\frac{\partial^2 p}{\partial t^2} \tag{2.29}$$

then

$$p^*(\mathbf{r}, t) = p(\mathbf{r} - \mathbf{v}_0 t, t) \tag{2.30}$$

is a solution of wave equation (2.28) for a homogeneous medium with a stationary and uniform windspeed, so

$$\nabla^2 p^* = \frac{1}{c_0^2}\left[\frac{\partial^2 p^*}{\partial t^2} + 2(\mathbf{v}_0 \cdot \nabla)\frac{\partial p^*}{\partial t} + (\mathbf{v}_0 \cdot \nabla)(\mathbf{v}_0 \cdot \nabla)p^*\right] \ . \tag{2.31}$$

This can be verified by substitution of

$$\nabla^2 p^* = \nabla^2 p \ ; \tag{2.32a}$$

$$\frac{\partial p^*}{\partial t} = -(\mathbf{v}_0 \cdot \nabla)p + \frac{\partial p}{\partial t} \ ; \tag{2.32b}$$

$$\frac{\partial^2 p^*}{\partial t^2} = (\mathbf{v}_0 \cdot \nabla)(\mathbf{v}_0 \cdot \nabla)p - 2(\mathbf{v}_0 \cdot \nabla)\frac{\partial p}{\partial t} + \frac{\partial^2 p}{\partial t^2} \tag{2.32c}$$

into Eq. (2.31), leading to Eq. (2.29).

In the same way it can be proved that when $\mathbf{v}(\mathbf{r}, t)$ is a solution of the wave equation in the flow-less medium:

$$\nabla^2 \mathbf{v} = \frac{1}{c_0^2}\frac{\partial^2 \mathbf{v}}{\partial t^2} \tag{2.33}$$

that

$$\mathbf{v}^*(\mathbf{r}, t) + \mathbf{v}(\mathbf{r} - \mathbf{v}_0 t \ , t) \tag{2.34}$$

is valid in the moving medium, so that

$$\nabla^2 \mathbf{v}^* = \frac{1}{c_0^2}\left[\frac{\partial^2 \mathbf{v}^*}{\partial t^2} + 2(\mathbf{v}_0 \cdot \nabla)\frac{\partial \mathbf{v}^*}{\partial t} + (\mathbf{v}_0 \cdot \nabla)(\mathbf{v}_0 \cdot \nabla)\mathbf{v}^*\right] \ . \tag{2.35}$$

2.4.2 Sound rays in a moving medium

Sound rays are defined as the lines along which the acoustic energy transport takes place.

We will first analyze the acoustic energy transport in a stationary medium with the same method as described by Pierce [17]. We start with the two basic equations (2.1) and (2.5) for a loss-free medium:

$$-\nabla p = \rho_0 \frac{\partial \mathbf{v}}{\partial t} \tag{2.36}$$

and

$$-\nabla \cdot \mathbf{v} = \frac{1}{\rho_0 c_0^2} \frac{\partial p}{\partial t} \quad . \tag{2.37}$$

Taking the inner product of Eq. (2.36) with $\mathbf{v}$ gives

$$\mathbf{v} \cdot \left(\rho_0 \frac{\partial \mathbf{v}}{\partial t} \right) = -\mathbf{v} \cdot \nabla p = -\nabla \cdot (p\mathbf{v}) + p\nabla \cdot \mathbf{v} \tag{2.38}$$

from which we find after substitution of Eq. (2.36) and (2.37):

$$\frac{\partial}{\partial t} E + \nabla \cdot \mathbf{I} = 0 \tag{2.39a}$$

with

$$E = \frac{1}{2}\rho_0 v^2 + \frac{1}{2} \frac{1}{\rho_0 c_0^2} p^2 \tag{2.39b}$$

and

$$\mathbf{I} = p\mathbf{v} \quad . \tag{2.39c}$$

Application of Gauss' theorem to Eq. (2.39a) gives

$$\frac{\partial}{\partial t} \iiint_V E \, dV + \iint_S \mathbf{I} \cdot \mathbf{n}_s \, dS = 0 \tag{2.40}$$

where V represents a volume with surface S and $\mathbf{n}_s$ is the normal to the surface. Note that $\iiint_V E \, dV$ represents the total potential and kinetic energy within the volume and Eq. (2.40) shows that $\iint_S \mathbf{I} \cdot \mathbf{n}_s \, dS$ represents the net power-flow through the closed surface S. If there are no acoustic sources within V, we obtain in a stationary situation after time averaging that $\iiint_V E_{av} \, dV$ will be constant (loss-free medium) and

$$\iint_S \mathbf{I}_{av} \cdot \mathbf{n}_s \, dS = 0 \quad . \tag{2.41}$$

We will now take for S a tube-shaped surface with S' in the direction of $\mathbf{I}_{av}$ and S_1 and S_2 perpendicular to it (see figure 2.2). For this surface, S' will not give any contribution to the integral of Eq. (2.41) and for this special surface we find $\iint \mathbf{I}_1 \cdot \mathbf{n}_s \, dS_1 = -\iint \mathbf{I}_2 \cdot \mathbf{n}_s \, dS_2$, showing that all energy, entering the tube through S_1, will leave the tube through S_2.

We will call such a tube a ray-tube and define a ray as a ray-tube of which the cross-section approaches zero. Hence, a ray is defined as the path along which the acoustic energy is transported. In a medium in rest, the rays have the same direction as $\mathbf{I}_{av}$.
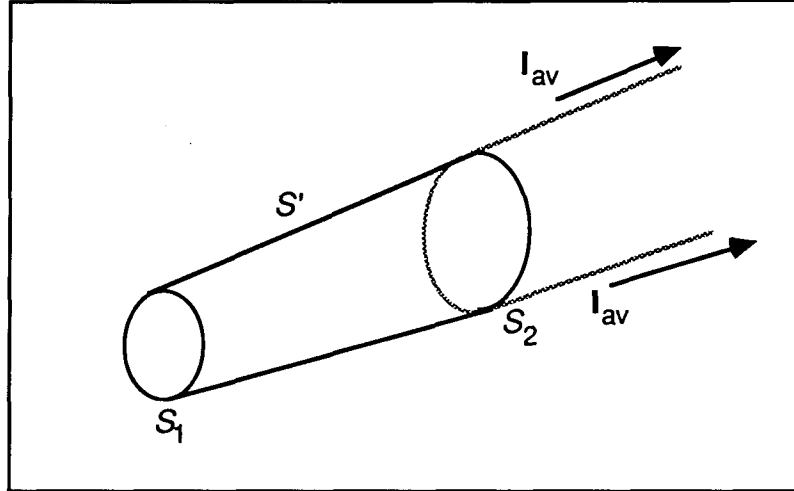
Figure 2.2: A tube-shaped surface along the direction of the particle velocities, representing a ray-tube in a stationary medium.

We will now derive the ray-paths in a moving medium, using the same argumentation as we used for the stationary medium. For a moving medium, the basic equations (2.36) and (2.37) must be replaced by (see also Section 2.3):

$$-\nabla p = \rho_0 D_t \mathbf{v} \tag{2.42}$$

and

$$-\nabla \cdot \mathbf{v} = \frac{1}{\rho_0 c_0^2} D_t p \tag{2.43}$$

where D_t stands for the total differential $D_t = \partial/\partial t + \mathbf{v}_t \cdot \nabla$. From these equations we find in the same way as above:

$$D_t E + \nabla \cdot \mathbf{I} = 0 \tag{2.44a}$$

or

$$\frac{\partial}{\partial t} E + \mathbf{v}_t \cdot \nabla E + \nabla \cdot \mathbf{I} = 0 \quad . \tag{2.44b}$$

Under the assumption of linear acoustics, $\mathbf{v}_t \cdot \nabla$ may be replaced by $\mathbf{v}_0 \cdot \nabla$ (we did the same in Section 2.3 when we derived the wave equation for a moving medium), giving:

$$\frac{\partial}{\partial t} E + \nabla \cdot (\mathbf{I} + \mathbf{v}_0 E) = 0 \quad . \tag{2.44c}$$

Application of Gauss' theorem gives:

$$\frac{\partial}{\partial t} \iiint_V E dV + \iint_S (\mathbf{I} + \mathbf{v}_0 E) \mathbf{n}_s dS = 0 \quad . \tag{2.45}$$

This result shows that in a medium, moving with velocity $\mathbf{v}_0$, the energy within a volume V is not only changed by the net power-flow of the acoustic field, but also by the energy transportation of the moving medium. From our definition that a ray is the path along which the acoustic energy is transported, we find that the rays are in the direction given by:

$$\mathbf{n}_r = (\mathbf{I}_{av} + \mathbf{v}_0 E_{av}) / \left| \mathbf{I}_{av} + \mathbf{v}_0 E_{av} \right| \quad . \tag{2.46}$$

From this result we can conclude that in a moving medium the sound rays generally are not in the direction of $\mathbf{I}_{av}$, as is the case in a flow-less medium.

2.4.3 Fermat's principle in a moving medium

The original *principle of least time* as formulated in 1657 by Pierre de Fermat, states that a ray-path, connecting two points in a wave field, is such that the travel time along the ray is a minimum. According to Pierce [17]: *"it was recognized by W.R. Hamilton (1833) that there are exceptions to this and the correct statement is that the actual path is stationary with respect to other adjacent paths"*. Fermat's principle, as modified by Hamilton, can be expressed with the variational equation:

$$\delta \int_A^B \frac{1}{c} ds = 0 \tag{2.47}$$

where c = propagation speed and ds is an incremental displacement along the path. Note that

$$\tau_{AB} = \int_A^B \frac{1}{c} ds \tag{2.48}$$

is the traveltime along the ray-path from A to B. It must be noted that Fermat formulated his principle for optical rays. Starting from Eq. (2.47), the law of rectilinear propagation in a homogeneous medium, the law of mirrors for reflections, and Snell's law of refraction can be derived, so Fermat's principle is a cornerstone of the classical optical ray theory. The principle can, however, also be applied to acoustic fields. There the theory usually starts with the wave equation, but when a ray description is appropriate, Fermat's principle can be used as well.

For a medium in rest, Fermat's principle can be applied in the same way as for optical rays. In a moving medium the situation is more complicated. For instance, it cannot be assumed a priori that Fermat's principle is valid then. The general proof that Eq. (2.47) holds in a moving medium is given by Ugincius [18]. He shows that along a ray-path Eq. (2.47) is valid if c is replaced by the ray velocity c_{ray}:

$$\delta \int_A^B \frac{1}{c_{ray}} \, ds = 0 \quad , \tag{2.49}$$

with c_{ray} given by:

$$\mathbf{c}_{ray} = c_0 \mathbf{n} + \mathbf{v}_0 \tag{2.50a}$$

or

$$c_{ray} = c_0 \mathbf{n} \cdot \mathbf{n}_r + \mathbf{v}_0 \cdot \mathbf{n}_r \quad , \tag{2.50b}$$

where $\mathbf{n}$ is the wavenormal and $\mathbf{n}_r$ is the ray-direction.

Incorrect results for the ray velocity can be found in the literature. Rayleigh [19] states that

"From Fermat's law of least time it follows that the course of a ray in a moving, but otherwise homogeneous, medium, is the same as it would be in a medium, of which all the parts are at rest, if the velocity of propagation be increased at every point by the component of the wind velocity in the direction of the ray".

In our notation this statement results in

$$c_{ray} = c_0 + \mathbf{v}_0 \cdot \mathbf{n}_r \quad . \tag{2.50c}$$

Comparison of Eq. (2.50b) and (2.50c) shows that Rayleigh's conclusion is only approximately correct when $|v_0/c_0| \ll 1$. In that case the directions of $\mathbf{n}$ and $\mathbf{n}_r$ differ only slightly and $\mathbf{n} \cdot \mathbf{n}_r \approx 1$. We will use the same approximation in § 3.2.3. However, generally speaking, Eq. (2.50c) is not correct. This has been recognized among others by Kornhauser [20], Warren [21], Thompson [22] and Ugincius [18].

The intuitive approach of Rayleigh has been followed by many authors. For instance the theory of flow measuring instruments, based on acoustic traveltime measurements, usually starts with Eq. (2.50c) (see for instance Herschy [23]), but from the foregoing it should be clear that the applicability of Eq. (2.50c) depends entirely on the ratio $|v_0/c_0|$ and the aimed accuracy of the method.

2.4.4 Propagation of a plane wave in a moving medium

The influence of the stationary windspeed on the propagation of a plane wave will first be investigated with the three-dimensional wave equation for a medium with a constant and uniform flow (Eq. (2.28):

$$\nabla^2 p = \frac{1}{c_0^2}\left[\frac{\partial^2 p}{\partial t^2} + 2(\mathbf{v_0} \cdot \nabla)\frac{\partial p}{\partial t} + (\mathbf{v_0} \cdot \nabla)(\mathbf{v_0} \cdot \nabla)p\right] \ . \tag{2.51}$$

Here, $\mathbf{v_0}$ is the windspeed vector, which will be assumed to be constant. Eq. (2.51) can be transformed to the frequency domain, where we use the wavenumber $k_0 = 2\pi f/c_0$ and the Mach-vector $\mathbf{m} = \mathbf{v_0}/c_0$:

$$\nabla^2 P + k_0^2 P - 2jk_0(\mathbf{m} \cdot \nabla)P - (\mathbf{m} \cdot \nabla)(\mathbf{m} \cdot \nabla)P = 0 \ . \tag{2.52}$$

The plane wave is defined in the frequency domain by

$$P(\mathbf{r}, f) = P(0, f)\exp(-j\mathbf{k} \cdot \mathbf{r}) \tag{2.53}$$

where $\mathbf{r} = (x, y, z)$ is the coordinate vector and $\mathbf{k} = (k_x, k_y, k_z)$ is the wavenumber vector with $k = \omega/c$. Since $\mathbf{k} \cdot \mathbf{r} = 0$ on the wavefront, $\mathbf{k}$ can be written as $k\mathbf{n}$, where $\mathbf{n}$ is the normal to the wavefront. If the wavefront normal $\mathbf{n}$ is given by $\mathbf{n} = (n_x, n_y, n_z)$, then the components of $\mathbf{k}$ are given by

$$k_x = kn_x; \qquad k_y = kn_y; \qquad k_z = kn_z,$$

and consequently, using $k_x = \omega/c_x$, $k_y = \omega/c_y$ and $k_z = \omega/c_z$:

$$c_x = c/n_x; \qquad c_y = c/n_y \ ; \qquad c_z = c/n_z.$$

Note from Eq. (2.53) that

$$\nabla P(\mathbf{r}, f) = -j\mathbf{k}P(\mathbf{r}, f) \ . \tag{2.54}$$

From Eq. (2.53) and (2.54) we find:

$$\nabla^2 P = -k^2 P \tag{2.55a}$$

$$(\mathbf{m} \cdot \nabla)P = -j(\mathbf{m} \cdot \mathbf{k})P = -j(\mathbf{m} \cdot \mathbf{n})kP \tag{2.55b}$$

$$(\mathbf{m} \cdot \nabla)(\mathbf{m} \cdot \nabla)P = -(\mathbf{m} \cdot \mathbf{k})^2 P = -(\mathbf{m} \cdot \mathbf{n})^2 k^2 P \ . \tag{2.55c}$$

Substitution of these results in Eq. (2.52) and dividing by P gives a quadratic equation in k:

$$[(\mathbf{m} \cdot \mathbf{n})^2 - 1]k^2 - 2(\mathbf{m} \cdot \mathbf{n})k_0 k + k_0^2 = 0 \tag{2.56}$$

with the solution

$$k = k_0 / (1 + \mathbf{m \cdot n}) \quad . \tag{2.57}$$

If we use the relations $k = \omega/c$ and $k_0 = \omega/c_0$, we find for the phase velocity of the plane wave, using Eq. (2.57):

$$c = c_0(1 + \mathbf{m \cdot n}) \quad . \tag{2.58}$$

The quantity c is called *phase velocity*, because it represents the speed with which the wavefronts (planes with equal phase) propagate in the direction normal to the wavefronts. Notice that c depends on the angle between the wavefront normal $\mathbf{n}$ and the Mach-vector $\mathbf{m}$. When Eq. (2.50c) is valid ($|v_0/c_0| \ll 1$), $\mathbf{n}$ and $\mathbf{n}_r$ are almost equal, and then the ray velocity and the phase velocity will be practically the same.

We will now derive the particle velocity and the specific acoustic impedance for a plane wave in a moving medium. This will be done by use of the equation of motion as given by Eq. (2.22), which can be written in the frequency domain as:

$$-\frac{1}{\rho_0} \nabla P = j\omega \mathbf{V} + (\mathbf{v}_0 \cdot \nabla)\mathbf{V} \tag{2.59}$$

where $P = P(\mathbf{r}, f)$ is given by Eq. (2.53) and $\mathbf{V} = \mathbf{V}(\mathbf{r}, f)$. We will assume a solution of the form:

$$\mathbf{V}(\mathbf{r}, f) = \mathbf{V}(0, f)\exp(-j\mathbf{k \cdot r}) \quad . \tag{2.60}$$

Note that Eq. (2.59) is a vector equation. In the x-direction we substitute:

$$\frac{\partial P}{\partial x} = -jkn_x P(0, f)$$

and with $\mathbf{V} = (V_x, V_y, V_z)$:

$$\frac{\partial V_x}{\partial x} = -jkn_x V_x(0, f) \; ; \quad \frac{\partial V_x}{\partial y} = -jkn_y V_x(0, f) \; ; \quad \frac{\partial V_x}{\partial z} = -jkn_z V_x(0, f) \quad ,$$

leading to:

$$\frac{kn_x}{\rho_0} P(0, f) = (\omega - \mathbf{v}_0 \cdot \mathbf{n}k) \, V_x(0, f) \quad . \tag{2.61}$$

With $k = \omega/c$ and $c = c_0(1 + \mathbf{m \cdot n})$, Eq. (2.61) gives:

$$V_x(0, f) = \frac{1}{\rho_0 c_0} P(0, f) n_x \quad . \tag{2.62}$$

Calculations in the y- and z-directions give similar results, so the particle velocity is given by:

$$V(\mathbf{r},f) = \frac{1}{\rho_0 c_0} P(0,f)\exp(-j\mathbf{k}\cdot\mathbf{r})\mathbf{n} \tag{2.63}$$

and the specific acoustic impedance is:

$$Z_s(\mathbf{r},f) = P(\mathbf{r},f) / V(\mathbf{r},f) = \rho_0 c_0 \quad . \tag{2.64}$$

These results show that:

• The specific acoustic impedance $Z_s = \rho_0 c_0$ is not influenced by the movement of the medium;

• The direction of $\mathbf{V}$ equals $\mathbf{n}$, so the particle velocity is in the direction of the wave normal, just as in a stationary medium.

The ray direction of the plane wave can now be calculated from Eq. (2.46) by substitution of

$$\mathbf{I}_{av} = \frac{p_{eff}^2}{\rho_0 c_0}\mathbf{n} \; ; \quad E_{av} = \frac{p_{eff}^2}{\rho_0 c_0^2} \; ; \quad \mathbf{v}_0 E_{av} = \frac{p_{eff}^2}{\rho_0 c_0}\mathbf{m} \quad ,$$

leading to

$$\mathbf{n}_r = (\mathbf{n} + \mathbf{m}) / |\mathbf{n} + \mathbf{m}| = (c_0\mathbf{n} + \mathbf{v}_0) / |c_0\mathbf{n} + \mathbf{v}_0| \quad . \tag{2.65}$$

The rays can be constructed as shown in figure 2.3. The figure shows a wavefront of a plane wave at the time $t = 0$ and $t = 1$ second. The ray velocity c_{ray} is shown as the vector sum $c_0\mathbf{n} + \mathbf{v}_0$. From this figure it is easily derived that the phase velocity, defined as the propagation speed of the wavefronts in the normal direction, equals $c = c_0 + \mathbf{v}_0\cdot\mathbf{n}$, which is in accordance with Eq. (2.58). The ray velocity can be computed from Eq. (2.50b), giving

$$c_{ray} = c_0 \cos\theta + v_0 \cos\beta \quad , \tag{2.66}$$

where θ is the angle between $\mathbf{n}$ and $\mathbf{n}_r$ and β is the angle between $\mathbf{v}_0$ and $\mathbf{n}_r$. From figure 2.3 we find $\sin\theta = a/c_0 = v_0 \sin\beta/c_0 = m \sin\beta$, so Eq. (2.66) can be written as

$$c_{ray} = c_0(1 - m^2 \sin^2\beta)^{1/2} + v_0 \cos\beta \quad . \tag{2.67}$$

For small values of $m^2 \sin^2\beta$, Eq. (2.67) can be approximated by

$$c_{ray} = c_0 + v_0 \cos\beta \quad . \tag{2.68}$$

Notice that this approximation is equivalent with the "Rayleigh approximation" of Eq. (2.50c). Figure 2.3 also shows that the angle θ between the soundrays and the wave normals is given by

$$\text{tg}\,\theta = (v_x \cos\psi + v_y \sin\psi)/c \quad . \tag{2.69a}$$
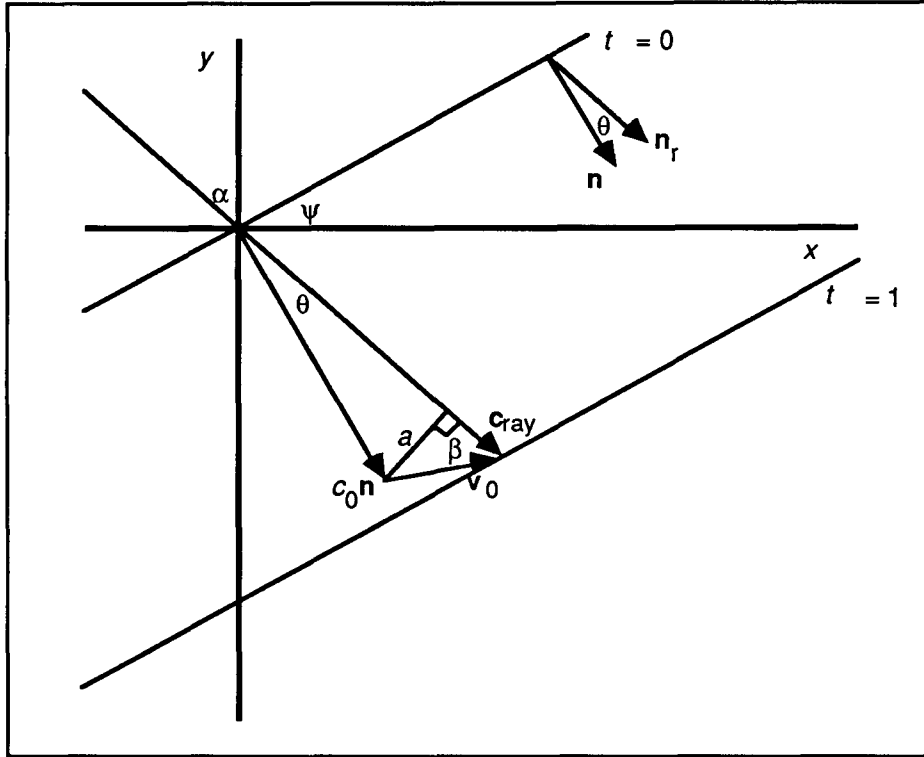
Figure 2.3: Propagation of a plane wave in a moving medium.

If $v_0 \ll c_0$ then $\mathbf{n_r \cdot n} \approx 1$, $c \approx c_0$ and Eq. (2.69a) may be replaced by

$$\sin \theta \approx m_x \cos \psi + m_y \sin \psi \ , \tag{2.69b}$$

a result that will be used in § 3.2.3.

From figure 2.3 we find that the ray velocity $\mathbf{c_{ray}} = c_0\mathbf{n} + \mathbf{v_0}$ is in agreement with the ray velocity of Fermat's principle, given by Eq. (2.50a). For a plane wave Fermat's principle can easily be verified. If we use the geometry of figure 2.3, substitution of $\mathbf{n} = (\sin \psi, -\cos \psi)$ and $\mathbf{n_r} = (\sin \alpha, -\cos \alpha)$ in Eq. (2.50b) gives

$$c_{ray} = c_0 \sin \psi \sin \alpha + c_0 \cos \psi \cos \alpha + v_{0x} \sin \alpha - v_{0y} \cos \alpha \ . \tag{2.70}$$

Eq. (2.49) requires that $(1/c_{ray})ds$ is stationary for small changes in the ray-direction α, when ds is kept constant in magnitude. This requirement is fulfilled when $\partial c_{ray}/\partial \alpha = 0$. Using Eq. (2.70) we find:

$$\mathrm{tg} \ \alpha = (c_0 \sin \psi + v_{0x}) / (c_0 \cos \psi - v_{0y}) \ . \tag{2.71}$$

Inspection of figure 2.3 shows that this result corresponds with the ray direction. Note that when $v_0 = 0$, the ray direction coincides with the wavenormal and $c_{ray} = c_0$. In that case Eq. (2.49) is equivalent with Eq. (2.47).

2.4.5 Propagation of spherical waves in a moving medium

In § 2.4.1 we showed that the sound pressure in a uniformly and stationary moving medium is given by the translation formula (2.30). Hence, the sound pressure due to a monopole is given by

$$p(x, y, z, t) = s(t - r/c_0)/r \qquad (2.72)$$

with

$$r(x, y, z, t) = \left[(x - x_s - v_{0x}t)^2 + (y - y_s - v_{0y}t)^2 + (z - z_s - v_{0z}t)^2 \right]^{1/2}. \qquad (2.73)$$

The geometry of the wavefronts is depicted in figure 2.4 for the two-dimensional case in the x–y plane. According to Eq. (2.72) and (2.73), the wavefronts are a set of non-concentric circles, whose radii expand in time with velocity c_0 and whose centers progress in the wind direction with velocity v_0.
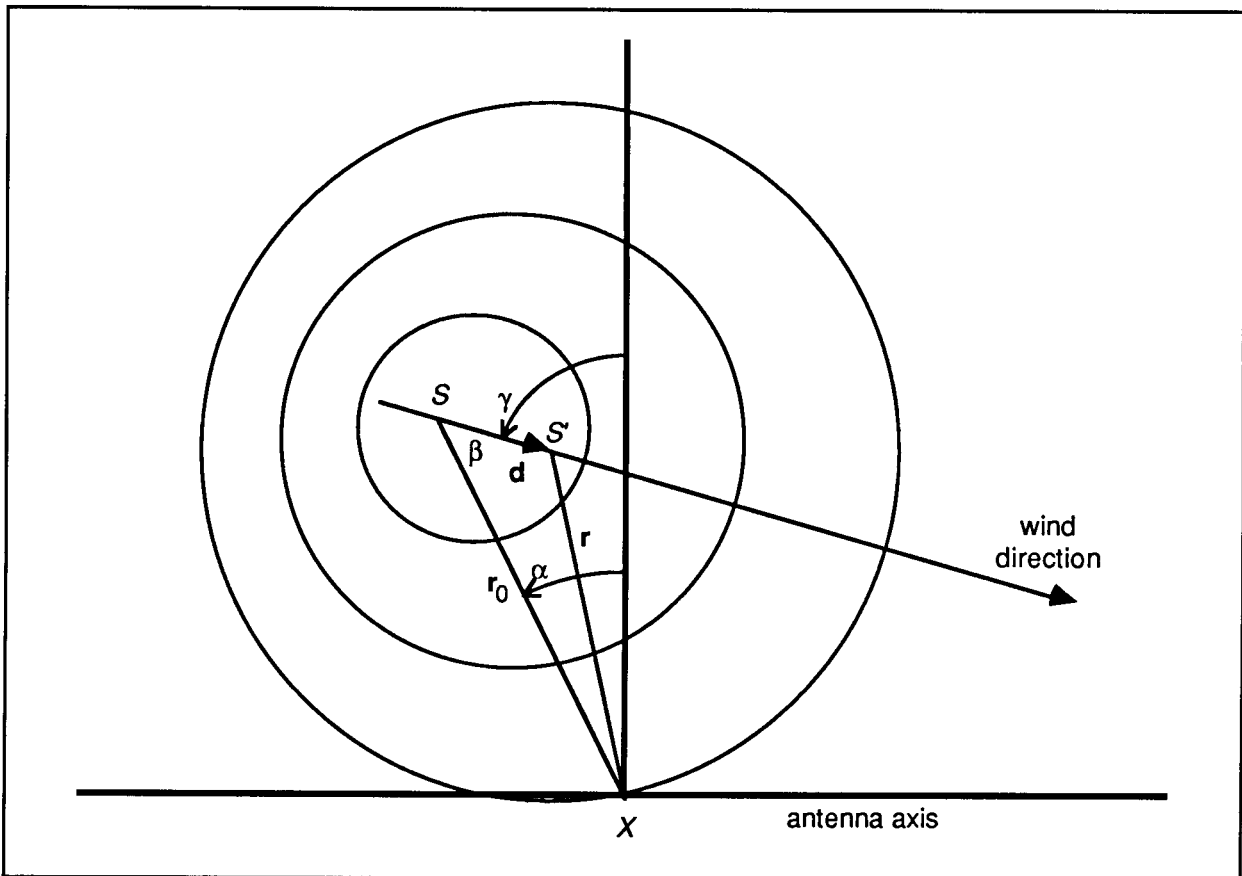
Figure 2.4: Due to the windspeed v_0, the center of the wavefronts moves with the same velocity.

The particle velocity and specific acoustic impedance are derived as follows. Because r is a function of t, the Fourier transform of $p(\mathbf{r}, t)$ is not easily derived. For that reason we consider a pressure recording with a finite duration and represent it by a Fourier series:

$$p(\mathbf{r}, t) = \sum_i p_i(\mathbf{r}, t) = \sum_i S_i \exp\left[j(\omega_i t - k_{0i} r)\right] / r \tag{2.74}$$

with $r = r(x, y, z, t)$ as given by Eq. (2.73) and $k_{0i} = \omega_i/c_0$.
For the particle velocity we write

$$\mathbf{v}(\mathbf{r}, t) = \sum_i \mathbf{v}_i(\mathbf{r}, t) = \sum_i \mathbf{A}_i S_i \exp[j(\omega_i t - k_{0i} r)] / r \ . \tag{2.75}$$

The direction of $\mathbf{A}_i$ gives the direction of $\mathbf{v}_i$ and $A_i = 1/Z_{si}$. The relation between $p_i(\mathbf{r}, t)$ and $\mathbf{v}_i(\mathbf{r}, t)$ can now be found by substitution of Eq. (2.74) and (2.75) in the equation of motion, Eq. (2.22). Special care must be taken here with the time derivative $\partial/\partial t \ \mathbf{v}_i$, because of the time dependence of r, leading to

$$\frac{\partial}{\partial t} \mathbf{v}_i = \left[j\omega_i - (jk_{0i} + \frac{1}{r}) \frac{\partial r}{\partial t} \right] \mathbf{v}_i \ . \tag{2.76}$$

From Eq. (2.73) we find

$$\frac{\partial r}{\partial t} = -v_{0x}(x-x_s-v_{0x}t) / r - v_{0y}(y-y_s-v_{0y}t) / r - v_{0z}(z-z_s-v_{0z}t) / r \quad = -\mathbf{v}_0 \cdot \mathbf{n} \tag{2.77}$$

with $\mathbf{n}$ being the wave normal at the position given by $\mathbf{r}$.
From Eq. (2.76) and (2.77) we find for the equation of motion:

$$-\frac{1}{\rho_0} \nabla p_i = (j\omega_i + (jk_{0i} + \frac{1}{r}) \ \mathbf{v}_0 \cdot \mathbf{n})\mathbf{v}_i + (\mathbf{v}_0 \cdot \nabla)\mathbf{v}_i \ . \tag{2.78}$$

In the x-direction this equation gives, with substitution of

$$\frac{\partial p_i}{\partial x} = \frac{\partial p_i}{\partial r} \frac{\partial r}{\partial x} = -(jk_{0i} + \frac{1}{r})p_i(\mathbf{r}, t)n_x$$

and $\qquad (\mathbf{v}_0 \cdot \nabla)v_{xi} = -(\mathbf{v}_0 \cdot \mathbf{n})(jk_{0i} + \frac{1}{r})v_{xi}(\mathbf{r}, t) \ :$

$$A_{xi} = (1/\rho_0 c_0)(1 + 1/jk_{0i} r)n_x \ .$$

Corresponding results are obtained in the y- and z-direction, so the particle velocity is:

$$\mathbf{v}_i(\mathbf{r}, t) = (1/Z_{si})p_i(\mathbf{r}, t)\mathbf{n} \tag{2.79}$$

with

$$Z_{si} = \rho_0 c_0 jk_{0i} r / (1 + jk_{0i} r) \ . \tag{2.80}$$

This result shows that the particle velocity is normal to the wavefront and the specific acoustic impedance is the same as in the medium in rest.

Let us now investigate the direction of the sound rays. For a spherical wave we find:

$$\mathbf{I}_{av} = \frac{p_{eff}^2}{\rho_0 c_0}\,\mathbf{n}\ ;$$

$$E_{av} = \tfrac{1}{2}\rho_0\,\frac{1}{\rho_0^2 c_0^2}\left(1 + \frac{1}{k_0^2 r^2}\right)p_{eff}^2 + \tfrac{1}{2}\,\frac{1}{\rho_0^2 c_0^2}\,p_{eff}^2 = \frac{1}{\rho_0 c_0^2}\left(1 + \frac{1}{2k_0^2 r^2}\right)p_{eff}^2\ ;$$

$$\mathbf{v}_0 E_{av} = \frac{p_{eff}^2}{\rho_0 c_0}\left(1 + \frac{1}{2k_0^2 r^2}\right)\mathbf{m}\ .$$

Application of Eq. (2.46) gives a sound ray direction:

$$\mathbf{n}_r' = \left(\mathbf{n} + \left(1 + \frac{1}{2k_0^2 r^2}\right)\mathbf{m}\right)\Big/\left|\mathbf{n} + \left(1 + \frac{1}{2k_0^2 r^2}\right)\mathbf{m}\right|\ . \qquad (2.81a)$$

In the far field ($k_0^2 r^2 \gg 1$), this expression becomes:

$$\mathbf{n}_r = (\mathbf{n} + \mathbf{m})\,/\,|\mathbf{n} + \mathbf{m}|\ , \qquad (2.81b)$$

which is the same as for a plane wave. In figure 2.4 we find $\mathbf{r}_0 = \mathbf{r} + \mathbf{d} = (c_0\mathbf{n} + \mathbf{v}_0)T = (\mathbf{n} + \mathbf{m})c_0 T$, where T is the travel time of the wave from S to X, so $\mathbf{n}_r$ has the same direction as $\mathbf{r}_0$. This shows that the rays $\mathbf{n}_r$ are straight lines in the far field of the point source and that $-\mathbf{n}_r$ points to the source position.

In the near field the situation is more complicated, as Eq. (2.81a) shows that $\mathbf{n}_r'$ deviates from the direction $\mathbf{n} + \mathbf{m}$. Notice that the deviation $\mathbf{m}/2k_0^2 r^2$ is caused by the increased kinetic energy, due to the reactive part of the specific acoustic impedance. This part of the particle velocity gives no contribution to the energy transportation to the far field. Because the sound rays represent the paths along which the energy is transported, the near field term should be discarded in Eq. (2.81a) to give a meaningful extension of the ray definition in the near field. With this argumentation, Eq. (2.81b) also holds in the near field of the source.

The ray velocity can be computed by application of the cosine-rule to triangle SXS' in figure 2.4, making use of the relations

$$T = r_0\,/\,c_{ray} = d\,/\,v_0 = r\,/\,c_0\ , \qquad (2.82)$$

leading to

$$c_{ray} = c_0(1 - m^2 \sin^2 \beta)^{1/2} + v_0 \cos \beta\ . \qquad (2.83)$$

This result is equivalent with Eq. (2.67) and for small values of $m^2 \sin^2 \beta$, Eq. (2.83) may be replaced by the "Rayleigh approximation" of Eq. (2.50c):

$$c_{ray} = c_0 + v_0 \cos \beta \ . \tag{2.84}$$

An example of the application of Eq. (2.84) is found in the acoustic flow meter that was already mentioned in § 2.4.3. The measurement principle is given by Herschy [23] and is illustrated in figure 2.5.
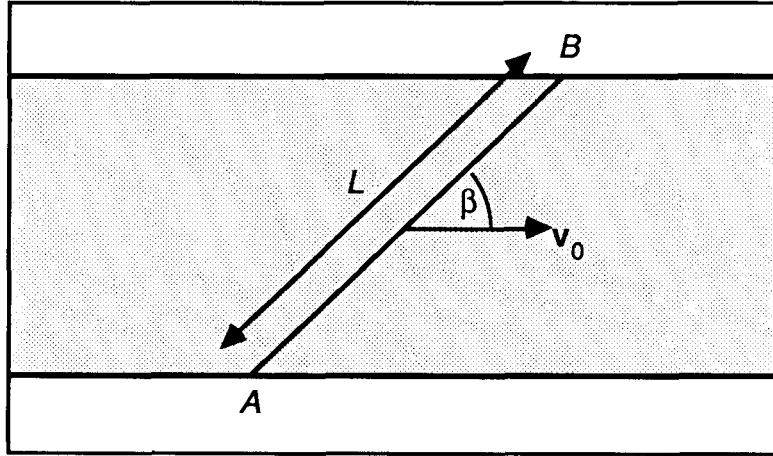
Figure 2.5: Principle of the acoustic flow meter.

A sound pulse is sent from location A to B and the traveltime is measured. Assuming a uniform flow and using Eq. (2.84), this traveltime equals

$$T_1 = L/(c_0 + v_0 \cos \beta) \ . \tag{2.85}$$

Because c_0 is usually not known, one also measures the traveltime of a pulse that is sent from B to A:

$$T_2 = L/(c_0 - v_0 \cos \beta) \ . \tag{2.86}$$

From these two measurements c_0 can be found as

$$c_0 = \tfrac{1}{2}(L/T_1 + L/T_2) \ . \tag{2.87}$$

From Eq. (2.85) and (2.86) we find for the difference in traveltime

$$\Delta T = T_2 - T_1 = 2Lv_0 \cos \beta \ / \ (c_0^2 - v_0^2 \cos^2 \beta) \tag{2.88a}$$

or, assuming that $v_0 \ll c_0$:

$$\Delta T = 2Lv_0 \cos \beta \ / \ c_0^2 \ . \tag{2.88b}$$

The flow velocity can now be calculated from

$$v_0 = \Delta T c_0^2 \ / \ 2L \cos \beta \ . \tag{2.88c}$$

We recall from § 2.4.3 that application of Eq. (2.84) is only correct if $v_0 \ll c_0$. Besides that, the method is only correct if v_0 is the mainstream direction, so no cross-flow component should be present. One way to eliminate this restriction is by using a second pair of transducers with a ray-path perpendicular to AB. Another possibility is the use of an array of receivers to measure the displacement of the apparent source direction due to the flow (see § 3.2.3).

2.4.6 Concluding remarks on the sound propagation in a stationary and uniformly moving medium

In the preceding paragraphs we have seen that there are important differences between the sound propagation in a medium at rest and in a moving medium. These differences are mainly due to the fact that the ray direction is normal to the wavefront in a medium at rest, but in general this is not the case in a moving medium. Our results for a stationary and uniformly moving medium can be summarized as follows:

a. The rays and wavefronts can be obtained by first calculating the solution for the medium in rest, and then converting the results with a translation of all wave coordinates over $v_0 T$, where T is the observation time.

b. The energy transport is in the ray direction given by Eq. (2.46) and consists of two terms: the power-flow of the acoustic field in the direction of the wave normal and the energy transport by the moving medium in the flow direction.

c. Fermat's principle is valid along a raypath, where the traveltime is defined by the ray velocity:

$$\mathbf{c}_{ray} = c_0 (\mathbf{n} + \mathbf{m}) \quad . \tag{2.89}$$

d. The phase velocity of a plane wave is given by Eq. (2.58) and can be constructed as shown in figure 2.6a:

$$c = c_0 (1 + \mathbf{m} \cdot \mathbf{n}) = c_0 + v_0 \cos \phi \tag{2.90a}$$

where $\mathbf{m}$ is the Mach-vector and $\mathbf{n}$ is the wavefront normal. It gives the speed with which the wave normals (planes with equal phase) propagate in the direction $\mathbf{n}$. From figure 2.6a we find that $\phi = \beta + \theta$ and $\sin \theta = m \sin \beta$, so Eq. (2.90a) can be written as

$$c = c_0 + v_0 \cos(\beta + \theta)$$

$$= c_0 + v_0 [\cos \theta \cos \beta - \sin \theta \sin \beta]$$

$$= c_0 + v_0 [(1 - m^2 \sin^2 \beta)^{1/2} \cos \beta - m \sin^2 \beta] \quad . \tag{2.90b}$$

If $m \sin^2 \beta$ is small, the phase velocity can be approximated by

$$c = c_0 + v_0 \cos \beta \quad . \tag{2.90c}$$

e. Using the geometry of figure 2.6a (see also figure 2.3) the ray velocity can be written as

$$c_{ray} = c_0 \mathbf{n} \cdot \mathbf{n}_r + v_0 \cdot \mathbf{n}_r = c_0 \left(1 - m^2 \sin^2 \beta\right)^{1/2} + v_0 \cos \beta \quad . \tag{2.91}$$

This result was already obtained for plane waves in Eq. (2.67) and for spherical waves in Eq. (2.83). If $m^2 \sin^2 \beta$ is small, the "Rayleigh approximation" is valid:

$$c_{ray} = c_0 + v_0 \cdot \mathbf{n}_r = c_0 + v_0 \cos \beta \quad . \tag{2.92}$$

Note that with small Mach-numbers, the ray velocity and the phase velocity have practically the same magnitude, as shown by Eq. (2.90c) and (2.92). This can also be understood by inspection of c and c_{ray} in figure 2.6a, realizing that θ is small in that case.
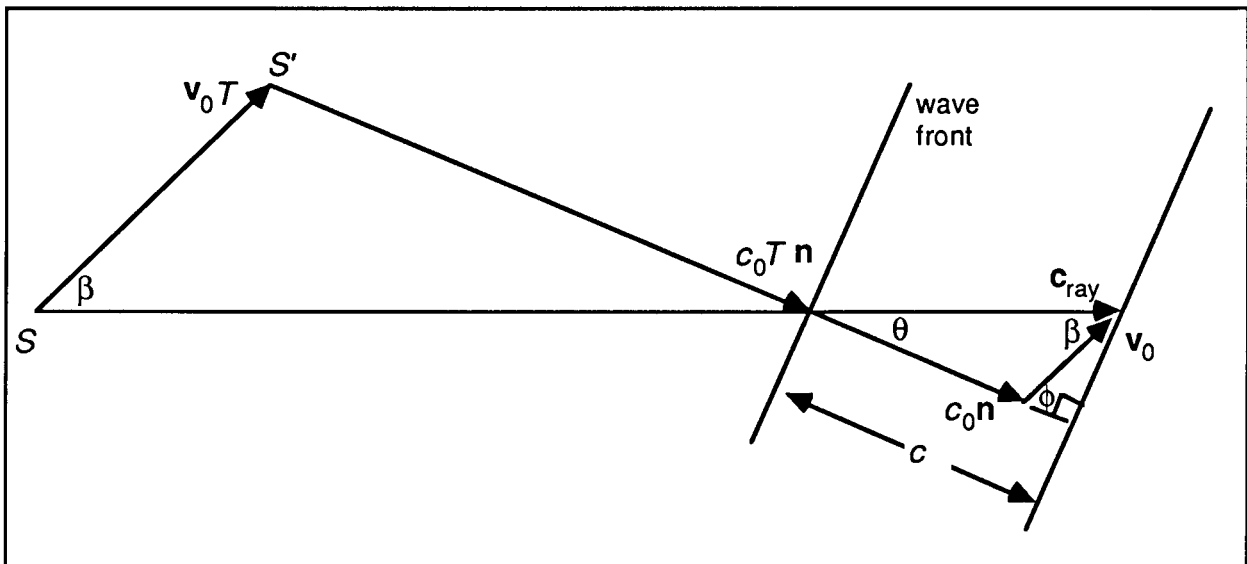
Figure 2.6a: Construction of the ray velocity c_{ray} and the phase velocity c in the far field of a point source after a traveltime T.
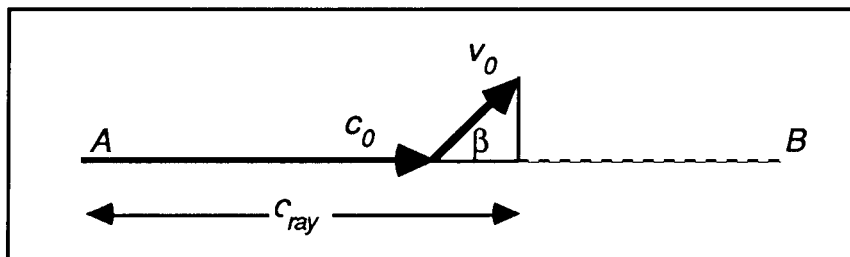
Figure 2.6b: Construction of the ray velocity according to the "Rayleigh approximation" by incrementing c_0 with the projection of the medium velocity v_0 on the raypath AB.

If the Rayleigh approximation is valid, the ray velocity is given by Eq. (2.92) and can be constructed as shown in figure 2.6b. This construction is often used for traveltime calculations of sound propagation in moving media, for instance in the theory of acoustic flow measurements. Notice however that it is only an approximation, valid for small Mach-numbers and that the correct construction is given by figure 2.6a.

f. For plane and spherical waves the specific acoustic impedance Z_s is not influenced by the movement of the medium.

2.5   PLANE WAVE DECOMPOSITION BY FOURIER TRANSFORMATION

Let us consider a number of noise sources, leading to plane waves, making angles α_n with the x-axis, and with sound pressures $s_n(t)$ at the origin of our coordinate system (see fig. 2.1). Then, according to Eq. (2.12), the acoustic pressure along the x-axis ($y = 0$) will be given by

$$s(x, t) = \sum_n s_n(t - x/c_n) \tag{2.93}$$

with $c_n = c/\sin \alpha_n$.

It is possible to calculate the individual source signals $s_n(t)$ by measuring the signal $s(x, t)$ according to the following procedure:

a. The function $s(x, t)$ is Fourier transformed from the time to the frequency domain:

$$S(x, f) = \int_{-\infty}^{+\infty} s(x, t) \exp(-j2\pi ft) dt$$

$$= \int_{-\infty}^{+\infty} \sum_n s_n(t - x/c_n) \exp(-j2\pi ft) dt$$

$$= \sum_n S_n(f) \exp(-j2\pi fx/c_n) \tag{2.94}$$

with

$$S_n(f) = \int_{-\infty}^{+\infty} s_n(t) \exp(-j2\pi ft) dt . \tag{2.95}$$

Notice that for the noise signals $s_n(t)$ the Fourier transforms of Eq. (2.94) and (2.95) do not exist. This makes proper time windowing of the signals necessary.

b. The function $S(x, f)$ is Fourier transformed from x to k_x':

$$\tilde{S}(k_x', f) = \int_{-\infty}^{+\infty} S(x, f) \exp(j2\pi k_x' x) dx$$

$$= \int_{-\infty}^{+\infty} \sum_n S_n(f) \exp\left[j2\pi(k_x' - f/c_n)x\right] dx$$

$$= \sum_n S_n(f) \delta(k_x' - f/c_n) \ . \tag{2.96}$$

Here again the signal $S(x, f)$ has to be limited in length, now as a function of x. As a consequence, the result will be convolved with the Fourier transform of the applied aperture window (see Section 2.7).

From Eq. (2.96) it can be seen that the plane wave from the direction α_n is projected in the $k_x'-f$ plane as the signal $S_n(f)$ on a straight line through the origin, given by

$$k_x' = f/c_n = (f/c) \sin \alpha_n \ . \tag{2.97}$$

Notice that plane waves from other directions will be projected on other lines in the $k_x'-f$ plane, which will not coincide with the first line. This property makes it possible to extract the signal $S_n(f)$ for one direction in the $k_x'-f$ domain and to calculate from that the original waveform $s_n(t)$ by inverse Fourier transformation:

$$s_n(t) = \int_{-\infty}^{+\infty} S_n(f) \exp(j2\pi ft) df \ . \tag{2.98}$$

It has to be recalled that only time windowed versions of the $s_n(t)$ functions can be calculated. Note that with industrial noise measurements, there is no interest in computing the original plane wave signals, but in finding the average sound pressure levels as a function of frequency (in $1/1$- or $1/3$-octave bands), which can be calculated from the power spectra of the plane waves. These power spectra can be estimated by averaging the amplitudes of the rough spectra $S_n(f)$ over several realizations of the measurement procedure as described here. However, in the next section it will be shown that the power spectra can be obtained directly from a two-dimensional Fourier transform of the spatial cross-correlation function of the wave field, instead of the wave field itself.

2.6 POWER SPECTRUM ESTIMATION FROM SPATIAL CROSS-CORRELATIONS

The power spectrum of a continuous and stationary signal $s_1(t)$ is given by the Fourier transform of the auto-correlation function of $s_1(t)$ (an overview of correlation functions and related properties is given by Bendat and Piersol [5]). The auto-correlation function $R_1(\tau)$ of an ergodic random signal equals

$$R_1(\tau) = \lim_{T \to \infty} \frac{1}{T} \int_0^T s_1(t)\, s_1(t+\tau)\mathrm{d}t \qquad (2.99)$$

and its Fourier transform is

$$\tilde{R}_1(f) = \int_{-\infty}^{+\infty} R_1(\tau)\, \exp(-j2\pi f\tau)\mathrm{d}\tau \quad . \qquad (2.100)$$

The cross-correlation function of two ergodic random signals $s_1(t)$ and $s_2(t)$ is

$$R_{12}(\tau) = \lim_{T \to \infty} \frac{1}{T} \int_0^T s_1(t)s_2(t+\tau)\mathrm{d}t \quad . \qquad (2.101)$$

and its Fourier transform is

$$\tilde{R}_{12}(f) = \int_{-\infty}^{+\infty} R_{12}(\tau)\, \exp(-j2\pi f\tau)\mathrm{d}\tau \quad . \qquad (2.102)$$

$\tilde{R}_{12}(f)$ is called the cross-spectrum of the signals $s_1(t)$ and $s_2(t)$. If the signals $s_1(t)$ and $s_2(t)$ are uncorrelated, as with independent random processes, then the cross-correlation and cross-spectrum of these signals are zero.

It will now be shown how — under certain conditions — the power spectra of the individual plane waves of the soundfield defined in Eq. (2.93) can be extracted from the spatial cross-correlation function of the total wavefield along the x-axis. It will be assumed that the sound pressures of the individual plane waves are stationary processes as a function of time. The spatial cross-correlation function is defined as the temporal cross-correlation between the signals at the positions $x_0 - \xi$ and x_0:

$$R(x_0, \xi, \tau) = \lim_{T \to \infty} \frac{1}{T} \int_0^T s(x_0 - \xi, t)s(x_0, t + \tau)\mathrm{d}t$$

$$= \lim_{T \to \infty} \frac{1}{T} \int_0^T \sum_n s_n(t - x_0/c_n + \xi/c_n) \sum_m s_m(t + \tau - x_0/c_m) dt$$

$$= \sum_{n,m} R_{nm}(\tau - \xi/c_n + x_0[1/c_n - 1/c_m]) \quad . \tag{2.103}$$

The cross-correlation functions $R_{nm}(\tau)$ are defined here for the position $x_0 = 0$ because the signals $s_n(t)$ and $s_m(t)$ are defined in that point. The spatial cross-correlation function could also have been defined between the positions x_0 and $x_0 + \xi$, but the definition of Eq. (2.103) gives a better agreement with the microphone positions of SYNTACAN (see Eq. 4.3).

Eq. (2.103) shows that the spatial cross-correlation function is not only dependent on the time lag τ and the displacement ξ, but also on the reference position x_0 on the x-axis. This is caused by the cross-correlation terms R_{nm} ($n \neq m$). If the noise sources $s_n(t)$ are uncorrelated, which is true in many practical situations, then Eq. (2.103) simplifies to

$$R(\xi, \tau) = \sum_n R_n(\tau - \xi/c_n) \quad , \tag{2.104}$$

which is independent of x_0. Under these conditions the power spectra of the individual plane waves can be extracted by a double Fourier transform, in the same way as in Section 2.5. Fourier transformation from time to frequency gives the cross-spectrum:

$$\tilde{R}(\xi, f) = \sum_n \tilde{R}_n(f) \exp(-j2\pi f \xi/c_n) \tag{2.105}$$

with $\tilde{R}_n(f)$ = power spectrum of source n, measured at the x-axis. A second Fourier transform, now from ξ to k_x' gives:

$$\tilde{R}'(k_x', f) = \int_{-\infty}^{+\infty} \tilde{R}(\xi, f) \exp(j2\pi \xi k_x') d\xi$$

$$= \sum_n \tilde{R}_n(f) \int_{-\infty}^{+\infty} \exp[j2\pi(k_x' - f/c_n)\xi] d\xi$$

$$= \sum_n \tilde{R}_n(f) \delta(k_x' - f/c_n) \quad . \tag{2.106}$$

From Eq. (2.106) it is seen that, with the same argumentation as in Section 2.5, the power spectrum of the plane wave from the direction α_n will be projected on a straight line through the origin, given by Eq. (2.97). This is illustrated in figure 2.7.
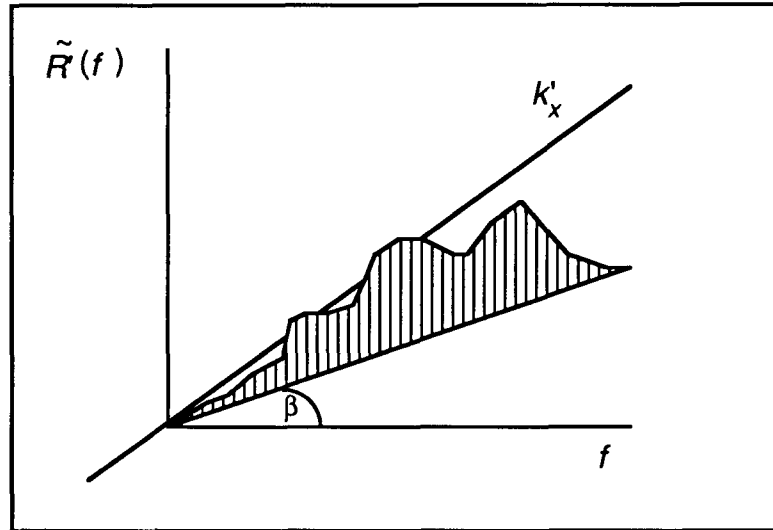
Figure 2.7: In the k_x'-f plane all energy from the direction α will be projected on a straight line through the origin with tan β = (sin α)/c.

An important difference with the method discussed in Section 2.5 is that there the wavefield must be measured with a full microphone array, whereas here the spatial cross-correlation function can be measured with a sparsed microphone array. The design of SYNTACAN is based on this kind of sparsed array processing. A detailed description of the theory of sparsed array processing of uncorrelated noise sources is presented by Nuttall et al. [24].

In case of correlated noise sources, the double Fourier transform can also be performed easily if the spatial cross-correlation function is related to one reference position x_0. For the special situation $x_0 = 0$ we may write:

$$R(x_0{=}0, \xi, \tau) = \sum_{n,m} R_{nm}(\tau - \xi/c_n) \tag{2.107}$$

and after double Fourier transformation:

$$\tilde{R}'(x_0{=}0, k_x', f) = \sum_{n,m} \tilde{R}_{nm}(f)\delta(k_x' - f/c_n) \tag{2.108}$$

From this result a number of conclusions may be drawn:

a. All contributions, also the part due to the cross-correlations, are distributed along the source directions;

b. The immission power in one direction is given by:

$$W_{av,n} = 2\text{Re} \left\{ \sum_m \tilde{R}_{nm}(f) \right\} \qquad (f > 0) \quad ; \tag{2.109}$$

c. The total immission power at $x_0 = 0$ is given by:

$$W_{av} = 2\,\mathrm{Re}\,\Big\{ \sum_{n,m} \tilde{R}_{nm}(f) \Big\} = 2\,\mathrm{Re}\,\Big\{ \tilde{R}(x_0{=}0,\,\xi{=}0,\,f) \Big\} \qquad (f > 0)\ . \qquad (2.110)$$

Notice that the total immission power in case of correlated noise sources depends on the position on the x-axis; the soundfield is said to be inhomogeneous, in contrast to the case of uncorrelated noise sources, which cause a homogeneous soundfield. As a consequence, the spatial cross-correlation function of a field of correlated plane waves can only be correctly measured with a full microphone array. Because SYNTACAN is based on sparsed array processing, some extra effects are introduced in case of correlated noise sources. These will be discussed in Chapter 5.

2.7 SAMPLING AND RESOLUTION BY DFT PROCESSING

In the preceding Sections it was assumed that the acoustic pressure $s(x, t)$ and its correlation function $R(x_0, \xi, \tau)$ can be measured as continuous functions of x, t, ξ and τ over arbitrary long intervals. In practice the measurements and computations are based on sampled versions of these functions with a finite sample interval and a finite observation length and use is made of the Discrete Fourier Transform (DFT) theory for spectral computations. On modern mini-computers the calculation of for instance a 1024-point complex-to-complex Fast Fourier Transform (FFT) takes less than 1 second (we measured 0.83 s on an HP1000/45 computer system with an FFT-subroutine written in assembler). With array processors the same calculations can be performed in 1 to 4 ms. In the future even smaller computation times are to be expected. We will now summarize the most important properties of the DFT in relation to our antenna design.

2.7.1 Sampling as a function of time

One of the most important results of the DFT theory is the periodicity of Fourier transformed sampled signals. If the sample interval in the time domain is Δt, then the periodicity in the frequency domain is $f_s = 1/\Delta t$. As a consequence, aliasing in the frequency domain will occur if $\Delta t > 1/(2f_h)$, where f_h is the highest frequency component of the signal. This is illustrated in figure 2.8. Notice that $|X(-f)| = |X(f)|$ for real time signals.

Aliasing in the frequency domain can be avoided by applying a lowpass filter to suppress the signal components above the frequency band of interest, and by choosing a sample interval Δt such that

$$\Delta t = 1/f_s < 1/(2f_h)\ . \qquad (2.111)$$
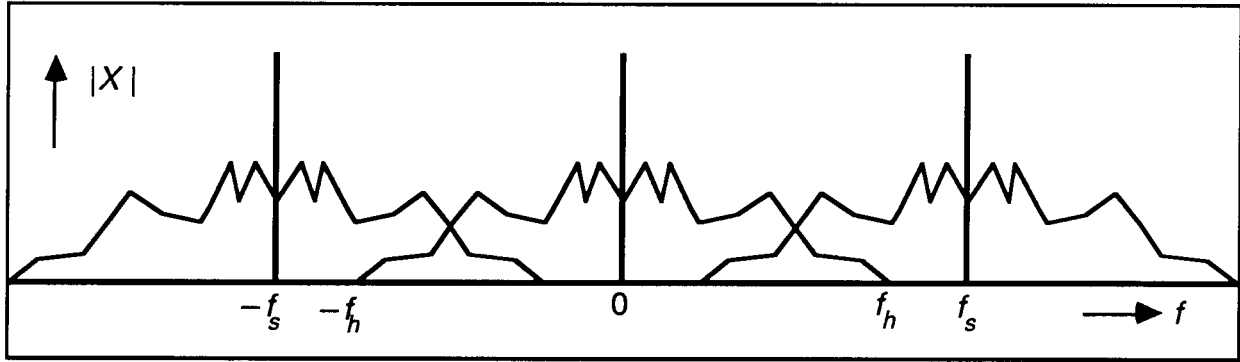
Figure 2.8: Due to sampling in the time domain, the frequency domain is periodic. In this example aliasing occurs, because $f_s < 2f_h$.

So, the highest frequency component f_h must be lower than $1/2 f_s = f_N$, which is called the Nyquist frequency. From figure 2.8 it is seen clearly that, although aliasing occurs, the frequency band for which

$$|f| < f_s - f_h \tag{2.112}$$

is aliasing free. This property is very useful for optimizing the cut-off frequency of anti-aliasing filters and the sample interval of the data-acquisition (see Chapter 4).

2.7.2 Sampling as a function of microphone spacing

In order to transform the spatial cross-correlation function from ξ to k_x' with DFT techniques, $R(\xi, \tau)$ has to be measured for a contiguous number of ξ-values, i.e. for $\xi = 0$, $\Delta\xi$, $2\Delta\xi$ etc. The sampling distance $\Delta\xi$ has to be chosen in such a way that the so-called spatial aliasing is avoided. Here the same rules apply as those discussed in § 2.7.1. An important difference, however, is that the k_x'-values are fundamentally limited, because the angles of incidence of the waves are restricted to $|\alpha_n| \leq 90°$. (Notice that a one-dimensional antenna cannot distinguish between waves from the front and the backside of the antenna.) This means that, according to Eq. (2.97), the k_x'-values are restricted to $|k_x'| \leq f_{max}/c_{min}$, where f_{max} is the maximum frequency of interest and c_{min} is the minimum sound velocity, which can be found from Eq. (2.9) by substitution of the lowest expected measurement temperature. It follows from Eq. (2.111), by changing Δt into $\Delta\xi$ and f_h into f_{max}/c_{min}, that spatial aliasing is avoided by using a microphone spacing

$$\Delta\xi < 1/2 \, c_{min}/f_{max} \, . \tag{2.113}$$

As we will show in § 2.7.4, the resolving power of a one-dimensional antenna gets worse for large angles of incidence. For that reason the computation of source directions of SYNTACAN is restricted to $|\alpha_n| \leq 30°$, allowing spatial aliasing for $|\alpha_n| > 30°$. The sample criterion is then computed in the same way as Eq. (2.112), leading to

$$k_s' = 1/\Delta\xi > (f_{max}/c_{min}) \sin 30° + (f_{max}/c_{min}) \sin 90°$$

or

$$\Delta\xi < {}^2/_3\, c_{min}\, /f_{max} \quad . \tag{2.114}$$

The periodicity in the k_x'-f domain is illustrated in figure 2.9.
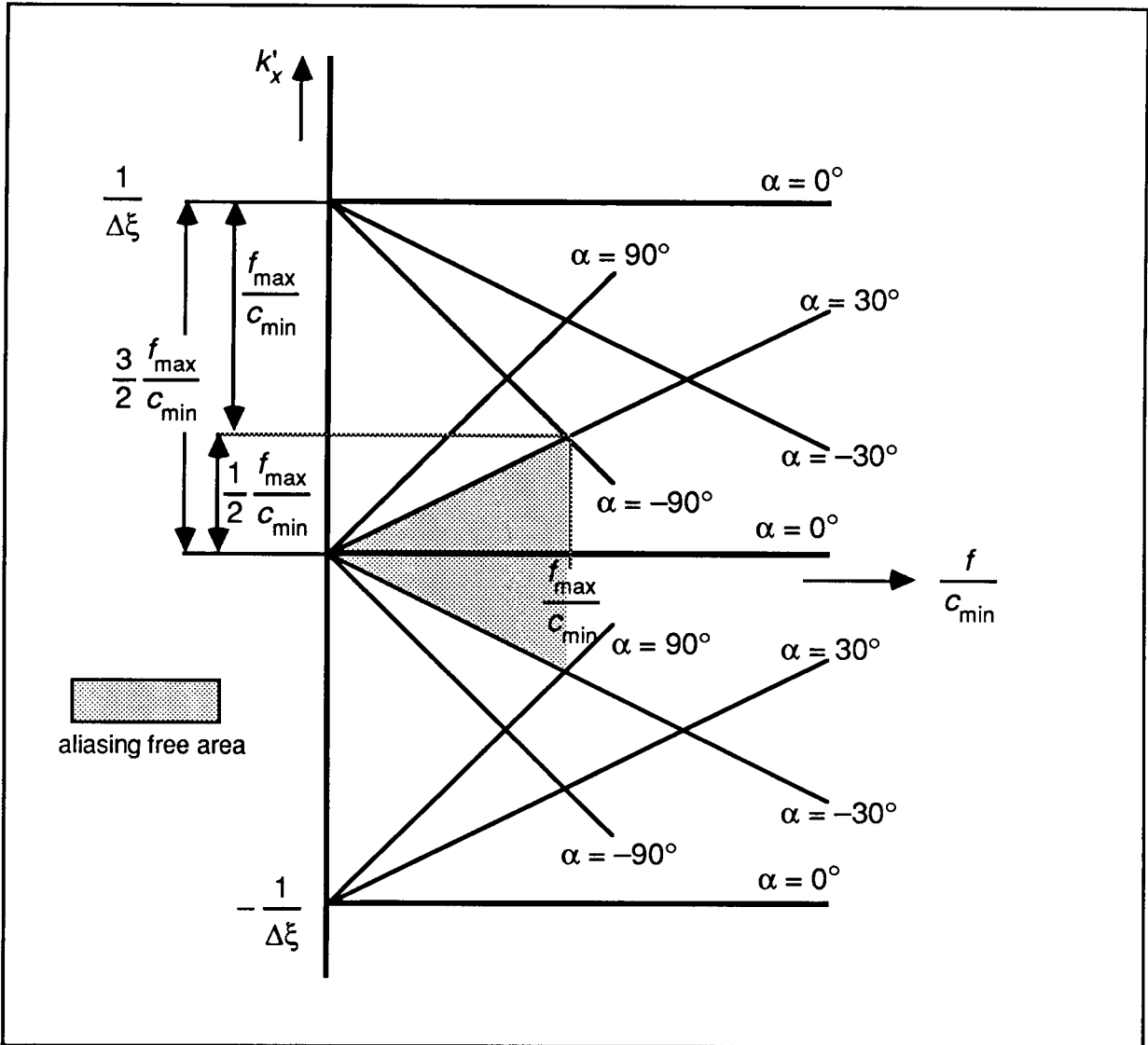
Figure 2.9: For a given f_{max} the microphone spacing $\Delta\xi$ can be chosen such that the angular area $(-30°, 30°)$ is aliasing-free.

2.7.3   Resolution in the frequency domain

The DFT signal processing assumes that the time signals are periodic within the observation interval T. As a consequence, the frequency spectrum only contains components at integer multiples of the fundamental frequency

$$\Delta f = 1/T = 1/(N\Delta t) \quad . \tag{2.115}$$

The quantity Δf can be interpreted as the sample interval in the frequency domain. The condition that the time signal is periodic with the observation interval is seldom met in practice. Here we consider two important situations:

a. The time signal is a transient with a duration smaller than T. In that case the DFT computes a sampled version of the (continuous) spectrum $X(f)$, which is exact at the sample points $n\Delta f$ ($n = 0, 1, ..., N-1$).

b. The time signal is continuous, or at least longer in duration than the observation interval T. In that case the signal $x(t)$ is first multiplied with a window function $w(t)$, which is zero for $t < -T/2$ and $t \geq T/2$. The windowed signal

$$x_w(t) = w(t)x(t) \tag{2.116}$$

can then be processed as a transient, giving a sampled version of the spectrum $X_w(f)$.

Note that due to the multiplication in the time domain in Eq. (2.116), the spectrum $X(f)$ will be convolved with the Fourier transform of the window:

$$X_w(f) = W(f) * X(f) \quad . \tag{2.117}$$

In the practice of industrial noise measurements, the time signals can almost always be described as continuous random signals, which are stationary during the observation interval. This means that a time window is always necessary for DFT processing, and the measured spectra will always be convolved with the Fourier transform of the applied window, which has consequences for the resolution in the frequency domain. We will discuss some important windows here, which are usually implemented in spectral analyzers.

a. The rectangle

This window just truncates the data. It is defined by

$$w(t) = 0 \qquad \text{for } t < -T/2 \text{ and } t \geq T/2$$
$$w(t) = 1/T \qquad \text{for } -T/2 \leq t < T/2 \quad . \tag{2.118}$$

Its Fourier transform is

$$W(f) = \int_{-\infty}^{+\infty} w(t) \exp(-j2\pi ft)dt = \frac{\sin (\pi fT)}{\pi fT} \quad . \tag{2.119}$$

b. The Hanning window, defined by

$$w(t) = 0 \qquad\qquad\qquad \text{for } t < -T/2 \text{ and } t \ge T/2$$

$$w(t) = (1 + \cos 2\pi t/T)/(2T) \qquad \text{for } -T/2 \le t < T/2 \ ,$$

(2.120)

with the Fourier transform

$$W(f) = \frac{1}{4}\ \frac{\sin \pi(fT+1)}{\pi(fT+1)} + \frac{1}{2}\ \frac{\sin \pi fT}{\pi fT} + \frac{1}{4}\ \frac{\sin \pi(fT-1)}{\pi(fT-1)} \ . \tag{2.121}$$

c. The Hamming window, which is a special case of the general window type defined by:

$$w(t) = 0 \qquad\qquad\qquad \text{for } t < -T/2 \text{ and } t \ge T/2$$

$$w(t) = [a + (1-a) \cos 2\pi t/T]/T \qquad \text{for } -T/2 \le t < T/2$$

(2.122)

with the Fourier transform

$$W(f) = \frac{1}{2}(1-a)\ \frac{\sin \pi(fT+1)}{\pi(fT+1)} + a\frac{\sin \pi fT}{\pi fT} + \frac{1}{2}(1-a)\frac{\sin \pi(fT-1)}{\pi(fT-1)} \ . \tag{2.123}$$

Note that if $a = 0.5$ we obtain the Hanning window, and for $a = 1$ the rectangular window. The Hamming window is defined for $a = 0.54$, which gives the lowest side lobe levels for this window type.

These windows and their Fourier transforms are presented in figure 2.10. Notice that the spectrum of the rectangle has a narrow main lobe but considerable side lobes. The use of the Hanning or Hamming window reduces the side lobe levels considerably, but gives a broader main lobe. This is a consequence of the fact that rounding of the edges of the window in the time domain gives a reduction of the higher frequencies (side-lobes), but it also reduces the effective length of the window, making the main lobe in the frequency domain broader.
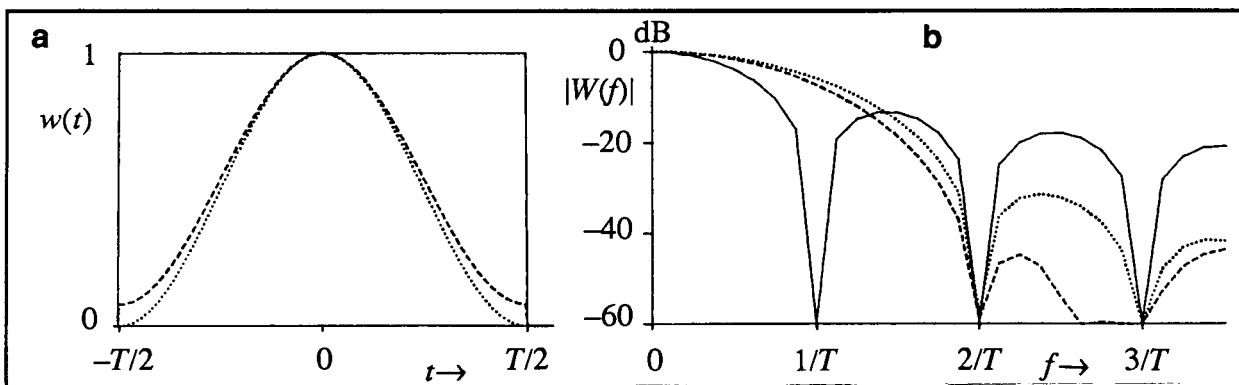
Figure 2.10: a. The rectangle (—), Hanning (·······) and Hamming (- - - -) windows; b. The amplitude of the frequency spectra of these windows, expressed in dB's.

The resolution is defined here as the minimum separation in frequency, necessary to resolve the main lobes of two spectral lines with equal amplitudes by visual inspection (see figure 2.11). Note that, because the frequency spectrum is complex, the resolution will depend on the phase relation between the two spectral lines. If the spectral lines are in phase, the resolution equals the -6 dB bandwidth of the mainlobe of the window. If the spectral lines are 90° out of phase, the -3 dB bandwidth has to be taken. This definition is practically identical with the Ricker criterion as used in seismology (e.g. Berkhout [7]).
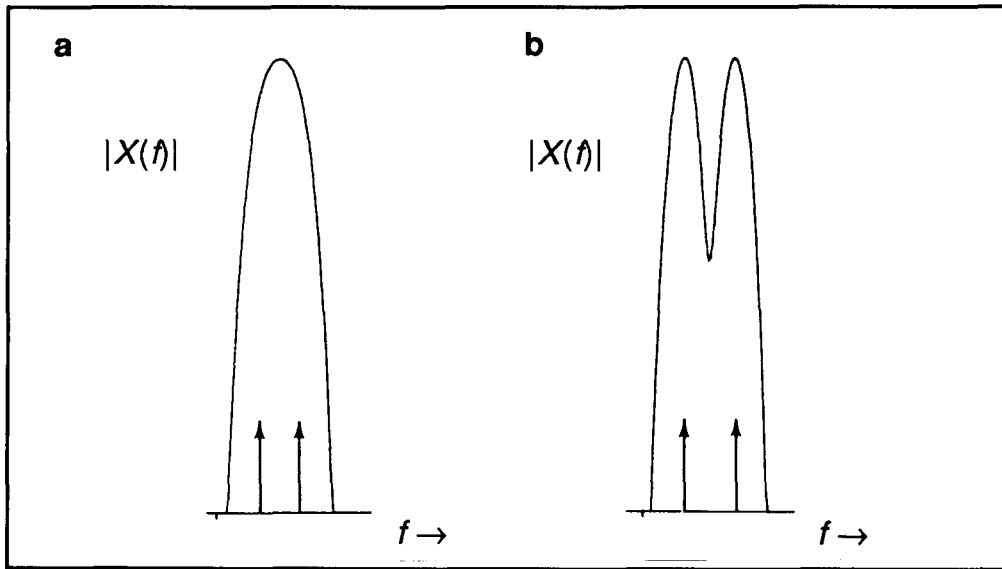
Figure 2.11: The amplitude spectrum of two non-resolvable (a) and two resolvable (b) spectral lines.

A thorough treatment of a large number of window types is given by Harris [25]. He shows that the window shape can be optimized to obtain excellent side lobe suppression, which is much better than with the Hanning window. Usually these special windows are only necessary if weak spectral lines have to be detected in the presence of a strong nearby line. The characteristics of some important windows are summarized in table 2.1. The bandwidth is expressed in bins. A bin is the fundamental frequency spacing, defined by Eq. (2.115).

Table 2.1

Windows and figures of merit in the frequency domain

window	highest side lobe level in dB	side lobe fall-off in dB/octave	-3 dB bandwidth in bins	-6 dB bandwidth in bins
Rectangle	-13	-6	0.89	1.21
Hanning	-32	-18	1.44	2.00
Hamming	-43	-6	1.30	1.81
Dolph-Chebyshev *)	-50	0	1.33	1.85
Blackman-Harris *)	-67	-6	1.66	1.81

*) These windows have several variants, of which only one is presented here.

For random noise analysis, the rectangular window is usually chosen as:

a. It gives an unbiased estimate of the power- and cross-spectra during the observation interval (true RMS-values);

b. Each spectral line is convolved with the Fourier transform of the window used, which causes spectral broadening and side lobes. For random noise signals, the spectral lines are usually summed over $1/12$ or $1/3$ octave bands. This averaging will smooth the results and diminish the effects of the window, especially in the higher part of the spectrum. Because of this spectral averaging it is not necessary to worry about special windows, and the rectangular window can simply be used.

2.7.4 Angular resolution

The angular resolution can be described in the same way as the frequency resolution. Because of the finite antenna length, the Fourier transform $\tilde{W}_a(k_x')$ of the spatial window of the antenna aperture $W_a(\xi)$, will modify Eq. (2.106) to

$$\tilde{R}'(k_x',f) = \sum_n \tilde{R}_n(f)\delta(k_x'-f/c_n) * \tilde{W}_a(k_x') = \sum_n \tilde{R}_n(f)\tilde{W}_a(k_x'-f/c_n) \ . \qquad (2.124)$$

There is however one principal difference with the situation in the previous paragraph. There the window was applied to the *linear* time signal, whereas here the window is applied to the *quadratic* spatial cross-spectrum. As a consequence the dB-values in table 2.1 are not applicable, but must be divided by a factor of 2, giving table 2.2.

Table 2.2

Windows and figures of merit in the k_x'-domain

window	highest side lobe level in dB	side lobe fall-off in dB/octave	−3 dB bandwidth in bins
Rectangle	−6.5	−3	1.21
Hanning	−16	−9	2.00
Hamming	−21.5	−3	1.81
Dolph-Chebyshev *)	−25	0	1.85
Blackman-Harris *)	−33.5	−3	1.81

*) These windows have several variants, of which only one is presented here.

If we define the resolution in the k_x'-domain as the minimum separation in k_x'-values that is necessary to distinguish between two signals with the same power (see fig. 2.11), then the −3 dB bandwidth has to be taken as presented in table 2.2. The $\tilde{R}'(k_x',f)$ values are always real, so the ambiguity of the definition due to out of phase addition (as is the case in the frequency domain), does not exist here.

From table 2.2 it can be seen that the side lobe levels of the rectangular window are very high (max. −6.5 dB), which is undesirable, not only because of the associated "power leakage", but also because a side lobe can easily be considered as the main lobe of another source. Further inspection of table 2.2 shows that a good side lobe suppression goes usually at the cost of a broad mainlobe. We noticed however that the Hamming window has both a lower side lobe level and a narrower mainlobe than the Hanning window. Because the rectangular, Hanning and Hamming windows are members of one family, that can be described by Eq. (2.123) by just changing the parameter a, it will be interesting to compare the −3 dB bandwidth and side lobe levels of this class of windows as a function of this parameter. The values are presented in figure 2.12. It shows that by selecting for instance $a = 0.6$, the sidelobe level is as low as that of the Hanning window (−16 dB), but that the −3 dB bandwidth is reduced from 2 to 1.6 bins. Figure 2.12 also clearly shows that it is possible to exchange the sidelobe level against the mainlobe bandwidth, which can be attractive in practical situations.
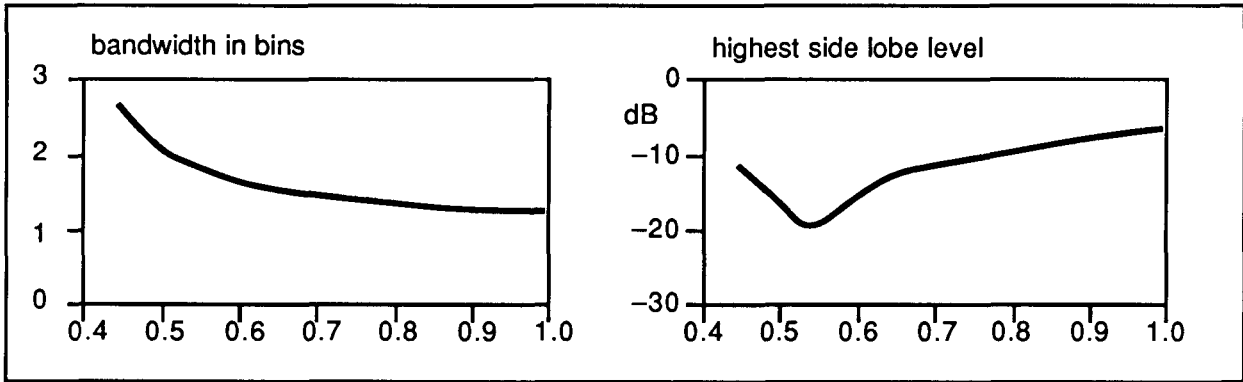
Figure 2.12: The bandwidth and sidelobe levels of the window type of Eq. (2.123), as a function of the parameter a.

If we call the −3 dB bandwidth of the spatial window B_w (in bins), then the −3 dB bandwidth in the k_x'-domain is:

$$B_k = B_w \Delta k_x' = B_w / (M\Delta\xi) \qquad (2.125)$$

where $\Delta k_x'$ is the sample interval in the k_x'-domain and $M\Delta\xi$ is the *synthetic aperture length* of the antenna, which — by making use of the property that $\tilde{R}(-\xi, f) = \tilde{R}^*(\xi, f)$ in a homogeneous soundfield — is twice the total antenna length X:

$$M\Delta\xi = 2X \quad . \qquad (2.126)$$

By differentiation of Eq. (2.97) with respect to α_n we find the relation between the k_x'-bandwidth and the angular bandwidth, normally called *beamwidth* $B_a(\alpha_n)$:

$$B_k = \frac{\partial k_x'}{\partial \alpha_n} B_a(\alpha_n) = (f/c) \cos \alpha_n B_a(\alpha_n) \ . \tag{2.127}$$

From Eq. (2.125), (2.126) and (2.127) we find for the angular beamwidth or resolving power:

$$B_a(\alpha_n) = \frac{1}{2} B_w c \ / \ (Xf \cos \alpha_n) = \frac{1}{2} B_w \lambda \ / \ (X \cos \alpha_n) \ . \tag{2.128}$$

This expression is in agreement with the general resolution formula of Eq. (1.3), if we realize that B_w is in the range of 1.6 to 2.0 for practical windows. It must be realized that expression (2.128) is a theoretical estimate of the beamwidth of the antenna. As we will see in the next chapter, the beamwidth is also a function of the sound transfer characteristics of the outdoor environment.

2.8 FOCUSSING

In Section 2.6 we discussed the theory of power spectrum estimation from spatial cross-correlations, based on the immission of plane waves that obey Eq. (2.93). We also mentioned that these spatial cross-correlation functions can be measured with a sparsed microphone array. Because this is a plane wave method, the results are focussed at an infinite source distance.

In practice the source distances are always finite. If the source distances are several orders of magnitude larger than the antenna length, the plane wave approximation is valid (Fraunhofer approximation). Under these conditions sparsed array processing can be applied directly. For shorter source distances the plane wave relation of Eq. (2.93) does not hold and a direct Fourier transformation of the cross-spectra to the k_x'-domain would result in unsharp images.

In this Section we will first investigate the general focussing problem using the concept of inverse wavefield extrapolation, and then show that there is a wide range of source distances for which the Fraunhofer condition of plane waves can be simulated if appropriate phase compensation is used.

2.8.1 Inverse wavefield extrapolation

For a general description of wavefield extrapolation, the reader is referred to Berkhout [26]. Here we will restrict our discussion to some important results of wavefield extrapolation in a homogeneous medium. The forward wave extrapolation of the pressure field in a homogeneous medium is given by the Rayleigh-II integral:

$$P(x_A, y_A, z_A, f) = \frac{\Delta z}{2\pi} \iint P(x, y, z_0, f) \ \frac{1 + jkr_A}{r_A^3} \exp(-jkr_A) dx dy \tag{2.129}$$

with $\Delta z = |z_A - z_0|$ and $r_A = (x_A - x, y_A - y, z_A - z_0)$. The integration takes place over the whole plane $z = z_0$. Note that Eq. (2.129) may only be used for forward extrapolation,

because it has been derived from the Kirchhoff integral, using the property that there are no sound sources beyond the plane $z = z_0$ in the direction of z_A. With Eq. (2.129) the sound pressure can be computed for each point in the plane $z = z_A$. The result can be described as a two-dimensional spatial convolution in x and y:

$$P(x, y, z_A, f) = W(x, y, z_A; z_0, f) * P(x, y, z_0, f) \qquad (2.130)$$

with

$$W(x, y, z_A; z_0, f) = \frac{\Delta z}{2\pi} \frac{1 + jkr}{r^3} \exp(-jkr) \quad . \qquad (2.131)$$

Equations (2.130) and (2.131) describe the forward propagation, i.e. from the sources to a receiver plane. With antenna techniques the aim is the opposite, i.e. to compute the spatial source distribution from a measurement of the sound pressures in a receiver plane. This procedure can be described as a deconvolution:

$$P(x, y, z_0, f) = F(x, y, z_0; z_A, f) * P(x, y, z_A, f) \quad . \qquad (2.132)$$

Substitution of Eq. (2.130) into (2.132) shows that under ideal circumstances, F is the exact inverse of W, such that

$$F(x, y, z_0; z_A, f) * W(x, y, z_A; z_0, f) = \delta(x)\delta(y) \quad . \qquad (2.133)$$

To find an expression for the inverse filter F, we will first transform Eq. (2.130) from the x, y to the k_x, k_y domain:

$$\tilde{P}(k_x, k_y, z_A, f) = \tilde{W}(k_x, k_y, z_A; z_0, f) \; \tilde{P}(k_x, k_y, z_0, f) \quad . \qquad (2.134)$$

An easy way to derive $\tilde{W}$ is obtained with a Fourier transformation of the wave equation to the k_x, k_y, z, f domain:

$$\frac{\partial^2 \tilde{P}}{\partial z^2} + (k^2 - k_x^2 - k_y^2)\tilde{P} = 0 \qquad (2.135)$$

with the solution

$$\tilde{P}(k_x, k_y, z_A, f) = \tilde{P}(k_x, k_y, z_0, f) \exp(-jk_z \Delta z) \qquad (2.136)$$

where

$$k_z = \left[k^2 - (k_x^2 + k_y^2)\right]^{1/2} \qquad \text{for } k_x^2 + k_y^2 \le k^2 \qquad (2.137\text{a})$$

and

$$k_z = -j\left[(k_x^2 + k_y^2) - k^2\right]^{1/2} \qquad \text{for } k_x^2 + k_y^2 > k^2 \quad . \qquad (2.137\text{b})$$

Hence,

$$\tilde{W}(k_x, k_y, z_A;z_0,f) = \exp(-jk_z\Delta z) \quad . \tag{2.138}$$

Note from Eq. (2.137) that the wavefield amplitudes decrease exponentially for $k_x^2 + k_y^2 > k^2$. It represents the so-called evanescent field, that is practically zero if $\Delta z > \lambda$. As a consequence, the exact inverse operator

$$\tilde{F}(k_x, k_y, z_0;z_A, f) = 1 \, / \, \tilde{W}(k_x, k_y, z_A;z_0,f) = \exp(jk_z\Delta z) \tag{2.139}$$

is unacceptable in any practical situation, as it would result in a large noise enhancement for $k_x^2 + k_y^2 > k^2$. For that reason the evanescent field is usually discarded by application of the matched filter:

$$\tilde{F}'(k_x, k_y, z_0;z_A, f) = \tilde{W}^*(k_x, k_y, z_A;z_0, f) \quad , \tag{2.140}$$

which is exact for $k_x^2 + k_y^2 \leq k^2$. Because of the complex conjugate relationship in Eq. (2.140), back transformation of this equation to the x, y domain gives, making use of Eq. (2.131):

$$F'(x, y, z_0;z_A, f) = W^*(-x, -y, z_A;z_0, f) = \frac{\Delta z}{2\pi} \frac{1-jkr}{r^3} \exp(jkr), \tag{2.141}$$

leading to the inverse Rayleigh-II integral:

$$P'(x_0, y_0, z_0, f) = \frac{\Delta z}{2\pi} \iint P(x, y, z_A, f) \frac{1-jkr}{r^3} \exp(jkr) dx dy \tag{2.142}$$

with

$$\mathbf{r} = (x_0-x, y_0-y, z_0-z) \quad .$$

Notice, that by neglecting the evanescent field, the inversion is not exact, but it gives a spatial bandlimited solution. If we consider a dipole in the plane $z = z_0$:

$$P(x, y, z_0, f) = S(f)\delta(x)\delta(y) \tag{2.143}$$

or in the k_x, k_y domain:

$$\tilde{P}(k_x, k_y, z_0, f) = S(f) \quad , \tag{2.144}$$

the forward extrapolation to the plane $z = z_A$ gives

$$\tilde{P}(k_x, k_y, z_A, f) = S(f) \exp(-jk_z\Delta z) \tag{2.145}$$

and inverse extrapolation, discarding the evanescent field gives

$$\tilde{P}'(k_x, k_y, z_0, f) = S(f) \qquad \text{for } k_x^2 + k_y^2 \le k^2$$

$$\qquad (2.146)$$

$$= 0 \qquad \text{for } k_x^2 + k_y^2 > k^2 \quad ,$$

leading in the x-y domain to

$$P'(x, y, z_0, f) = S(f) \frac{J_1(kr)}{2\pi r} \qquad (2.147)$$

with $r = (x^2 + y^2)^{1/2}$ and J_1 being the first order cylindrical Bessel function. In a two-dimensional situation, when P does not depend on y, we obtain in a similar way:

$$P'(x, z_0, f) = S(f) \frac{\sin (kx)}{\pi x} \quad . \qquad (2.148)$$

Eq. (2.147) and (2.148) represent the highest possible resolution of an infinite large antenna. The resolution that is obtained with a finite aperture is given by Berkhout [7] and results for a two-dimensional antenna with radius ρ in

$$P'(x, y, z_0, f) = S(f) \frac{J_1(kr \sin \beta_{max})}{2\pi r} \qquad (2.149)$$

with $\sin \beta_{max} = \rho/\sqrt{\rho^2 + (\Delta z)^2}$, and for a one-dimensional antenna with length D:

$$P'(x, z_0, f) = S(f) \frac{\sin (kx \sin \beta_{max})}{\pi x} \qquad (2.150)$$

with $\sin \beta_{max} = \frac{1}{2}D/\sqrt{z^2 + \frac{1}{4}D^2}$. Note that this result leads to the nearfield resolution given by Eq. (1.4).

Going back to Eq. (2.142) we see that if the measurement takes place at distances such that $kr >> 1$, Eq. (2.142) can be reduced to

$$P'(x_0, y_0, z_0, f) = \frac{-jk}{2\pi} \iint P(x, y, z_A, f) \cos \phi \, \frac{\exp(jkr)}{r} \, dxdy \quad . \qquad (2.151)$$

where $\cos \phi = \Delta z/r$.

Let us assume that there is a source at the position S. This source may be a monopole, a dipole, or it may even have a more complicated character. In all cases, if the antenna is in the far field of the source, the sound pressure at the plane $z = z_A$ can be written as:

$$P(x, y, z_A, f) = A(x, y, z_A, f) \, S(f) \, \exp(-jkr_s)/r_s \qquad (2.152)$$

where A is a real amplitude factor, depending on the type of sound source ("directivity pattern") and $S(f)$ represents the (complex) source strength. Substitution of Eq. (2.152) into (2.151) shows — when the inversion takes place for the source point S — that $r = r_s$, so the phase terms compensate and an in-phase integration occurs. If the inversion is carried out for another point, destructive phase interference will occur and the integration result will tend to zero.

When the source is in the far field of the antenna, i.e. the antenna aperture is small compared to the source distance, Eq. (2.151) can be approximated by:

$$P'(x_0, y_0, z_0, f) = \frac{-jk}{2\pi r_0} e^{jkr_0} \int\!\!\int P(x, y, z_A, f) \, \exp(jk \cdot \Delta r) dx dy \qquad (2.153)$$

where $\Delta r = r - r_0$ and $k \cdot \Delta r = k_x x + k_y y$.

Notice that the integral represents a Fourier transform from x, y to k_x, k_y and that this is in agreement with the plane wave decomposition as presented in Section 2.5 for the one-dimensional case. If the far field condition is not met, the Fourier relationship is not valid and appropriate nonlinear phase corrections will have to be made. This will be discussed in the next paragraphs.

2.8.2 Beamforming with phased arrays

In the preceding paragraph we found that under the condition that $kr \gg 1$, the inverse extrapolation consists of (see Eq. (2.151)):

1. an amplitude correction, given by a factor $\cos \phi/r$;
2. a phase correction, given by the factor $\exp(jkr)$.

The effect of both corrections is quite different. The amplitude correction is only a weight-factor in the addition and acts as a spatial window in the same way as the windows that can be used to reduce sidelobes (see Section 2.7). If the distance to the sources is not too small, its effect can usually be neglected. The phase correction is much more important. Notice that a distance change of only $1/2 \, \lambda$ results in a phase shift of 180°.

These considerations are reflected in the design of so-called "phased-arrays". These are transducer arrays in one- or two dimensions. They perform a discretized inverse Rayleigh-II integration with a phase compensation according to the factor $\exp[jk(r-r_0)]$, where r_0 is the distance between the focal point and a reference point on the antenna, usually the center of the aperture. This procedure is called "beamsteering" and can be formulated for a one-dimensional antenna by

$$S(f) = \int P(x,f) \exp[jk(r-r_0)]dx \quad .$$

(2.154)

We will now investigate how this expression depends on the source distance r. In figure 2.13 the situation of a spherical wave which enters the antenna axis with angle α is depicted, together with a plane wave with the same angle of incidence.
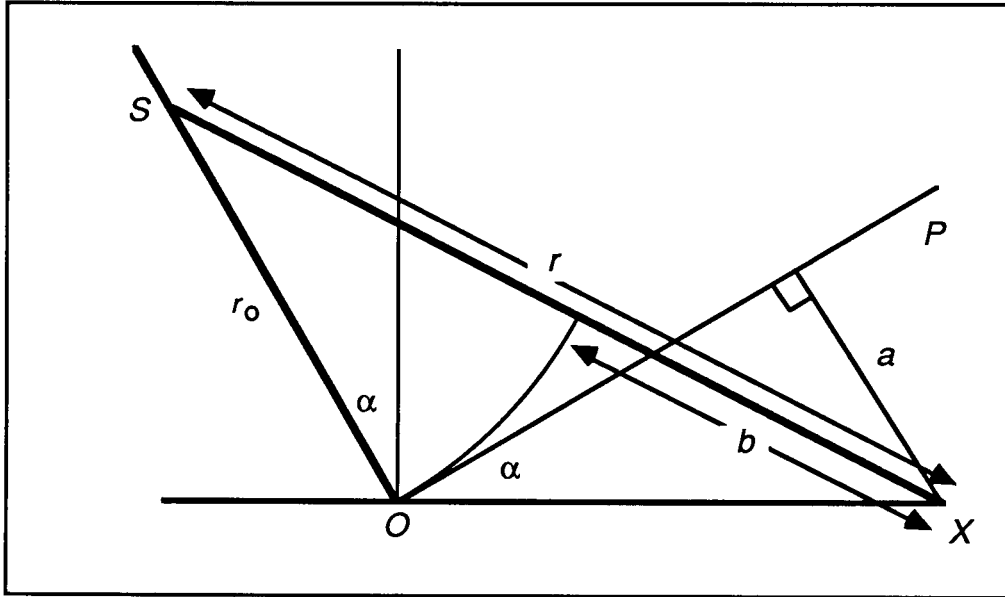
Figure 2.13: Comparison between a plane wave with wavefront OP and a spherical wave from source S with the same angle of incidence α.

From this figure it follows that the distance r $(= r_0 + b)$ between the source and the position x on the antenna axis is given by

$$r = (r_0^2 + x^2 + 2r_0 x \sin \alpha)^{1/2} \quad .$$

(2.155)

This expression can be developed into a Taylor expansion of x, resulting in

$$r = r_0 + x \sin \alpha + \frac{1}{2}\frac{x^2}{r_0}(1 - \sin^2\alpha) + \frac{1}{2}\frac{x^3}{r_0^2}(\sin^3\alpha - \sin \alpha)$$

$$+ \frac{1}{24}\frac{x^4}{r_0^3}(-15\sin^4\alpha + 18\sin^2\alpha - 3) + 0\left(\frac{x^5}{r_0^4}\right) \quad .$$

(2.156)

Dependent on the source distance, Eq. (2.156) can be approximated as follows:

a. Fraunhofer approximation

Only the linear dependence of x is taken into account, corresponding with the plane wave approximation:

$$r_a = r_0 + x \sin \alpha \quad . \tag{2.157}$$

b. Fresnel approximation

Here the quadratic term is included:

$$r_b = r_0 + x \sin \alpha + \frac{1}{2} \frac{x^2}{r_0} (1 - \sin^2 \alpha) \quad . \tag{2.158}$$

Note that this approximation is very accurate for small values of α.

If the source distance is very large, the Fraunhofer or plane wave condition is valid, so $r - r_0 = x \sin \alpha$ and Eq. (2.154) can be written as

$$S(f) = \int P(x, f) \exp(jk_x x) dx \tag{2.159}$$

with $k_x = k \sin \alpha$. Hence, in the far field the phased array output $S(f)$ is the Fourier transform of $P(x, f)$ from x to k_x, which is in agreement with the theory of Section 2.5.

If the source is at a smaller distance, the processing with Eq. (2.159) will result in an unsharp image. This is caused by the fact that the phase factor $\exp(jk_x x)$ will not compensate the phase factor of the source, given by $\exp[-j(r-r_0)]$. The resulting phase factor is given by $\exp(-j\Phi)$, where $\Phi = k\Delta r = k(r - r_0 - x \sin \alpha)$. It has been found from simulations that sharp images are obtained when $|\Phi| < 1/2\pi$. In that case only positive summations will occur in Eq. (2.159). From Eq. (2.156) it is found that this criterion is met when

$$\Delta r = 1/2 \frac{X^2}{r_0} < 1/4 \lambda \tag{2.160a}$$

or

$$r_0 > 2 X^2 / \lambda \tag{2.160b}$$

where X is the outer microphone position. If the reference point is taken at the center of the aperture, X equals half the aperture length.

2.8.3 Sparsed array processing

SYNTACAN is based on sparsed array processing of the spatial cross-correlation field. We pointed out in Section 2.6 that there is a large similarity between plane wave decomposition and the power spectrum estimation from the spatial cross-correlation function. It was found that under plane wave conditions, the angular source power can be computed with a Fourier transform of the spatial cross-spectrum as given by Eq. (2.106). As a consequence, the criterion for the validity of far-field processing, given by Eq. (2.160) is also applicable in sparsed array processing. Notice however that a sparsed array is usually one-sided — by making use of the property that $R(-\xi, f) = R^*(\xi, f)$, so the reference point must be taken at one side of the antenna and X now indicates the total antenna length.

2.8.4 Simulation of the Fraunhofer condition in the near field

At closer distances the linear travelpath relation of the Fraunhofer approximation does not hold. This has been investigated for several source directions and distances as indicated in figure 2.14. The results are presented in figure 2.15.
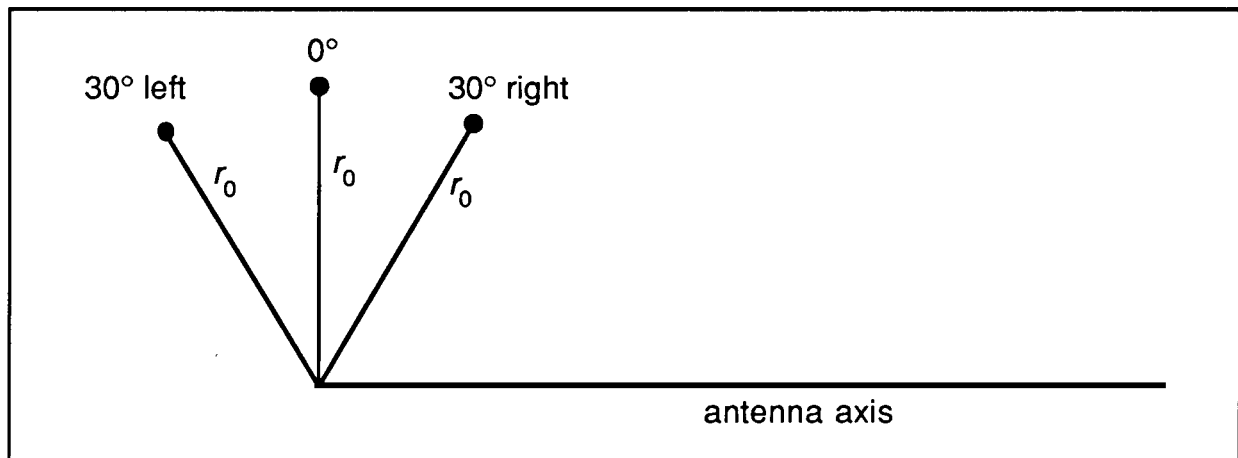
Figure 2.14: Source positions used in the traveltime calculations of figure 2.15.

The traveltimes are computed from the relation $T(x) = r/c$, where r is given by Eq. (2.155) and c = 342 m/s (air at 20 °C). It is possible, however, to apply traveltime corrections to the incoming spherical wavefront in such a way that it behaves as a plane wavefront from the same direction. After such a correction, the data can be processed as for plane waves, and sparsed array processing can also easily be applied. These corrections are also given in figure 2.15. From figure 2.13 and Eq. (2.155) it follows that the difference between the raypath length SO and SX of the spherical wave equals:

$$b = [r_0^2 + x^2 + 2r_0 x \sin \alpha]^{1/2} - r_0 \qquad (2.161)$$

whereas the raypath difference of the plane wave from the same direction equals $x \sin \alpha$.
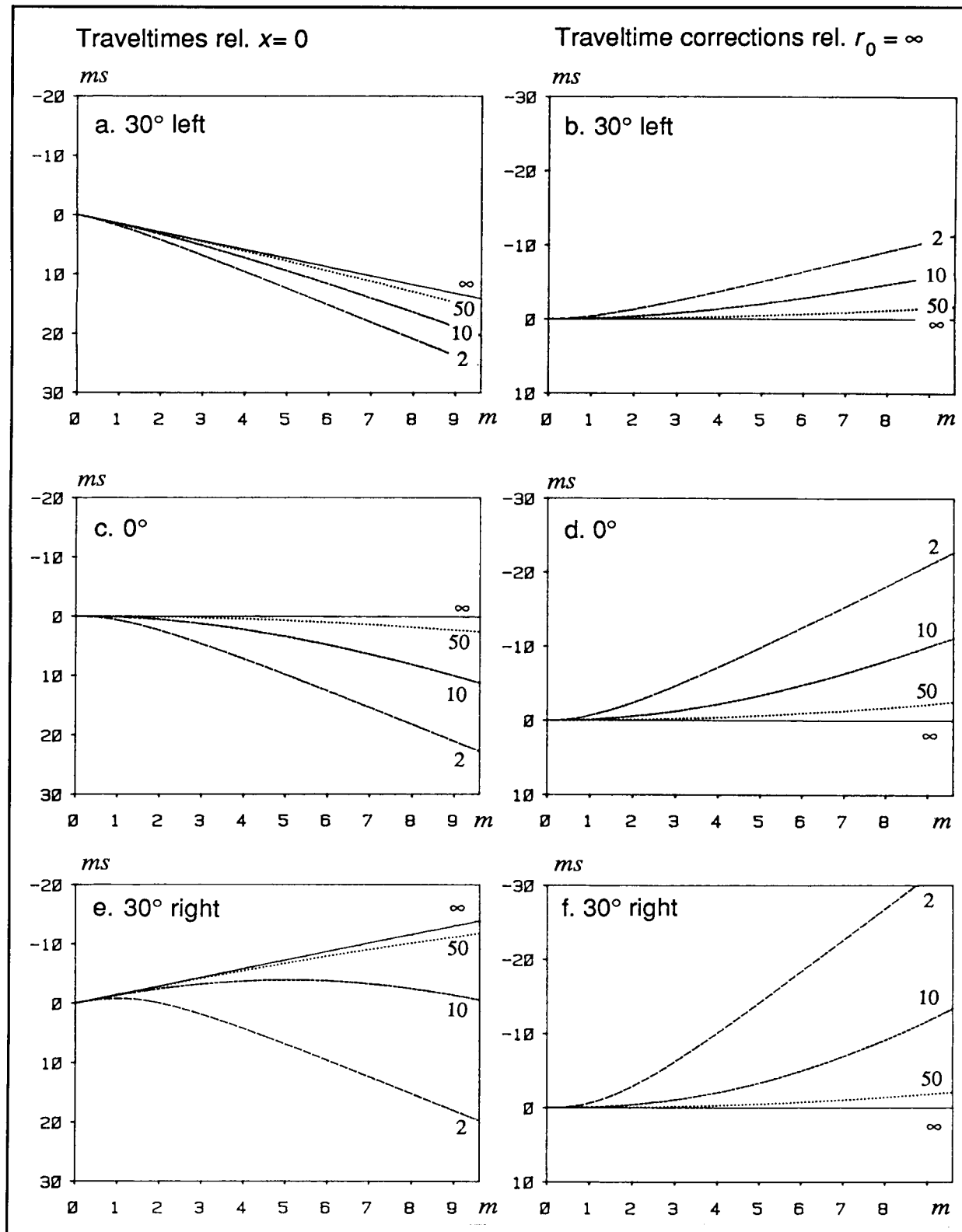
Figure 2.15: Traveltimes along the antenna axis for different source distances and directions. The left figures show the traveltime differences for source distances of $r_0 = \infty$, 50, 10 and 2 m and source angles of 30° left, 0° and 30° right. The traveltimes are shown with the axis pointing downwards as is usual in seismics and echoacoustics. The right figures show the necessary traveltime compensation to simulate the Fraunhofer condition.

Hence, the phase correction for Fraunhofer simulation on the point (r_0, α) can be attained by multiplication of the microphone signals in the frequency domain with the factor

$$D(r_0, \alpha, x) = \exp[jkh(r_0, \alpha, x)] \tag{2.162}$$

with

$$h(r_0, \alpha, x) = [r_0^2 + x^2 + 2r_0x \sin \alpha]^{1/2} - r_0 - x \sin \alpha \quad . \tag{2.163}$$

After this correction Eq. (2.157) is valid for the source position (r_0, α), and the beamsteering can be performed with a Fourier transform to the k_x'-domain. Notice from Eq. (2.162) and (2.163) that the phase correction is different for each point (r_0, α), so strictly speaking, the corrections and Fourier transforms have to be repeated for all possible source positions. However, some deviations from the ideal focussing are allowed and according to Eq. (2.160a) the images will be sharp when $|\Delta r| < 1/4\lambda$, where Δr is the error in the correction term.

Inspection of figure 2.15 shows that the traveltime corrections depend both on the source distance and on the angle of incidence; but when the sources are at larger distances, the corrections are small and approximately equal for different angles of incidence. This is very attractive, because a focussing correction for one point can then be applied for a range of source angles and distances, and sharp images within that zone are obtained with only one Fourier transform.

We will examine this criterion for the case that the focussing is performed for a position $(r_f, 0)$, so for frontal incidence at a distance r_f. The correction is then given by

$$D'(r_f, x) = \exp[jkh'(r_f, x)] \tag{2.164a}$$

with

$$h'(r_f, x) = (r_f^2 + x^2)^{1/2} - r_f \quad . \tag{2.164b}$$

The exact correction for a point (r_0, α) is given by Eq. (2.163), so the condition for sharp images reads:

$$\left| h(r_0, \alpha_0, X) - h'(r_f, X) \right| =$$

$$\left| [r_0^2 + X^2 + 2r_0X \sin \alpha]^{1/2} - r_0 - X \sin \alpha - [r_f^2 + X^2]^{1/2} + r_f \right| < 1/4 \lambda \quad . \tag{2.165}$$

The focal zones are illustrated in figure 2.16 for several focal distances r_f for an antenna with $X = 30 \lambda$ (this is approximately true for the SYNTACAN design). From this figure it is seen that the phase focussing according to Eq. (2.164) is adequate for all angles of incidence $|\alpha| < 30°$ if $r_f > 20X$. At shorter distances the resolution will be improved if the phase corrections are carried out for a number of angular sections.
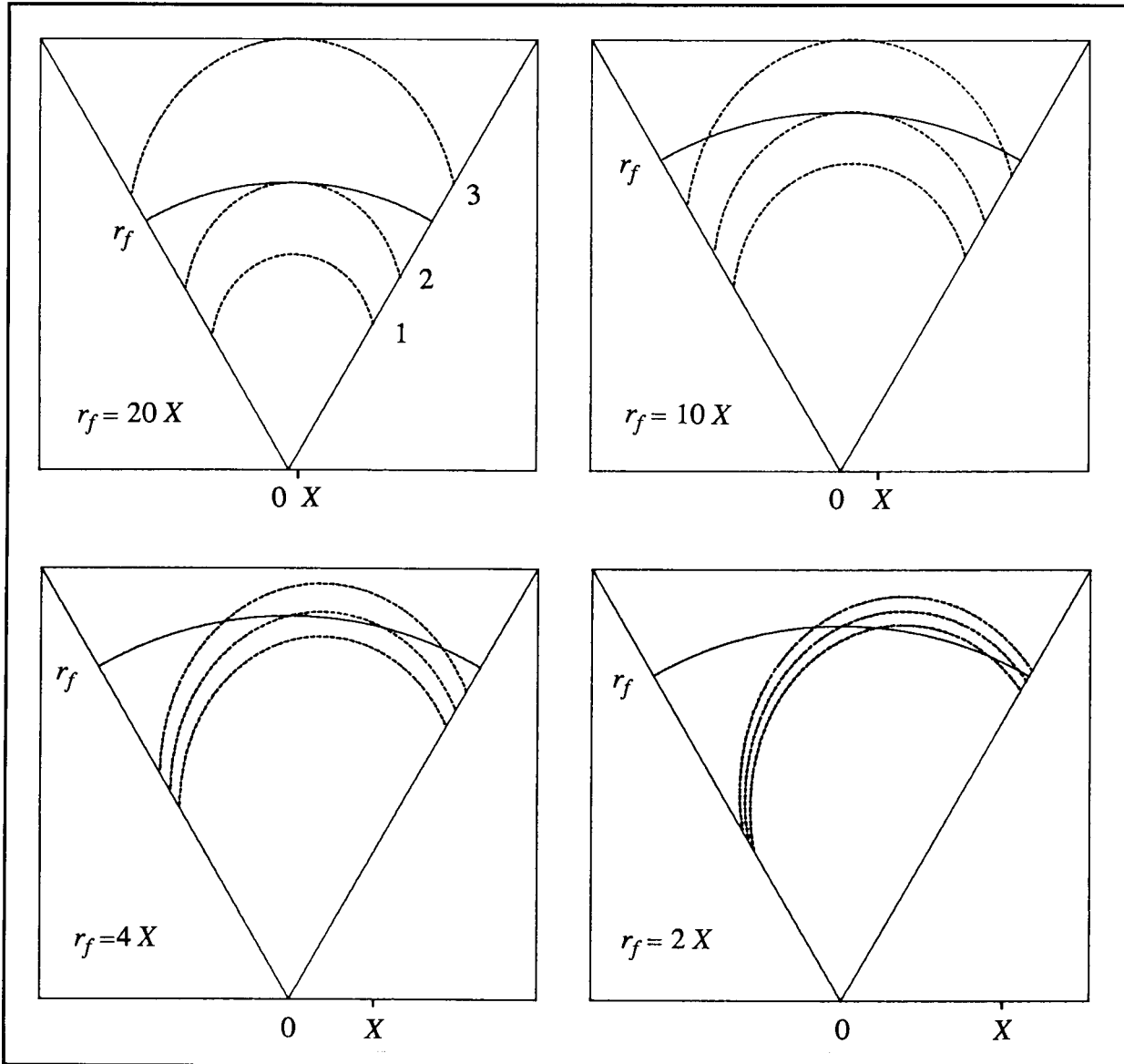
Figure 2.16: Focal zones according to Eq. (2.165) for several focal distances r_f of an antenna with a length of $X = 30\,\lambda$. The contours 1 and 3 correspond with a maximum deviation from the plane wave condition of $1/4\lambda$ for the outer microphone and contour 2 gives the line for which the focussing is exact for that microphone.

We will now derive a condition for sharp images that is valid for large distances, when the Fresnel approximation is valid. In that case Eq. (2.158) may be substituted into Eq. (2.165), giving

$$\left| \frac{1 - \sin^2\alpha}{r_0} - \frac{1}{r_f} \right| < \frac{\lambda}{2X^2} \; . \tag{2.166}$$

Evaluation of Eq. (2.166) shows that if we focus at $r_f = 2X^2/\lambda$, the image will be sharp from $1/2r_f (1 - \sin^2 \alpha)$ to ∞. Notice that this focal distance coincides with the Fraunhofer boundary given by Eq. (2.160). For SYNTACAN $X \approx 30\lambda$, so the Fraunhofer boundary is given by $r = 60X$.

In conclusion it can be stated that the Fraunhofer condition can be simulated for finite source distances by appropriate phase compensations of the microphone signals. This gives the possibility to apply the same sparsed array processing as for plane waves. If the sound sources are at distances > $20X$, where X is the antenna length of the sparsed array, the focal zone is large and independent of α, so far field processing by Fourier transformation to the k_x'-domain is very efficient. At closer distances this processing is also possible but the focal zone is small and the focussing procedure will have to be repeated for different source areas, also as a function of the angle of incidence.

The simulation of the Fraunhofer condition for near field sources is very attractive, as it allows for use of sparsed array processing that would otherwise only be applicable for far field sources. This procedure also elegantly separates the focussing problem into range and direction finding and clearly shows the different nature of axial (range) and lateral (direction) resolution.

Considering the way of imaging, the angular resolution is based on the Fraunhofer condition and, for antenna length X, is given by Eq. (2.128):

$$B_a(\alpha) = 1/2B_w \lambda / X \cos \alpha \quad . \tag{2.167}$$

Note that this expression is independent of the source distance.

On the other hand, as no traveltime information from the sources to the receivers is available, the range finding is based on an iterative process of focussing for different source distances until the sharpest image is obtained. Hence, the axial resolution is completely determined by the depth of field or focal zone, which is dependent on the source distance r_0 and is given in Fresnel approximation by Eq. (2.166):

$$\left| \frac{\cos^2 \alpha}{r_0} - \frac{1}{r_f} \right| < \frac{\lambda}{2X^2} \quad . \tag{2.168}$$

Notice that this focussing procedure is directly comparable with the imaging with a fixed focus optical lens. Here the lateral resolution is also practically independent of the source distance, and the Fraunhofer situation is simulated by changing the distance between the lens and the image plane in such a way that objects within the depth of field present sharp images. Hence, range finding with an optical lens can be performed by changing the focus distance until the sharpest image is obtained. The distance can then be read from the distance scale of the lens.

CHAPTER 3

OUTDOOR SOUND PROPAGATION

3.1 INTRODUCTION

In Chapter 2 we discussed antenna theory under the assumption that sound propagation obeys the linear homogeneous wave equation for a stationary medium. In practice there are many factors that disturb sound propagation with respect to the flow-free homogeneous medium. The disturbances can be roughly divided into deterministic and statistic propagation effects, which we will discuss in the next two sections. It must be realized that many of these factors also apply to conventional immission measurements with a single microphone, but because of the spatial character of these effects, they will influence the angular resolving power of the antenna.

3.2 DETERMINISTIC SOUND TRANSFER CHARACTERISTICS

3.2.1 Effects which are homogeneous along the antenna axis

These effects will not have a direct consequence on the antenna performance, as the disturbance is independent of the microphone position. Some important factors are:

a. **Atmospheric absorption**, usually expressed in dB/m. As shown in table 3.1 it is strongly dependent on frequency and this effectively eliminates the high frequencies over large distances.

b. **Ground absorption and reflection.** If the sound sources are at a large distance compared to the source and microphone heights and if the reflection path is homogeneous over the antenna length, then all microphones will measure the same influence of ground reflections, usually as an interference dip in the transfer function in the frequency region between 200 and 500 Hz and as several interference dips at higher frequencies. A theoretical description of ground effects is given by Attenborough et al. [27]. In figure 3.1 calculations by Koers [28] are presented, showing the transfer functions above grassland for a point source at a distance of 200 m and a height of 5 m, while the receiver height was varied between 1.5 and 10 m. It illustrates that the ground effects are less pronounced at higher receiver positions.

Table 3.1

Atmospheric absorption

according to ISO 3891–1978 at 10 °C and 80% relative humidity

octave band in Hz	absorption in dB/m
125	0.000
250	0.001
500	0.002
1000	0.003
2000	0.007
4000	0.019
8000	0.046
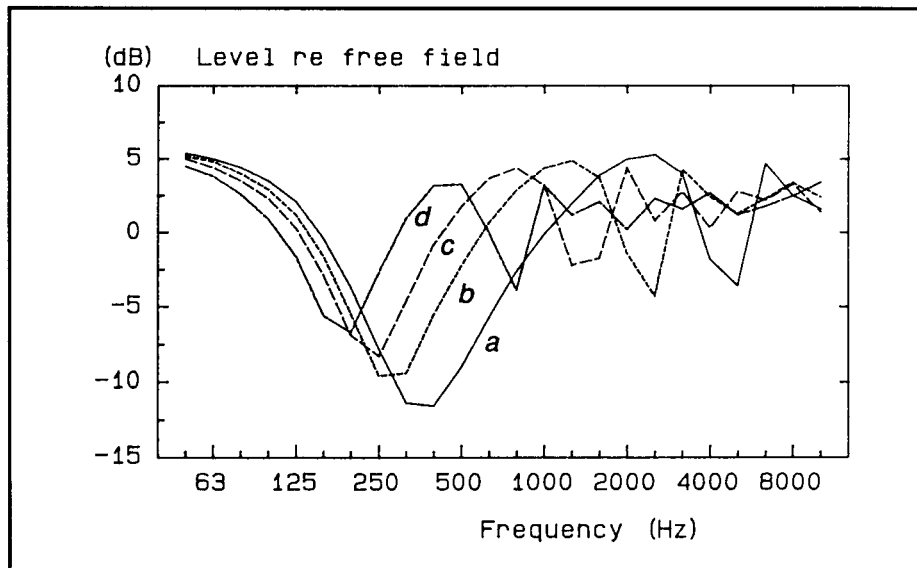
Figure 3.1: The ground effect ΔL_b for a monopole source at a distance of 200 m and a height of 5 m for different receiver heights: a = 1.5 m; b = 3.0 m; c = 5.0 m and d = 10.0 m (calculations by Koers [28]).

c. Wind and temperature profiles. Under the conditions that wind and temperature profiles are independent of time (turbulence is neglected) and if the profile only depends on the height z above the ground (stratified medium), their effects will be homogeneous along the antenna axis. Sound propagation under these conditions has been studied theoretically by De Jong [29]. Due to the inhomogeneity in the vertical direction, the sound rays will be curved as illustrated in figure 3.2. It is known from practice that the wave propagation in the upwind direction is unstable at distances of more than 50 m. Therefore measurements under this condition should be avoided. The same applies for the situation without wind during day-time, when a negative temperature gradient exists. For that reason the Dutch Government has prescribed that immission measurements should only take place within the

so-called "meteorological window" (summarized in table 3.2). It is also recommended that immission measurements take place at a receiver height of 5 m, where the influence of ground reflections and wind- and temperature effects is much smaller than at lower receiver positions.
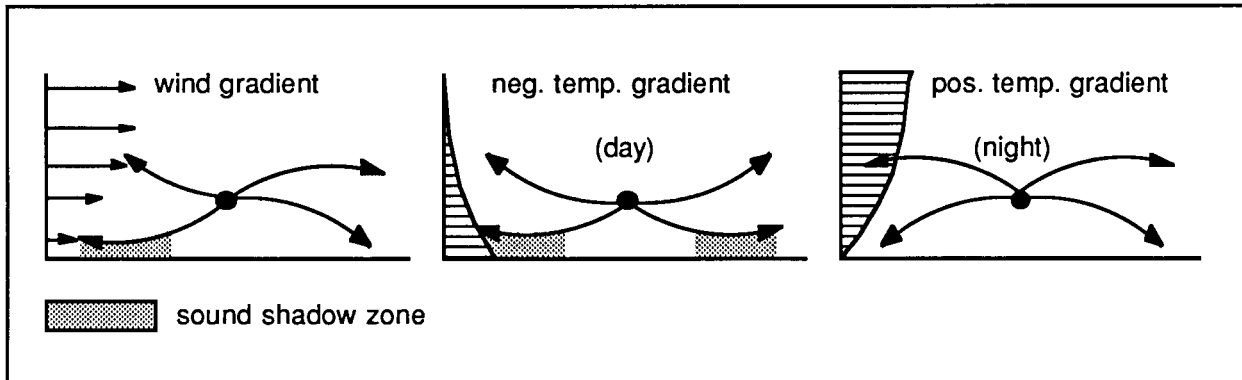
Figure 3.2: Wind and temperature gradients cause curved sound rays.

Table 3.2

Meteorological window for immission measurements of industrial noise
as prescribed by the Dutch Government

time and conditions		max. windspeed in m/s	max. windangle relative source-receiver direction
day	October – May	> 1	60°
	June – September	> 2	
night	> 1/8 cloudiness	> 1	75°
	< 1/8 cloudiness	> 0	
		0	all directions

3.2.2 Effects which are inhomogeneous along the antenna axis

Deterministic propagation effects which give an inhomogeneity along the microphone axis will result in an extra spatial window $W_p(\xi, f) = A(\xi, f)\exp[-j2\pi f\tau(\xi, f)]$, so that the beam pattern in the k_x-domain will be convolved with its Fourier transform $\tilde{W}_p(k_x', f)$ (see also Section 2.7.4 and Eq. (2.124)). In general, this will lead to a deterioration of the resolving power of the antenna. At large source distances these inhomogeneities can be the result of variations in the ground absorption, for instance if a part of the antenna is placed above asphalt and another part above grassland. Another reason may be the partial screening by obstacles between the sources and the antenna.

At small distances the geometrical spreading and directivity of the sources will produce an inhomogeneity of the soundfield over the antenna aperture. As discussed in Section 2.8, these amplitude effects are usually not taken into account, but when the sources have a multipole character, then the radiation characteristic can vary over the antenna aperture and influence the beam pattern.

3.2.3 The influence of a stationary and uniform wind

Sound propagation in a stationary and uniform wind has been studied in Section 2.4. It was found that the soundrays are in the direction away from the sound sources, but that in general the soundrays are not perpendicular to the wavefronts. In this paragraph we will investigate how this influences the performance of the antenna.

Plane wave approximation

If the sound sources are at a sufficient distance from the antenna, a plane wave approximation is justified (see Section 2.8). The geometry for this case is given in figure 2.3. The ray velocity c_{ray} is given by $c_{ray} = c_0 \mathbf{n} + \mathbf{v_0}$, where c_0 is the sound velocity in the flow-less medium, $\mathbf{n}$ is the wavefront normal and $\mathbf{v_0}$ is the windspeed.

The antenna is placed on the x-axis and measures the spatial cross-spectrum (see Section 2.6):

$$\tilde{R}(\xi, f) = \tilde{R}_1(f) \exp(-jk_x \xi) \tag{3.1}$$

with

$$k_x = \frac{\omega}{c} \sin \psi \quad , \tag{3.2}$$

where c is given by Eq. (2.58):

$$c = c_0(1 + \mathbf{m \cdot n}) = c_0(1 + m_x \sin \psi - m_y \cos \psi) \quad . \tag{3.3}$$

The antenna computes the source direction α' with Eq. (2.97) according to

$$\sin \alpha' = \frac{c_0}{\omega} k_x \quad . \tag{3.4}$$

Substitution of Eq. (3.2) and (3.3) into (3.4) gives

$$\sin \alpha' = \sin \psi / (1 + m_x \sin \psi - m_y \cos \psi) \quad , \tag{3.5}$$

or, for $v_0 \ll c_0$:

$$\sin \alpha' \approx \sin \psi (1 - m_x \sin \psi + m_y \cos \psi) \quad . \tag{3.6}$$

The true source direction is found from the ray direction (see figure 2.3):

$$\sin \alpha = \sin (\psi+\theta) = \sin \psi \cos \theta + \cos \psi \sin \theta \quad . \tag{3.7}$$

If $v_0 << c_0$, then θ is small, so Eq. (3.69b) is valid and $\cos \theta \approx 1$. Eq. (3.7) may then be replaced by

$$\sin \alpha = \sin \psi + m_x \cos^2 \psi + m_y \sin \psi \cos \psi \quad . \tag{3.8}$$

From Eq. (3.6) and (3.8) we find for $v_0 << c_0$:

$$\Delta \sin \alpha = \sin \alpha' - \sin \alpha = -m_x \quad . \tag{3.9}$$

So, the antenna measures with an angular error $\phi = \alpha' - \alpha$, given by:

$$\frac{\Delta \sin \alpha}{\phi} = \frac{d}{d\alpha} \sin \alpha = \cos \alpha \quad , \text{ or}$$

$$\phi = -m_x / \cos \alpha \quad . \tag{3.10}$$

Notice that the angular error only depends on the windspeed component in the x-direction and not on the component in the y-direction.

Spherical waves

A direct approach to obtain the performance of the antenna for spherical waves is by calculation of the traveltime $T(x)$ from the source S to the position X on the antenna axis. The geometry is given in figure 2.4. It shows that the center S' of the spherical wavefront which enters the antenna axis, has moved over a distance $\mathbf{d}$ in the wind direction, given by

$$\mathbf{d} = v_0 T(x) \quad . \tag{3.11}$$

Table 3.3 shows a rough indication of the source displacement d for a range of source distances and windspeeds. Application of the cosine-rule to triangle SXS' in figure 2.4, and making use of the relations

Table 3.3

Source displacement in meters in a uniform wind

source distance in m	windspeed in m/s		
	3	5	10
100	0.9	1.5	2.9
500	4.4	7.4	14.7
1000	8.8	14.7	29.4
2000	17.6	29.4	58.8

$$T(x) = r_0 / c_{ray} = d / v_0 = r / c_0 \qquad (3.12)$$

shows that

$$c_{ray} = c_0(1 - m^2 \sin^2\beta)^{1/2} + v_0 \cos\beta \qquad (3.13)$$

where $m = v_0/c_0$ is the Mach-number and β is the angle between the wind direction and the source-receiver direction and equals $\gamma - \alpha$ (see figure 2.4). For small values of $m^2\sin^2\beta$, Eq. (3.13) can be simplified to

$$c_{ray} = c_0 + v_0 \cos\beta \quad . \qquad (3.14)$$

We will now compute $T(x)$ for $x \ll r_0$. From this expression the antenna performance can be evaluated. The traveltime $T(x)$ will be computed from the relation

$$T(x) = r_x / c_{ray} \quad . \qquad (3.15)$$

Application of the cosine-rule to triangle SOX of figure 3.3 gives:

$$r_x = (r_0^2 + x^2 + 2r_0 x \sin\alpha_0)^{1/2} \quad . \qquad (3.16)$$
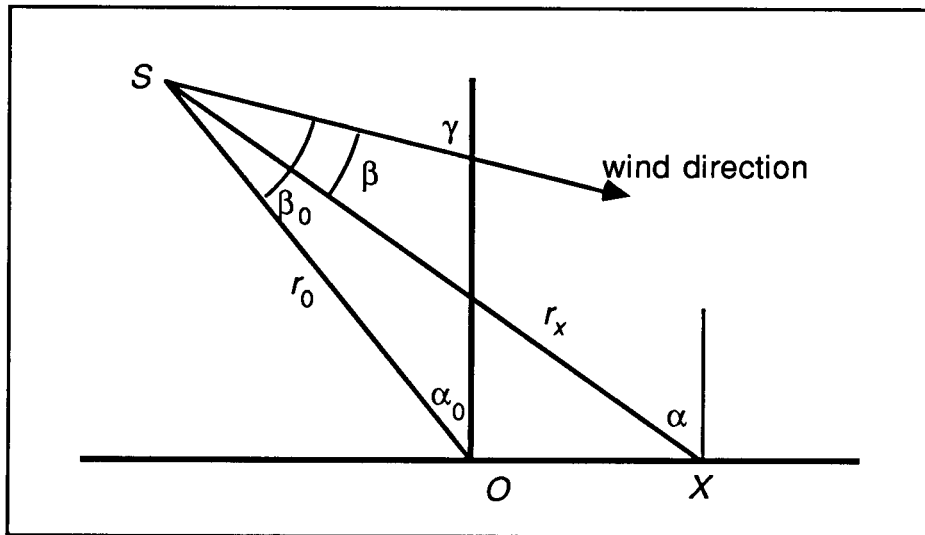
Figure 3.3: Soundrays SO and SX have different propagation speeds because they have different wind angles.

This relation may be simplified for $x \ll r_0$ as

$$r_x = r_0 + x \sin\alpha_0 \quad . \qquad (3.17)$$

Combination of Eq. (3.14), (3.15) and (3.17) gives

$$T(x) \quad = (r_0 + x \sin\alpha_0) / c_0(1 + m \cos\beta)$$

$$\approx (1/c_0)(r_0 + x \sin \alpha_0)(1 - m \cos \beta)$$

$$= (1/c_0)(r_0 - mr_0 \cos \beta + x \sin \alpha_0 - xm \sin \alpha_0 \cos \beta) \quad . \tag{3.18}$$

Notice, that in this expression β is a function of x. Around $x = 0$, $T(x)$ can be approximated by a Taylor expansion:

$$T(x) = T(0) + T'(0)x \quad . \tag{3.19}$$

From Eq. (3.18) we find:

$$T'(0) = \frac{1}{c_0} \left[\sin \alpha_0 - m \left(r_0 \frac{d \cos \beta}{dx} + \sin \alpha_0 \cos \beta \right) \right] \quad . \tag{3.20}$$

The factor $d \cos \beta / dx$ can be worked out as follows:

$$\cos \beta = \cos (\gamma - \alpha) = \cos \gamma \cos \alpha + \sin \gamma \sin \alpha \quad ,$$

$$\frac{d \cos \beta}{dx} = \cos \gamma \frac{d \cos \alpha}{dx} + \sin \gamma \frac{d \sin \alpha}{dx} \quad .$$

From figure 3.3 we can find that

$$tg\ \alpha = \frac{r_0 \sin \alpha_0 + x}{r_0 \cos \alpha_0} = tg\ \alpha_0 + \frac{x}{r_0 \cos \alpha_0}$$

so

$$\frac{d\ tg\ \alpha}{dx} = \frac{1}{r_0 \cos \alpha_0} = \frac{1}{\cos^2 \alpha_0} \frac{d\alpha}{dx} \quad , or\ \frac{d\alpha}{dx} = \frac{\cos \alpha_0}{r_0} \quad .$$

Now we find:

$$\frac{d \cos \alpha}{dx} = \frac{-\sin \alpha_0 \cos \alpha_0}{r_0} ; \quad \frac{d \sin \alpha}{dx} = \frac{\cos^2 \alpha_0}{r_0} \quad .$$

Substitution of these results in Eq. (3.20) gives

$$T'(0) = \frac{1}{c_0} [\sin \alpha_0 - m_x] \tag{3.21}$$

or, using Eq. (3.19):

$$T(x) = T(0) + \frac{x}{c_0} [\sin \alpha_0 - m_x] \quad . \tag{3.22}$$

The wavefield on the antenna-axis can now be written as (in the Fraunhofer approximation):

$$s(x, t) = s\left(0, t - \frac{x}{c_0} [\sin \alpha_0 - m_x]\right)$$ (3.23)

so the antenna will measure the spatial cross-spectrum

$$\tilde{R}(\xi, f) = \tilde{R}_1(f) \exp(-jk_x \xi)$$ (3.24)

with

$$k_x = (\omega/c_0)(\sin \alpha_0 - m_x) \quad .$$ (3.25)

The source direction will be computed according to Eq. (3.4), leading to

$$\Delta \sin \alpha = \sin \alpha' - \sin \alpha = -m_x \quad .$$ (3.26)

This expression is identical to Eq. (3.9) and gives the same angular error as for a plane wave:

$$\phi = -m_x / \cos \alpha \quad .$$ (3.27)

Focussing

When the noise sources are not very distant compared with the antenna length, a focussing operation has to be done to transform the spherical wavefronts into plane wavefronts, before the spatial Fourier transform is performed. This procedure was discussed in Section 2.8. It was found that a correct focussing is obtained with a timeshift of

$$T_c(x) = (r_x - r_0 - x \sin \alpha_0) / c_{ray}$$ (3.28)

where r_x, r_0, x and α_0 are as given in figure 3.3 and c_{ray} is given by Eq. (3.13). Application of the timeshift to the arrival times $T(x)$ of Eq. (3.15) gives

$$T_f(x) = T(x) - T_c(x) = (r_0 + x \sin \alpha_0) / c_{ray} \quad ,$$ (3.29)

representing the Fraunhofer condition as given by Eq. (3.15) in combination with Eq. (3.17). This means that after focussing, the influence of the wind will be the same as for far-field sources, resulting in the angular error given by Eq. (3.27). Notice that correct focussing is only obtained with c_{ray} given by Eq. (3.13). In practice windspeeds are small and c_{ray} in Eq. (3.29) may then be replaced by c_0 without violation of the focussing criterion of Eq. (2.160).

The validity of this approximation has been investigated with traveltime calculations along an antenna with a length of 9.6 m (SYNTACAN design in the 1 kHz octave band). Results are shown in figure 3.4, where a comparison has been made between the traveltime differences in a cross-wind situation and the approximation for a flow-less medium. Figure 3.4a shows the traveltime differences along the antenna axis for a sound source at a distance of 50 m and frontal incidence with a cross-wind in the positive x-direction of 0, 10, 50 and 100 m/s. Figure 3.4b shows the same results but now in the extreme situation of a source at a distance of 2 m and frontal incidence.
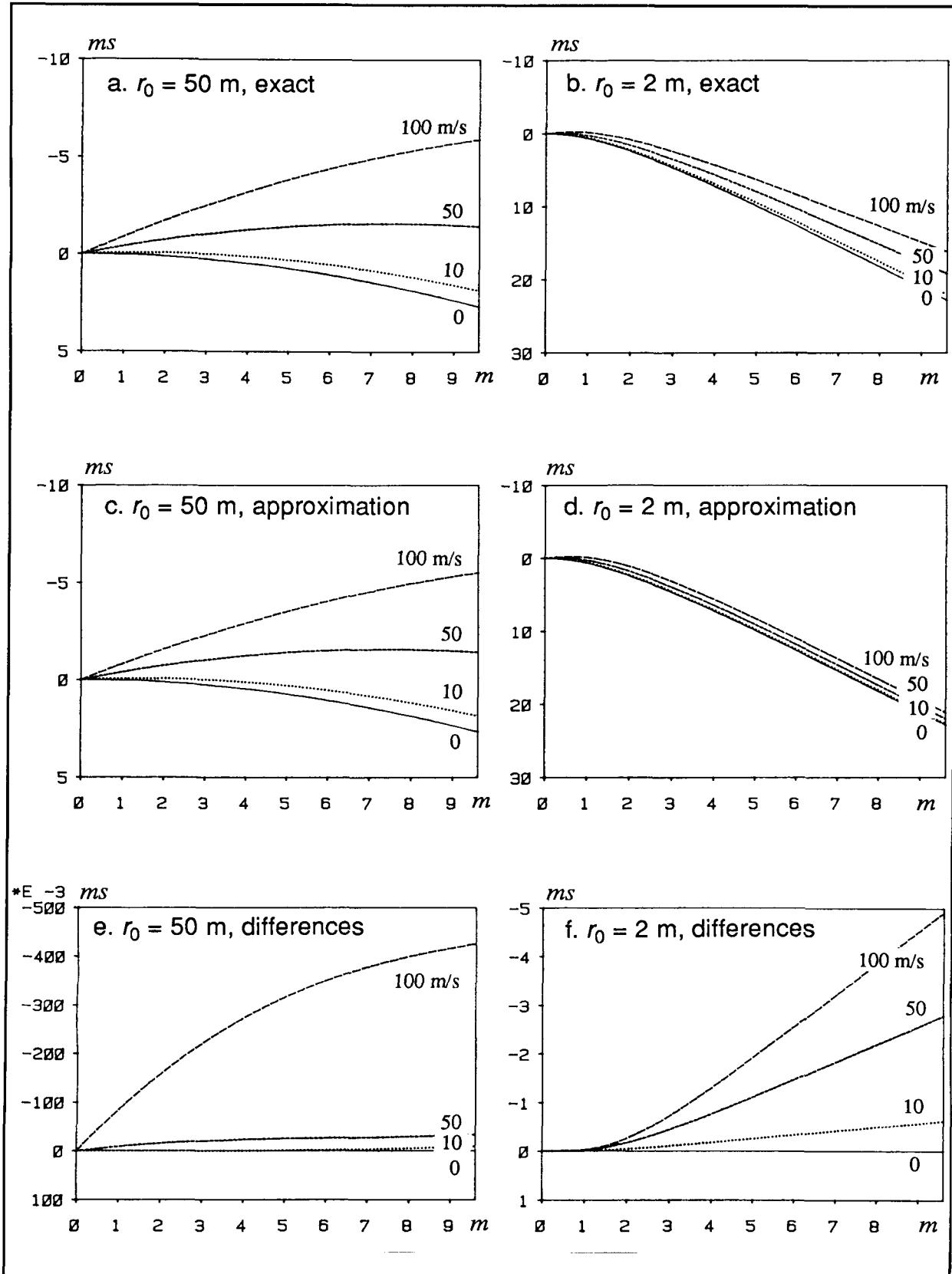
Figure 3.4: Comparison of the exact traveltime differences along the antenna axis and the approximation by using c_0 instead of c_{ray}.

These traveltime differences have been compared with the situation in a flow-less medium, when the sources are placed at the same distance from the origin of the antenna, but now at angles corresponding with the angular error given by Eq. (3.27). The results are given in figures 3.4c and d, while fig. e and f show the differences with the exact traveltimes. The results are in focus when the traveltimes stay within $1/4\lambda$ (see Eq. (2.160). At 1 kHz this corresponds with a traveltime difference of 0.25 ms so, with a source distance of 50 m the procedure is applicable with cross-winds up to more than 50 m/s. At a source distance of 2 m the focussing is very critical and the applicability of this simplified focussing procedure is restricted to small windspeeds.

Conclusions

In conclusion it can be stated that the horizontal moving of the medium by the wind causes errors in the observed source directions as given by Eq. (3.27). Notice that, within the approximations which are valid for small Mach-numbers, $\phi = 0$ if $\gamma = 0$ (no cross-wind). In practical situations, the windspeed will not be higher than, say 5 m/s. If the measurements take place within the meteorological window as given in table 3.2, and if all source directions within $\pm 30°$ are taken into account, γ must not exceed $\pm 30°$ during day-time or $\pm 45°$ during the night. Under these conditions, $|\phi|$ will not exceed 0.7°, and usually it will not be necessary to compensate for these effects.

Because the curvature of the waves is only slightly modified at low Mach-numbers, the normal focussing will be adequate in all practical situations.

3.3   STATISTIC SOUND TRANSFER CHARACTERISTICS

3.3.1   Sound propagation through a turbulent atmosphere

In the preceding paragraph we discussed some important factors which influence the outdoor sound propagation in a deterministic way. In reality this is only partly true. Especially the assumption of a stratified medium in which the wind- and temperature profiles are time-independent is not true. In this paragraph we will concentrate on the random fluctuations in wind and temperature, caused by atmospheric turbulence. A detailed theoretical discussion of wave propagation through a random turbulent medium would be beyond the scope of this thesis; it is presented in books by Tatarskii [30] and, more recently by Ishimaru [31]. These authors mainly concentrate on optical wave propagation. Because of the similarity between the optical and acoustical wave equations, the theory can also be applied to acoustic wave propagation. The general theory is usually presented in terms of variations of the index of refraction n, defined for acoustical waves as

$$n = c_0 / c(x, y, z, t) \quad .$$

(3.30)

Here c_0 is the sound velocity of the quiescent medium and $c(x, y, z, t)$ is the momentary and local sound velocity. It is usually written as

$$n = 1 + \mu \quad , \tag{3.31}$$

with μ = the fluctuation of the index of refraction. These fluctuations are caused by eddies of moving air. These eddies are usually formed by two physical phenomena: instability of the air near the ground due to the wind and instability due to thermal effects. It is usually observed that the thermal effects are predominant if there is little or no wind, especially in the case of direct sun radiation.

It is difficult to give a deterministic or even a statistical description of this so called *source region* of the eddies, but their diameters are several meters or even larger. This is called the *outer scale of turbulence*. These large eddies are the input for a cascade process where energy is exchanged with eddies of smaller sizes and so on, until the so called *inner scale of turbulence* is reached at an eddy diameter of about 1 mm. At this size the energy is exchanged into heat due to the viscosity of the air. The availability or probability of eddy sizes in the inertial region, i.e. between the source and the viscous regions, follows the "$^{11}/_3$-law" of Kolmogorov. This is illustrated in figure 3.5, which shows the availability of eddy sizes in the atmosphere $\Phi(\kappa)$, where κ is the spatial Fourier component of the eddy size.

Due to the fluctuations in the index of refraction, the received signals will show amplitude and phase fluctuations. This is the main reason why the source-receiver correlation technique which was briefly discussed in Chapter 1, does not work properly in the outdoor environment.
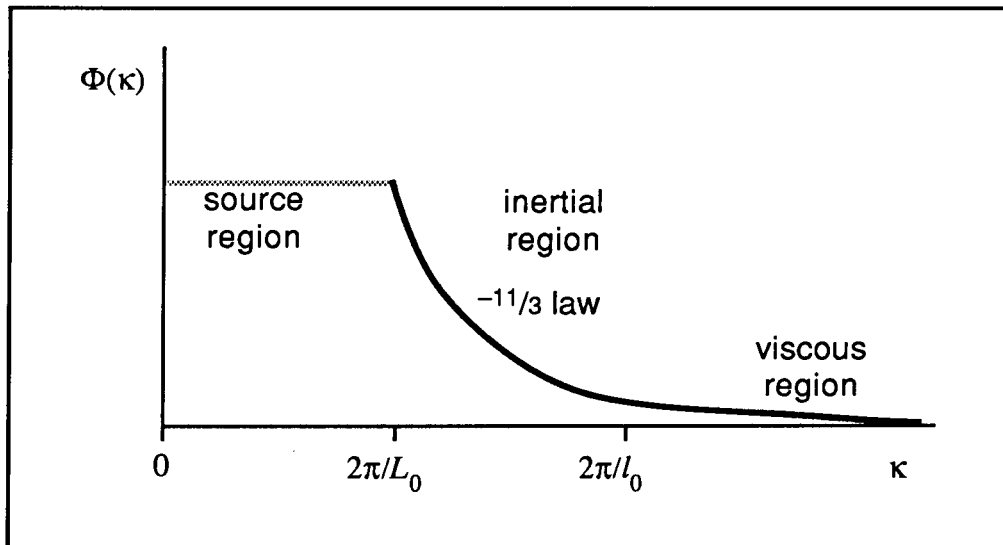
Figure 3.5: Availability of eddy sizes in the atmosphere. The distribution in the source region ($\kappa < 2\pi/L_0$) depends on meteorological and geometrical conditions. For $\kappa > 2\pi/L_0$ the spectrum follows the $^{-11}/_3$ law of Kolmogorov until the viscous region ($\kappa > 2\pi/l_0$) is reached.

3.3.2 Amplitude fluctuations of sound propagating through a turbulent atmosphere

The amplitude fluctuations have been studied theoretically by Hidaka et al. [32] for the special case of a source and a receiver near the ground. They assume that the turbulence obeys the Kolmogorov spectrum and use Rytov's method [30] to compute the mean value and standard deviation of the immission level. With the Rytov approximation, the immission level has a log-normal distribution. It is found that for frequencies below the primary ground interference dip (see par. 3.2.1) the variance of the immission level is very low, but above this frequency a standard deviation of 1 to 4 dB is found, dependent on the source distance and the turbulence of the air.

3.3.3 Transverse coherence loss in a turbulent medium

The turbulence of the propagation medium will also influence the spatial cross-correlation functions, because the propagation from a source to one receiver will be disturbed by different eddies than the propagation to another receiver. It will be evident without proof that, if the two receivers are placed close together, then the received signals will be distorted by almost the same eddies, which means that the correlation between the two received signals will be high. If the two receivers are placed at a longer distance from each other, then the signals will be distorted by different eddies and the correlation will be lower. Because the measurement technique of SYNTACAN is based on the estimation of the spatial cross-correlation of the wave field over the antenna aperture, it is important to know the effects of spatial decorrelation due to atmospheric disturbances. An elegant way to quantify these disturbances is by measuring the transverse coherence function, defined by

$$\gamma_n(\xi, f) = |\tilde{R}_n(\xi, f)| / \tilde{R}_n(\xi=0, f) \tag{3.32}$$

for a source n. Notice that γ_n depends on the source position and height. Combination of Eq. (2.105) and (3.32) and also taking into account the spatial window $W_a(\xi)$ (see par. 2.7.4) gives the disturbed cross-spectrum

$$\tilde{R}(\xi, f) = \sum_n \tilde{R}_n(f) \exp(-j2\pi f\xi/c_n) W_a(\xi) \gamma_n(\xi, f) \tag{3.33}$$

where $\tilde{R}_n(f) = \tilde{R}_n(\xi=0, f)$. Transformation to the k_x'-f domain gives:

$$\tilde{R}'(k_x', f) = \sum_n \tilde{R}_n(f) \delta(k_x' - f/c_n) * \tilde{W}_a(k_x') * \tilde{\gamma}_n(k_x', f) \ . \tag{3.34}$$

This result shows that the angular response of the antenna will not only be convolved with the Fourier transform of the spatial window, but also with that of the transverse coherence function. An interesting property can be found by taking the special case of $\xi = 0$ in Eq. (3.33), making

use of the fact that $W_a(0) = 1$ and $\gamma_n(0, f) = 1$:

$$\tilde{R}(\xi=0, f) = \sum_n \tilde{R}_n(f) \quad . \tag{3.35}$$

$\tilde{R}(\xi=0, f)$ can also be written as a Fourier transform of $\tilde{R}'(k_x', f)$ for the special case of $\xi = 0$:

$$\tilde{R}(\xi=0, f) = \int_{-\infty}^{+\infty} \tilde{R}'(k_x', f) dk_x' \quad . \tag{3.36}$$

Combination of Eq. (3.34, 3.35 and 3.36) gives the important result:

$$\sum_n \tilde{R}_n(f) = \sum_n \tilde{R}_n(f) \int_{-\infty}^{+\infty} \delta(k_x' - f/c_n) * \tilde{W}_a(k_x') * \tilde{\gamma}_n(k_x', f) dk_x' \quad . \tag{3.37}$$

This equation can be interpreted as an integration of the source spectra over the k_x'-values, which are related to the angles of incidence of the wave fronts. From Eq. (3.37) it follows that the correct power spectra of the different noise sources can be obtained by selective integration as a function of k_x', then the spatial window and the transverse coherence loss only influence the resolving power, but not the amplitudes of the power spectra. The latter property is of great importance in practical applications.

3.3.4. Measurements of the transverse coherence loss

As discussed in the preceding paragraph, the transverse coherence loss plays a key role for the angular resolution of an acoustic antenna in the outdoor environment.

An important investigation has been carried out by Ningre [14] as a part of the development of the antenna system by Métravib and Electricité de France [12]. In order to get a better understanding of the atmospheric turbulence, he measured the sound propagation over a distance of 2500 m over the sea. The source was located on a lighthouse and the receivers on the beach. An important reason to measure over sea was to have uniform turbulence conditions over the entire propagation path. From his results he found an important empirical expression for the transverse coherence function:

$$\gamma(\xi, f) = \exp(-\beta f|\xi|) \quad , \tag{3.38}$$

with β being a parameter which depends on atmospheric conditions and falling in the range of $1.5 \times 10^{-4} < \beta_n < 4 \times 10^{-4}$. The agreement of his measurements with Eq. (3.38) is illustrated in figure 3.6.

Relation (3.38) has been tested at our laboratory by Hoyer [16] for propagation over grassland. He measured the transverse coherence loss with a loudspeaker fed with pink noise
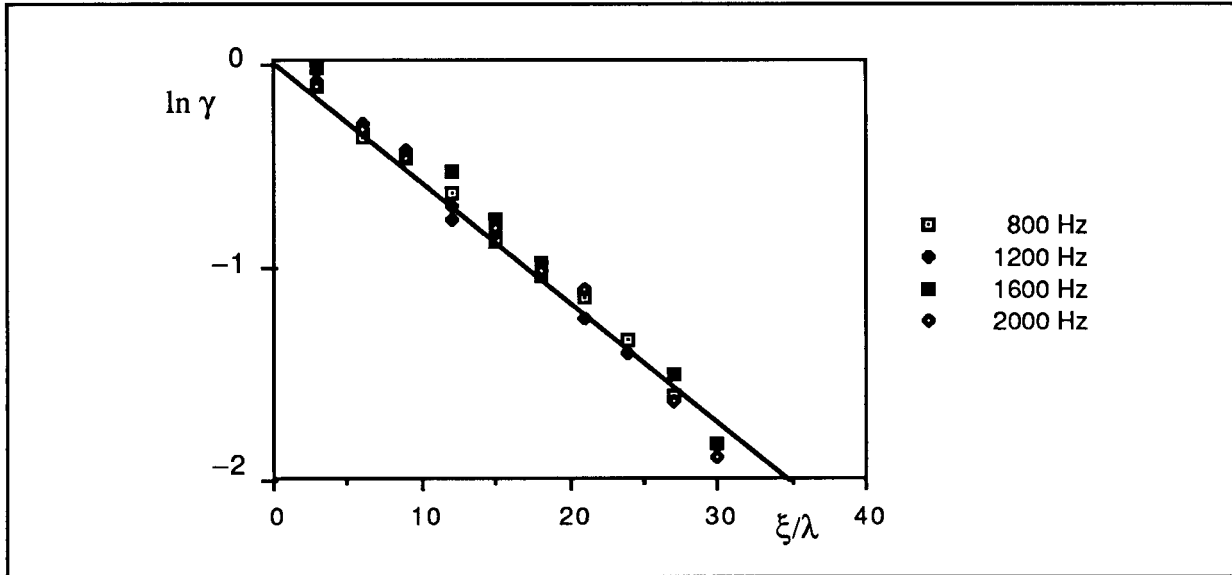
Figure 3.6: The transverse coherence as a function of ξ/λ for different frequencies (by Ningre [14]).

and placed at a height of 2 m above the ground. The transverse coherence loss was calculated from the auto- and cross-spectra that were obtained from two microphones, placed on a line perpendicular to the source direction. Each measurement was carried out with one specific microphone spacing ξ, and it was observed that Eq. (3.38) agreed well as a function of frequency in the range from 700 to 1500 Hz. The measurements were repeated for several microphone spacings ξ, ranging from 0.13 to 16 m, and for each distance the parameter β was estimated from a least squares fit of Eq. (3.38) as a function of frequency. In that way, values of β were found to be in the range $1 \times 10^{-5} < \beta < 3 \times 10^{-5}$ for a source-receiver distance of 160 m. The variance of these results is caused by meteorological changes and by statistical uncertainties in the estimated auto- and cross-spectra.

After the realization of SYNTACAN, new data on the transverse coherence function have become available. With the antenna it was possible to calculate $\gamma(\xi, f)$ as a function of ξ from simultaneous measurements of the spatial cross-spectra, now with the frequency f as a parameter. These measurements have been performed by Hertsig [33]. He found an excellent agreement with the Ningre-model in the observed frequency range from 700 to 1400 Hz. Hertsig performed his measurements for several source distances and found that β is strongly dependent on the source distance. His results have been averaged over the 1 kHz octave band and are summarized in figure 3.7. Note the strong dependence of β with the source distance. This dependence is almost linear on a log-log scale. The range of values found by Hoyer and Ningre are also presented in figure 3.7. As shown, the results of Hoyer agree well with the measurements of Hertsig, but the range of values found by Ningre is remarkably low for such a large source distance.
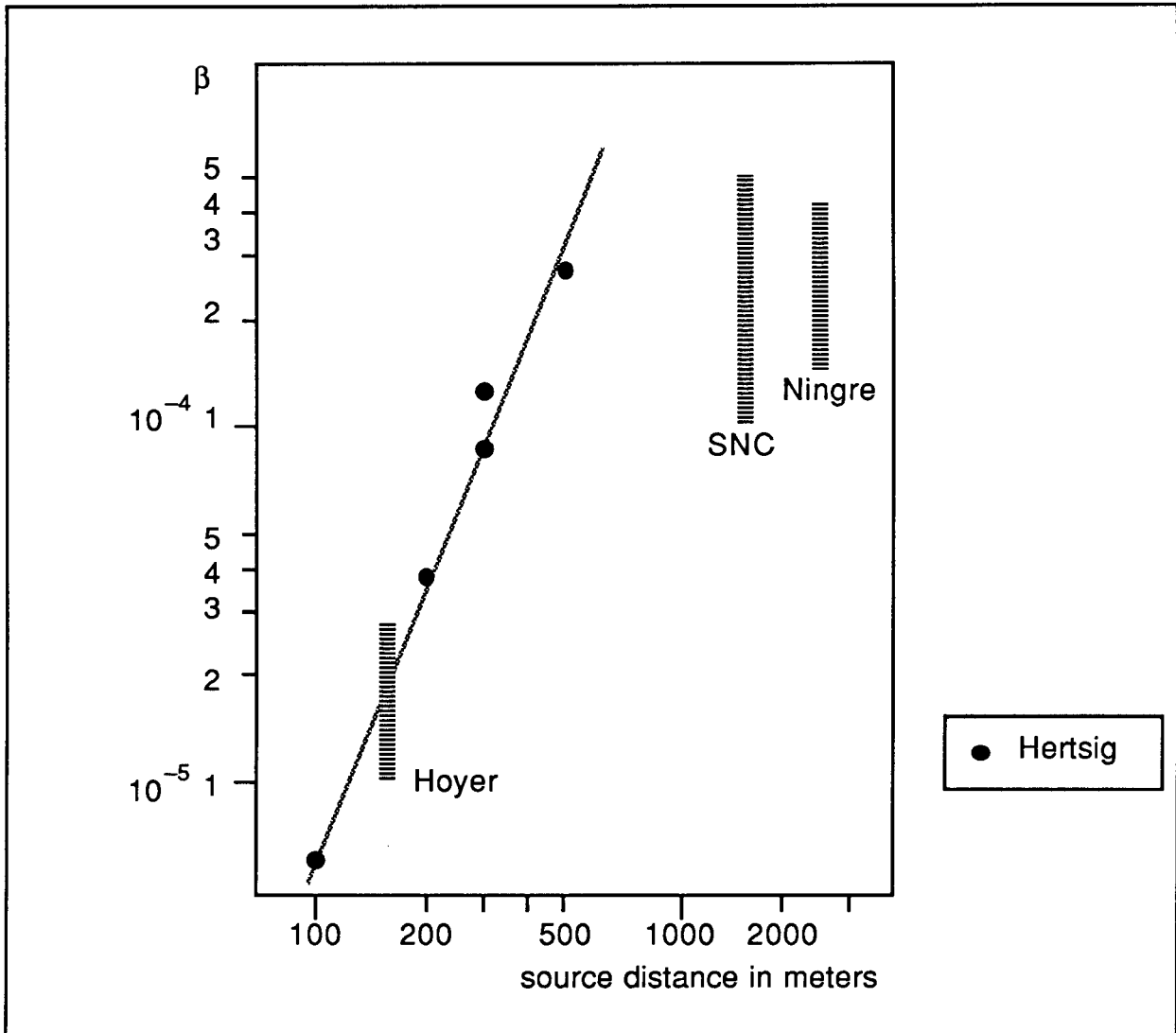
Figure 3.7: The parameter β of the coherence function of Eq. (3.24) as a function of the source distance, as measured by Hertsig. Also shown are the range of values found by some investigations, performed at fixed source distances.

The data indicated by SNC are from test measurements with SYNTACAN on a petro-chemical factory, where (due to technical trouble, but fortunate for us) steam escaped from one of the installations, giving a wide band acoustic point source at a distance of 1500 m from our antenna, with a high signal to noise ratio over all measured frequency bands (125 to 1000 Hz octave bands). Because SYNTACAN measures the spatial cross-spectra in $1/12$-octave bands (see Chapter 4), we were able to compute the coherence parameter β from this source for each $1/12$-octave band. The results are summarized in table 3.4. These results show that the variance of the estimated values is larger for lower frequencies — as can be expected for smaller absolute bandwidths — but the average values do not vary considerably as a function of frequency. The range of β-values of the SNC noise source is also given in figure 3.7. They are in good agreement with the range of values found by Ningre. The relative high values found by Hertsig

Table 3.4

Summary of the computed values of β for the SNC noise source
at a distance of 1500 m

octave band in Hz	$\beta \times 10^4$ (calculated per 1/12-octave band)		
	minimum	maximum	average
125	1.01	4.76	3.26
250	1.94	4.45	2.78
500	1.78	3.69	2.49
1000	2.11	3.28	2.67

can probably be explained by the fact that these measurements (and those of Hoyer) were performed near to the ground with source and receiver heights of 1 to 2 m, whereas the source heights of the SNC and the Ningre measurements were at more than 10 m (exact figures are not known).

Another investigation of acoustic outdoor propagation has been published by Daigle et al. [34]. They formulate a statistical model of the sound propagation through a turbulent medium on the assumption of a Gaussian distribution of eddy sizes (in the source as well as in the inertial
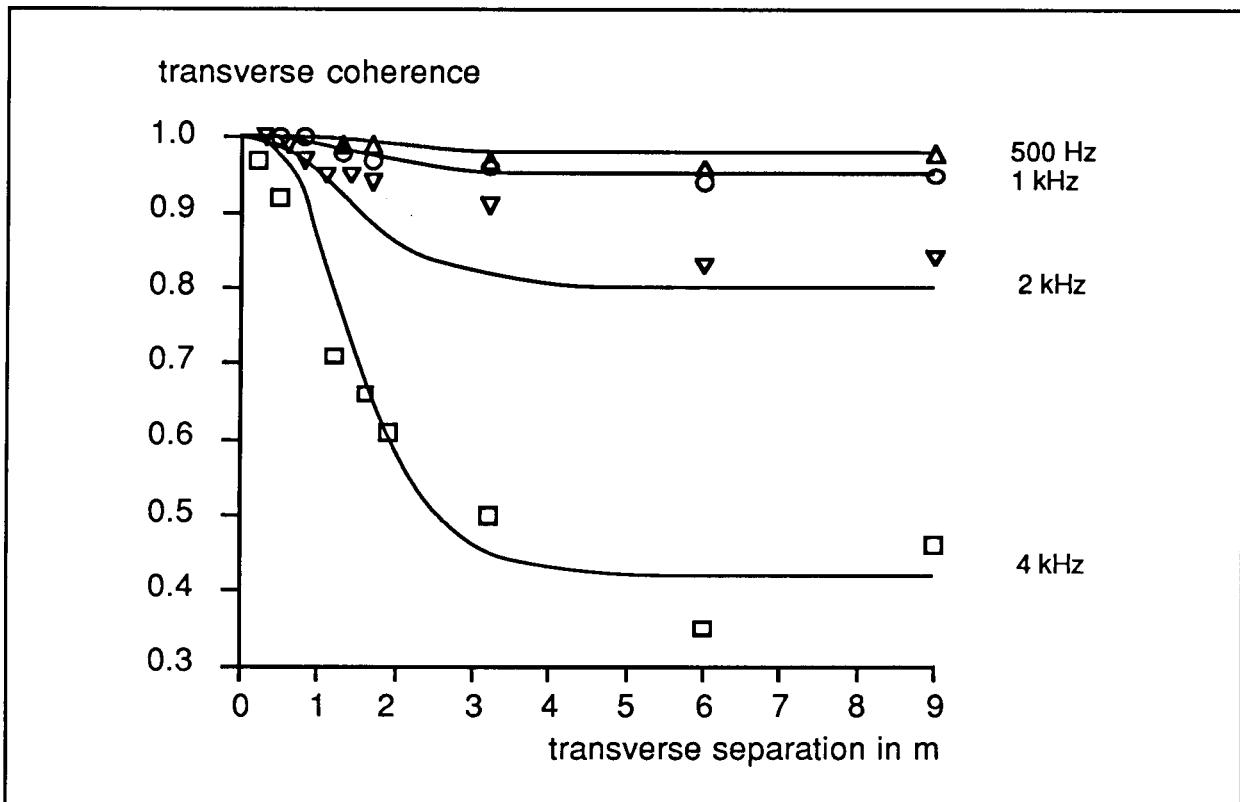
Figure 3.8: The transverse coherence function for a source-receiver distance of 100 m, according to Daigle et al. [34].

region). From this model they derive a formula for the transverse coherence function which is depicted in figure 3.8, for a source-receiver distance of 100 m. The figure shows measurement results that are in good agreement with this model, but there is a great discrepancy between these results and the Ningre-model. It must be realized that Daigle did not measure the transverse coherence directly, but computed it from estimations of the spherical wave structure function, which depends on the log-amplitude and phase fluctuations of the wave propagation through the medium.

3.3.5 Angular resolution due to the transverse coherence loss

As shown in Eq. (3.34), the antenna response in the k_x'-f domain will be convolved with the Fourier transform of the transverse coherence function. As discussed in par. 3.3.4, the Ningre model described by Eq. (3.38) gives a good description of the transverse coherence function in practical situations. Its Fourier transform is given by:

$$\tilde{\gamma}(k_x',f) = 2\beta f \, / \, (\beta^2 f^2 + 4\pi^2 k_x'^2) \quad . \tag{3.39}$$

Both functions are depicted in figure 3.9.
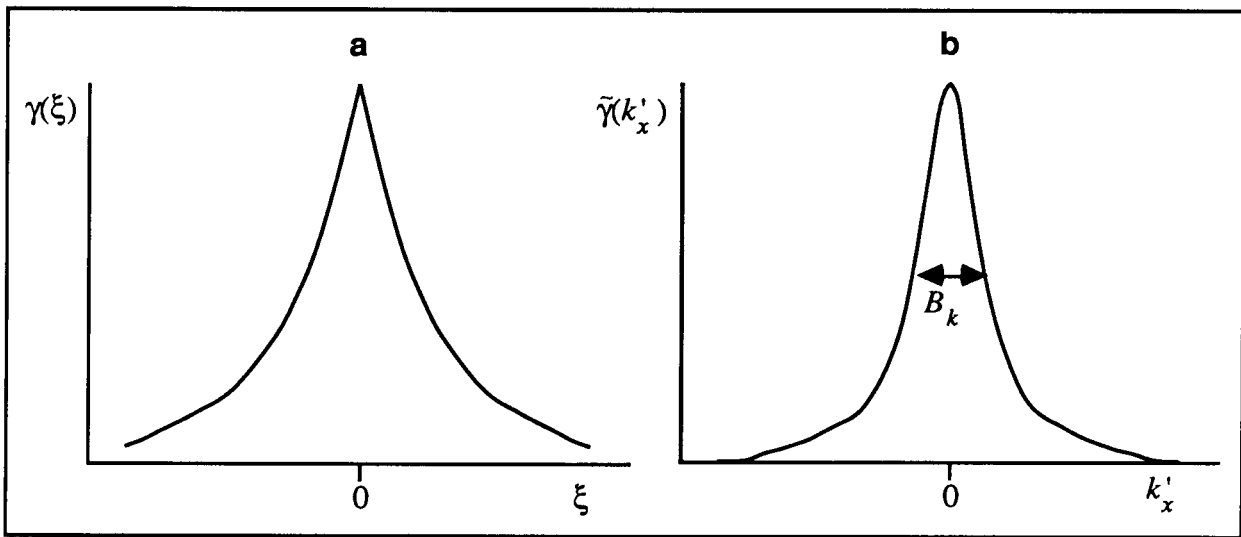
Figure 3.9: a. The transverse coherence function γ, according to the model of Ningre [14]; b. its spatial Fourier transform $\tilde{\gamma}$.

From Eq. (3.39) it follows that the −3 dB bandwidth of the transverse coherence function is:

$$B_k = \beta f \, / \, \pi \tag{3.40}$$

or, using Eq. (2.127), we find for the angular beamwidth

$$B_a(\alpha) = c\beta \, / \, (\pi \cos \alpha) \qquad (\text{rad}) \quad . \tag{3.41}$$

If we take for example $\beta = 3 \times 10^{-4}$ (for source distances > 500 m), then the angular resolution for $\alpha = 0$ is 0.0325 rad or 1.86 degrees.

The effect of the transverse coherence loss might be compensated for by applying the inverse function to the measured data. It must be realized however, that Eq. (3.38) gives an average, whereas with short measurement times large deviations from this average may be found. Furthermore, the value of β depends on the source distance and the source height, which makes compensation difficult in practical situations.

In conclusion, it can be stated that when the measurements are performed within the so-called "meteorological window", the transverse coherence loss does not affect the directional immission levels, as long as the results are integrated over the entire image of the observed source region (see Eq. (3.37)). The only effect of the transverse coherence loss is a reduced angular resolution. At small source distances this can usually be neglected, but at source distances > 500 m, it can restrict the antenna beamwidth to about 2 degrees.

CHAPTER 4

SYSTEM DESIGN AND DEVELOPMENT

4.1 INTRODUCTION

From the results of the measurements of the transverse coherence function, which are presented in Section 3.3, it follows that a synthetic acoustic antenna, based on the measurement of the spatial cross-correlations along the antenna aperture can have an angular resolution of less than 0.2 degrees for source distances up to 200 m, widening to about 2 degrees for source distances up to 2000 m. This means that atmospheric turbulence will not be a limiting factor for an antenna having a resolution of 1 to 2 degrees, but it also gives the indication that it is pointless to extend the antenna-aperture beyond a certain length. Another limiting factor is the stationary windspeed. As discussed in Section 3.2 it can cause a change in the perceived source direction of about 1 degree at a lateral windspeed of 5 m/s. Due to variations in the windspeed during the measurements, the beamwidth of the antenna will be broadened with the same amount. From these considerations we deduced that it should be possible to construct an acoustic antenna having a beamwidth of 1 to 2 degrees in practical outdoor situations, but that it would be idle to strive for better angular resolution by extending the aperture.

In the next sections we will discuss the hardware and software design, and the development of SYNTACAN. The system is based on the power spectrum estimation from spatial cross-correlations, as presented in Section 2.6. It is assumed that the noise sources are uncorrelated, so that Eq. (2.104) can be applied, and a sparsed microphone array can be used. The consequences of the use of this antenna for measuring correlated noise sources will be discussed in Chapter 5.

4.2 THE ANTENNA

4.2.1 Microphone array sparsing

One of the main problems met in the development of SYNTACAN was to minimize the total number of microphones. This minimalization was necessary in order to cut the hardware costs of the system, to keep the system manageable in the field, and to restrict the computational effort for getting the required noise immission levels.

There are two important design criteria for the construction of the antenna:

a. The microphone spacing $\Delta\xi$ must obey Eq. (2.114):

$$\Delta\xi < {}^{2}/3\ \lambda_{min}\ ,\tag{4.1}$$

where $\lambda_{min} = c_{min} / f_{max}$;

b. The angular resolution in terms of the beamwidth B_a depends on the aperture length X and angle of incidence α according to Eq. (2.128), from which follows:

$$B_a(\alpha) < {}^{1}/2\ B_w\ \lambda_{max} / (X \cos \alpha)\ ,\tag{4.2}$$

where $\lambda_{max} = c_{max} / f_{min}$ and B_w equals the bandwidth of the window-dependent smoothing function.

From relations (4.1) and (4.2) it follows that the sampling spacing $\Delta\xi$ is dictated by the smallest wavelength — or the highest frequency — whereas the antenna length must be long compared to the largest wavelength, in order to keep the beamwidth small at low frequencies. For that reason the bandwidth of the system had to be limited. We decided to restrict the frequency range of SYNTACAN to the 125 – 1000 Hz octave bands (89 – 1413 Hz). In many practical situations these octave bands give the major contribution to the A-weighted noise immission level.

The basic sampling interval $\Delta\xi$ can now be computed from Eq. (4.1). For c_{min} we take 324 m/s, which is valid at a temperature of –10 °C. We then find $\Delta\xi$ = 0.15 m. The aperture length of the antenna is found from Eq. (4.2), in which we substitute the following values:

✎ beamwidth $B_a(0)$ = 0.035 rad or 2 degrees;

✎ bandwidth of the smoothing function due to spatial windowing B_w = 1.6;

✎ λ_{max} = 3.9 m (for 89 Hz at 30 °C);

giving X = 90 m or 600 $\Delta\xi$.

It must be realized that if we would use the basic sample interval $\Delta\xi$ over the entire frequency interval, the data would possess a large amount of redundancy, because a microphone spacing of 2.4 m would be sufficient at the lower frequency bound of 89 Hz. The same applies for the sampling as a function of time. For the high frequencies a sampling interval of less than 3.5×10^{-4} s is needed (a value of 2×10^{-4} is used in practice), but this value can be made

larger for lower frequencies, if precautions are taken against aliasing. For these reasons we decided to split the data analysis into octave bands. If we start in the 1 kHz octave band with sample intervals of $\Delta t = 2 \times 10^{-4}$ s and $\Delta\xi = 0.15$ m then both values can be doubled for the 500 Hz band without the risk of aliasing, while having the same angular resolution as in the 1000 Hz band. Besides, the measurement interval will be doubled with the same computational effort. This doubling is repeated for the 250 and 125 Hz bands. So actually SYNTACAN is not built with one sparsed array, but with four, with sample intervals of 0.15, 0.30, 0.60 and 1.20 m.

As discussed in Chapter 2, we can restrict the microphone positions to those from which a contiguous set of cross-correlation functions $R(n\Delta\xi, \tau)$ can be computed, with n ranging from $-1/2 M$ to $+1/2 M$, for a synthetic aperture with a length of $M\Delta\xi$.

To give an example: if we place microphones at the positions $x = (0, 1, 4, 7, 9)\Delta\xi$, then all microphone distances of $(-9, -8, ..., 0, ..., 8, 9)\Delta\xi$ can be found, giving a synthetic aperture of $18\Delta\xi$ with only 5 microphones. A number of sparsing schemes have been published by Leech [35]. These schemes use a minimum number of positions for a complete difference set. As a consequence, these positions are usually irregularly divided over the interval. Because we need four sparsed arrays, with $\Delta\xi = 0.15, 0.30, 0.60$ and 1.20 m respectively, such an irregular scheme is not optimal, as it will not be possible to combine many microphones for different octave bands.

We found a very efficient sparsing scheme by placing the microphones at the positions

$$x = (-7, -6, -5, -4, -3, -2, -1, 0, 8, 16, 24, 32, 40, 48, 56)\Delta\xi \quad . \qquad (4.3)$$

From these microphone positions the cross-correlations can be measured for $\xi = -63\Delta\xi$ to $+63\Delta\xi$, using the combination scheme of table 4.1.

Table 4.1

Combination scheme of the sparsed array used by SYNTACAN.
The table gives the values of ξ which are obtained from the corresponding
left (*l*) and right (*r*) microphone positions. All values are given in units $\Delta\xi$.

r \ *l*	0	-1	-2	-3	-4	-5	-6	-7
0	0	1	2	3	4	5	6	7
8	8	9	10	11	12	13	14	15
16	16	17	18	19	20	21	22	23
24	24	25	26	27	28	29	30	31
32	32	33	34	35	36	37	38	39
40	40	41	42	43	44	45	46	47
48	48	49	50	51	52	53	54	55
56	56	57	58	59	60	61	62	63

The negative ξ-values are not computed, but use is made of the property that $\tilde{R}(-\xi, f)$ = $\tilde{R}*(\xi, f)$. So only 15 microphones are needed to perform a 128-point FFT from the ξ to the k_x'-domain.

This sparsing scheme is used for all four octave bands, where such a relative placement of the four sparsed arrays is chosen that an optimum combination of the microphone positions appears. This has resulted in the sparsing scheme which is illustrated in figure 4.1 and table 4.2. The result is an array of 32 microphones, placed on a straight line over a length of 76.65 m with spacings of 0.15 to 9.60 m. Notice that this sparsing scheme could be extended to a wider frequency range with only 4 microphones per octave.
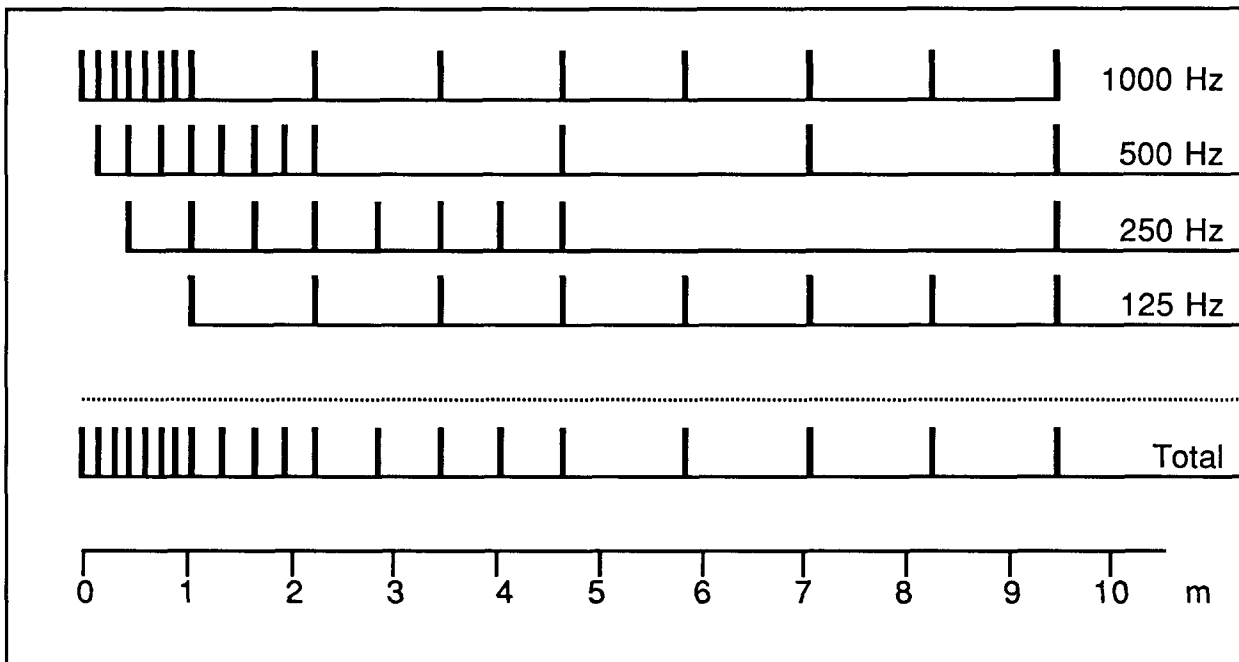
Figure 4.1: The sparsing scheme of SYNTACAN for the first 10 m. Notice the ideal combination of microphones for the different octave bands.

In each octave band use is made of 15 microphones, resulting in a synthetic aperture length of 128 $\Delta\xi$. From Eq. (2.128) the beamwidth can be computed. If we take B_w = 1.6 and we assume a temperature of 20 °C, so that the sound velocity is 342 m/s, we find a beamwidth for frontal incidence of 1.15 degrees at the upper frequency bound and 2.3 degrees at the lower frequency bound of the octave band.

Table 4.2

The sparsing scheme of SYNTACAN

microphone channel	position in m	sequence nr. per octave band			
		1000 Hz	500 Hz	250 Hz	125 Hz
1	0.00	1			
2	0.15	2	1		
3	0.30	3			
4	0.45	4	2	1	
5	0.60	5			
6	0.75	6	3		
7	0.90	7			
8	1.05	8	4	2	1
9	1.35		5		
10	1.65		6	3	
11	1.95		7		
12	2.25	9	8	4	2
13	2.85			5	
14	3.45	10		6	3
15	4.05			7	
16	4.65	11	9	8	4
17	5.85	12			5
18	7.05	13	10		6
19	8.25	14			7
20	9.45	15	11	9	8
21	11.85		12		
22	14.25		13	10	
23	16.65		14		
24	19.05		15	11	9
25	23.85			12	
26	28.65			13	10
27	33.45			14	
28	38.25			15	11
29	47.85				12
30	57.45				13
31	67.05				14
32	76.65				15

4.2.2 Microphone selection

Microphone selection was based on the following criteria:

a. Because a one-dimensional array cannot distinguish between waves incident from front and rear, we preferred to use microphones with a good front/back ratio, to facilitate measurements in case of disturbing noise from the backside;

b. The microphones must be robust enough to be used in the field, furthermore they should be insensible to humidity and wind;

c. All microphones should have identical amplitude and phase characteristics, preferably independent of the angle of incidence for all angles between −30° and +30°;

d. The initial expense had to be limited because of the large number of microphones involved.

These criteria are not fulfilled by the types of microphones that are normally used for noise measurements, because those microphones have an omni-directional sensitivity. Besides that, they are very expensive.

A type of microphone with a good front/back ratio is the so-called *yard-stick* or *shot-gun* microphone, which makes use of a leaky wave conducting tube. These microphones are often used for sound recording purposes. In an investigation conducted by ir. G. Faber and reported by Sinnema [36], we found a suitable microphone of this type, manufactured by Nakamichi. The transducer element is a cardioid electret microphone with a built-in FET-preamplifier. This microphone is presented in figure 4.2, together with some specifications as supplied by the manufacturer. Its functional electronic diagram is also presented in this figure.

Specifications		**b**
Frequency range	30 – 20,000 Hz ± 3.5 dB	
Output Impedance (1 kHz)	200 ohms ± 20%	
Sensitivity (1 kHz 0 dB = 1 V/μbar)	−76 dB ± 2.5 dB	
Attenuation Pad	−10 dB	
Signal to Noise Ratio (Weighted)	Better than 50 dB	
Maximum SPL At 3% Distortion	118 dB	
Current Consumption	Less than 0.5 mA	
Operating Voltage	7 V – 10 V DC	
Battery	9.1 V Mercury	
Dynamic Range	Better than 94 dB	
Low Cut	−10 dB / 100 Hz	
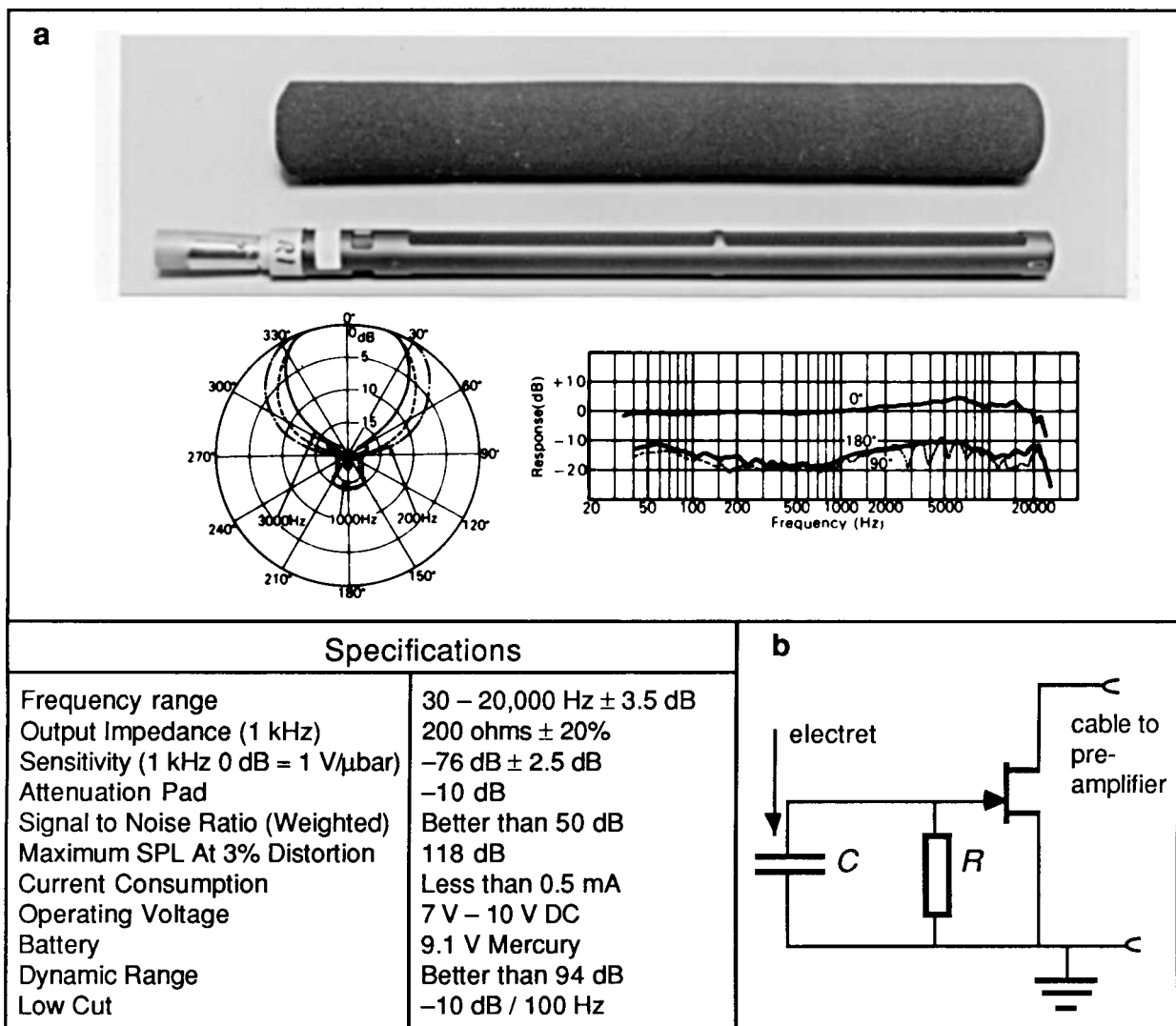
Figure 4.2: a. The Nakamichi microphone, the foam windscreen and some specifications as supplied by the manufacturer; b. functional electronic diagram.

A number of microphones were purchased to investigate their overall performance and their individual differences. It was found that the polar diagram and the frequency response as presented in figure 4.2a are somewhat flattered, but that the amplitude characteristic is almost flat between −30° and +30°, while sound from other directions is strongly suppressed (the front/back ratio is 8 dB at 200 Hz and 16 dB at 1000 Hz).

The frequency response is not flat at low frequencies, as suggested by the frequency response curve of figure 4.2a, because a low-cut filter is formed by the RC-network made up by the capacity of the electret foil and the input resistance of the FET-preamplifier. This RC-network caused some trouble, because its value is different for each microphone, leading to amplitude and phase differences at frequencies below 200 Hz. It was possible, however, to compensate this with correction networks in the pre-amplifiers (see § 4.3.1). It was also found that there was a spread in the overall sensitivity of the microphones of about 7 dB, but this could also easily be compensated in the pre-amplifiers. With these corrections the differences in amplitude and phase were less than 0.5 dB and 5° between 100 and 1400 Hz. These results led to building the acoustic antenna with these microphones and the microphones still to be bought were purchased. In the total set, the differences are a bit wider, but they stay within 1 dB and 10° (see also § 4.4.5).

At that time it was difficult to predict the exact influence of these variations on the antenna performance. Later, Hertsig [33] performed simulations to test the effect of changing the gain of one of the microphones, which was an increased side lobe level. A main lobe to side lobe ratio of 20 dB was reached with a gain error of 0.4 to 1.3 dB, dependent on the position of the microphone. He also investigated the influence of a mis-alignment of the microphone array, with the same kind of results. Here a side lobe level of −20 dB was reached with a mis-alignment in the source direction of 0.02 to 0.10 m at 1 kHz, corresponding to a phase error of 20° to 100°.

4.2.3 Antenna construction and installation

As indicated in table 4.2, the antenna has a total length of 76.65 m, with microphone spacings of 0.15, 0.30, 0.60, 1.20, 2.40, 4.80 and 9.60 m. If we use the criterion of Hertsig [33], which was already mentioned in the preceding paragraph, the microphones have to be positioned with a tolerance of no more than 0.02 m at the high frequency side, where the microphones are placed close together, to about 0.5 m at the low frequency side.

Because of the small tolerance at the high frequency side and also because those microphones are placed very near to each other, we constructed an *acoustic rail*. It consists of four bars, made of aluminum profile, each with a length of about 2.5 m for ease of transportation. These bars are mounted on tripods to form a total length of 10 m. These bars have clamps in which the first 20 microphones are mounted. The remaining 12 microphones are

placed on individual tripods. This is illustrated in figure 4.3. The tripods are normal camera stands, which give the antenna a maximum height of 1.5 m. It must be mentioned that this is not in accordance with the recommendations of the Dutch Government [2], which prescribe a measurement height for immission measurements of 5 m. However, it would be very difficult to install our antenna at that height. A solution to that problem is by measuring the immission levels simultaneously with an additional microphone, at an height of 5 m. The SYNTACAN results can then be corrected with the level differences found between the antenna and this reference microphone. The procedure is only correct for the individual source directions if the level differences are equal for all sources, but this is true in many practical situations.
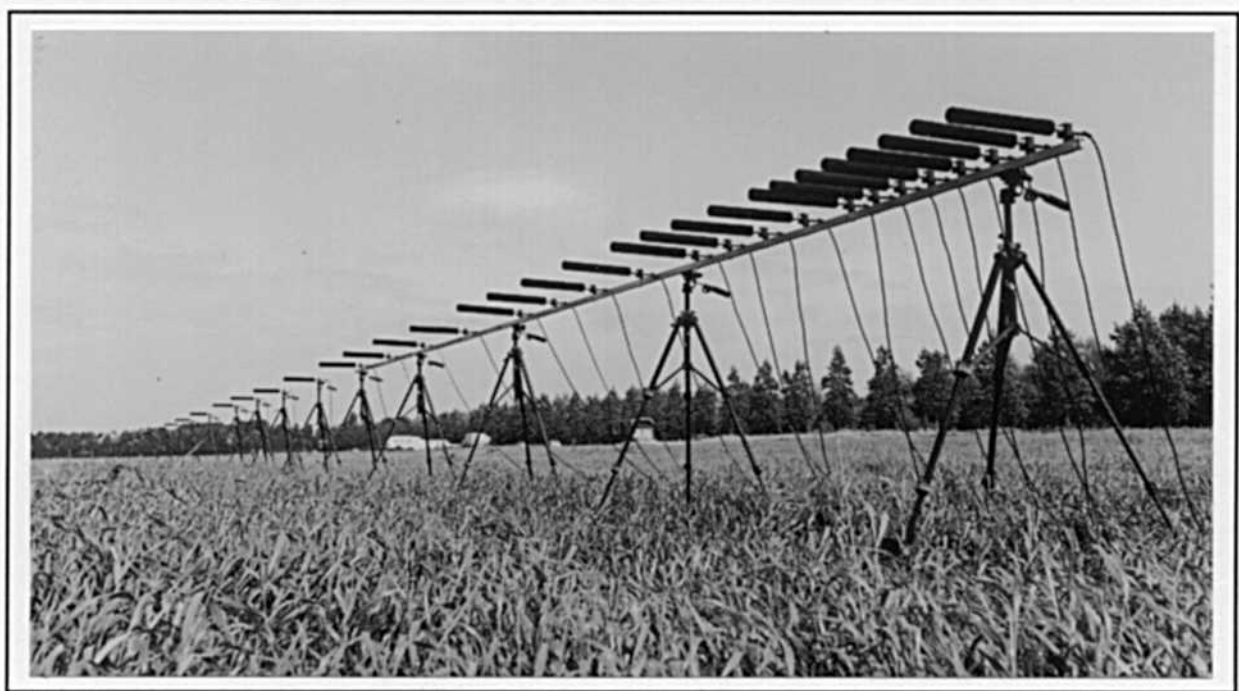
Figure 4.3: The antenna is mounted on an "acoustic rail" and tripods.

The tripods are placed in position by using a steel cable with marks for each tripod position. In that way the x-position can be measured with sufficient accuracy. The emplacement of the microphones in one line is performed best by visual inspection in the antenna direction, usually with the help of some simple surveying tool. A proven method is to mark the first and end point of the microphone array with a pair of ranging poles (red and white painted sticks) and to bring each microphone "in-line" with the aid of a pentagon prism. With this optical device one can view two half-images: one looking 90° to the left and the other 90° to the right. If the pentagon prism is in-line between the two ranging poles, their images are in a direct line.

It is possible to install only a part of the antenna. This can be useful if no room is available for the whole antenna length, or when the high directivity at the low frequencies is not necessary.

After the microphones have been installed, they are connected with normal microphone cables to one of two connector panels (see figure 4.4). The panels are connected to the data acquisition system through two multi-channel microphone cables, each with a capacity of 16 channels and a length of 50 m.
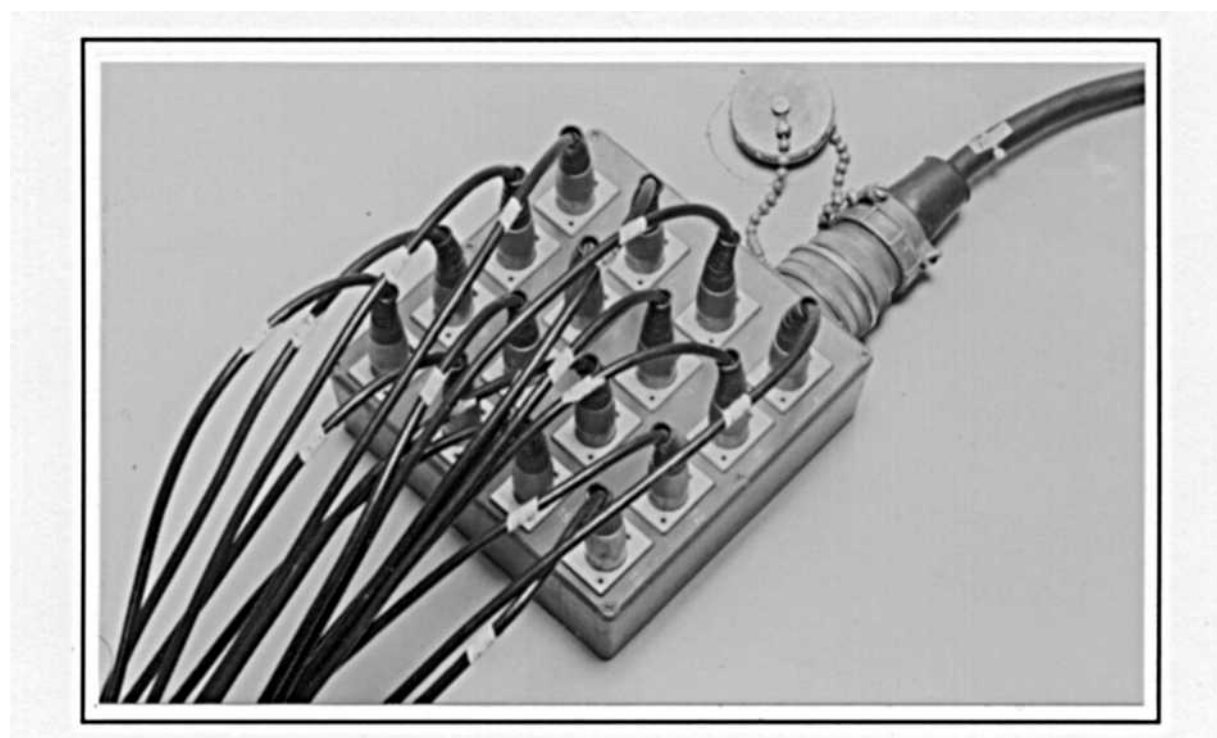
Figure 4.4: One of the connector panels used for the connection of the microphone cables to the multi-channel cables.

4.3 THE DATA ANALYSIS SYSTEM

All data acquisition and digital signal processing equipment is installed in a motor van (figure 4.5). The van has been adapted to enable the installation of the equipment, and to transport the microphones, tripods, cables etc. There are drawers for tools, a bookcase for manuals etc., and a small desk. We also installed a mobilophone/portophone system for local communication.

The total electrical power consumption of all equipment is 1500 W, which must be supplied from a 220 V / 50 Hz power source. If a connection to the public electricity network is not available, use can be made of a battery powered conversion system owned by the TPD (TPD stands for "Technisch Physische Dienst", TNO Institute of Applied Physics), from which the system can run for more than 5 hours on one battery charge (figure 4.6).

Figure 4.5: The motor van which houses all data analysis equipment.

Figure 4.6: The battery-operated 220 V/ 50 Hz power supply of the TPD, mounted on a trailer.
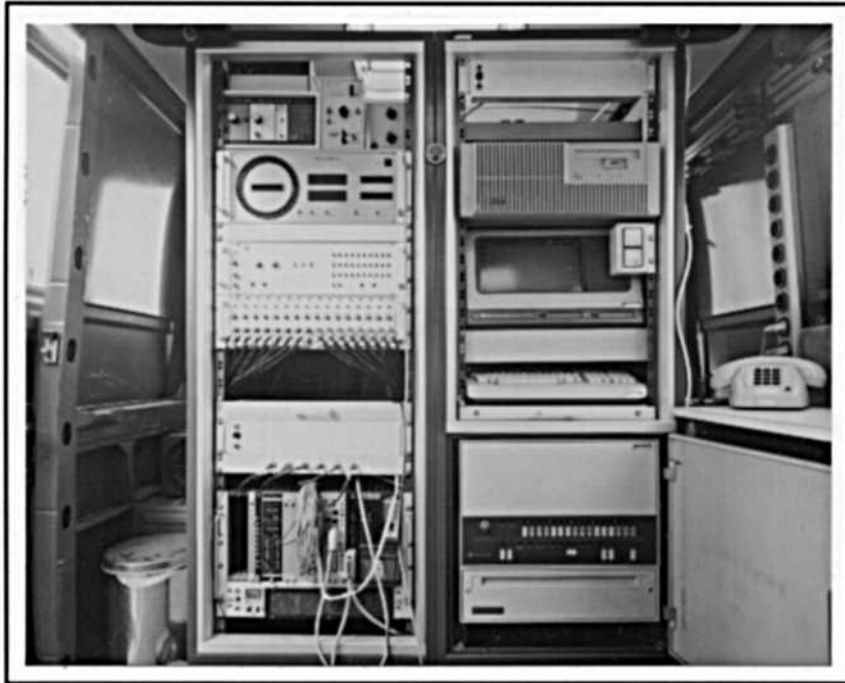
Figure 4.7: The data analysis system in the motor van.
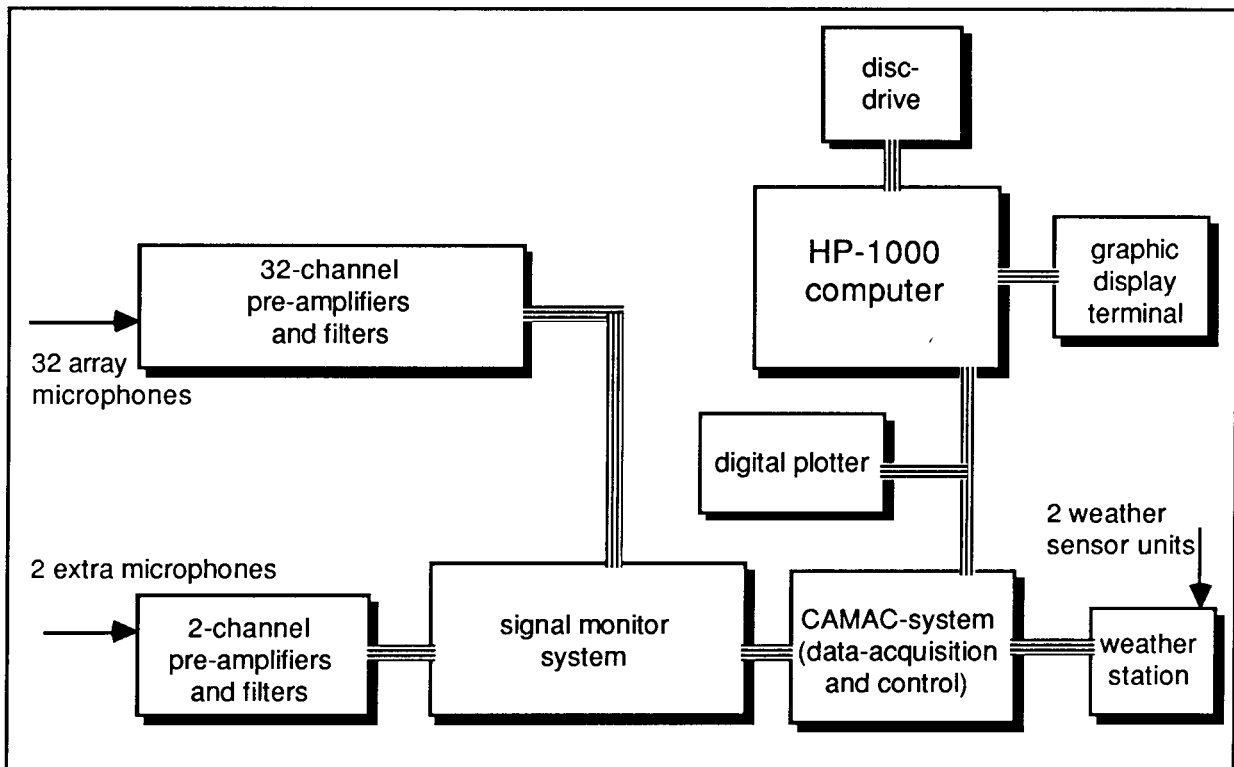
Figure 4.8: Functional block diagram of the data analysis equipment.

If the system is "at home", the van is housed in a garage at the laboratory. There electricity is available and a hardwired communication link gives access to other computer systems at our laboratory.

The data analysis system is shown in figure 4.7. It is placed in a two-bay cabinet that is mounted in the van with shock absorbing springs. A functional diagram of the system is presented in figure 4.8. We will now briefly describe each component of the system.

4.3.1 The preamplifiers and filters

The preamplifiers and anti-aliasing filters for the array microphones were developed at our laboratory and built together in one 19"-instrument rack on 16 printed circuit boards with 2 channels on one board. A block diagram of one channel is given in figure 4.9.
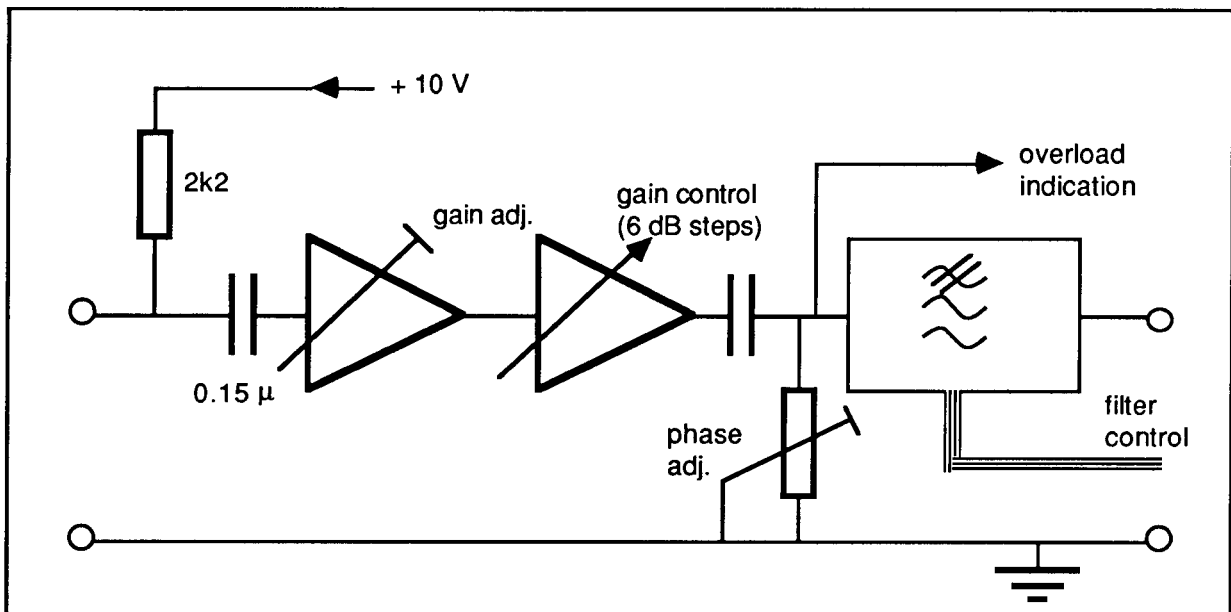
Figure 4.9: Diagram of a pre-amplifier and filter channel.

The FET-preamplifier of the microphone (see figure 4.2b) is fed by a 10 V dc source through the 2k2 resistor and the microphone cable. This eliminates the need for external power supplies or batteries. The first amplifier stage has a variable gain adjustment which is used for calibration. The second stage has a gain control in 6-dB steps. Its setting is combined for two channels. It is followed by a simple phase adjusting network to compensate for phase differences between the different microphones. The signal then passes the anti-aliasing filter. It has a 6th-order Butterworth characteristic with a programmable cut-off frequency of $f_c = n \times 100$ Hz, where n may be any integer between 1 and 255. Its value must be supplied as a parallel binary TTL-signal, for which an output register of the CAMAC-system is used. The modulus of the transfer function of this filter is given by the relation

$$|H(f)| = 1 / \sqrt{1 + (f/f_c)^{12}} \quad . \tag{4.4}$$

For the 1 kHz octave band (708 – 1413 Hz) we take f_s = 5 kHz and f_c = 1600 Hz. From Eq. (2.112) we find that relevant aliasing occurs if f > 3587 Hz, for which the filter damping is better than 42 dB.

The overload indication is effective for signals > +5 V or < –5 V. The overload status is indicated by a red LED (one for two channels) on the front panel of the module. All overload signals, also those from the extra two microphone channels, discussed in the next paragraph, are OR-ed together and connected to a status flip-flop of the CAMAC-system. This gives the facility to check programmatically if overload has happened during a measurement.

4.3.2 The signal monitor system

This laboratory-built device gives the possibility to monitor the amplified and filtered microphone signals through headphones or a loudspeaker. It can overrule the filter setting of the CAMAC-system, so that the microphone signals can be monitored without filtering. Because this is illegal during a measurement, the overrule action is OR-ed together with the overload signals, and such a measurement will be discarded.

As indicated in the functional block diagram of figure 4.8, two additional microphone amplifiers and filters are built into the signal monitor system. These extra channels are connected with two additional microphones that are placed at a height of 5 m. One of these microphones is of the same type as the array microphones and is used to transform the SYNTACAN results to a receiver height of 5 m (see § 4.2.3), the other microphone is omni-directional and measures the total immission level at 5 m height. These extra channels can be monitored before the anti-aliasing filters. This gives the operator a much better indication of extraneous noise sources, than by monitoring the filtered array microphones.

Because the CAMAC-system contains a data-acquisition module with only 32 channels, there was the problem of sampling the extra two microphone channels together with the 32 array microphones. As discussed earlier, only 15 array microphones are used per octave band. So, the extra channels can always take the place of 2 other microphones. The switching is performed by multiplexers which are built into the monitor system for connection of these microphone signals to channels 1 and 2 or 31 and 32 of the data-acquisition module.

4.3.3 The weather station

The windspeed, winddirection and temperature are measured with two units, each consisting of a propeller vane and a thermo sensor that is placed in an open white box to protect it against direct sun radiation (see figure 4.10). These units are placed in the field and are connected to an in-house constructed processing and display unit that is connected to the CAMAC-system.

Figure 4.10: The sensors of the weather station.

4.3.4 The CAMAC-system

This is the heart of the data-acquisition system. CAMAC stands for Computer Aided Measurement And Control and is an interface standard, originally developed for the research field of nuclear physics. Later on, modules have become available for many other applications. All modules are placed in a so-called CAMAC-crate. This is a cabinet with internal power supply and a standardized back-plane connector system.

Our CAMAC-system contains the following modules:

a. a 32-channel data-logger with 32 simultaneous sample and hold circuits, a 12-bit ADC and an internal memory to store up to 64K digitized samples (2048 per channel);

b. a timing generator to generate the clock pulses for the data logger;

c. a 2-channel trigger unit, to trigger the measurements on external events;

d. a 32-channel ADC for the measurement of slowly varying events. It is used to measure the windspeed, winddirection and temperature from the analog outputs of the weather station;

e. parallel input and output registers for controlling the filter settings and to sense the overload indicators;

f. an HPIB-interface to connect the CAMAC-system and the HP-1000 computer. HPIB stands for Hewlett-Packard Interface Bus and is HP's implementation of the IEEE-488 standard for the interfacing of computer peripherals;

g. a PDP-MIK-11 crate controller. All CAMAC modules are controlled with this processor. It is a small 16-bit computer, controlled by a stripped version of the RT-11 operating system and

running an application program that makes the CAMAC-system an intelligent peripheral, to be controlled with simple commands through the HPIB-interface. All software is permanently installed in EPROM-modules.

4.3.5 The HP-1000 computer system

This mini-computer system controls all measurements, performs the digital signal processing and stores the data on disc. After post-processing, the results are presented on the terminal, the plotter, or the data is sent to another computer system.

The system includes the following items:

a. a 21-MX-F computer with floating point hardware and 2 Mbytes of internal semi-conductor memory;

b. a disc-drive with 16 Mbytes memory and an internal tape backup system with a capacity of 64 Mbytes/tape cassette;

c. a graphic display terminal;

d. a digital plotter;

e. interfaces for data communications with other HP-1000 computer systems;

f. an HPIB-interface to control the CAMAC-system, the digital plotter and occasionally other HPIB-controlled devices.

4.4 THE SOFTWARE

4.4.1 The operating system

When the system was purchased in 1979, the HP-1000 included a flexible disc subsystem as a mass-storage device with a capacity of 500 Kbytes. The system executed under control of the RTE-M operating system. This gave some limitations in program development and data storage capacity. In 1983 the flexible disc was replaced by a 16 Mbytes Winchester disc-drive and the system now runs under control of the RTE-VI operating system. Most software was upward compatible from RTE-M to RTE-VI, so that only minor changes had to be made to the application software.

The RTE-VI operating system is a multi-user real-time system in which many programs can be scheduled in parallel, to run on a priority base. Although only one program can execute at one time, a program can execute during the time that another program is I/O-suspended. These actions are transparent to the user, so with a right choice of program priorities, a kind of time sharing is obtained.

The programs reside in different memory partitions and can be swapped to the disc when necessary. The system offers facilities for synchronized program execution, scheduling on external events, output spooling and job processing.

Program development is supported by an interactive editor, assembler, compilers and a loader or linker. Most application programs and user libraries are written in FORTRAN-77. The

program and data-files are stored on disc through a file management system. Communication with other HP-1000 systems is controlled by the DS-1000 Distributed Systems software. We also installed the Session Monitor. This subsystem prompts the user for identification before access is given to the system. It also manages an account system of the connect- and CPU-times.

4.4.2 User interface

The usual interface between the operator and a computer system is through the keyboard and the display on a terminal. The same procedure is followed with the application software of SYNTACAN. Because this software runs under the Session Monitor of the RTE-VI operating system, the operator must be acquainted with the most important operator commands. In order to facilitate the use of the application programs, a special control program has been developed. The program makes extensive use of the soft-key capabilities of the terminal, and leads the operator through a menu to set measurement parameters, to start and stop the measurements and to execute post-processing commands. The terminal has 8 soft-keys. Each key is software-labeled in an 8-character long display field and corresponds with a certain action of the menu program. Some examples are given in figure 4.11.

main menu							
COMMENTS	FL=125	FH=1000	T = 14.0	CAL/TEST	ACQUIS	PLOTTEN	FMGR

acquisition menu							
NAME	FL=125	FH=1000	1000 m	Verzw. 9	START	Trig.aan	Terug

plot menu							
NAME	Terminal	15 dB	1000 m	Tabel	Spectrum	Polair	Terug
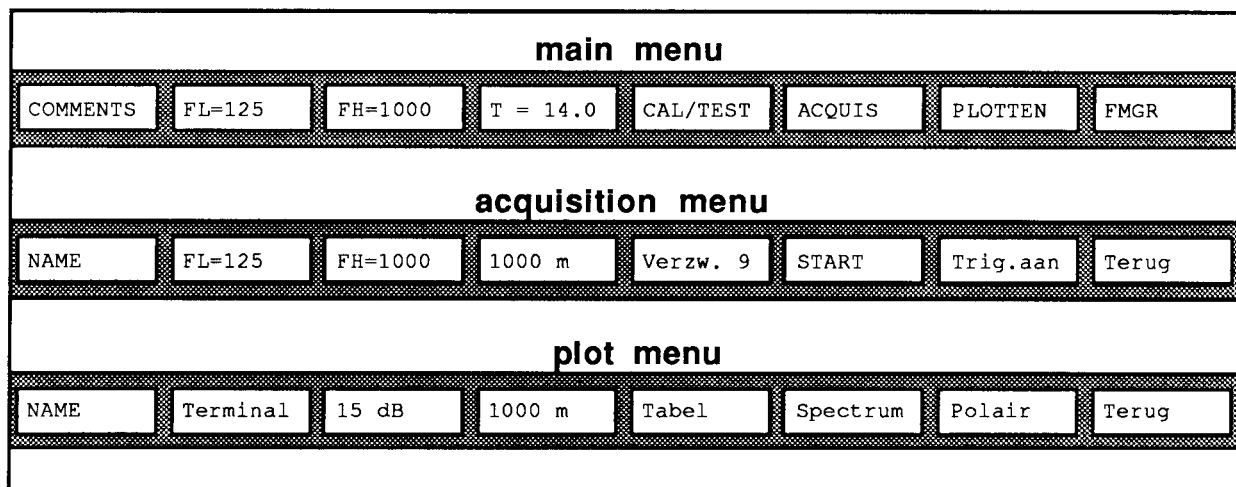
Figure 4.11: The menu program is controlled through single key-strokes of one of the 8 soft-keys. Pressing one key can result in a direct command execution, or it can branch to another menu.

4.4.3 Acquisition

After the antenna has been installed with all cables connected, the microphones are calibrated absolutely with a special calibrator (see §4.4.5). This procedure also eliminates possible mistakes in the microphone cabling: if a microphone is connected to a wrong input channel, no response will be measured. The correction factors are kept in memory for the acquisition program. They can also be written to disc, so that they can be inspected afterwards or even be

used again, although this is not recommended if the antenna has been disassembled in between. A typical calibration result is shown in figure 4.12. When the calibration is completed, the gain of the microphone amplifiers is adjusted to the ambient sound field and all channels are monitored to check their correct functioning.

The next step is to check the homogeneity of the soundfield. This is performed by measuring the sound pressure level per octave band with all relevant microphones. The level differences are then displayed as shown in figure 4.13.

In each octave band the 8th microphone of the sub-array acts as the reference microphone, because that channel is used to compute $\tilde{R}(\xi=0, f)$. At these reference positions the $1/1$-octave levels are also measured with a sound level meter. This gives an extra check on the correct functioning of the antenna.
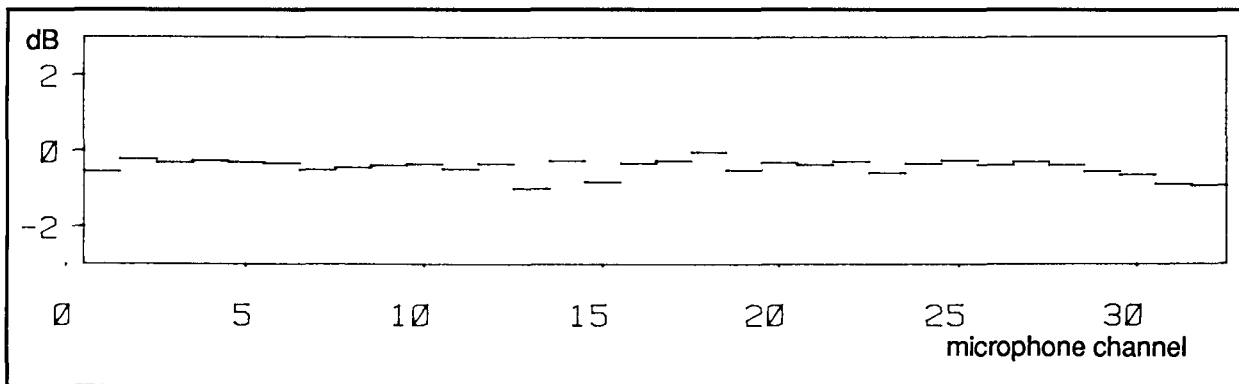
Figure 4.12: Calibration corrections in a practical situation.
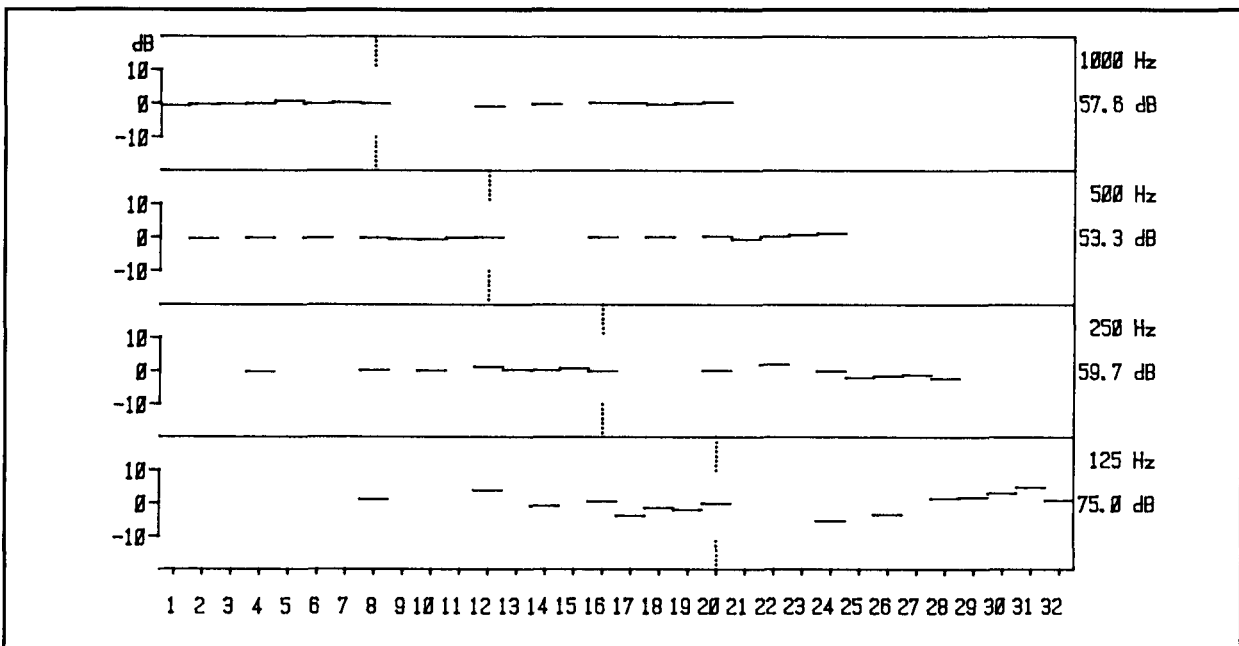
Figure 4.13: Graphic display of the level differences along the antenna as a check for the homogeneity of the ambient soundfield.
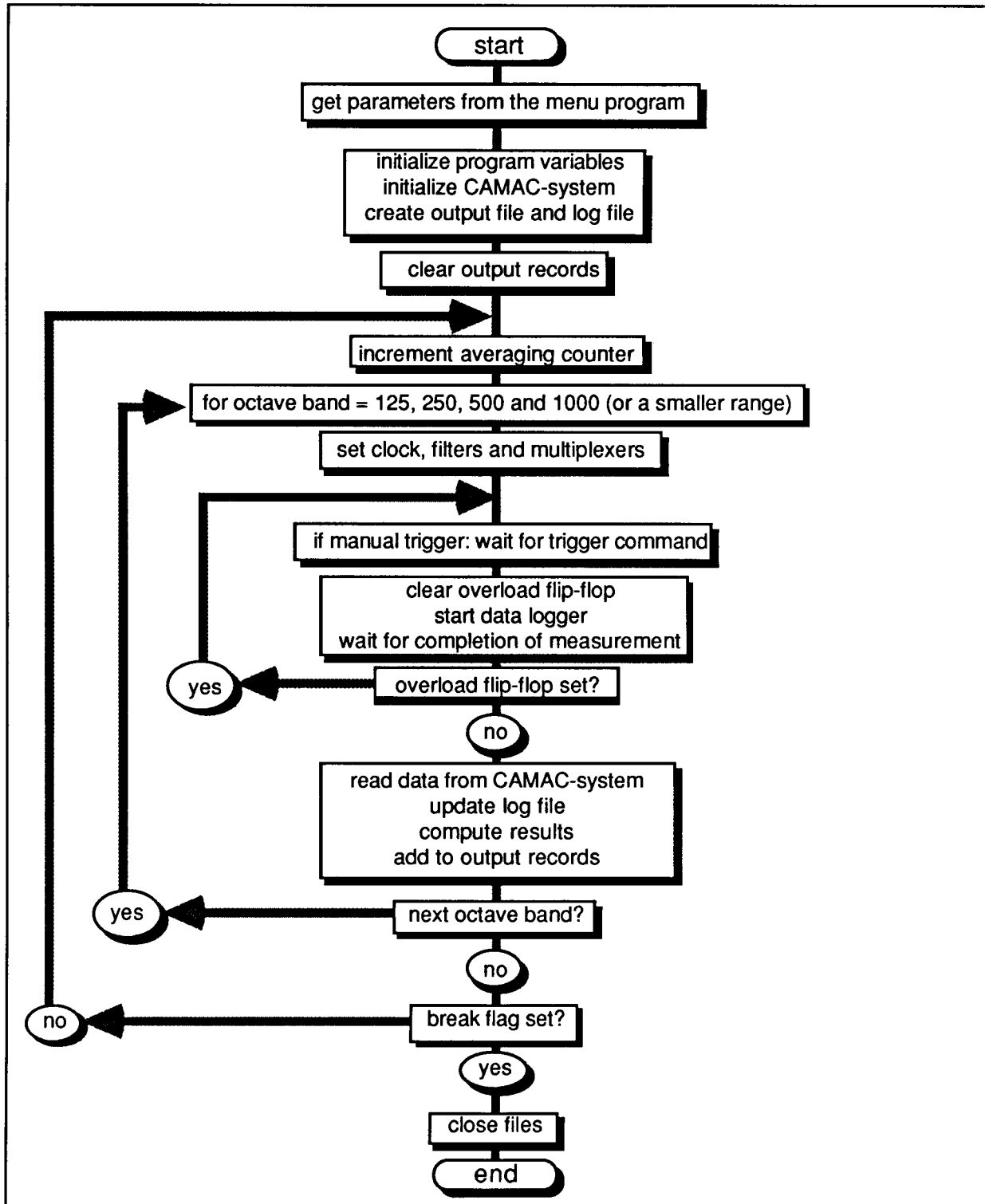
Figure 4.14: Flowchart of the acquisition program.

Before the measurements start, the software has to be informed about the frequency range to be measured, the number of microphones, the kind of triggering which will be used, etc. All these parameters are set through the menu program discussed in § 4.4.2. This program is also used to start and stop the measurements. A start command causes the scheduling of the acquisition program and a stop command sets a break flag for that program. The acquisition procedure is summarized in the flowchart of figure 4.14. It shows that measurements are performed successively in the 125, 250, 500 and 1000 Hz band. The data logger measures 32 channels in parallel with 2048 samples per channel. The sample intervals and measurement times are given in table 4.3.

Table 4.3

Sample intervals and measurement times per octave band

octave band in Hz	sample interval in μs	measurement time in s
125	1600	3.2768
250	800	1.6384
500	400	0.8192
1000	200	0.4096

The cross-spectra are computed from the microphone channels as indicated in table 4.2 using the combination scheme of table 4.1. The computation is performed by Fourier transformation from time to frequency and complex-conjugate multiplication, using the relation:

$$\tilde{R}(\xi, f) = \tilde{R}^*(x_1, f) \, \tilde{R}(x_2, f) \qquad (\xi = x_2 - x_1) \quad . \qquad (4.5)$$

This computation results in 1024 complex frequency components from dc to the Nyquist frequency. These cross-spectra are rough estimates of the average cross-spectra that are needed to compute the immission levels. An efficient averaging, which also gives considerable data reduction, is obtained by summing all frequency components within $1/12$-octave band.

This bandwidth was chosen as:

a. The $1/12$-octave bandwidth is a standard measure for narrow-band sound analysis;

b. The results can easily be summed to obtain the standardized $1/3$- and $1/1$-octave bands;

c. The bandwidth is small enough in relation to the angular resolution of the antenna to avoid unsharp images as a result of spectral averaging.

To understand this latter property, we recall Eq. (2.97):

$$k_x' = (f/c) \sin \alpha \quad . \qquad (4.6)$$

This relation shows that the k_x'-value of a source from a direction α depends linearly on frequency. By spectral averaging, all frequency components between f_{low} and f_{high} are processed with the same midband frequency f_{mid}. This results in an apparent source direction

$$\alpha_{high} = \arcsin[(f_{high} / f_{mid}) \sin \alpha] \tag{4.7a}$$

at the high frequency bound and

$$\alpha_{low} = \arcsin[(f_{low} / f_{mid}) \sin \alpha] \tag{4.7b}$$

at the low frequency bound. This angular spread is maximum at the extreme angles of incidence, for SYNTACAN at $-30°$ and $+30°$.

A $1/12$-octave band is defined by

$$f_{high} / f_{mid} = f_{mid} / f_{low} = 10^{1/80} \; . \tag{4.8}$$

From Eq. (4.7–4.8) it follows that the angular spread is not more than $\pm 1°$ at $\alpha = \pm 30°$.

Averaging over $1/12$-octave bands gives a data reduction from 290 to 12 spectral lines in one octave. The results are written to the output discfile as a function of ξ in records of 64 complex points. In that way the results are ready for post-processing (see § 4.4.4). The extra microphone channels (for the 1.5 to 5 m conversion) are also analyzed in $1/12$-octave bands. The results are written to the log-file together with other relevant measurement parameters, like the weather conditions and the time of measurement.

As shown in the flowchart (see figure 4.14), the measurements are repeated automatically as long as the breakflag has not been set. This will result in a summation of all measured cross-spectra, which gives a better estimate of the equivalent immission noise levels. Practice has taught however that it is safer not to use this feature, because one wrong measurement can ruin all other results. It is better to store all measurements in different output files and to average all approved measurements afterwards.

The acquisition program has been written in such a way that the data processing time is minimized as much as possible. This is accomplished by keeping intermediate results, which can be used later, in temporary scratch files. Furthermore the data processing takes place in parallel with the data transfer from the CAMAC-system. The processing times are given in table 4.4. It shows that the measurement of a complete cycle of 4 octaves takes about 3 minutes.

Table 4.4

Processing times for a complete measurement cycle of 4 octaves

octave band Hz	measurement s	processing s	total s
initialization	–	5	5
125	3.3	40	43.3
250	1.6	40	41.6
500	0.8	40	40.8
1000	0.4	40	40.4
Total	6.1	165	171.1

4.4.4 Post-processing and output of results

Several computer programs have been written for post-processing of the measured data. Most of these programs are scheduled with the soft-keys of the user interface program. This enables the operator to display results during measurements, so that the quality of the measurements can be easily controlled.

The main features of the post-processing are:

a. Focussing on any distance by phase corrections in the cross-spectra using the procedure of Section 2.8;

b. Averaging over a number of measurements to obtain better estimates of the cross-spectra. This is important if fluctuations occur in the source powers and in the atmospheric propagation. As the cross-spectra are proportional to the squared sound pressures, averaging gives an unbiased estimate of the equivalent sound pressure levels (L_{eq}). Averaging can also be performed during the measurements, but it is safer to do it afterwards. It not only gives the possibility to eliminate bad measurement cycles, but also to compute the variance of the immission levels as a quality measure of the obtained results;

c. Plotting of the A-weighted octave diagrams. This is the basic presentation format of the results, as it shows the immission levels as a function of the angle of incidence;

d. Plotting and printing of the A-weighted $1/12$-octave immission spectra for any direction between $-30°$ and $+30°$ and integrated over an arbitrary angular range. The $1/12$-octaves can also be summed to $1/3$- and $1/1$-octaves;

e. Calculation of the level differences between the measurement height of the antenna and the standard measurement height of 5 m, from the data of the additional microphones.

All results are A-weighted, according to IEC-651. This is necessary for the polar diagrams, because a linear weighting would over-emphasize the low-frequency components in this presentation format. The A-weighting was chosen because it is the standard weighting curve for immission levels. For a uniform presentation of the results, it was decided to perform the A-weighting for the immission spectra as well. The post processing also contains algorithms for calibration of the output results as a function of frequency and as a function of the angle of incidence. The details of the different calibration steps will be discussed in § 4.4.5.

The directional information is obtained by Fourier transformation of the $R(\xi, f)$-records to the k_x'-domain, according to Eq. (2.106). Side lobes are suppressed by using the generalized Hamming window with $a = 0.6$ (see Section 2.7):

$$W_a(\xi) = 0 \qquad\qquad \text{for } |\xi| > X$$

$$W_a(\xi) = 0.6 + 0.4 \cos (\pi\xi / X) \qquad \text{for } |\xi| \leq X \ .$$

<div align="right">(4.9)</div>

This window has a highest side lobe level of -16 dB and a -3 dB bandwidth B_w of only 1.6 bins.

For the presentation of the results in polar diagrams, the $1/12$-octave results have to be summed for each direction. A direct summation is not possible because of the frequency-dependent relation between the k_x'-values and the angle of incidence. For that reason — and also to get a smooth curve for plotting — the $1/12$-octave results are first interpolated at 128 angles α_i over the interval $-30°$ to $+30°$ with

$$\alpha_i = \arcsin(-1/2 + i/128) \qquad (i = 1, \ldots ,128) \ . \qquad (4.10)$$

Each increment corresponds with approximately 0.5 degrees or 0.6 $\Delta k_x'$ at the high frequency bound. If the true angle of incidence of a plane wave is exactly midway between two interpolation angles, then the interpolated result is not more than 0.4 dB lower than the true maximum. The interpolation is performed with a technique described by Van der Wal [37]. It is based on the convolution of the measured data with the Fourier transform of the spatial window:

$$\tilde{R}'(k_x',f) = \sum_n \tilde{R}'(n\Delta k_x',f) \ \tilde{W}_a(k_x' - n\Delta k_x') \ . \qquad (4.11)$$

This relation shows that $\tilde{R}'(k_x',f)$ can be computed for each k_x'-value if the spatial window function is known at the position $(k_x' - n\Delta k_x')$. Notice that Eq. (4.11) is a result of the sampling theorem of Shannon and that it is only valid for band-limited signals.

The summation in Eq. (4.11) is restricted to ± 2 $\Delta k_x'$ around the interpolated k_x'-value because of the fact that $\tilde{W}_a$ has only significant values in this region. The $\tilde{W}_a(k_x')$-values have been computed with $1/8$ $\Delta k_x'$ intervals and are implemented as a look-up table. This makes the interpolation very fast. Notice that the spatial windowing must not be performed explicitly in the ξ-domain, because it forms a part of the interpolation procedure. Only when a shorter antenna is used, the cross-spectra are first windowed in the ξ-domain with a window that is effective over the actual aperture length. In that case the interpolation gives an extra windowing but this does not have a noticeable influence on the resolution.

After the interpolation has been performed for all $1/12$-octave bands, a summation over all frequency bands can be carried out to obtain the polar diagrams. The polar diagrams are presented in dB re 20 μPa. The calibration is performed in such a way that the peak-level of the main lobe shows the immission level of a noise source that produces a plane wave on the antenna. This is also true for a monopole at a finite distance with correct focussing. In case of transverse coherence loss, the peak level will be too low.

The immission spectra for one direction are computed in the same way as the polar diagrams, but now the interpolation is carried out for only one direction. This gives only calibrated results for correctly focussed point sources (or plane waves) and for a negligible transverse coherence loss. For that reason it is better to integrate over an angular area that contains the whole main

lobe of a source area. As discussed in § 3.3.2 this will always give the correct immission values. The angular integration is performed by direct summation over the $\tilde{R}'(k_x',f)$-values, where the boundaries of the summation are computed from Eq. (4.6). In this case the spatial window of Eq. (4.9) is implemented as a multiplication in the ξ-domain.

A special spectral presentation is obtained by calculation of the immission spectra over an angular range for all individual measurements in $^1/_3$-octave bands. From these results the energetic average is computed as a measure for the L_{eq}. Furthermore the standard deviation of the noise levels (in dB's) is computed. It is assumed that these levels have a random Gaussian distribution during the measurement interval and the 95% confidence limits of the average levels are computed, using the Student-t distribution. The average level and the 95% confidence limits are then tabulated and plotted on a standard presentation form.

The output results can be displayed on the terminal for preview. The final results are then plotted on paper or tranparences and tabulated output can also be sent to a printer. For examples of the various presentation formats of the results, the reader is referred to Chapters 5 and 6.

4.4.5 Calibration

Because SYNTACAN uses so many microphone channels, and also because of the complex measurement technique, calibration of the antenna was carried out by a special method.

The first step in the calibration process was the elimination of all amplitude and phase differences between the microphone channels. This was done as follows. Two microphones were placed close together in the anechoic room of our laboratory and were submitted to a spherical soundfield of a swept sine wave, reproduced by a loudspeaker. The microphone signals were sampled by the data-acquisition system and the amplitude- and phase differences were computed and displayed. With this procedure, channel 1 acted as a reference and the comparison was carried out with all other channels. The differences in amplitude and phase were minimized over the relevant frequency range (from 89 to 1413 Hz) by tuning of the gain and phase adjustments of the pre-amplifiers (see § 4.3.1), resulting in differences of not more than ±1 dB and ±10°, as shown in figure 4.15.

The next step in the calibration was to find the frequency and angle dependent gain factors that must be applied to get calibrated results. To reach this goal, a plane wave was simulated by using only one microphone and using its signal for all input channels (not really, but in software). The microphone was placed in the anechoic room, close to a calibrated measurement microphone, connected to a $^1/_3$-octave spectrum analyzer. The sound field of pink noise reproduced by a loudspeaker was analyzed with SYNTACAN and with the spectrum analyzer. The measurement was repeated for several angles of incidence in order to find the angle-dependence of the SYNTACAN microphones. As we found in Eq. (3.35), the total immission is obtained from the auto-spectrum $\tilde{R}(\xi=0,f)$ and that function is measured with microphone channels 8, 12, 16 and 20 for the 1000, 500, 250 and 125 Hz octave bands respectively.
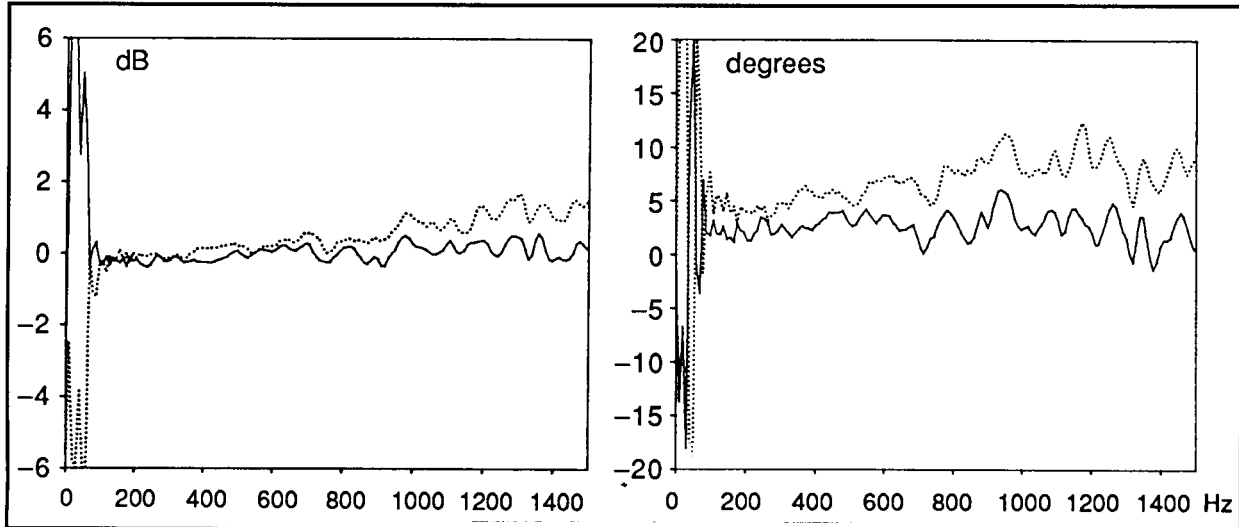
Figure 4.15: The amplitude and phase differences between the microphone channels after adjustment of the amplitude and gain: —— best case (channels 3 and 1); ····· worst case (ch. 27 and 1).

For that reason the absolute calibration was carried out with these microphone channels for the different octave bands. The calibration thus found is implemented in the post-processing software and consists of:

a. A constant multiplication factor dependent on microphone sensitivity, amplifier gain and scaling factors from the data analysis;

b. A frequency dependent factor because of the frequency characteristic of the microphones and the pre-amplifiers.

This compensation is performed in two steps:

1. multiplication with a factor $A(f)$, given by

$$A(f) = [1 + (146/f)^4] / [1 + (f/1450)^4] \ , \tag{4.12}$$

2. a final correction in $1/3$-octave intervals from a look-up table. These corrections are not more than 2 dB and are adapted when the system is re-calibrated;

c. An angle-dependent factor $A(\alpha)$, given by

$$A(\alpha) = 4 / [1 + (\cos \alpha)^{3.7}]^2 \ . \tag{4.13}$$

This correction is not more than 2 dB at 30°.

There is one calibration step that is carried out at the measurement site and forms a part of the acquisition procedure: the on-site calibration already mentioned in § 4.4.3. It has been developed because it was observed in practice that the gain of some of the microphones is dependent on temperature, especially below 5 °C. For that reason and because a normal pistonphone cannot be used here, we developed a special on-site calibrator for these microphones (see figure 4.16). It consists of a 35 cm long tube with a diameter of 5 cm.

Figure 4.16: The specially developed calibrator for the on-site calibration of the antenna-microphones.

At one side a small loudspeaker is mounted, driven by a battery-operated sinewave oscillator. The other side is terminated by a rubber ring, through which a microphone can be inserted into the tube. We observed that this calibrating device itself is temperature dependent, which is caused by the following factors:

a. The standing wave pattern in the tube depends on the wavelength and wavelength is a function of temperature. This effect was studied by varying the frequency at a constant temperature, because that is much easier to do. It was found that the influence on the output of the microphones could be minimized by tuning the oscillator on the $1/2\lambda$-resonance of the tube (506 Hz at 20 °C);

b. The output of the loudspeaker is a function of the temperature of the rather small cavity behind the diaphragm. This effect is eliminated by measuring the output of the calibrator with a 1"-microphone of a sound level meter, which fits precisely into the opening of the rubber ring at the entrance of the tube.

The overall accuracy of this calibrator is ±0.5 dB over a temperature range from −10 to +40 °C. The correction factors found by the on-site calibration are applied directly to the measured data, so that the calibration factors in the post-processing are independent of these variations.

CHAPTER 5

TEST RESULTS

5.1 INTRODUCTION

In this Chapter we will discuss several tests that have been carried out to examine how the system behaves under different conditions. In the first place we will examine the antenna performance under ideal circumstances, by presenting the basic antenna response for uncorrelated monopole sources in the far field and in the near field of the antenna. Subsequently, we will test the behavior of the antenna system in case of correlated sound sources and finally, some tests on propagation effects will be discussed.

A part of these tests could be done before the system was built, by execution of appropriate computer simulations. In that way it was possible to predict the influence of the antenna length and the transverse coherence loss under simulated conditions. Other tests have been done after experience was gained from practical situations, which had lead to questions as: "How well is the absolute calibration of the antenna?" and "What is the influence of inhomogeneities in the transmission path?"

In order to answer these questions and to find out under which conditions SYNTACAN can replace or supplement the standard measurement procedures, a special evaluation study has been carried out, supported by the Dutch Ministry of Housing, Physical Planning and Environment and reported by Brackenhoff [38] and Van Overbeek et al. [39]. In this Chapter the most important results of this investigation are reported, together with some other test results, in order to show how the instrument behaves under various measurement conditions.

5.2 GENERAL CHARACTERISTICS

5.2.1 Basic response for a single monopole source

In case of a single monopole source at a large distance, the spatial cross-spectrum is given by Eq. (2.105), which reduces for one source to:

$$\tilde{R}(\xi, f) = \tilde{R}_1(f) \exp(-j2\pi f\xi/c_1) \tag{5.1}$$

with $c_1 = c \, / \sin \alpha_1$ (α_1 = source direction).

This situation has been simulated by computing the spatial cross-spectrum as given by Eq. (5.1) for discretized values of f and ξ and storing the results in a normal output file for SYNTACAN measurements. The discretization as a function of frequency was directly carried out at the $1/12$-octave midband frequencies, so that frequency averaging was not necessary. Note that this "advance averaging" is not fully correct because of the phase differences for the different frequencies within the $1/12$-octave band (see also § 4.4.3). For small values of α this effect can be neglected.

Figure 5.1a shows the polar diagram for a simulated monochromatic noise source with a frequency of 1029 Hz and unit amplitude at an angle of incidence of 0.5°. It displays the immission level in dB's as a function of the angle of incidence over a range from –30° to +30°. Notice that the angles are displayed in a right turning angle system, in accordance with geodetic practice.

As the legend of fig. 5.1a shows, the simulation was performed at a temperature of 20 °C and a focal distance of 99999 m was used, which is infinite in practice. The level range is 15 dB from the center of the plot to the maximum value, which is 0 dB in this figure. Figure 5.1b shows the same simulation, but now plotted with a level range of 30 dB, showing the side lobes of the synthetic beam pattern of this simulated monochromatic source. It must be noted that the polar diagrams are drawn for a discretized set of angles. For that reason the appearance of the side lobes strongly depends on the angle of incidence of the noise sources. The angle of incidence was chosen such that the side lobes are maximum. It can be found from figure 5.1b that the maximum side lobe level equals –14.2 dB. In § 2.7.4 it was stated that the applied spatial window would give a maximum side lobe level of –16 dB. The difference is caused by the fact that the spatial window is not explicitly applied, but approximated in the finite length interpolation filter (see § 4.4.4). Figures 5.1c and 5.1d show the polar diagrams on a 15 dB and a 30 dB scale for a simulated wide band point source with $\tilde{R}_1(f) = 1$ for each $1/12$-octave band (so-called *pink-noise*). The small diagrams show the results for the individual octave bands and the large diagrams show the integrated results over all octave bands. The small and the large diagrams use the same maximum level and dB-range from center to maximum value. The level differences between the octave bands are caused by the A-weighting. The A-weighting is essential to emphasize the important noise sources in practical situations. From fig. 5.1b and 5.1d it is seen that the side lobes of the wide band source are considerable lower than for a monochromatic source. This is caused by destructive interference of the side lobes from the different frequency components. Figure 5.1d shows that the maximum side lobe level from a pink noise source is 22 dB lower than the main lobe level.

a

```
File  : Q1                    Schaal:  15 dB
Temp. : 23.0 °C               Max.  :  -.0 dB
Focus :99999 m                Midd. :   1
                                        -30 °


                                          °


1000 Hz                                 30 °
```

b

```
File  : Q1                    Schaal:  30 dB
Temp. : 20.0 °C               Max.  :  -.0 dB
Focus :99999 m                Midd. :   1
                                        -30 °


1000 Hz                                 30 °
```

c

```
File  : PINK                  Schaal:  15 dB
Temp. : 23.0 °C               Max.  : 12.8 dB
Focus :99999 m                Midd. :   1
                              250 Hz   -30 °

                    125 Hz



                    500 Hz

                    1000 Hz           30 °
```

d

```
File  : PINK                  Schaal:  30 dB
Temp. : 20.0 °C               Max.  : 12.8 dB
Focus :99999 m                Midd. :   1
                              250 Hz   -30 °

                    125 Hz



                    500 Hz

                    1000 Hz           30 °
```
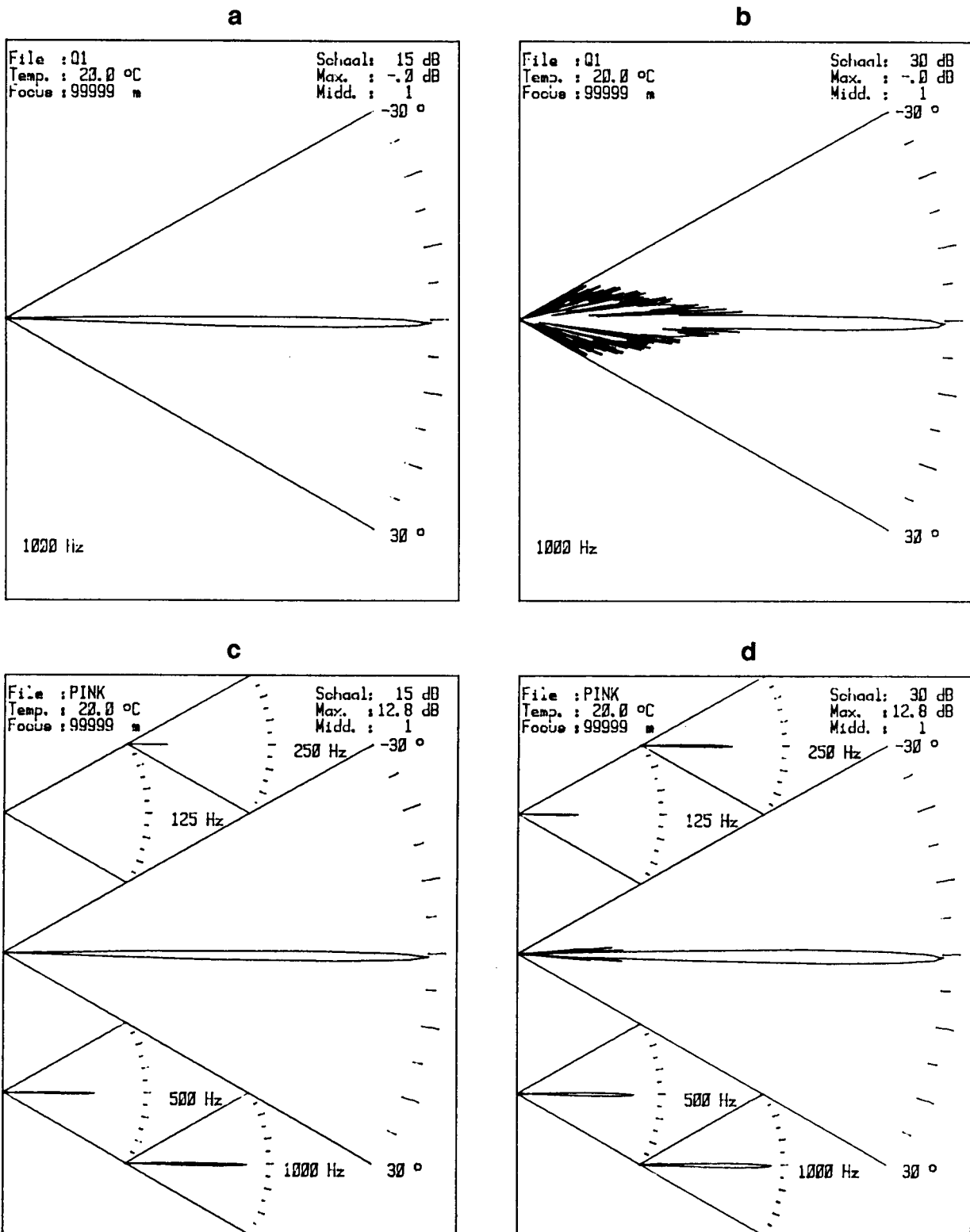
Figure 5.1: Polar diagrams of simulated noise sources at an angle of incidence of 0.5°: a. and b. show a monochromatic source of 1029 Hz, plotted with a dB range of 15 dB and 30 dB; c. and d. show a source with a pink spectrum, also plotted with a range of 15 and 30 dB.

Note from figure 5.1 that the applied dB-range has a strong influence on the appearance of the polar diagrams. It has become practice to use a range of 15 dB under normal circumstances, as this gives a clear indication of the direction of the most important noise sources without confusion due to side lobes or the unimportant small noise sources.

Figure 5.2 shows the A-weighted immission spectrum with $^1/_{12}$-octave resolution for the pink noise source as obtained from the simulation file and calculated for an angle of incidence of 0.5°. Because the unweighted immission level of this source is 0 dB for each $^1/_{12}$-octave, this figure shows the implemented A-weighting curve, which is very close to the recommendation of IEC-651, as shown in table 5.1. Notice that deviations from the recommended weighting are eliminated for real measurements with the calibration procedure of § 4.4.5.
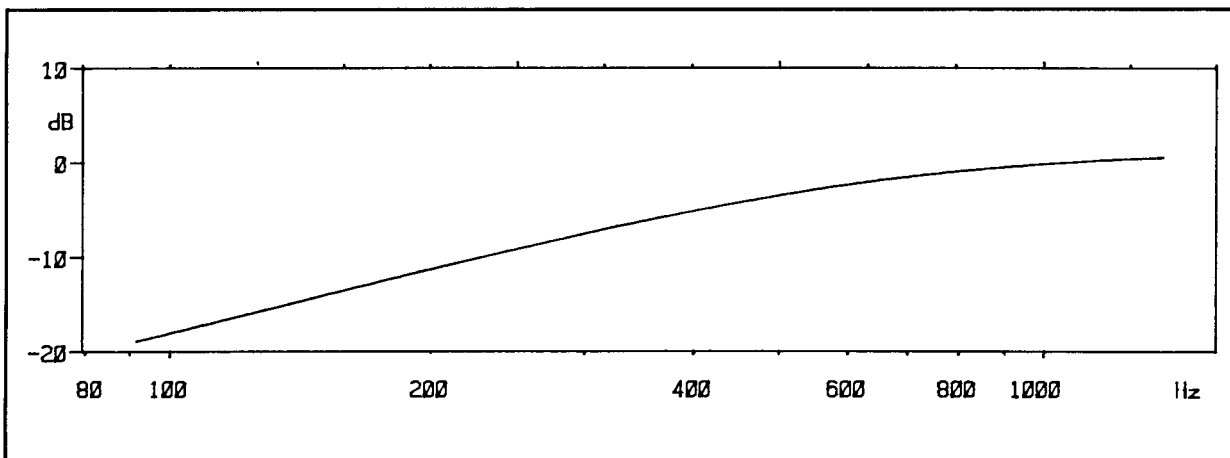
Figure 5.2: A-weighted immission spectrum with $^1/_{12}$-octave resolution of the pink noise source from figure 5.1 c and d.

Table 5.1

Comparison between the A-weighting of SYNTACAN
and the recommendation of IEC-651

1/3-octave midband freq. in Hz	A-weighting in dB rel. 1 kHz		difference in dB
	SYNTACAN	IEC-651	
100	−17.9	−19.1	1.2
125	−15.6	−16.1	0.5
160	−13.3	−13.4	0.1
200	−11.1	−10.9	−0.2
250	−9.0	−8.6	−0.4
315	−6.9	−6.6	−0.3
400	−5.0	−4.8	−0.2
500	−3.3	−3.2	−0.1
630	−1.9	−1.9	0.0
800	−0.8	−0.8	0.0
1000	0.0	0.0	0.0
1250	0.5	0.6	−0.1

5.2.2 Angular resolution for two uncorrelated monopole sources

The angular resolution of SYNTACAN is best demonstrated in the simulation of two closely spaced uncorrelated monopole sources. Figures 5.3a-d show the polar diagrams of two uncorrelated, quasi monochromatic noise sources with a frequency of 1029 Hz and unit amplitude, with one source at an angle of $0°$ and the other source at $1.5°$, $1.6°$, $1.7°$ and $1.8°$ respectively. Use of Eq. (2.128) with $B_w = 1.6$, $c = 340$ m/s, $X = 9.60$ m, $f = 1029$ Hz and $\alpha = 0°$, gives a -3 dB beamwidth of $1.6°$, which is in accordance with figure 5.3. Figure 5.3 clearly shows that when the sources are visually resolved as in figures 5.3c and 5.3d, the peak levels of the individual sources are not noticeably influenced; simulation of only one monochromatic source with a frequency of 1029 Hz and unit amplitude at a direction of $0°$ would also show a peak level of 0.1 dB (the emphasis of 0.1 dB is caused by the A-weighting). It is interesting to investigate the angular integration in case of two closely spaced sources. The results, corresponding with figure 5.3d, i.e. two sources at $0°$ and $1.8°$, are presented in table 5.2. It shows that the calculated levels of the individual sources have only a small deviation (±0.2 dB) from the expected value of 0.1 dB. This is mainly caused by the discretization as a function of the angle of incidence. Notice that the total level of both sources is exactly 3.1 dB as expected from two uncorrelated sources with individual immission levels of 0.1 dB.

Table 5.2

Angular integrated immission levels for two uncorrelated, quasi monochromatic noise sources with $f = 1029$ Hz and unit amplitude at angles of $0°$ and $1.8°$.

α_{min} in $°$	α_{max} in $°$	A-weighted immission level in dB(A)
-2.0	0.9	0.3
0.9	4.0	-0.1
-2.0	4.0	3.1

So far we discussed the resolution for monochromatic sources. Because the resolution is frequency dependent, the resolution of wideband sources will depend on the source spectra. A good indication can be obtained from the simulation of pink sources (with $R(f) = 1$ for each $1/12$-octave band), as shown in figure 5.4. In figure 5.4a the sources are simulated at $0°$ and $1.5°$; in figure 5.4b at $0°$ and $1.6°$. These results show that the effective angular resolution for wideband sources is about $1.5°$ to $1.6°$. We tested the angular integration for the situation of figure 5.4b, summed over $1/3$-octave bands by comparison with a single source. The results are presented in table 5.3. It is seen that the total level of the two sources is exactly 3 dB higher than the expected level for a single source. The integrated levels of the individual sources show deviations of -1.4 and $+1.0$ dB in the $1/3$-octave bands of 100, 200, 400 and 800 Hz, where the resolution is poorest. In the bands of 160, 315, 630 and 1250 Hz the resolution is so high that no deviations from the expected values are observed.

a

```
File  :QS              Schaal:  15 dB
Temp. : 20.0 °C        Max.  :  .6 dB
Focus :99999  m        Midd. :   1
                                    -30 °




1000 Hz                              30 °
```

b

```
File  :QS              Schaal:  15 dB
Temp. : 20.0 °C        Max.  :  .3 dB
Focus :99999  m        Midd. :   1
                                    -30 °




1000 Hz                              30 °
```

c

```
File  :QS              Schaal:  15 dB
Temp. : 20.0 °C        Max.  :  .1 dB
Focus :99999  m        Midd. :   1
                                    -30 °




1000 Hz                              30 °
```

d

```
File  :QS              Schaal:  15 dB
Temp. : 20.0 °C        Max.  :  .1 dB
Focus :99999  m        Midd. :   1
                                    -30 °




1000 Hz                              30 °
```
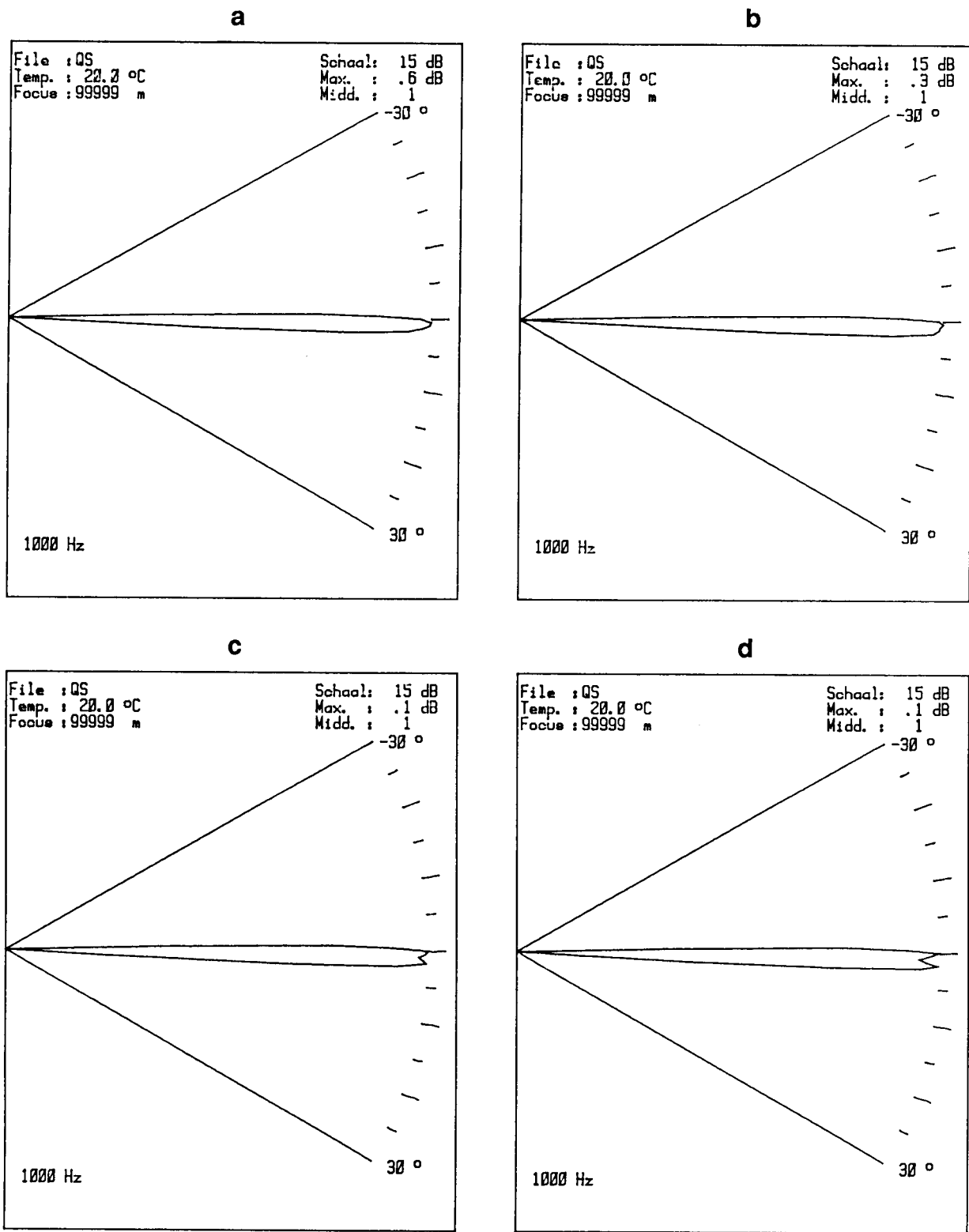
Figure 5.3: Simulation of two monochromatic noise sources with a frequency of 1029 Hz at different angles of incidence: a. 0° and 1.5°; b. 0° and 1.6°; c. 0° and 1.7°; d. 0° and 1.8°.
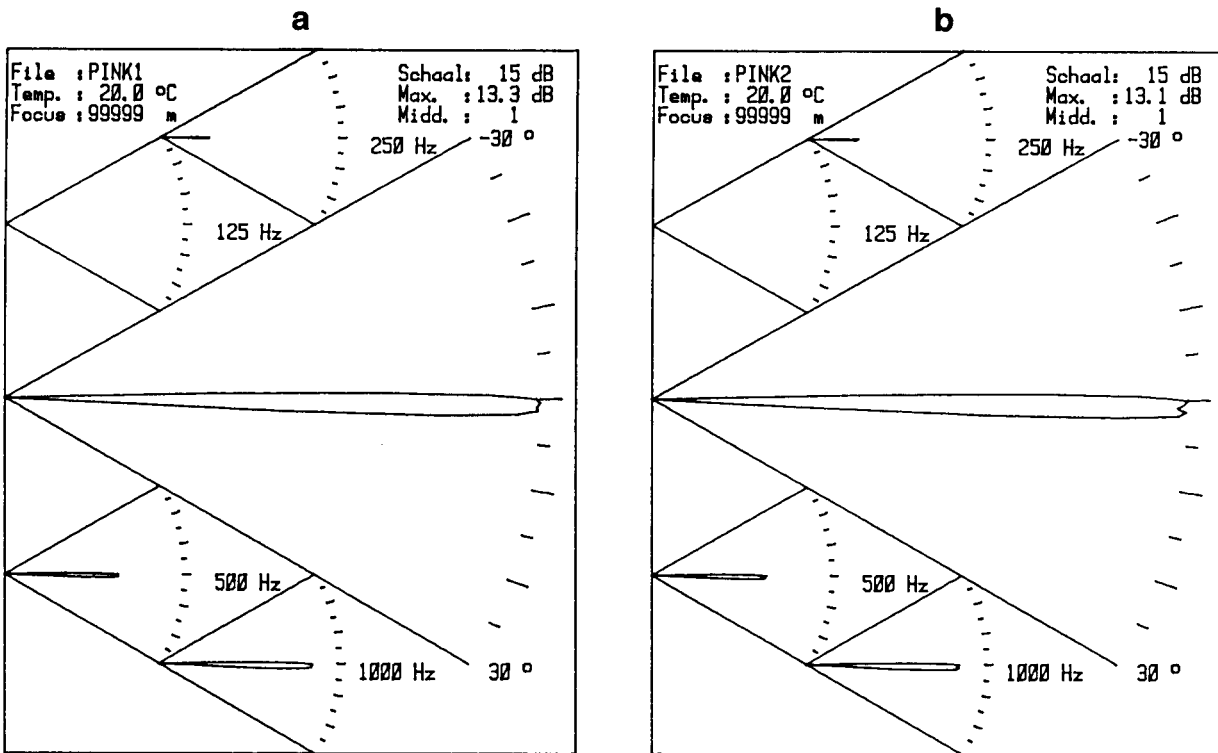
Figure 5.4: Simulation of two pink noise sources at different angles of incidence: a. 0° and 1.5°; b. 0° and 1.6°.

Table 5.3

Angular integrated immission levels for two uncorrelated, pink noise sources at angles of 0° and 1.6°, summed over ⅓-octave bands, compared with a single source having the same spectrum.

1/3-octave midband freq. in Hz	expected immission level of a single source in dB(A)	integrated immission levels for two sources at 0° and 1.6° in dB(A)		
		−2° to 0.8°	0.8° to 4°	−2° to 4°
100	−11.9	−10.9	−13.3	−8.9
125	−9.6	−9.1	−10.2	−6.6
160	−7.3	−7.3	−7.3	−4.3
200	−5.1	−4.1	−6.5	−2.1
250	−2.9	−2.4	−3.5	0.1
315	−0.9	−0.9	−0.9	2.1
400	1.0	2.0	−0.4	4.0
500	2.7	3.2	2.1	5.7
630	4.1	4.1	4.1	7.1
800	5.2	6.2	3.8	8.2
1000	6.0	6.6	5.4	9.0
1250	6.6	6.6	6.6	9.6
total	12.9	13.4	12.4	15.9

5.2.3 Focussing

As discussed in § 2.8.4, the focussing at finite source distances is performed by a phase compensation of the measured cross-spectra in such a way that the Fraunhofer situation is simulated for a certain region. This procedure has been tested with simulations of monopoles at finite distances. The sound pressure of a monopole in a homogeneous, stationary and flow-less medium is given by Eq. (2.14):

$$p(r, t) = s(t - \tau) / r \qquad \qquad (5.2a)$$

with

$$\tau = r / c \quad . \qquad \qquad (5.2b)$$

Hence, the cross-spectra of the antenna can be simulated by the expression

$$\tilde{R}(\xi, f) = \tilde{R}(f) \exp(j2\pi f \tau_1) \frac{r(0)}{r(x_1)} \exp(-j2\pi f \tau_2) \frac{r(0)}{r(x_2)} \qquad (5.3)$$

where $\tilde{R}(f)$ is the autospectrum of the source at the antenna origin, $r(0)$, $r(x_1)$ and $r(x_2)$ are the distances from the source to the antenna origin and the microphone positions x_1, x_2 respectively and τ_1, τ_2 are the traveltimes given by $\tau_1 = r(x_1) / c$ and $\tau_2 = r(x_2) / c$. Here $x_2 = x_1 + \xi$ and the positions x_1 and x_2 are chosen according to the sparsing scheme of SYNTACAN.

The simulations have been performed for monochromatic sources at a frequency of 1029 Hz and for the SYNTACAN antenna in the 1 kHz band, so $\lambda = 0.33$ m and $X = 9.6$ m $\approx 30\lambda$. We found in § 2.8.4 that under these conditions, the Fraunhofer boundary is at a distance of $60X = 576$ m. Hence, without additional phase compensations (focus at infinity), sources at distances smaller than, say 600 m, will not give sharp beam patterns. This is illustrated in figure 5.5.
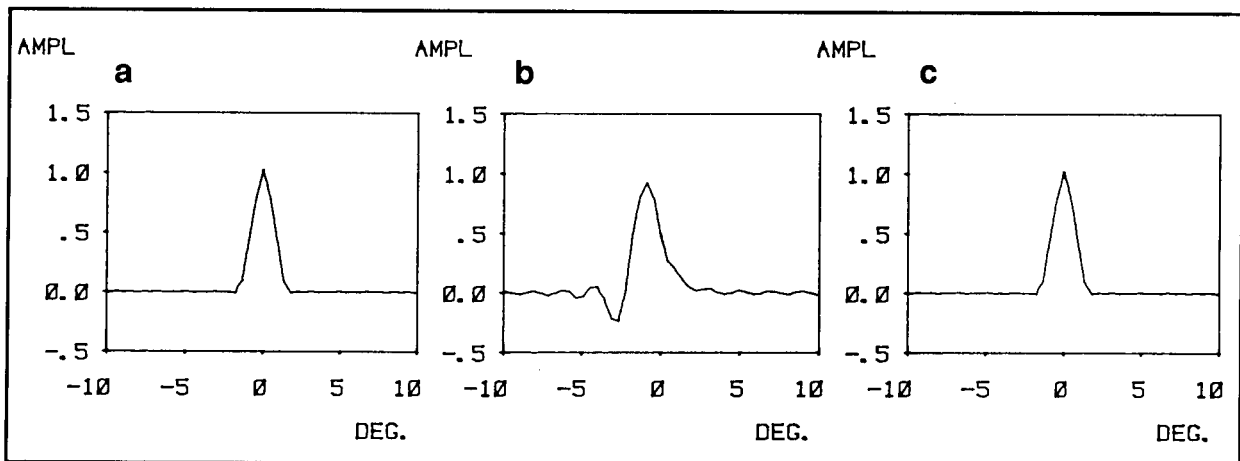
Figure 5.5: The effect of focussing on the beam forming of SYNTACAN for a 1029 Hz source at 0°: a. source at ∞ and focus at ∞; b. source at 200 m and focus at ∞; c. source at 200 m and focus at 200 m.

In the first place, we will discuss the simulation of 5 monopole sources at a distance of 200 m and with angles of incidence of $-25°$, $-15°$, $0°$, $15°$ and $25°$. Figure 5.7a shows the polar diagram of this simulation, with the focussing practically at infinity. From this figure it is seen that due to the incorrect focussing:

a. The measured source directions deviate from the true source directions;

b. The main lobes have broadened;

c. The side lobes have raised.

In figure 5.7b the focussing is performed at a distance of 200 m for frontal incidence. Here all sources are measured with a correct beampattern, not only at $0°$, where the focussing is exact, but also for the other angles of incidence. As expected, the beampattern shows a slight increase of the main lobe for wider source angles, in accordance with the beamwidth formula of Eq. (2.128):

$$B_a(\alpha) = \frac{1}{2} B_w \lambda / (X \cos \alpha) \ . \tag{5.4}$$

Figures 5.7c and d show comparable simulation results, but now for a source distance of 50 m. At this source distance the focussing is critical. Figure 5.7d shows that the normal focussing at $0°$ incidence gives sharp results for the sources at $0°$, $15°$ and $25°$, but the results for $-15°$ and $-25°$ are not fully in focus. This corresponds with the shape of the focal zones at small distances as given in figure 2.16. Notice that the asymmetry for positive and negative angles is due to the fact that the antenna is also asymmetric: the reference point is at $x = 0$ and the microphones are placed only at positive x-values.

In figure 5.8 the situation for source distances of 20 m is depicted. Here the focussing is very critical and sharp images are only obtained when the correct focussing direction is applied. Notice that the angle dependence is less critical for positive angles of incidence, where the sources are more or less in front of the aperture, than for negative angles of incidence, where the sources are aside of the antenna. This situation is shown in figure 5.6.
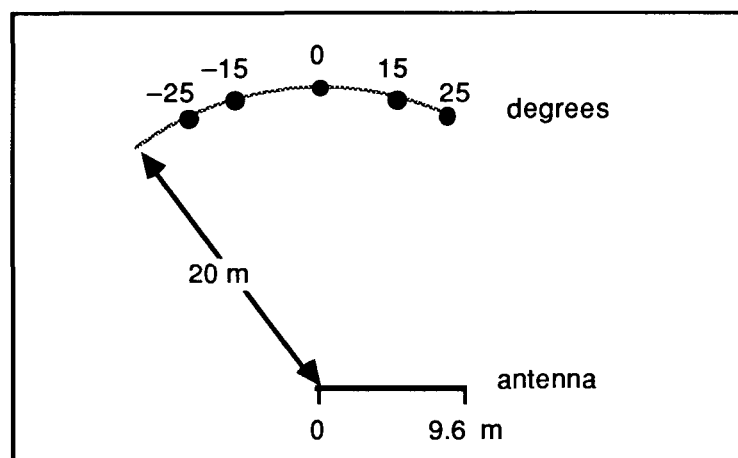
Figure 5.6: Location of sound sources for the simulation of figure 5.8.

a

```
File  :F2                      Schaal:  15 dB
Temp. : 20.0 °C                Max.  : -.2 dB
Focus :99999 m                 Midd. :  1
                                      -30 °

1000 Hz                        30 °
```

b

```
File  :F2                      Schaal:  15 dB
Temp. : 20.0 °C                Max.  :  .1 dB
Focus :  200 m                 Midd. :  1
                                      -30 °

1000 Hz                        30 °
```

c

```
File  :F3                      Schaal:  15 dB
Temp. : 20.0 °C                Max.  :-1.4 dB
Focus :99999 m                 Midd. :  1
                                      -30 °

1000 Hz                        30 °
```

d

```
File  :F3                      Schaal:  15 dB
Temp. : 20.0 °C                Max.  :  .1 dB
Focus :   50 m                 Midd. :  1
                                      -30 °

1000 Hz                        30 °
```
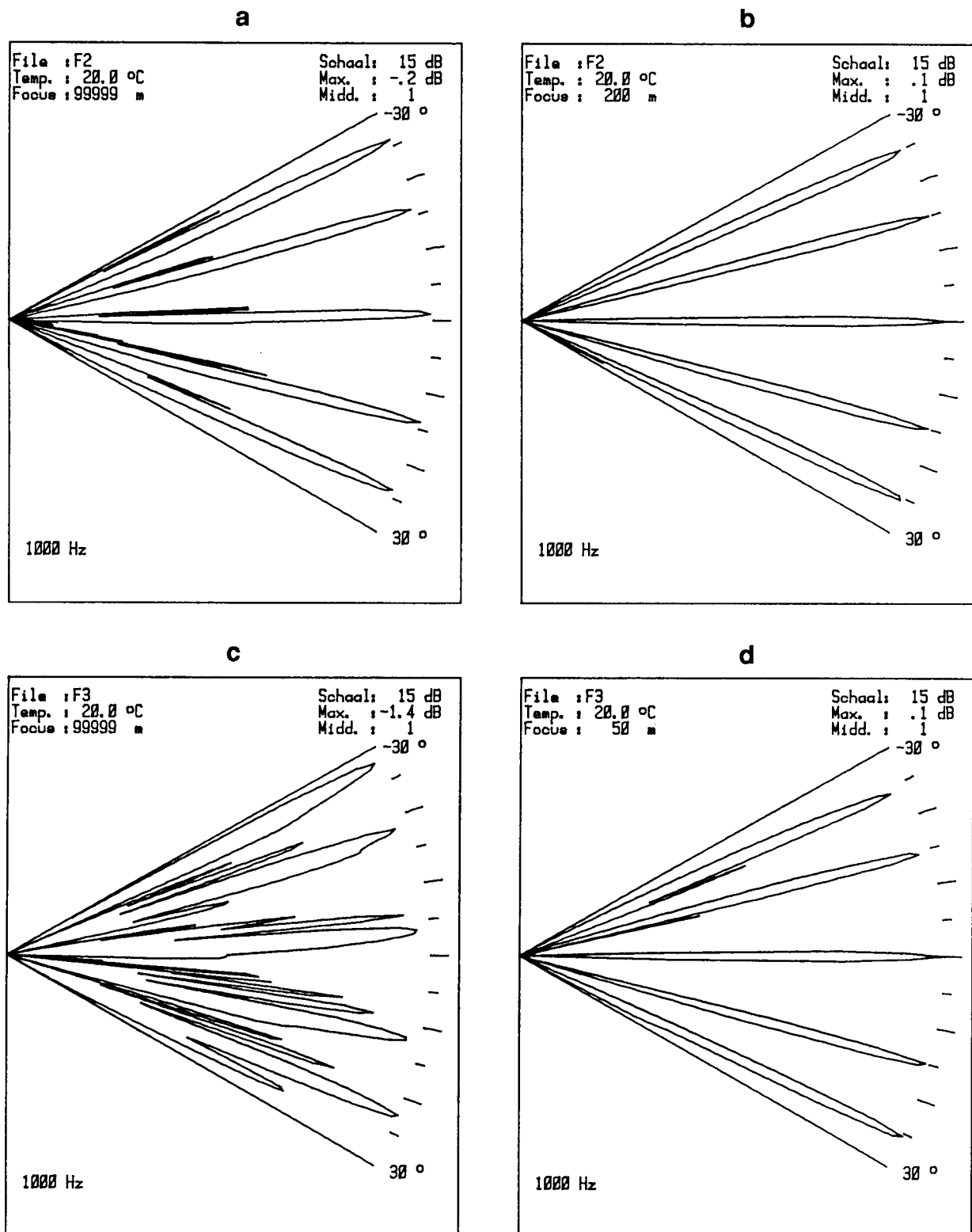
Figure 5.7: Polar diagrams of simulated monopoles at angles of incidence of −25°, −15°, 0°, 15° and 25°. a, b: source distances of 200 m, focussed at ∞ and 200 m, 0°; c, d: source distances of 50 m, focussed at ∞ and 50 m, 0°.
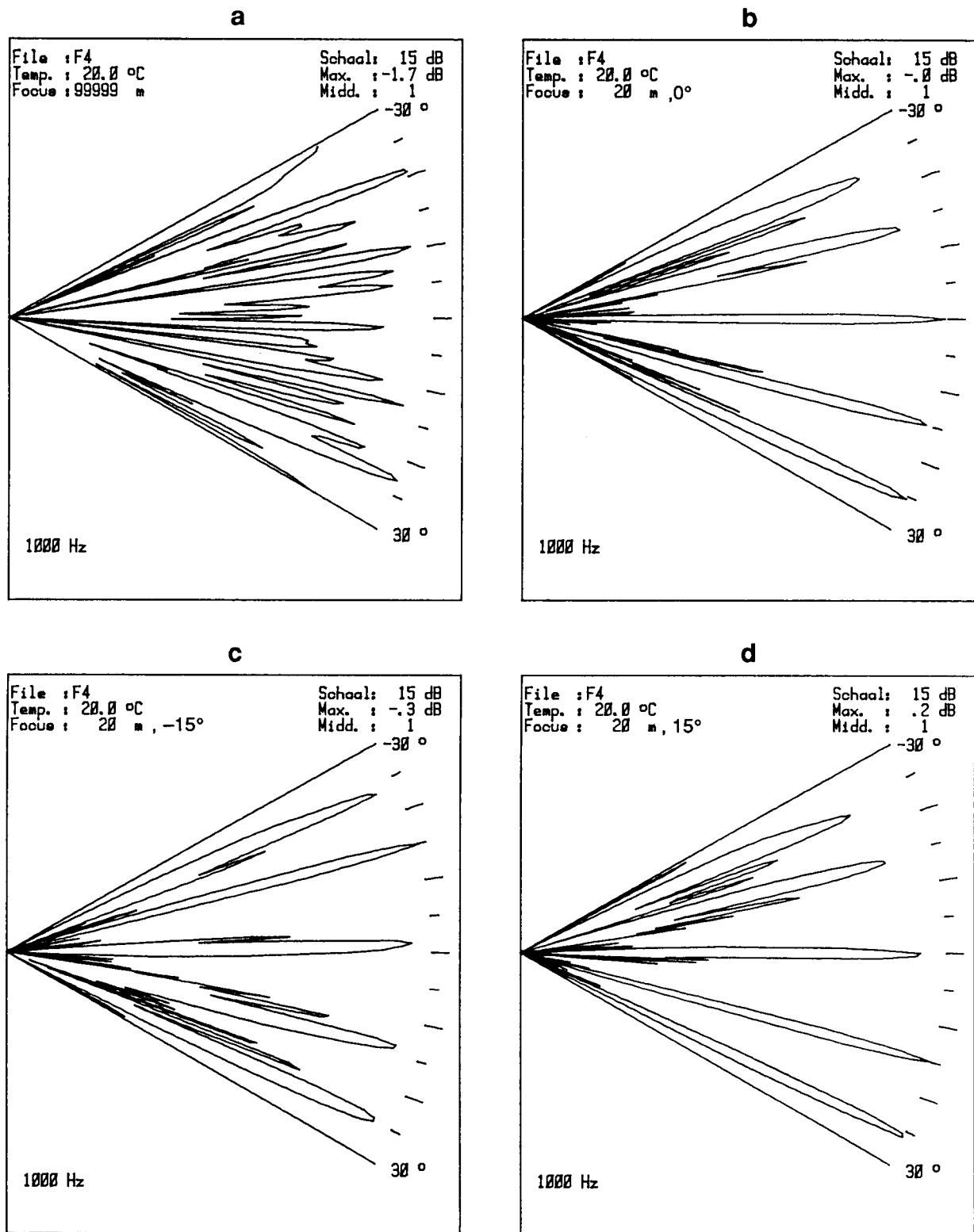
Figure 5.8: Polar diagrams of simulated monopoles at angles of incidence of −25°, −15°, 0°, 15° and 25° at distances of 20 m. a: focussed at ∞; b: focussed at 20 m, 0°; c: focussed at 20 m, −15°; d: focussed at 20 m, 15°.

We will now discuss the depth of field of the antenna. When the sources are not too close to the antenna, the Fresnel approximation is valid and the depth of field can be found from Eq. (2.166):

$$\left| \frac{\cos^2\alpha}{r_0} - \frac{1}{r_f} \right| < \frac{\lambda}{2X^2} \, , \tag{5.5}$$

where r_f is the focus distance and focussing takes place for frontal incidence. Notice that true focussing is obtained (also within the Fresnel approximation), when

$$r_0 = r_f \cos^2\alpha \ . \tag{5.6}$$

Using Eq. (5.5) and (5.6), the true focus point and the depth of field have been calculated for a focussing distance r_f of 250 m, with $\lambda = 0.33$ m (1029 Hz) and $X = 9.6$ m. The results for several angles of incidence are given in table 5.4.

Table 5.4

True focus distances and depths of field for different angles
of incidence with $r_f = 250$ m, $f = 1029$ Hz and $X = 9.6$ m.

α in °	true focus distance in m	depth of field (from – to) in m
0	250	172 – 455
± 15	233	161 – 425
± 25	205	142 – 374

To visualize the effect of unsharp images, simulations have been performed with sources at the positions given in table 5.5, corresponding with true focussing at ∞ and at 250 m and with the depth of field boundaries for focussing at 250 m (see table 5.4). The results are given in figure 5.9. The source directions have been chosen in such a way that, when the focussing is exact, as in figures 5.9a and b, the "double sources" are just resolved. In figures 5.9c and d, where the sources are placed at the depth of field boundaries, the resolution has clearly diminished, but the beam patterns are still acceptable. This indicates that Eq. (5.5) is a good measure for the depth of field in the Fresnel region.

Table 5.5

Source positions of the simulations in figure 5.9.

α in °	source distance in m			
	fig. 5.9a	fig. 5.9b	fig. 5.9c	fig. 5.9d
± 0.9	∞	250	172	455
± 14.07; ± 15.93	∞	233	161	425
± 24; ± 26	∞	205	142	374

a

b

File :F7   Schaal: 15 dB
Temp. : 20.0 °C   Max. : .2 dB
Focus :99999 m   Midd. : 1
                           -30 °

1000 Hz   30 °

File :F8   Schaal: 15 dB
Temp. : 20.0 °C   Max. : .2 dB
Focus : 250 m   Midd. : 1
                           -30 °

1000 Hz   30 °

c

d

File :F9   Schaal: 15 dB
Temp. : 20.0 °C   Max. : .3 dB
Focus : 250 m   Midd. : 1
                           -30 °

1000 Hz   30 °

File :F10   Schaal: 15 dB
Temp. : 20.0 °C   Max. : .3 dB
Focus : 250 m   Midd. : 1
                           -30 °

1000 Hz   30 °
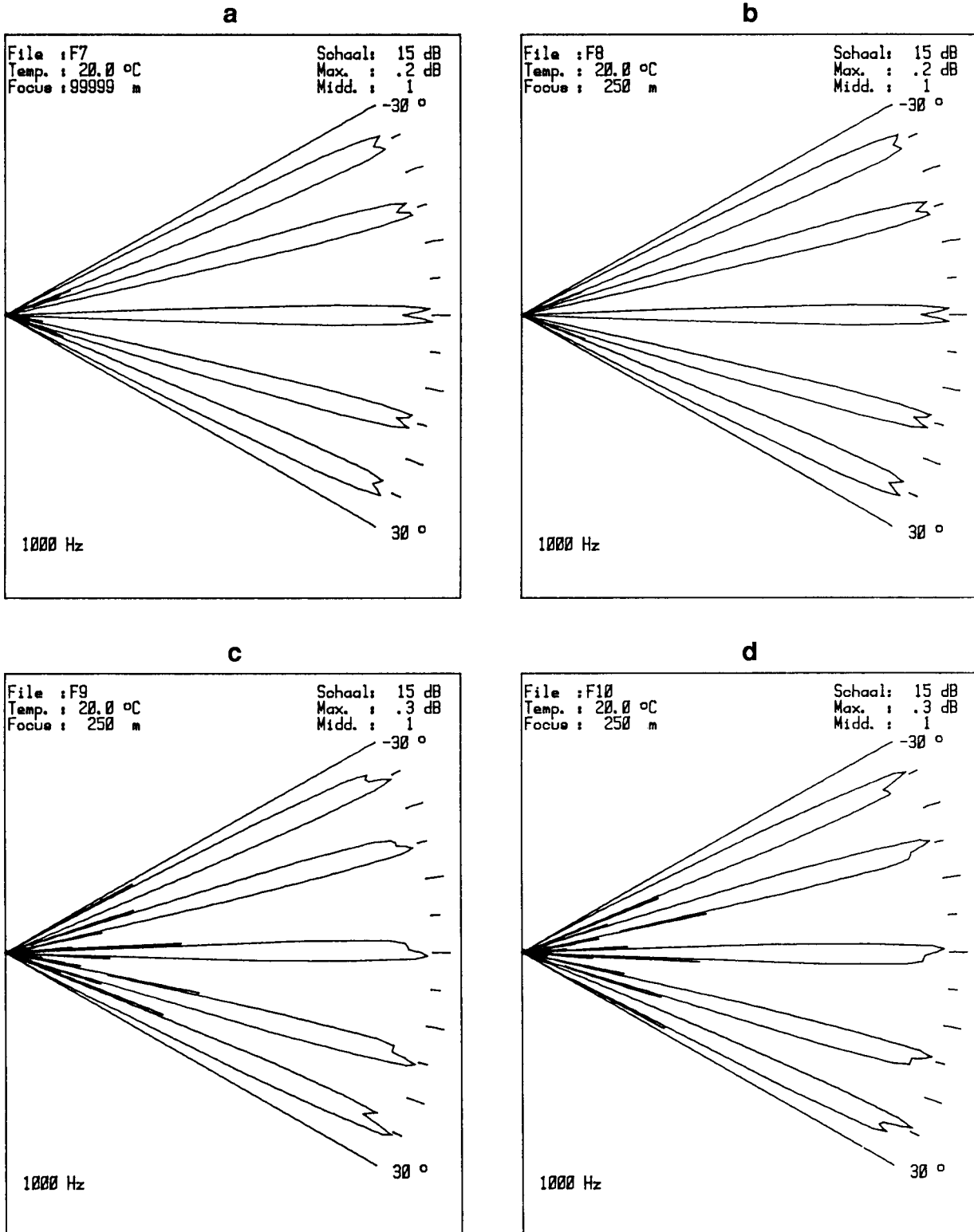
Figure 5.9: Polar diagrams of the monopoles given in table 5.5, showing correct focussing (fig. a and b) and focussing at the depth of field boundaries (fig. c and d).

From these simulations we can conclude that the Fraunhofer simulation for near field sources gives sharp images, even for small source distances.

The following focal regions can be distinguished:

a. $r_0 > 60X$: This is the Fraunhofer region where focussing at infinity gives sharp images;

b. $20X < r_0 < 60X$: The depth of field is large and focussing at frontal incidence gives sharp images for all source directions;

c. $5X < r_0 < 20X$: The depth of field decreases with the source distance. Focussing at frontal incidence usually is adequate, especially for positive angles of incidence. For negative angles of incidence it can be necessary to carry out a separate focussing for a few angular sections, to improve the resolution;

d. $r_0 < 5X$: Focussing is critical and must be performed separately for each source distance and direction, when the full angular resolution of the antenna is necessary.

5.2.4 Absolute calibration

As stated in § 4.4.5, the absolute calibration of the antenna is actually done as a plane wave simulation in an anechoic room, using only one microphone. Although this procedure is exact from a theoretical point of view, we checked this calibration in a more realistic situation, using a high power loudspeaker system fed with a pink noise source.

As a measurement site the airport of Rotterdam, Zestienhoven, was used. This location was selected because it gave the possibility of using high power acoustic sources without getting complaints from residents in the neighborhood. Besides, the airport could supply us with all necessary meteorological information. The activity at the airport was such that there was sufficient time between the take-offs and landings for carrying out our measurements. The only disadvantage of this measurement site was the rather high background noise level, caused by the traffic at a passing road nearby.

The measurements were done above the grassland of the airport, with the loudspeaker at a height of 1.75 m and the antenna at 1.25 m. The loudspeaker was placed at a distance of 50 m from the origin of the antenna in a direction of $\alpha = 0°$. At this distance the influence of meteorological factors like wind and temperature turbulence was small, and the signal to noise ratio was adequate, although limited due to the traffic noise.

The measurements were carried out around noon, it was a sunny day without clouds, the temperature was 26° and the wind velocity was 4 ± 1 m/s, measured at a height of 2 m, from a direction of 2° $\pm$ 12° (in antenna coordinates), so the situation was well within the meteorological window.

Table 5.6

Comparison between SYNTACAN and a conventional
measurement of the immission level due to a single source

1/3-octave midband freq. in Hz	SYNTACAN angular integr. level in dB(A)	omni-directional level in dB(A)	difference in dB	signal to noise ratio in dB
100	40.4	39.7	0.7	6
125	41.5	42.3	–0.8	11
160	43.2	43.2	0.0	7
200	42.9	43.0	–0.1	13
250	42.3	42.4	–0.1	12
315	40.6	41.2	–0.6	9
400	43.3	42.9	0.4	11
500	49.8	49.6	0.2	15
630	54.2	54.5	–0.3	14
800	60.0	60.7	–0.7	19
1000	61.8	62.3	–0.5	21
1250	64.7	66.3	–1.6	24

The results are given in table 5.6, showing the averaged results over 5 measurement cycles of SYNTACAN, and the results obtained from a conventional measurement with an omni-directional microphone, which was placed near the corresponding reference microphone of SYNTACAN for each octave band. The table also shows the signal to noise ratio, as obtained from a measurement of the background level with the omni-directional microphone. The omni-directional measurements were not corrected for the limited signal to noise ratio. The results show good agreement (within 1.6 dB) between the conventional measurements and the results obtained with SYNTACAN. It must be stated that at the time of measurement it was not possible to do the omni-directional measurements simultaneously with the SYNTACAN measurements, as this feature was added to the system at a later time. Hence, the differences between both methods may be partly the result of immission fluctuations as a function of time, especially at those frequencies where the signal to noise ratio was moderate.

5.3 CORRELATED SOUND SOURCES

Because SYNTACAN is based on a sparsed microphone array, it only functions correctly in case of uncorrelated noise sources. In this Section we will show what kind of effects can be observed in case of some well defined correlated noise sources. It turns out that the effects are most pronounced for monochromatic sound sources. This is shown from simulations as well as from test measurements with real sources.

5.3.1 Theoretical considerations

In case of far field correlated noise sources, the spatial cross-correlation function on the antenna axis is given by Eq. (2.103), which is recalled here:

$$R(x_0, \xi, \tau) = \sum_{n,m} R_{nm}(\tau - \xi/c_n + x_0[1/c_n - 1/c_m]) \quad . \tag{5.7}$$

$R(x_0, \xi, \tau)$ is the temporal cross-correlation between the signals at the microphone positions $x_0 - \xi$ and x_0. Fourier transformation of Eq. (5.7) from time to frequency gives:

$$\tilde{R}(x_0, \xi, f) = \sum_{n,m} \tilde{R}_{nm}(f) \exp(-j2\pi f \xi/c_n + j\phi) \tag{5.8}$$

with $\phi = 2\pi f x_0(1/c_n - 1/c_m)$. Note that with a non-sparsed antenna, x_0 can be made zero. In that case $\phi = 0$, so Eq.(2.107) and (2.108) are valid and the correct immission levels are measured in the correct directions.

If, however the antenna is sparsed, as with SYNTACAN, x_0 varies with ξ, leading to a phase factor ϕ which varies with ξ. It will be clear that this variable phase factor will influence the Fourier transform of Eq. (5.8) from the ξ- to the k_x-domain and that the ideal relationship as given by Eq. (2.108) will not hold. It follows from table 4.1 that the sparsing scheme of SYNTACAN leads to

$x_0 = (\ 0, \qquad 8, \qquad 16, \qquad 24, \qquad 32, \qquad 40, \qquad 48, \qquad 56) \ \Delta\xi$, for
$\xi = \ 0...7, \qquad 8...15, \qquad 16...23, \qquad 24...31, \qquad 32...39, \qquad 40...47, \qquad 48...55, \qquad 56...63$
respectively, which gives a phase factor

$$\phi = 2\pi f 8 i \Delta\xi (1/c_n - 1/c_m), \qquad\qquad i = 0 \ ... \ 7 \quad . \tag{5.9}$$

It will be clear that in those cases where $\phi = 0$ for all ξ-values, the antenna will behave "ideally". This is also true for those correlated sources for which $c_n \approx c_m$. In practice this occurs for sources which are observed within the angular beamwidth of the antenna. For correlated noise sources at larger angles that can be resolved separately, the factor ϕ can take all values, dependent on f, $\Delta\xi$, c_n and c_m. We will discuss some special cases of this "phase-interference" in the next paragraphs.

5.3.2 Two correlated monopole sources

Because the phase factor given by Eq. (5.9) is frequency dependent, the effects will be most pronounced in case of monochromatic sources. Notice that a worst case situation is found when $\pm 2 f 8 \Delta\xi (1/c_n - 1/c_m) = 1, 3, 5, ...$, because this will result in phase changes of $\pm\pi$. If however $\pm 2 f 8 \Delta\xi (1/c_n - 1/c_m) = 2, 4, 6, 8, ...$, the phase changes will be $\pm 2\pi$ and this will not influence the ideal performance.

The effects of these phase changes can be demonstrated with a simulation of 2 mono-chromatic noise sources, in the same way as in Section 5.2, but now using Eq. (5.8) in which we substitute $\tilde{R}_{11}(f) = \tilde{R}_{22}(f) = \tilde{R}_{12}(f) = \tilde{R}_{21}(f) = 1$ for the 1029 Hz ^{1}/12-octave band and zero for other frequencies. This means that the two monochromatic sources have equal amplitude and phase at the origin of the antenna axis. In the simulation we used $\Delta\xi = 0.15$ m, $c = 340$ m/s, $\alpha_1 = -3.0°$ and $\alpha_2 = +4.9°$, giving a worst case situation for the phase factor .

Figure 5.10a shows the polar diagram of this simulation. Due to the variation of the phase factor in the cross-terms, the main lobes have become wider and there are considerable side lobes. It must be realized that these side lobes will not be restricted to the displayed angular range from $-30°$ to $+30°$, but they will extend to all computed k_x'-values.
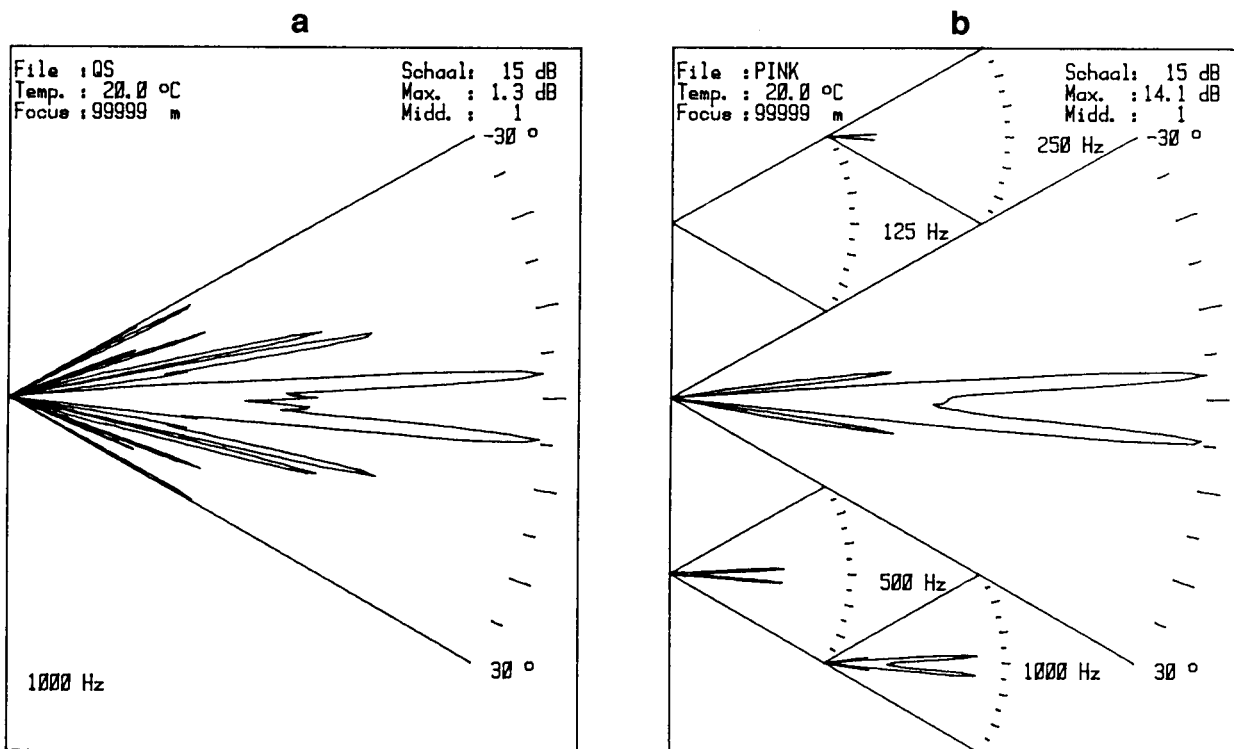
Figure 5.10: Polar diagrams of simulated correlated noise sources at −3.0° and +4.9°, representing a worst case situation concerning the interference side lobes. a: monochromatic sources of 1029 Hz; b: pink noise sources.

Table 5.7 gives the immission levels of this simulation, integrated over several angular ranges. The results show that the total immission level is correct, but that the main lobes are 1.5 dB too low.

If the noise sources have a wide spectrum, the situation changes drastically. Figure 5.10b shows the polar diagram for two correlated pink noise sources, also at −3° and +4.9°. Here most side lobes are cancelled because of the frequency-dependence of the effect. The angular integrated immission levels are presented in table 5.8. This table shows that the total immission levels are correct, but that the main lobe levels are also about 1.5 dB too low.

Table 5.7

Immission levels for the simulation of
figure 5.10a for several angular ranges.

angular range in °	immission level in dB(A)
–90 to +90	+6.1
–90 to –5	–6.4
–5 to –1	+1.6
–1 to +3	–1.8
+3 to +7	+1.6
+7 to +90	–6.2

Table 5.8

Immission levels in ¹/₃-octave bands for the simulation of figure 5.10b for
several angular ranges, compared with the ideal immission levels.

1/3-octave midband freq. in Hz	ideal response in dB(A)	integrated immission levels in dB(A) for several angular ranges						
		–90°/90°	–90°/–5°	–5°/–1°	–1°/3°	3°/7°	–5°/7°	7°/90°
100	–5.9	–5.9	–21.2	–10.3	–13.0	–10.0	–6.1	–21.7
125	–3.6	–3.6	–15.6	–8.0	–11.3	–8.2	–4.1	–16.0
160	–1.3	–1.3	–11.5	–5.9	–9.8	–6.2	–2.2	–11.7
200	0.9	0.9	–15.1	–3.5	–6.2	–3.2	0.7	–12.2
250	3.1	3.1	–8.9	–1.4	–4.6	–1.4	2.5	–8.1
315	5.1	5.2	–5.1	0.4	–3.3	0.3	4.2	–4.2
400	7.0	7.0	–9.0	2.6	–0.1	2.9	6.8	–4.5
500	8.7	8.7	–3.4	4.2	1.1	4.2	8.2	–0.6
630	10.1	10.1	–0.2	5.5	1.6	5.2	9.2	2.6
800	11.2	11.2	–4.8	6.5	4.1	7.3	11.0	–2.4
1000	12.0	12.0	–0.2	7.3	4.4	7.6	11.5	–0.3
1250	12.6	12.6	2.3	7.7	4.2	7.9	11.7	1.5
total	18.9	18.9	7.1	14.3	11.1	14.5	18.3	8.2

If however the area between the two main lobes from –1° to +3° is included in the integration, the errors reduce to about –0.6 dB. Note that this simulation represents a worst case situation for wide band sources, because the chosen angles of –3° and +4.9° give maximum phase shifts at the midband frequencies of each octave band.

The behavior of the antenna for correlated noise sources has been tested in practice by Van Overbeek et al. [39], with two loudspeakers fed by the same signal generator, and placed at a distance of 100 m from the microphone array on the grassland of a sports-field. It must be mentioned that in this experiment the loudspeakers were driven in opposite polarity. The measurements were carried out within the meteorological window. Figure 5.11a shows the polar diagram of one measurement cycle for two monochromatic sources of 125 Hz with source directions of 0° and 8°, representing a worst case situation for the phase interference.

a

```
File :M8B01                Schaal: 15 dB
Temp. : 17.3 °C            Max.  :61.2 dB
Focus : 100  m             Midd. :    1
                                      -30 °



125 Hz                                30 °
```

b

```
File :M8B                  Schaal: 15 dB
Temp. : 17.3 °C            Max.  :60.3 dB
Focus : 100  m             Midd. :   20
                                      -30 °



125 Hz                                30 °
```

c

```
File :M7B01                Schaal: 15 dB
Temp. : 17.3 °C            Max.  :62.9 dB
Focus : 100  m             Midd. :    1
                                      -30 °



1000 Hz                               30 °
```

d

```
File :M7B                  Schaal: 15 dB
Temp. : 17.3 °C            Max.  :64.0 dB
Focus : 100  m             Midd. :   20
                                      -30 °



1000 Hz                               30 °
```
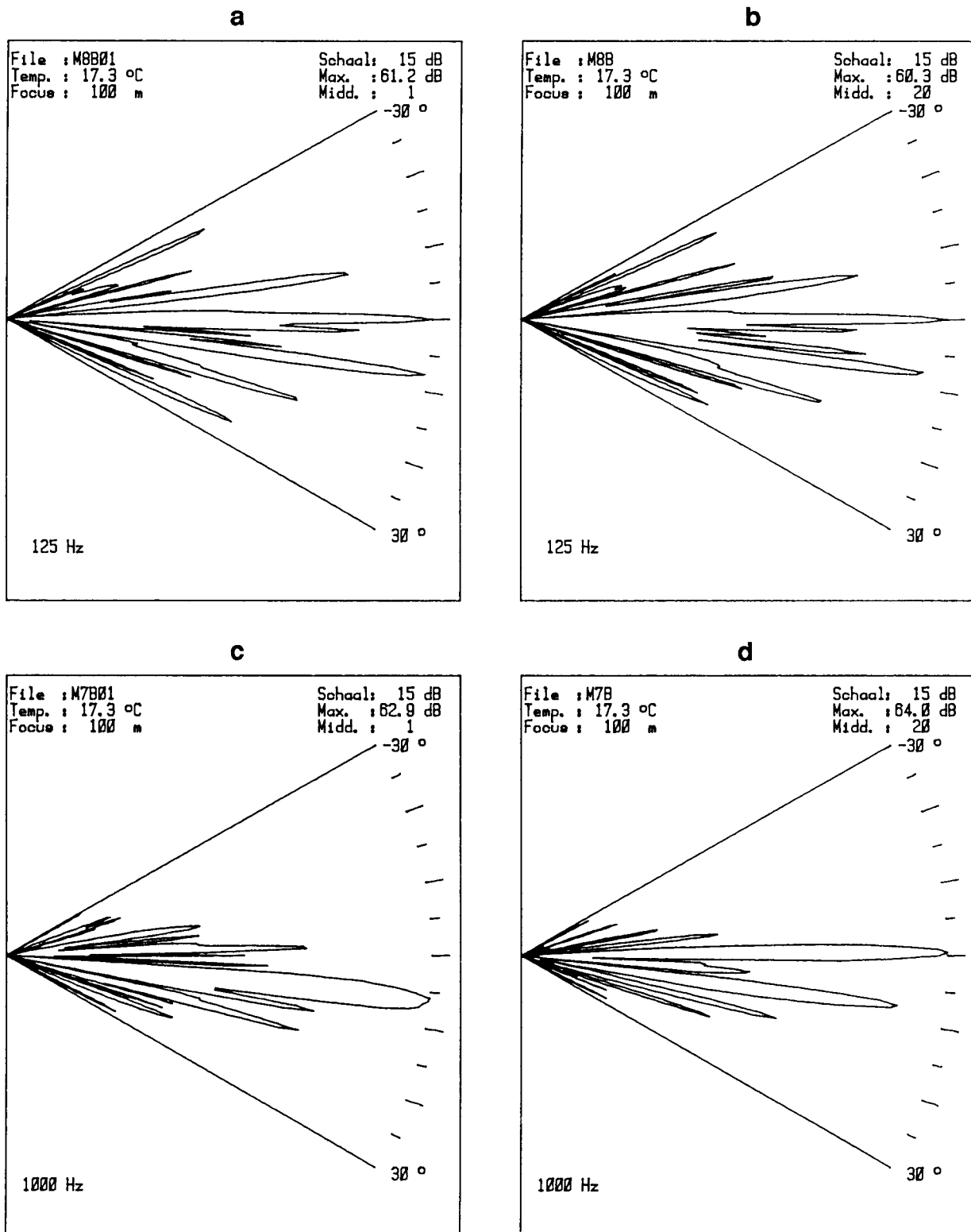
Figure 5.11: Polar diagrams of measured correlated monochromatic sources at a distance of 100 m and at angles of 0° and 8°. a: a single measurement at 125 Hz; b: averaged result of 20 measurements at 125 Hz; c: a single measurement at 1000 Hz; d: averaged result of 20 measurements at 1000 Hz.

This result shows a strong resemblance with figure 5.10a, although there are differences caused by the outdoor propagation and the precise phase relationship of the source signals at the antenna origin. Figure 5.11b gives the same results but now averaged over 20 measurement cycles. Notice the strong resemblance between figures 5.11a and b, indicating that the propagation was very stable. Figures 5.11c and d present the same results, also for a single measurement cycle and averaged over 20 cycles, but now for a pure tone of 1000 Hz. In this case a single measurement cycle shows strong deviations from the expected results, so the influence of turbulence is much stronger at higher frequencies than at lower frequencies. These effects cancel out with averaging, however,as shown in figure 5.11d.

The effect of wideband correlated noise sources was tested by feeding the loudspeakers with pink noise. It must be mentioned that this does not result in a pink immission spectrum because of the frequency characteristics of the loudspeaker systems and also due to propagation effects over the absorbing ground. Figure 5.12a shows the polar diagram of the average over 20 measurement cycles with the loudspeakers at 0° and 8°, giving a worst case phase interference. The results show interference side lobes of the same magnitude as in figure 5.10b. Figure 5.12b gives the same results but now for source angles of 0° and 16°. For these angles the antenna should act "ideally" at the midband frequencies. As can be seen, the side bands are much lower. Figure 5.12b also shows that almost no signal is measured in the 500 Hz octave band. This must be caused by destructive interference of the two loudspeaker signals at the reference microphone for this octave band.

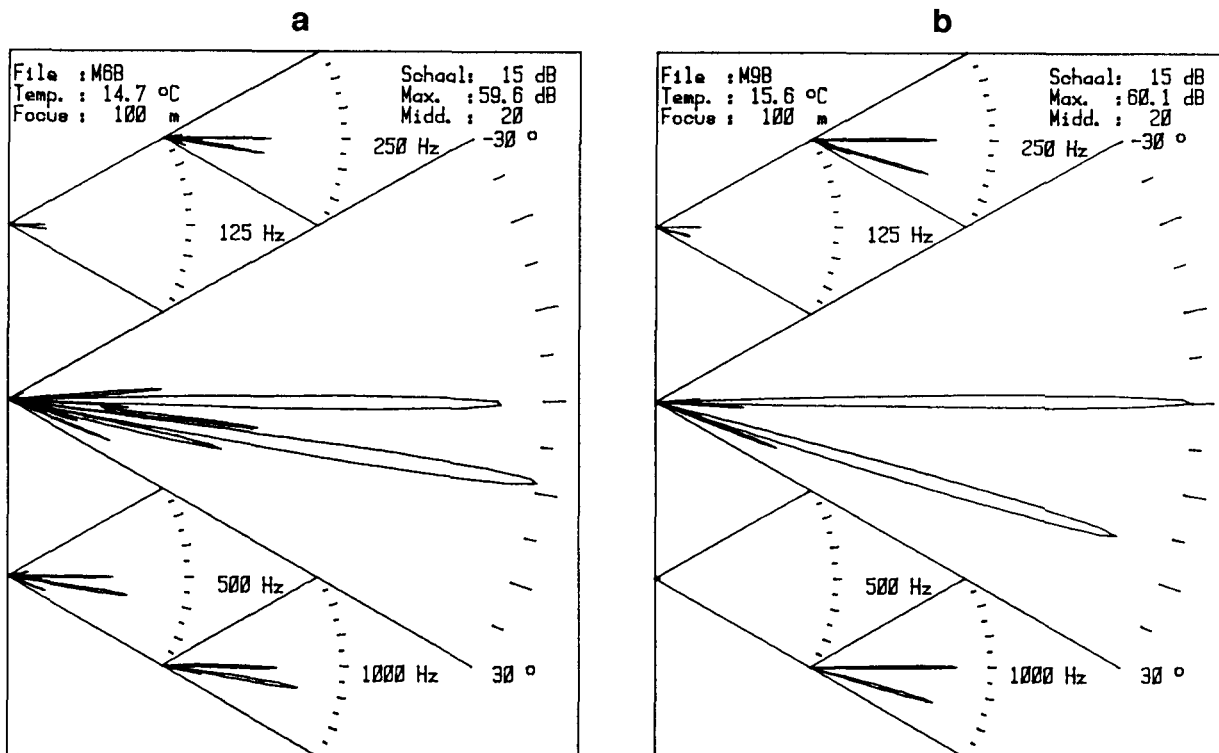a   b

Figure 5.12: Polar diagrams of measured correlated wideband sources at a distance of 100 m. a: worst case situation for source angles of 0° and 8°; b: best case situation for source angles of 0° and 16°.

5.3.3 Distributed sound sources

A special kind of correlation of sound sources can be expected in those circumstances where a large area radiates coherent sound. To some extent this might be the case with radiating ducts and vibrating plates.

It is interesting to see how SYNTACAN will respond to these conditions. The situation has been simulated by application of Eq. (5.8) for 11 sources at angles of 0, 1, 2, ..., 10°, all with equal amplitudes and phases at the origin of the antenna, so that all $R_{nm}(f)$ are equal. Figure 5.13a and b give the results of this simulation for a monochromatic (1029 Hz) and a wideband (pink) situation respectively. The results show that the angular spread of the sources leads to an effective cancellation of the side lobes. Hence, our antenna is well suited for measurement of distributed sound sources, even in case of coherent radiation.

a **b**

File : QS	Schaal: 15 dB
Temp. : 20.0 °C	Max. : 13.8 dB
Focus : 99999 m	Midd. : 1

-30 °

30 °

1000 Hz

File : PINK	Schaal: 15 dB
Temp. : 20.0 °C	Max. : 26.5 dB
Focus : 99999 m	Midd. : 1

250 Hz   -30 °

125 Hz

500 Hz

1000 Hz   30 °
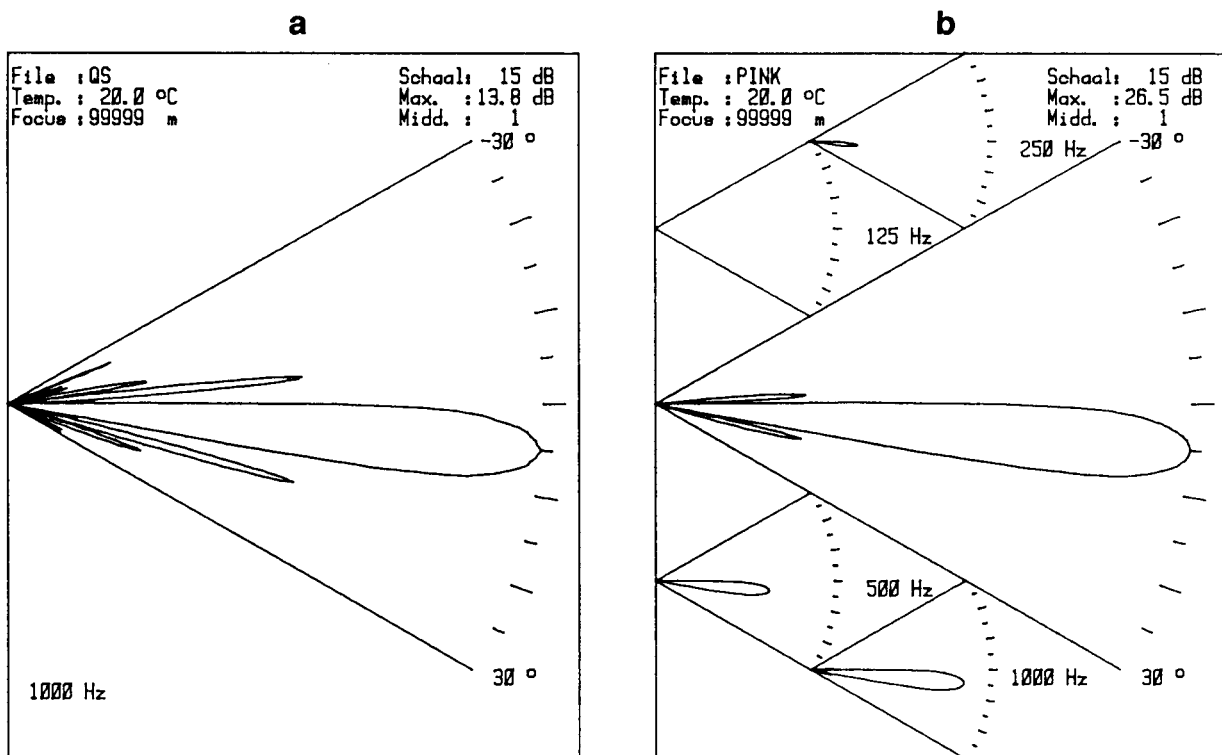
Figure 5.13: Polar diagram of simulations of correlated sound sources at angles of 0, 1, 2, ..., 10°, as an approximation of distributed and correlated sources. a: monochromatic at 1029 Hz; b: wideband with a pink spectrum.

5.3.4 Correlation of sources by reflection

The reflection of a soundfield by a screen or a wall of a building can lead to strongly correlated image sources. Because this situation can easily occur in practice, we conducted a test where we used two loudspeakers, fed by the same source signal and a reflecting screen of 2.5 m height and 10 m long.

The loudspeakers and the screen were placed at a distance of 95 m from the antenna in such a way that one loudspeaker was faced directly to the antenna, at an angle of incidence of 8° and

a

b

c

d
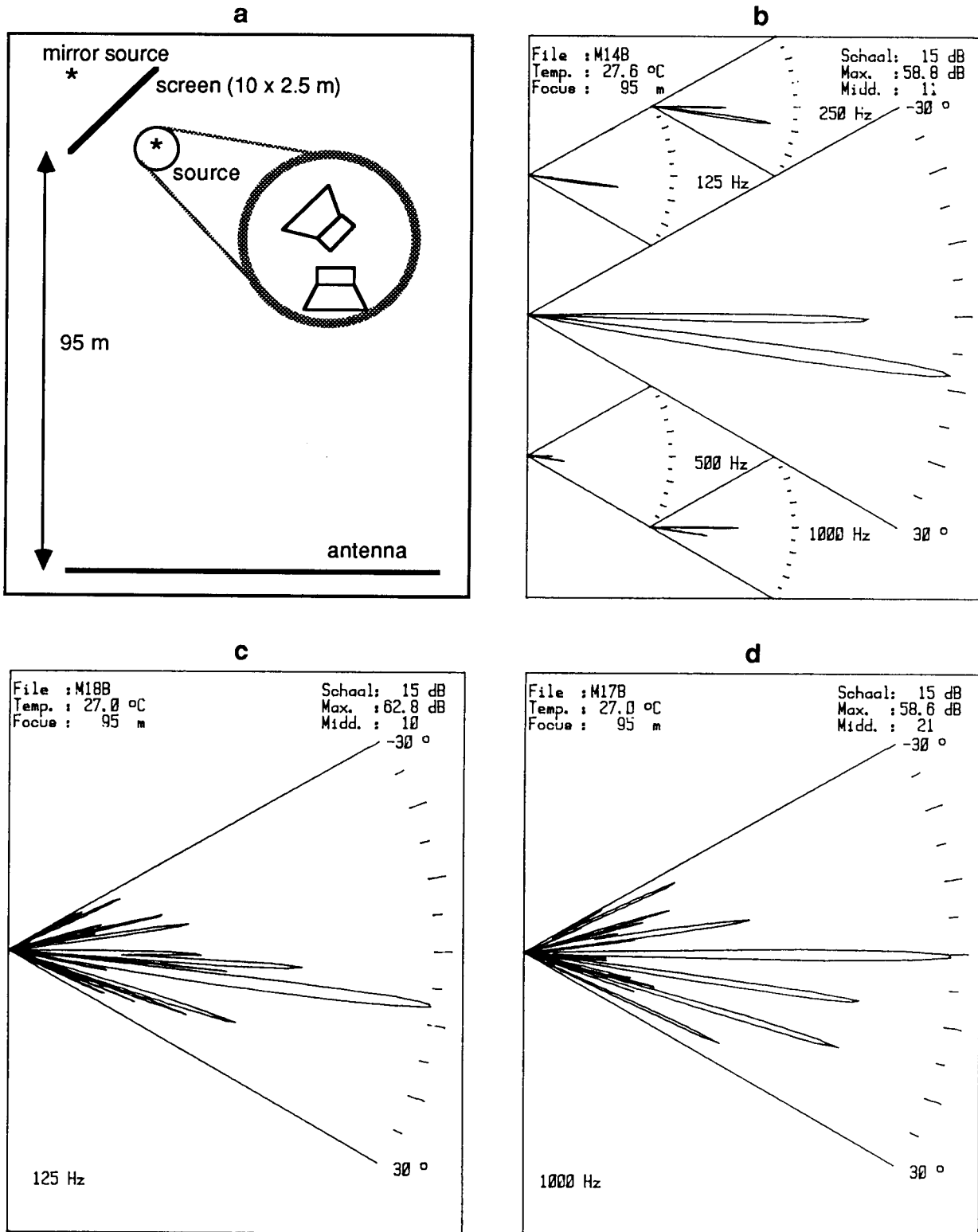
Figure 5.14 a: Geometry used for the measurement of correlated sound by a reflecting screen; b: polar diagram of a measurement with pink noise excitation; c: pure tone excitation of 125 Hz; d: pure tone excitation of 1000 Hz.

the other loudspeaker was faced to the reflecting screen, giving a mirror-source at 0° (see figure 5.14a). This geometry presents a worst case situation for interference side lobes. Figure 5.14b shows the polar diagram when the loudspeakers are fed with wideband pink noise for an average of 11 measurements. At low frequencies the image source is weak, due to the finite dimensions of the screen. At high frequencies the opposite appears. This is caused by a small inclination of the screen, giving a raising of the image source height and therefore less ground absorption in this frequency region. In figures 5.14c and d the results are presented for pure tones of 125 Hz and 1 kHz. The high side lobes indicate that the source and the image source are strongly correlated.

In conclusion it can be stated that reflections will lead to correlated image sources giving symptoms which are comparable to those of two correlated sources. If the noise sources radiate over a wide frequency range, the side lobes will be negligible, but in case of narrow band radiation, high side lobes can occur. The immission level of the image source will strongly depend on the size and orientation of the reflector.

5.4 PROPAGATION EFFECTS

In this Section we will discuss some measurements for testing propagation effects. We will first present some simulation results of the antenna behavior in a stationary and uniform wind. Subsequently, we will discuss the transverse coherence loss which has a major influence on antenna performance. Another point of concern is inhomogeneity in the transmission path, and we will finally deal with the fluctuations in sound transmission due to meteorological factors.

5.4.1 Stationary and uniform wind

The theory of sound propagation in a moving medium was given in Section 2.4. It was found in § 3.2.3 that a stationary and uniform wind v_0 will lead to an angular error ϕ in measurements by the antenna, which is given by Eq. (3.27) for small Mach-numbers ($v_0 \ll c_0$). Because we use a right turning angle system here, the minus sign is dropped, giving

$$\phi = m_x / \cos \alpha \qquad (5.10)$$

where $m_x = v_{0x} / c_0$ is the Mach-vector component in the x-direction (antenna axis) and α is the source direction. Eq. (5.10) is valid for both plane and spherical waves. This relation has been tested in a simulation in which the cross-spectra along the antenna axis have been computed for monopoles in a uniformly and stationary moving medium. In § 2.4.5 we found that under these conditions the sound pressure of a monopole is given by Eq. (2.72) and (2.73). If we restrict ourselves to source and antenna positions in the x-y plane and to horizontal wind velocities, we obtain:

a

```
File  : WA0              Schaal:  15 dB
Temp. : 20.0 °C          Max.  :  .1 dB
Focus : 1000  m          Midd. :   1
                                    -30 °
```

$v_{0x} = 0$

$v_{0y} = 0$

```
1000 Hz                             30 °
```

b

```
File  : WA10             Schaal:  15 dB
Temp. : 20.0 °C          Max.  :  .1 dB
Focus : 1000  m          Midd. :   1
                                    -30 °
```

$v_{0x} = 0$

$v_{0y} = -10$ m/s

```
1000 Hz                             30 °
```

c

```
File  : WA50             Schaal:  15 dB
Temp. : 20.0 °C          Max.  :  .1 dB
Focus : 1000  m          Midd. :   1
                                    -30 °
```

$v_{0x} = 0$

$v_{0y} = -50$ m/s

```
1000 Hz                             30 °
```

d

```
File  : WA100            Schaal:  15 dB
Temp. : 20.0 °C          Max.  :  .1 dB
Focus : 1000  m          Midd. :   1
                                    -30 °
```

$v_{0x} = 0$

$v_{0y} = -100$ m/s

```
1000 Hz                             30 °
```
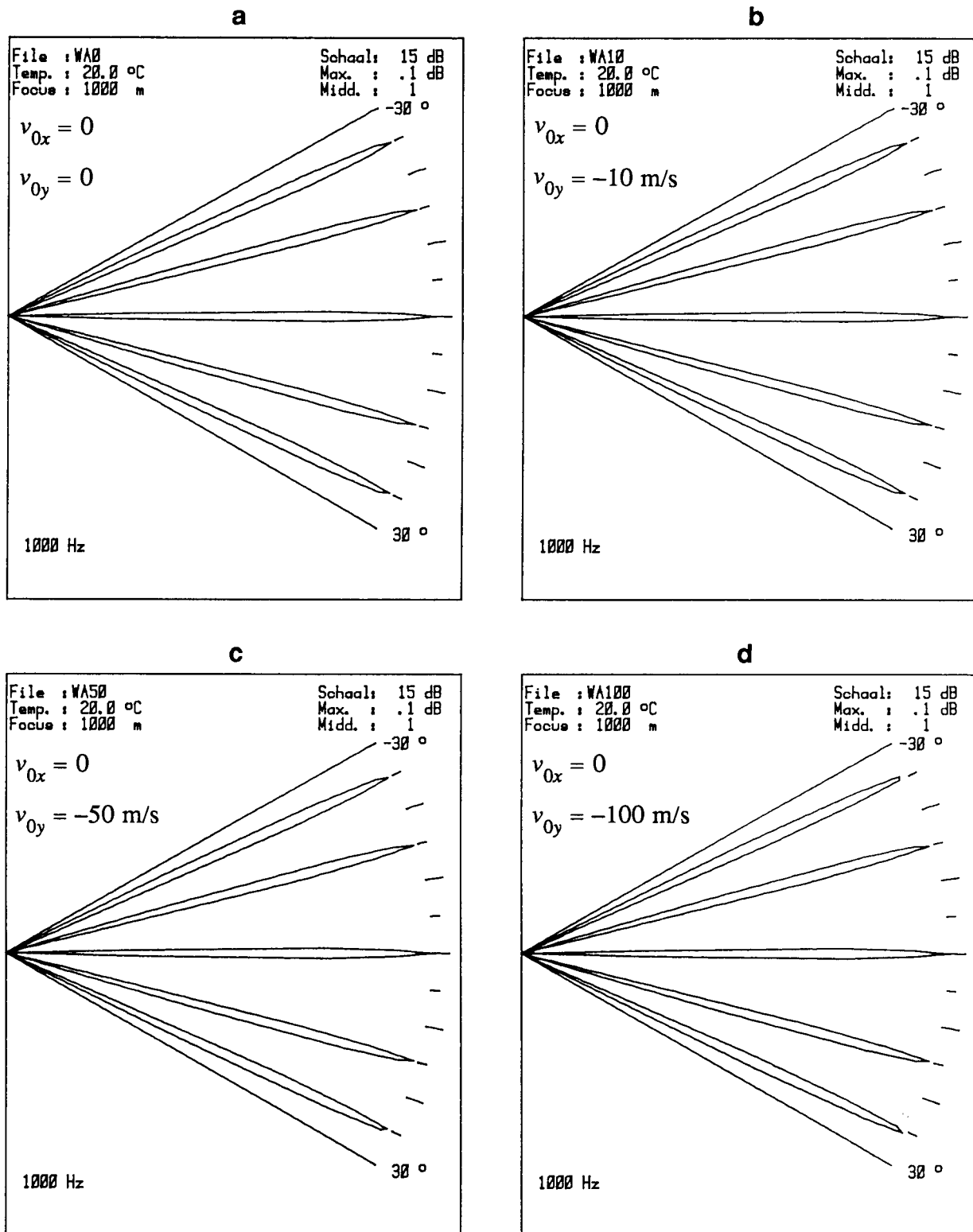
Figure 5.15: Polar diagrams of simulated monopoles at angles of incidence of $-25°$, $-15°$, $0°$, $15°$ and $25°$ at a distance of 1000 m for different windspeeds in the negative y-direction ($\gamma = 0$).

$$p(x, y, t) = s(t - \tau) / r \tag{5.11a}$$

with

$$\tau = r / c_0 \tag{5.11b}$$

and

$$r(x, y, t) = [(x - x_s - v_{0x}t)^2 + (y - y_s - v_{0y}t)^2]^{1/2} . \tag{5.11c}$$

The cross-spectra can now be computed in the same way as discussed in § 5.2.3, using Eq. (5.3):

$$\tilde{R}(\xi, f) = \tilde{R}(f) \exp(j2\pi f\tau_1) \frac{r(0)}{r(x_1)} \exp(-j2\pi f\tau_2) \frac{r(0)}{r(x_2)} \tag{5.12}$$

where the distances $r(0)$, $r(x_1)$, $r(x_2)$ and the traveltimes τ_1, τ_2 are computed according to Eq. (5.11).

To test Eq. (5.10), we have performed simulations with different wind directions and velocities. We will first present the results of simulations where the wind direction angle $\gamma = 0$ (see figure 2.4), so v_0 is in the negative y-direction. In figure 5.15 polar diagrams are given for 5 sources at a distance of 1000 m and with angles of incidence of $-25°$, $-15°$, $0°$, $15°$ and $25°$. The windspeed for the figures a, b, c and d is 0, 10, 50 and 100 m/s respectively. Notice that in practice the windspeed during measurements will never be higher than about 5 m/s. The results show that the windspeed in the y-direction does not have any influence at all on the measured source directions. This is in accordance with Eq. (5.10).

In figure 5.16 the results are presented for the same simulations but now with the windspeed in the positive x-direction ($\gamma = -90°$). As expected from Eq. (5.10), the cross-wind gives considerable angular errors. In table 5.9 a comparison has been made between the source directions $\alpha + \phi$, as expected from Eq. (5.10) (approximation for small Mach-numbers) and the exact simulation results of figure 5.16.

Table 5.9

Comparison of source directions, measured by the antenna for different cross-wind speeds, according to the theory for small Mach-numbers (Eq. 5.10) and exact simulations.

source direction α in °	windspeed					
	10 m/s		50 m/s		100 m/s	
	Eq. (5.10)	sim.	Eq. (5.10)	sim.	Eq. (5.10)	sim.
−25	−23.2	−23	−15.8	−16	−6.5	−9
−15	−13.3	−13	−6.3	−6.5	2.3	1.5
0	1.7	2	8.4	8.5	16.8	19
15	16.7	17	23.7	24.5	32.3	−
25	26.8	27	34.2	−	43.5	−

a

```
File  : WB0                    Schaal:  15 dB
Temp. : 20.0 °C                Max.  :  .1 dB
Focus : 1000  m                Midd. :   1
                                        -30 °
```

$v_{0x} = 0$

$v_{0y} = 0$

```
1000 Hz                                 30 °
```

b

```
File  : WB10                   Schaal:  15 dB
Temp. : 20.0 °C                Max.  :  .0 dB
Focus : 1000  m                Midd. :   1
                                        -30 °
```

$v_{0x} = 10$ m/s

$v_{0y} = 0$

```
1000 Hz                                 30 °
```

c

```
File  : WB50                   Schaal:  15 dB
Temp. : 20.0 °C                Max.  : -.0 dB
Focus : 1000  m                Midd. :   1
                                        -30 °
```

$v_{0x} = 50$ m/s

$v_{0y} = 0$

```
1000 Hz                                 30 °
```

d

```
File  : WB100                  Schaal:  15 dB
Temp. : 20.0 °C                Max.  : -.0 dB
Focus : 1000  m                Midd. :   1
                                        -30 °
```

$v_{0x} = 100$ m/s

$v_{0y} = 0$

```
1000 Hz                                 30 °
```
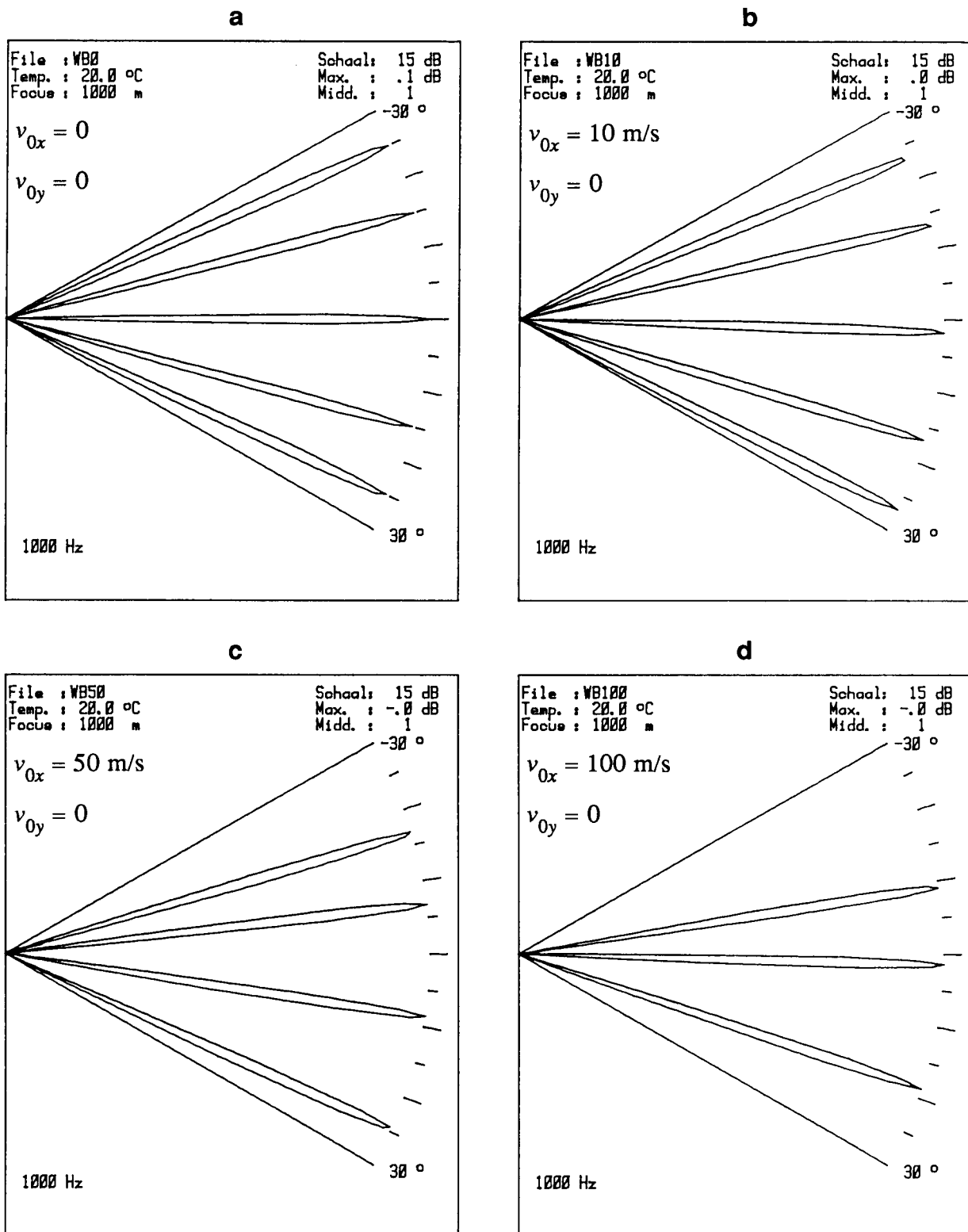
Figure 5.16: Polar diagrams of simulated monopoles at angles of incidence of −25°, −15°, 0°, 15° and 25° at a distance of 1000 m for different windspeeds in the positive x-direction ($\gamma = -90°$).

The results show a perfect agreement for small Mach-numbers; even at high windspeeds the deviations are small. Notice from Eq. (5.10) that the angular error is only weakly dependent on the angle of incidence for source angles $|\alpha| < 30°$, so in first order approximation, the angular error can be compensated for with a rotation of the coordinate system over m_x radians. If $v_{0x} < 10$ m/s, which is the case in all practical situations, this approximation is well within the antenna resolution, as clearly shown by comparison of figure 5.16a and b.

In summary it can be concluded that when the measurements take place in a downwind situation, the antenna measures the correct angles of incidence of the noise sources. In situations with a cross-wind component, small angular errors occur ($\phi \approx 1°$ if $v_{0x} = 5$ m/s). These angular errors are almost independent of the source direction and can be compensated for with a simple rotation of the coordinate system of the antenna.

5.4.2 Transverse coherence loss

The transverse coherence loss is a measure of the decorrelation of the wave field over the antenna aperture caused by random fluctuations of wind and temperature. We discussed the transverse coherence loss γ in Section 3.3. It was found that it can be described for practical situations by Eq. (3.38):

$$\gamma(\xi, f) = \exp(-\beta f |\xi|) \tag{5.13}$$

with β being a parameter which depends on source and receiver positions, and on meteorological conditions. In practical situations, when the measurements take place within the meteorological window, β ranges from 1×10^{-5} s/m for sources at a distance of 100 to 200 m, to 5×10^{-3} s/m for sources at a distance of 2000 m. The effect of the transverse coherence loss can easily be simulated by multiplication of the undisturbed cross-spectra with the factor given by Eq. (5.13). Figure 5.17a shows simulations of a pink monopole source at $0°$ incidence with $\beta = 0$, 1×10^{-4} and 5×10^{-4} s/m. As expected theoretically, the transverse coherence loss causes a lowering of the peak level and a broadening of the mainlobe. The total immission level does not change however (see Eq. (3.37)). The broadening of the mainlobe results in a reduced angular resolution. This is shown in figure 5.17b, which gives the results of two uncorrelated pink noise sources at $0°$ and $3°$, simulated with $\beta = 5 \times 10^{-4}$ s/m. The sources are just resolved and this is in agreement with Eq. (3.41). From this equation, an angular resolution of $3.1°$ is found for $\beta = 5 \times 10^{-4}$ s/m and frontal incidence.
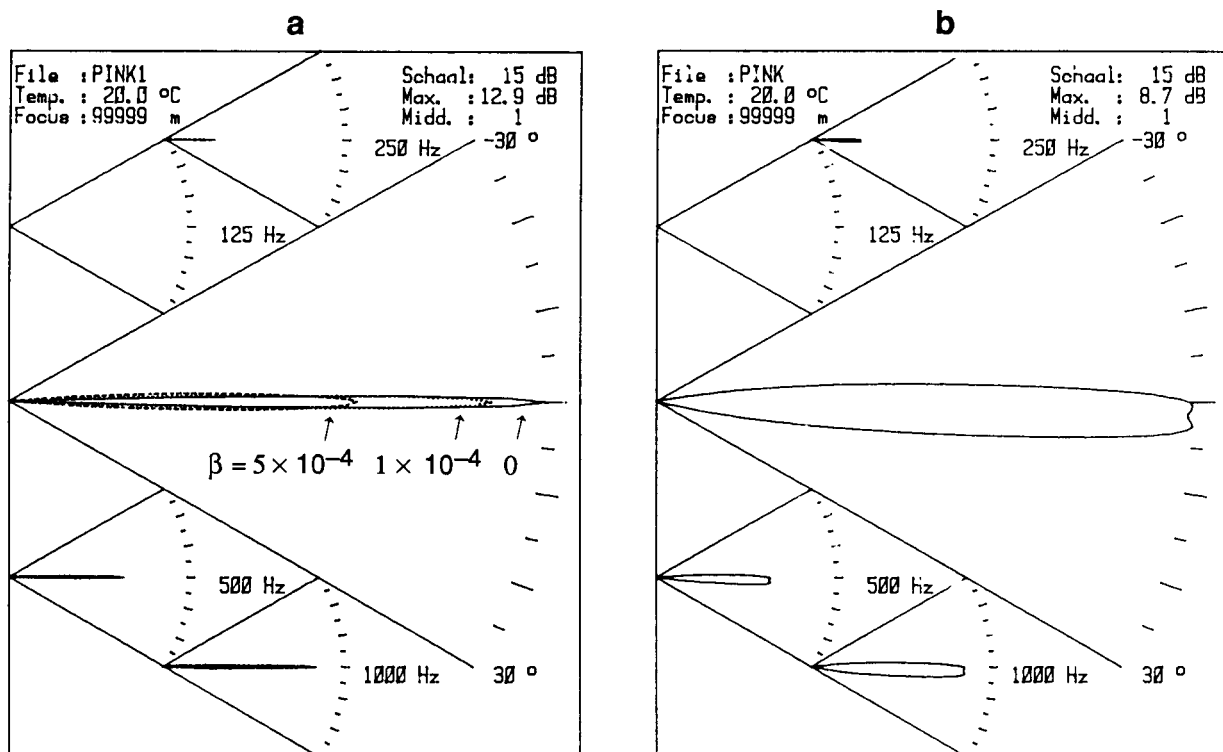
a

```
File  :PINK1                    Schaal:   15 dB
Temp. :  20.0 °C                Max.  : 12.9 dB
Focus :99999  m                 Midd. :    1
                               250 Hz    -30 °

         125 Hz

                    ↑        ↑    ↑
         β = 5 × 10⁻⁴  1 × 10⁻⁴   0

         500 Hz

              1000 Hz    30 °
```

b

```
File  :PINK                     Schaal:   15 dB
Temp. :  20.0 °C                Max.  :  8.7 dB
Focus :99999  m                 Midd. :    1
                               250 Hz    -30 °

         125 Hz

         500 Hz

              1000 Hz    30 °
```

Figure 5.17 a: simulation of a pink noise source with several coherence losses; b: two uncorrelated pink noise sources at angles of 0° and 3°, simulated with a coherence loss of β = 5 × 10⁻⁴.
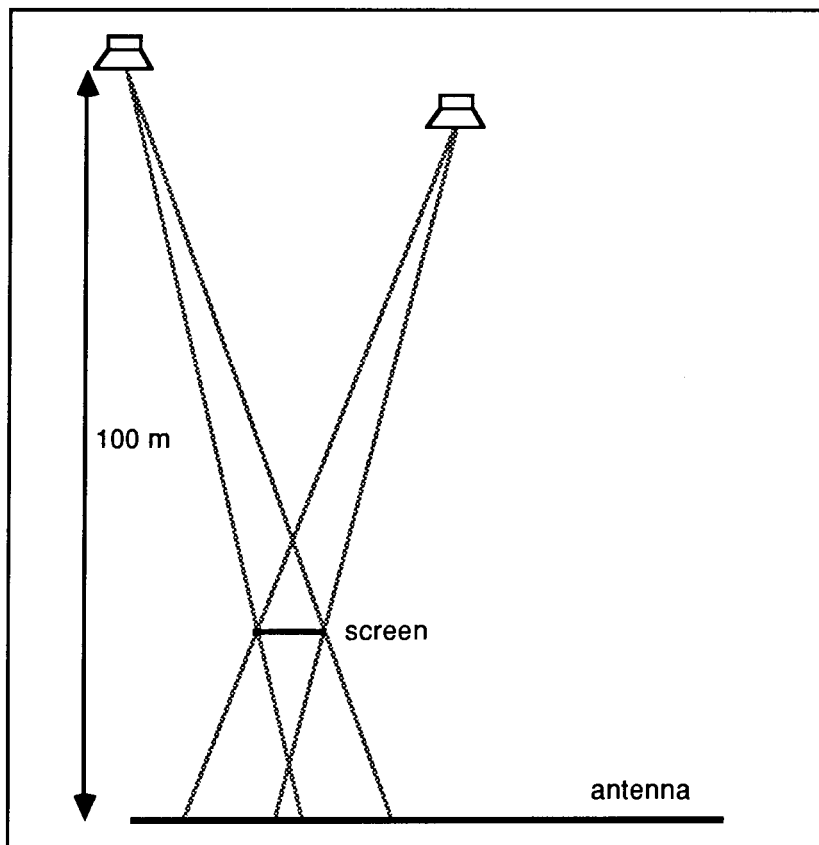
Figure 5.18: Experimental set-up to investigate the influence of partial screening on the antenna performance.

5.4.3 Inhomogeneities in the transmission path

In many practical situations it will be difficult or even impossible to install the antenna in such a way that the sound propagation of each source is uniform for all microphones. If, for instance, the antenna is placed partly over asphalt and partly over grassland, the transmission to one part of the antenna will differ from the transmission to the other part. An even more severe inhomogeneity will occur when a part of the antenna is screened by obstacles. As has been stated in § 3.2.2, this inhomogeneity will give rise to a deterioration of the resolving power of the antenna.
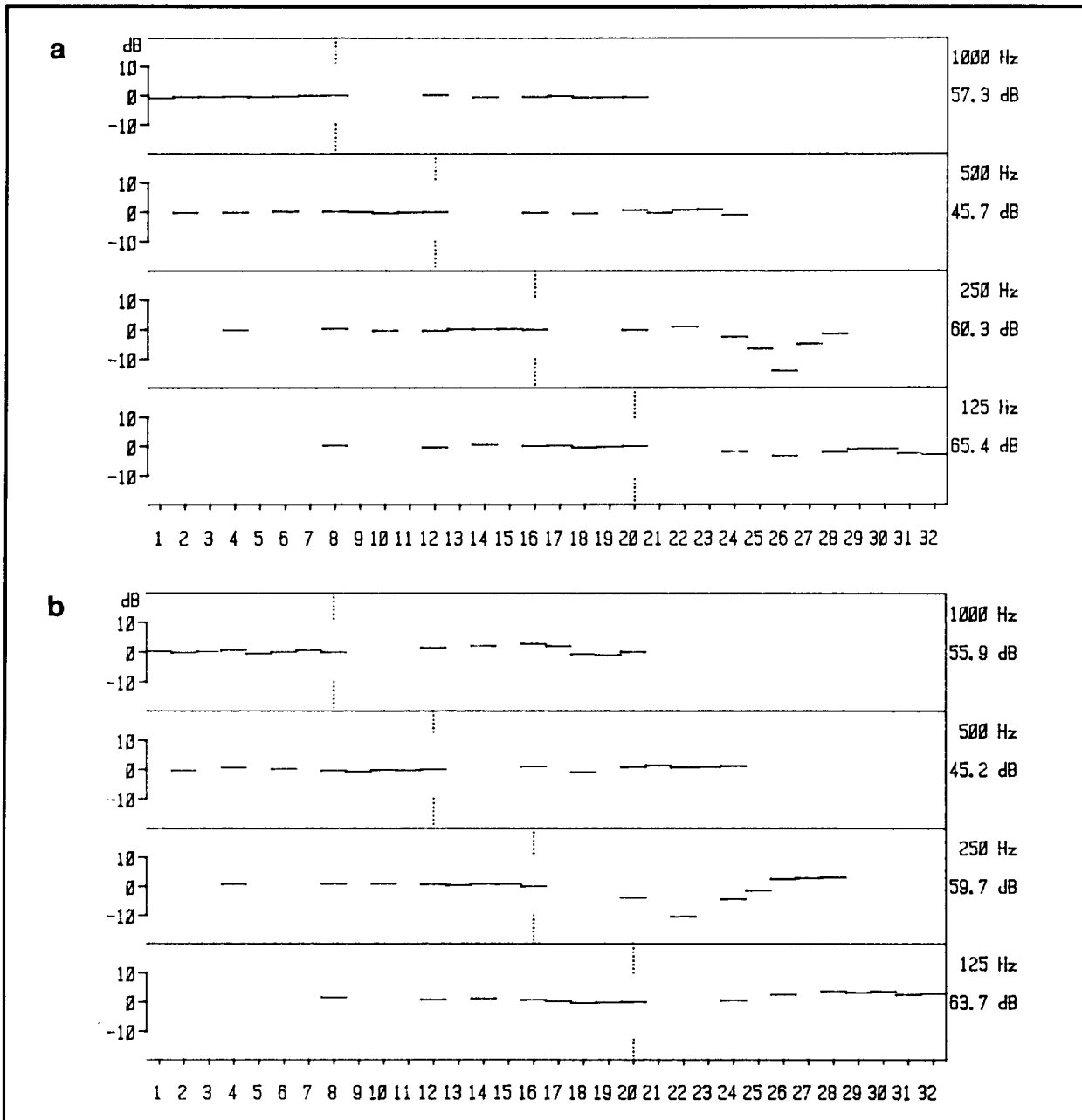

Figure 5.19: The $^1/_1$-octave immission levels, measured by the antenna microphones in the screening experiment of figure 5.18. a: source at $-1°$; b: source at $25°$.

We investigated the influence of such obstacles with a test experiment where we used the 10 m long and 2.5 m high screen, also used in the reflection experiment of § 5.3.4. The screen was placed at a distance of 25 m from the antenna, and a loudspeaker was placed at a distance of 100 m in a direction of –1° and +25° resp. (see fig. 5.18). The loudspeaker was fed with pink noise. Due to the screen, some of the antenna microphones were clearly in a shadow zone: microphones nr. 25–27 for the source at –1° and microphones nr. 19–24 for the source at 25°. The effects are shown in figure 5.19, the diagrams show the $^1/_1$-octave band immission levels for each microphone. Note that without screening or other disturbances all curves should be flat, indicating a homogeneous sound field over all octave bands (see also § 4.4.3). The polar diagrams of these measurements are shown in figure 5.20. Figure 5.20a presents the results for the loudspeaker at –1°. The results do not indicate any deviation from the ideal situation. Only if we take a close look at the 250 Hz band (fig. 5.20b), some small side lobes can be observed. For the source at 25°, the situation is not so perfect (figure 5.20c and d). Obviously, there a more important part of the antenna was screened. In conclusion it can be stated that the antenna will only function ideally in a homogeneous field. If obstacles disturb the sound propagation it is still possible to get valuable results, but such results should be interpreted with great care!

5.4.4 Fluctuations of the sound transmission due to meteorological factors

At larger source distances, the immission levels of stationary sound sources will fluctuate due to instabilities in the propagation paths. The variations are mainly caused by wind and temperature changes, leading to changes in the direct soundpath and the ground reflections. Usually, the measurement procedures are chosen in such a way that these fluctuations will average out statistically. For instance the "Guide for measuring and calculating industrial noise" of the Dutch Government [2], prescribes that the equivalent sound pressure level (L_{eq}) has to be computed over such a long time that the results converge to a fixed value within ± 1 dB(A). For continuous sound sources this criterion is usually met by a measurement period of 3 to 5 minutes.

Because SYNTACAN measures over short periods of time (0.4 to 3.2 seconds, see § 4.4.3), it will usually be necessary to average over a number of measurements. Notice that because of the processing time of the antenna signals (40 seconds per octave band), the measurements are spread over a considerable amount of time. For instance the measurement of 20 cycles of all 4 octave bands takes about 1 hour, assuming that the measurements need not to be interrupted for traffic noise, weather conditions etc.

There are indications that a one hour averaging period is optimal, taking into account the fluctuations in sound transmission. As already discussed in Chapter 3, the windspeed gradient has a major effect on the sound propagation over larger distances, so variations in windspeed
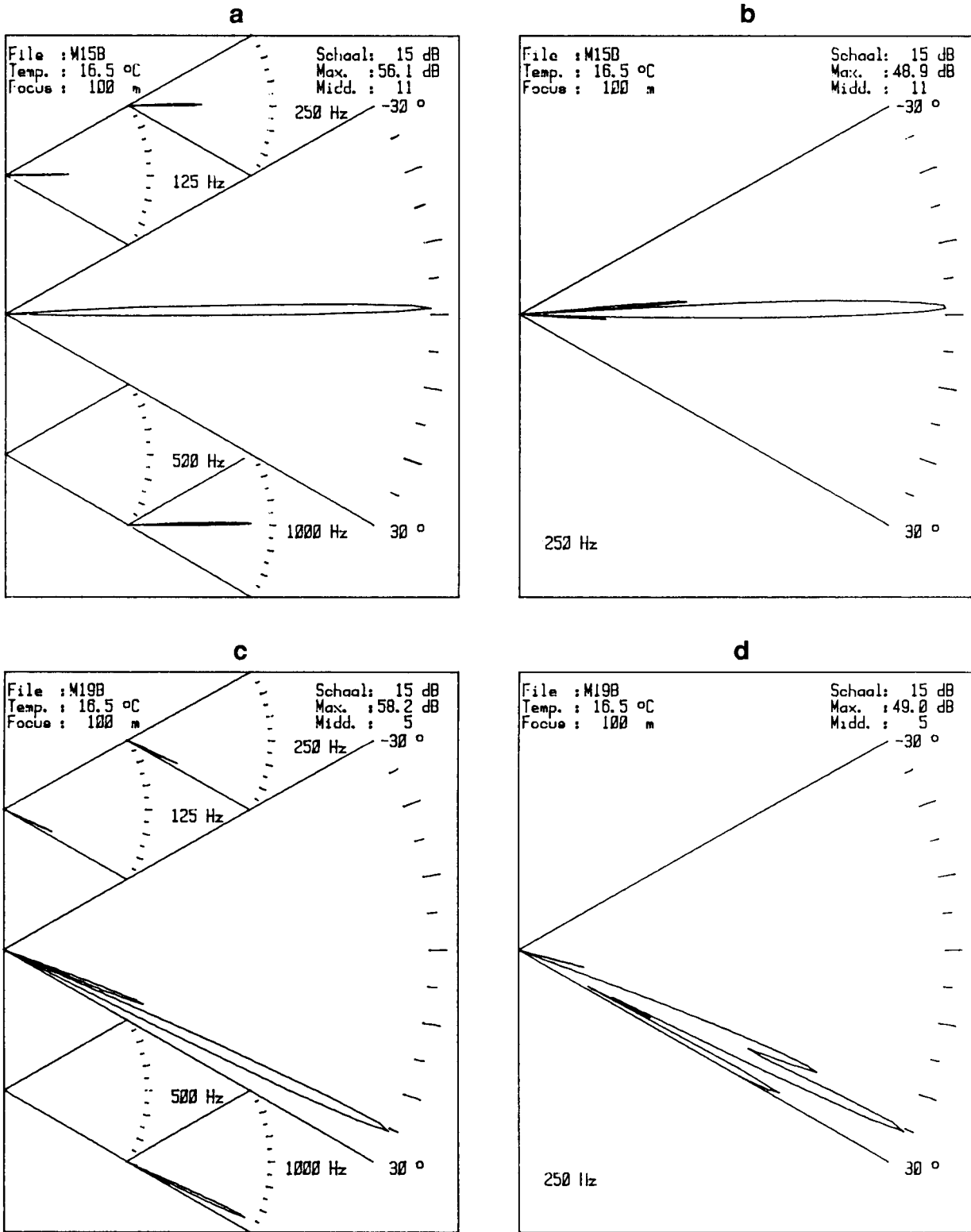
a

```
File  :M15B                    Schaal:  15 dB
Temp. : 16.5 °C                Max.  :56.1 dB
Focus : 100  m                 Midd. :  11
                          250 Hz    -30 °

             125 Hz

             500 Hz

             1000 Hz   30 °
```

b

```
File :M15B                     Schaal:  15 dB
Temp. : 16.5 °C                Max.  :48.9 dB
Focus : 100  m                 Midd. :  11
                                      -30 °

  250 Hz                              30 °
```

c

```
File :M19B                     Schaal:  15 dB
Temp. : 16.5 °C                Max. :58.2 dB
Focus : 100  m                 Midd. :   5
                          250 Hz    -30 °

             125 Hz

             500 Hz

             1000 Hz   30 °
```

d

```
File :M19B                     Schaal:  15 dB
Temp. : 16.5 °C                Max. :49.0 dB
Focus : 100  m                 Midd. :   5
                                      -30 °

  250 Hz                              30 °
```

Figure 5.20: Polar diagrams of the screening experiment with pink noise. a, b: source at –1°; c, d: source at +25°.

(and in windspeed gradient) will give rise to immission fluctuations. Figure 5.21 shows the power spectrum of the windspeed fluctuations at a height of 10 m. Notice that large fluctuations occur with periods of one year and with one to several days. Within one day, the fluctuations mainly occur between 1 second and 5 minutes. Hence, averaging over a one hour period will eliminate the effect of the fast fluctuations, but will preserve the average properties of the meteorological conditions of the day or night of measurement.
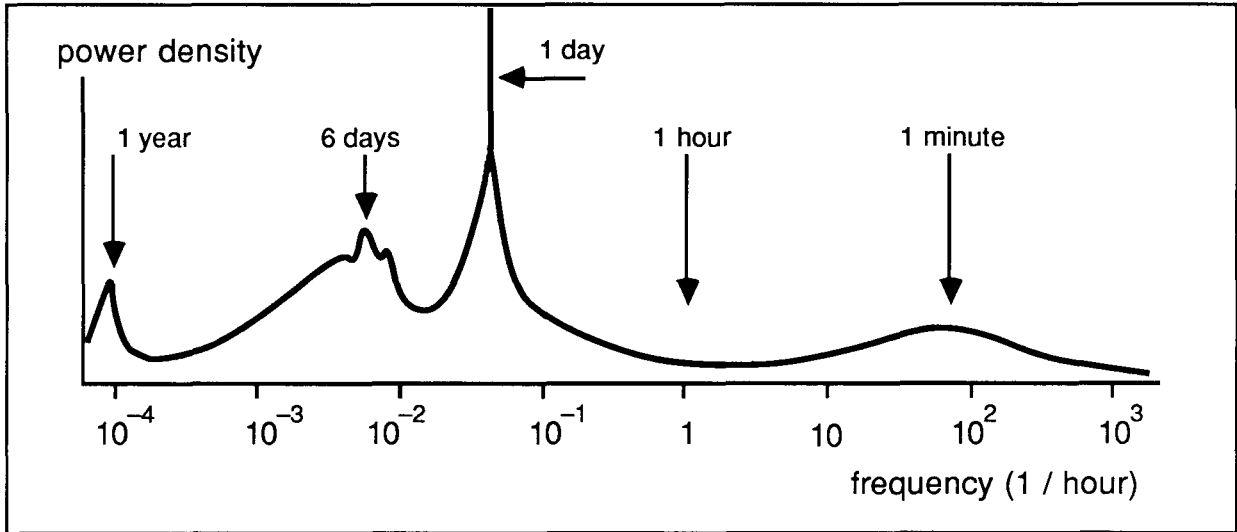
Figure 5.21: Power spectrum of the windspeed fluctuations at a height of 10 m. Quantitative representation of the data published by Gomes and Vickery [40].
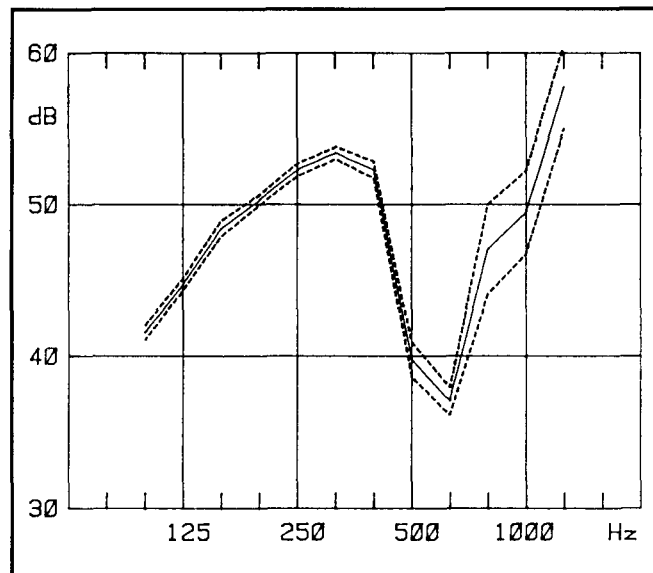
Figure 5.22: A-weighted $^1/_3$-octave immission levels from a loudspeaker at a distance of 100 m, fed with pink noise. The solid curve shows the average L_{eq} over 20 measurement cycles; the dashed curves mark the 95%-confidence limits, due to fluctuations in the propagation.

The averaging procedure of SYNTACAN has been tested in a downwind situation over grassland, with a loudspeaker placed at a distance of 100 m and a height of 1 m. The meteorological conditions were cloudy with sunny intervals and the windspeed varied strongly between 0 and 5 m/s, measured at a height of 2 m. The loudspeaker was fed with pink noise. We took 20 measurements with SYNTACAN in the 125 to 1000 Hz octave bands. From these measurements we calculated the $^1/_3$-octave immission levels. The results are summarized in figure 5.22.

It shows the average immission levels and the 95%-confidence limits (see also § 4.4.4). The strongest fluctuations in the immission levels occur in the 1 kHz octave band and this can be understood by realizing that a change in the wind profile will affect the interference pattern between the direct and the ground-reflected sound. It will change the position of the dip and the high-frequency slope of the transfer function. A comparison has been made with a conventional measurement carried out with an omni-directional microphone, placed on the antenna axis, next to the 22nd array microphone. With this microphone, we measured the immission in two ways:

a. Synchronized with the SYNTACAN measurements over 1 second intervals, giving L_{eq} values computed over 20 seconds for each octave band;

b. Quasi-continuous over 3 measurement periods of 5 minutes each.

The results are summarized in table 5.10. From the small differences between the different measurement procedures, it can be concluded that the SYNTACAN measurements are representative for the L_{eq} during the measurement period.

Table 5.10

Averaging of propagation fluctuations by SYNTACAN and conventional measurements. S5 = SYNTACAN, averaged over 5 cycles, S20 = SYNTACAN, averaged over 20 cycles; M20S = omni dir. micr. with 20 s averaging; M15M = omni dir. micr. with 15 minutes averaging.

1/1-octave band in Hz	immission level in dB(A)			
	S5	S20	M20S	M15M
125	51	51	50	50
250	57	57	58	58
500	53	53	54	53
1000	62	62	61	61
125–1000	62	62	61	61

In conclusion it can be stated that, although SYNTACAN measures only during short time intervals, averaging over a number of measurement cycles gives a good estimate of the equivalent sound pressure levels. The necessary number of cycles will depend on the actual situation and is strongly dependent on the fluctuations in the windspeed gradient. A good measure for the accuracy of the estimate is the 95%-confidence limit, which can be evaluated "on the spot" to see if the number of measurement cycles has been sufficient. This procedure is not only applicable for averaging of fluctuations in the transfer function, but also in case of a fluctuating source strength, as far as these fluctuations have a random character.

CHAPTER 6

PRACTICAL RESULTS

6.1 INTRODUCTION

The construction of SYNTACAN was completed in 1982. Since then the instrument has been used for the investigation of industrial and other noise sources. Practical experience with SYNTACAN has led to improvements in accuracy and ergonomy. In addition, practical demands have resulted in an extension of the applicability of the instrument, for instance by the use of triggered time windowing for the measurement of windturbines, and by a vertical antenna design for measuring the source height of passing vehicles.

Most measuring campaigns have been carried out in conjunction with the TNO Institute of Applied Physics (TPD); they are reported to the clients in confidential reports. For that reason it is not always possible to present results in full detail. However, all essential information that the reader needs for understanding the possibilities of SYNTACAN, will be provided. Details on the exact situation are deleted.

6.2 MEASUREMENTS ON LARGE FACTORIES WITH STATIONARY SOUND SOURCES

6.2.1 A measurement at large distance with full antenna length

We will first discuss a measurement in the vicinity of a large chemical factory. The antenna was placed over its full length on grassland, at a distance of about 1000 m from the relevant source areas, as indicated in figure 6.1. The measurements were carried out at night to eliminate the influence of traffic noise. During the measurements, the wind direction varied between –45° and +50° and the windspeed was 1 to 5 m/s, measured at a height of 2 m. So the measurement conditions were within the meteorological window for the relevant sound sources.

We took 20 measurement cycles at well selected points of time when road traffic was absent. Inspection of the results showed that one cycle was disturbed due to wind turbulence in the microphones. This cycle was discarded.
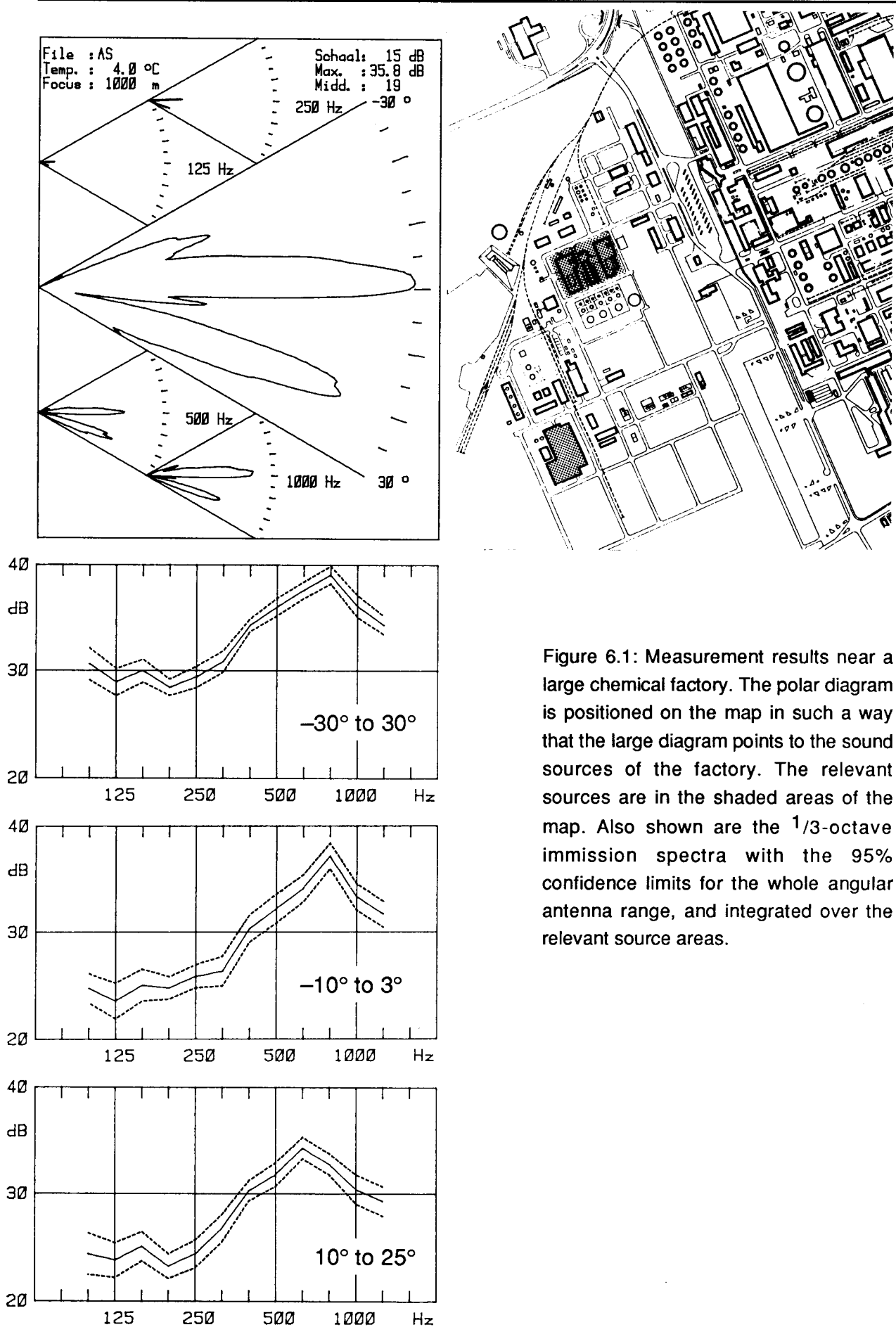
Figure 6.1: Measurement results near a large chemical factory. The polar diagram is positioned on the map in such a way that the large diagram points to the sound sources of the factory. The relevant sources are in the shaded areas of the map. Also shown are the $1/3$-octave immission spectra with the 95% confidence limits for the whole angular antenna range, and integrated over the relevant source areas.

Figure 6.1 shows the polar diagram of the averaged measurements with the center of the large, total diagram at the antenna origin on the factory map, so that this diagram points to the right source directions. Large main lobes are found in the direction of the relevant source areas at about $-2°$ and $+20°$. The mainlobes are very wide here, caused by the distributed source areas and, to some extent, also by scattering objects and coherence loss. The small responses at $-18°$ and $+5°$ are caused by weak, small sound sources. Also shown are the immission spectra for the whole angular antenna range from $-30°$ to $+30°$ and integrated over the relevant source areas ranging from $-30°$ to $3°$ and from $10°$ to $25°$. The results have 95% confidence limits between $\pm$ 0.6 dB and $\pm$ 1.9 dB. Note that the confidence limits are wider for the individual sources than for the whole immission spectra, as can be expected.

At the time of measurement, the extra microphones of the monitor system were not yet installed. Instead, we measured the total sound field with two additional omni-directional microphones, one at the antenna height of 1.5 m and the other at the standard measurement height of 5 m. These microphones were connected to a two-channel tape recorder with an additional cue track on which synchronization pulses were recorded. This enabled us to analyse 1-second intervals of the recorded tape, exactly at the time when the SYNTACAN measurements were taken. Figure 6.2a shows a comparison between the SYNTACAN measurement, integrated from $-30°$ to $+30°$, and the omni-directional measurements at 1.5 and 5 m. The SYNTACAN- and omni-directional measurement at 1.5 m should coincide. The curves are very similar. Only at low frequencies the SYNTACAN measurements are somewhat higher, due to wind turbulence in the microphones of the array. The level difference between the omni-directional measurements at 5 m and 1.5 m is shown in figure 6.2b. This correction curve was used to convert the SYNTACAN measurements from 1.5 to 5 m.
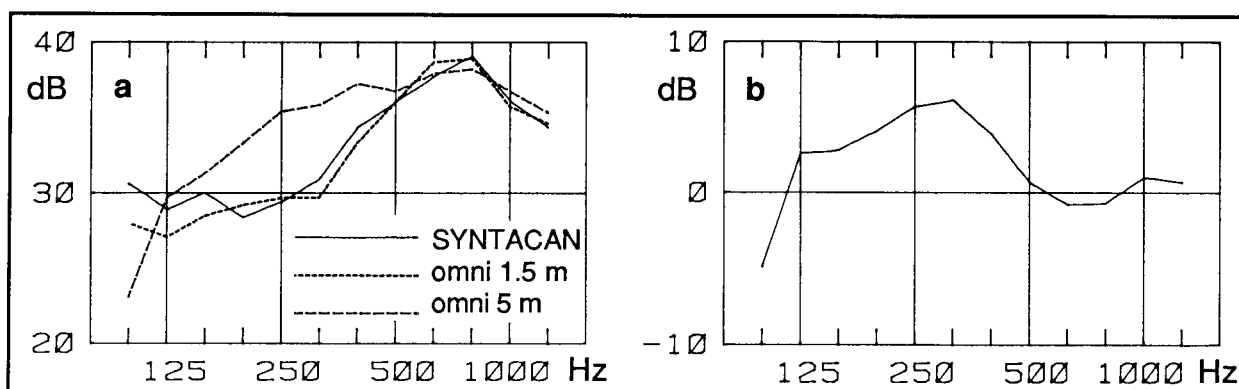

Figure 6.2: a. Comparison between the immission spectra of SYNTACAN, integrated from $-30°$ to $+30°$ and omni-directional measurements at 1.5 and 5 m. b. Level differences between the omni-directional measurements at 5 m and 1.5 m.

6.2.2 Measurements at small distances

In this paragraph we present the results of measurements on a drilling plant. The relevant sound sources are depicted in figure 6.3 and consist of:

1, 2, 3   : Generators. The main sources are the exhaust pipes of the Diesel engines;

4, 5   : Mud pumps;

6   : Drilling rig.

Figure 6.3 shows the polar diagrams, summed over the 125 – 1000 Hz octave bands for two antenna positions A and B. Both diagrams have the usual range of 15 dB. At position A, the antenna was placed at its full length and 10 measurement cycles were taken. The diagram shows the averaged result, focussed at 75 m and for frontal incidence. At this distance, focussing is critical, in particular at low frequencies when the whole antenna length is used. At high frequencies focussing is not so critical because a smaller antenna length is used here. The results show that all relevant noise sources are resolved, and that the source directions are reasonably correct. The responses from the directions between $-15°$ and $-5°$ are not caused by stationary sound sources, but by a cleaning truck, active in the area between the generators and the mud pumps. Notice that this disturbing source can be eliminated by selective angular integration.
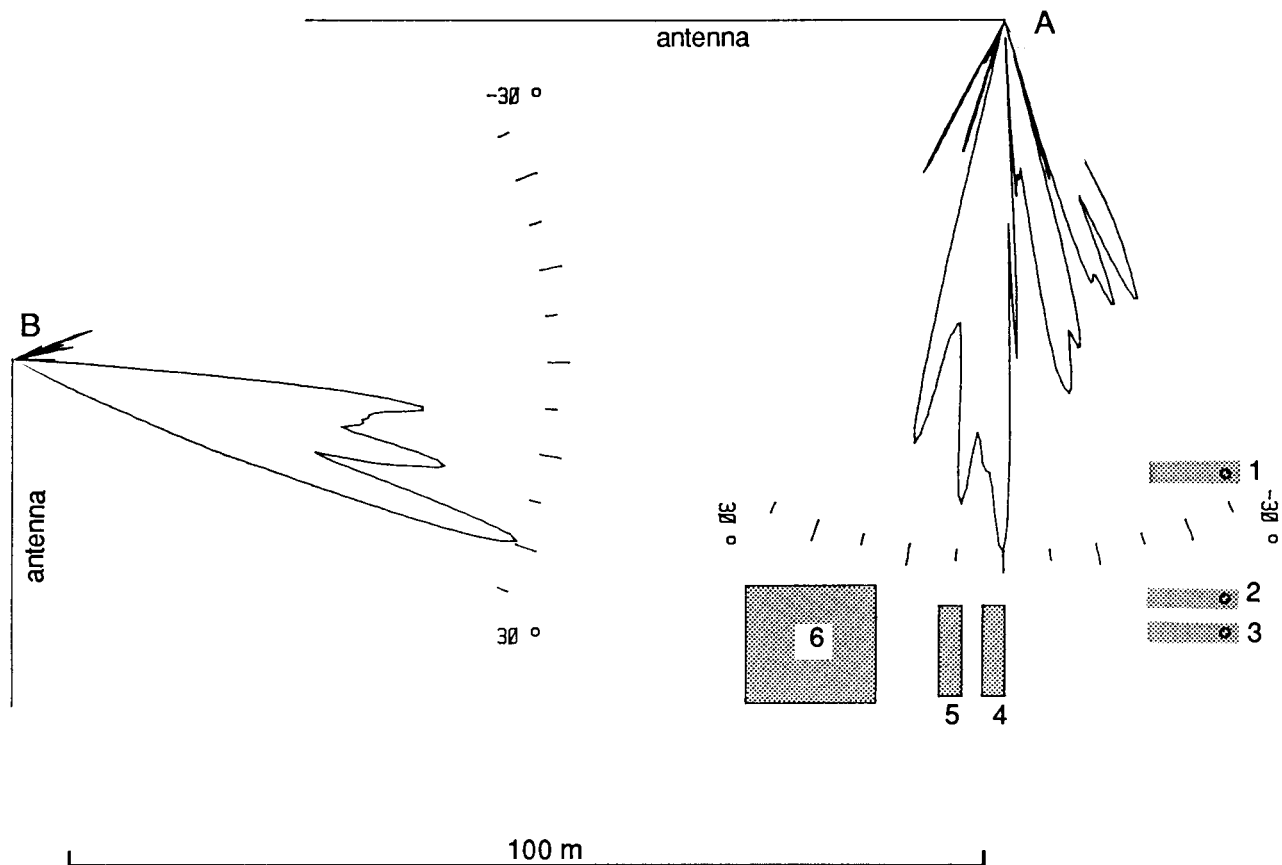

Figure 6.3: Polar diagrams of two measurements near a drilling plant.

At position B, the antenna length was reduced to 40 m (28 microphones), because of the restricted space at this position. The polar diagram shows the averaged results of 10 measurements, focussed at 110 m. As figure 6.3 shows, the source distances for antenna position B range from 85 to 140 m. Using the criteria of Section 2.8, we find that the focal depth in the 1 kHz octave band is $92 - 136$ m ($r_f = 110$ m and frontal incidence), so all sources are practically in focus. However, at lower frequencies the focal depth is smaller and the focussing should be repeated for the different source distances. These results are not presented here, as they give only small differences in the main lobe beamwidths and source directions, compared with the polar diagram of figure 6.3. The results show that sources 2 and 3 are not resolved separately at this measurement position. This is probably caused by the fact that for these sources a considerable part of the antenna was screened by the drilling rig. The mud pumps (sources 4 and 5) are not measured at all as they are completely screened by the drilling rig.

The drilling rig itself can be considered as a large building with interior sources. The observed source directions of the drilling rig correspond with door-openings in the walls of this structure.

The results clearly show the high directionality of the source area, caused by internal screening. SYNTACAN can be successfully used in such situations, but special attention must be given to screening effects, and focussing must be carried out with great care.

6.3 NOISE SOURCE IDENTIFICATION OF WINDTURBINES

A special application is the directional measurement of the sound sources of a windturbine. Here a distinction can be made between two kinds of noise sources:

* noise produced by the gearbox and the generator, which are placed in the nacelle behind the rotor hub;

* aerodynamic noise, produced by the interaction between the wind and the rotorblades.

In this investigation the main object was finding the location and the acoustic power of the aerodynamic sources on the rotorblades. As a consequence, not only high directivity was needed to distinguish between the nacelle noise and the aerodynamic noise, but the measurements had to be done in such a way that sharp images could be obtained from the moving sources on the rotorblades.

This was accomplished by a modification of the software in such a way that measurements were only taken in the time gate in which the rotorblades were acoustically observed in a horizontal position. This time gate was chosen in such a way that during a measurement cycle, the projection of the rotortips on the horizontal plane did not vary more than 1.5°, as seen from the antenna origin. This principle is illustrated in figure 6.4.
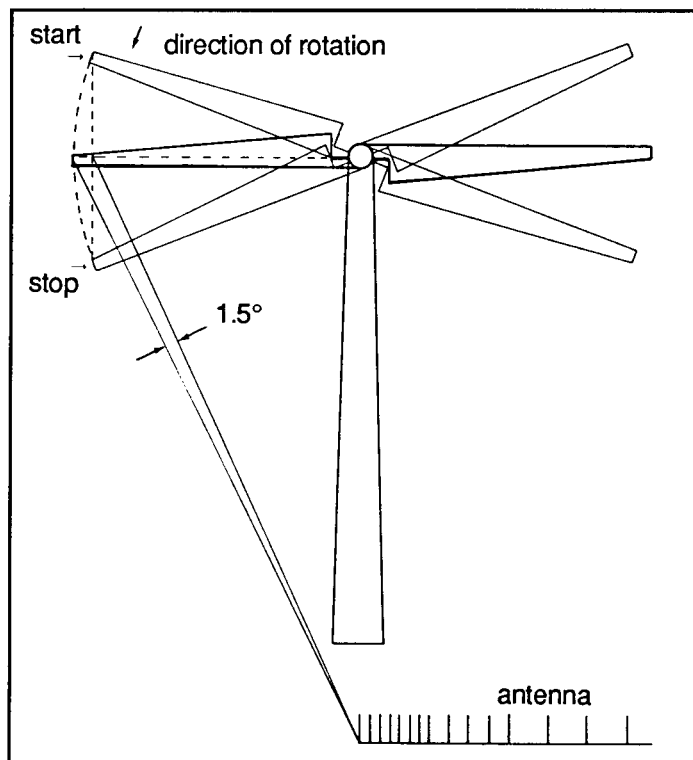
Figure 6.4: To get sharp images of the aerodynamic sound sources of the rotorblades, appropriate time gating is necessary.

Figure 6.5: SYNTACAN measuring the noise sources of a windturbine.

The time gate is usually so short that it falls within the maximum of 0.4 s measurement time for the 1 kHz octave band. For that reason it was decided to analyse the lower octave bands from the same dataset as used for the 1 kHz octave band. This procedure has the benefit that results for all octave bands can be obtained from a single measurement.

One of our measurements on a wind turbine is shown in figure 6.5. We positioned our antenna at a distance of 40 m from the turbine tower in the downwind direction with the microphones directed to the nacelle, which was at a height of 35 m, giving a source distance of 53 m. The rotorblades had a radius of 13.25 m, so all sources were seen within an angle of 28°. For geometrical reasons we had to position our antenna in such a way that the nacelle was seen at −12° and the rotortips at −26° and +2°. The synchronization for the time gating was obtained from an electro-optical device, consisting of a telelens and a photocell, which gave a trigger pulse on the change of light intensity when the image of the rotortip passed the photocell. Note that the trigger signal must be corrected for the propagation delay of the soundfield from rotor to antenna. The rotor had a speed of 50 rpm and a time gating of 190 ms was used.

Figure 6.6 shows the polar diagram obtained by averaging of 20 measurements, together with a schematic drawing of the rotor profile. Because no low frequency noise was present, the measurements could be restricted to the 500 Hz and 1000 Hz octave bands.
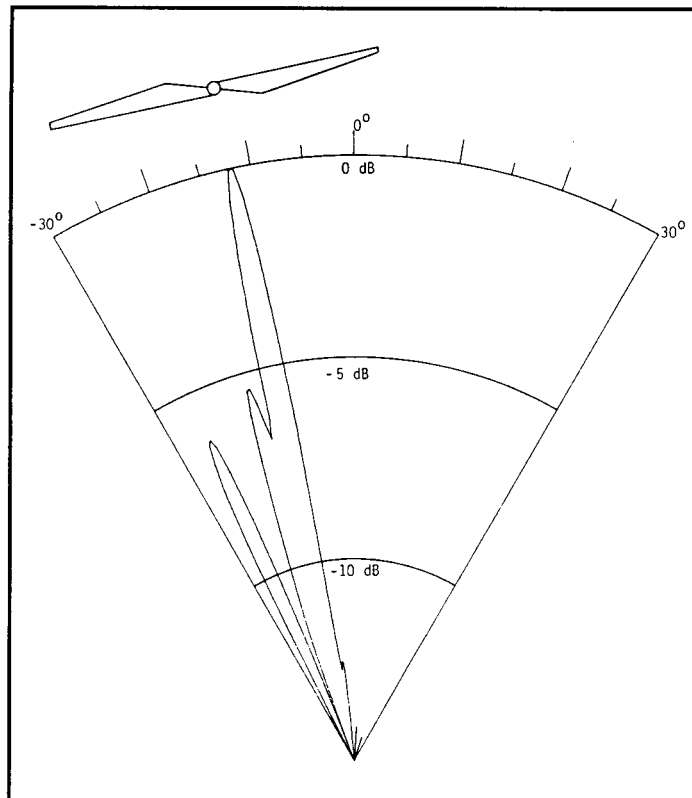

Figure 6.6: Polar diagram of the noise sources of the windturbine, showing three distinct noise sources: the nacelle (−12°), the left rotor root (−16°) and the left rotortip (−24.5°).

The results show clearly that there are three distinct noise sources at $-12°$, $-16°$ and $-24.5°$, corresponding with the nacelle, the left rotor root (where the rotorblade originates) and the left rotortip. Practically no noise was measured coming from the right rotorblade. This is caused by the directionality of the aerodynamic noise sources, pointing downwards for the left (downgoing) and upwards for the right (upgoing) rotorblade. The measurement of the position and directivity of these noise sources is of special interest for the improvement of the aerodynamic behavior of rotorblades, and for predictions of the noise production of larger windturbines.

6.4 SOURCE HEIGHT LOCALIZATION OF PASSING VEHICLES

Traffic noise is one of the most important noise problems in the outdoor environment. For correct modeling of the propagation of traffic noise it is essential to have a good idea of the acoustic source strength of the vehicles and of the height of the sources over the road. This is important for noise reduction measures depending on screens and walls.

The measurement of the source heights of moving sources with SYNTACAN has been investigated by Bakker [41] and Van Overbeek [42]and is summarized here.

For the measurement of the source height, the antenna has to be placed vertically. By using a telescopic support (a so-called *high-spy*), the antenna can be put up vertically having a length of 10 m, as shown in figure 6.7.

To obtain high resolution results, the vehicles must pass very close to the antenna, at distances of about 6 to 10 m. At this distance, the directivity of the individual microphones makes it necessary to turn the higher placed microphones downward in the source direction. Furthermore, focussing depends very critically on source distance and source direction. Note that at measurement distances smaller than the antenna length, the resolving power is not given by the far field expression Eq. (1.3), but by the near field expression Eq. (1.4). At these close distances, it is not the antenna length (expressed in wavelengths) but the aperture angle β (see figure 1.3b) which determines the resolution, and a larger antenna does not give much improvement in resolution. Hence, the usual enlargement of the antenna for lower frequencies is pointless here, and the resolution is restricted to the order of one wavelength. Fortunately, the determination of the source height with a resolution of about one wavelength is sufficient for correct modeling of the propagation of the traffic noise.

Synchronization with passing vehicles can be done with the same photo-electronic trigger device as used for windturbines. In this case a stable triggering is obtained with a spot-light at the other side of the road aimed at the trigger unit, so that the light beam is intercepted by passing cars.
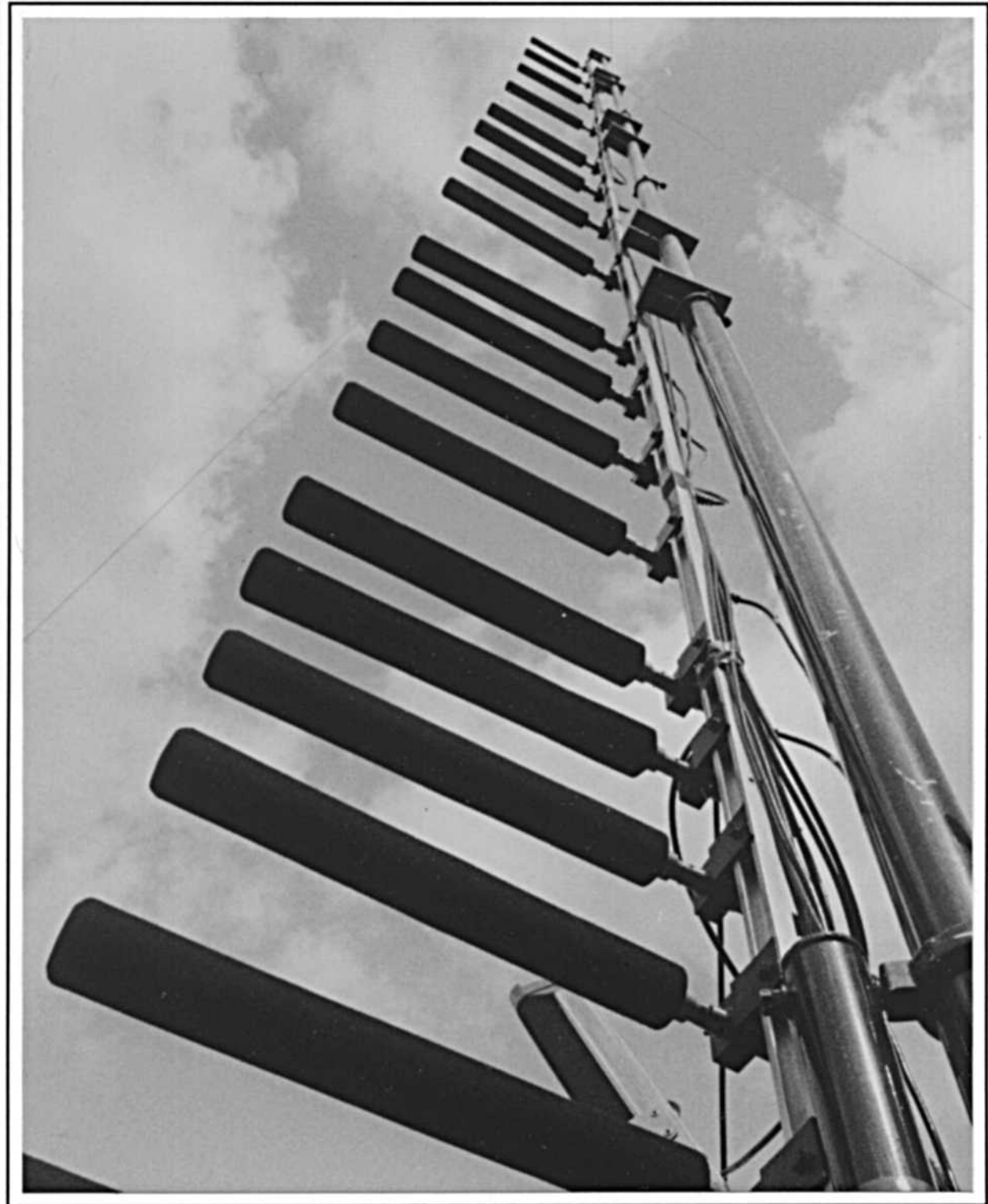
Figure 6.7: For the measurement of source heights the antenna can be installed vertically with a length of 10 m.
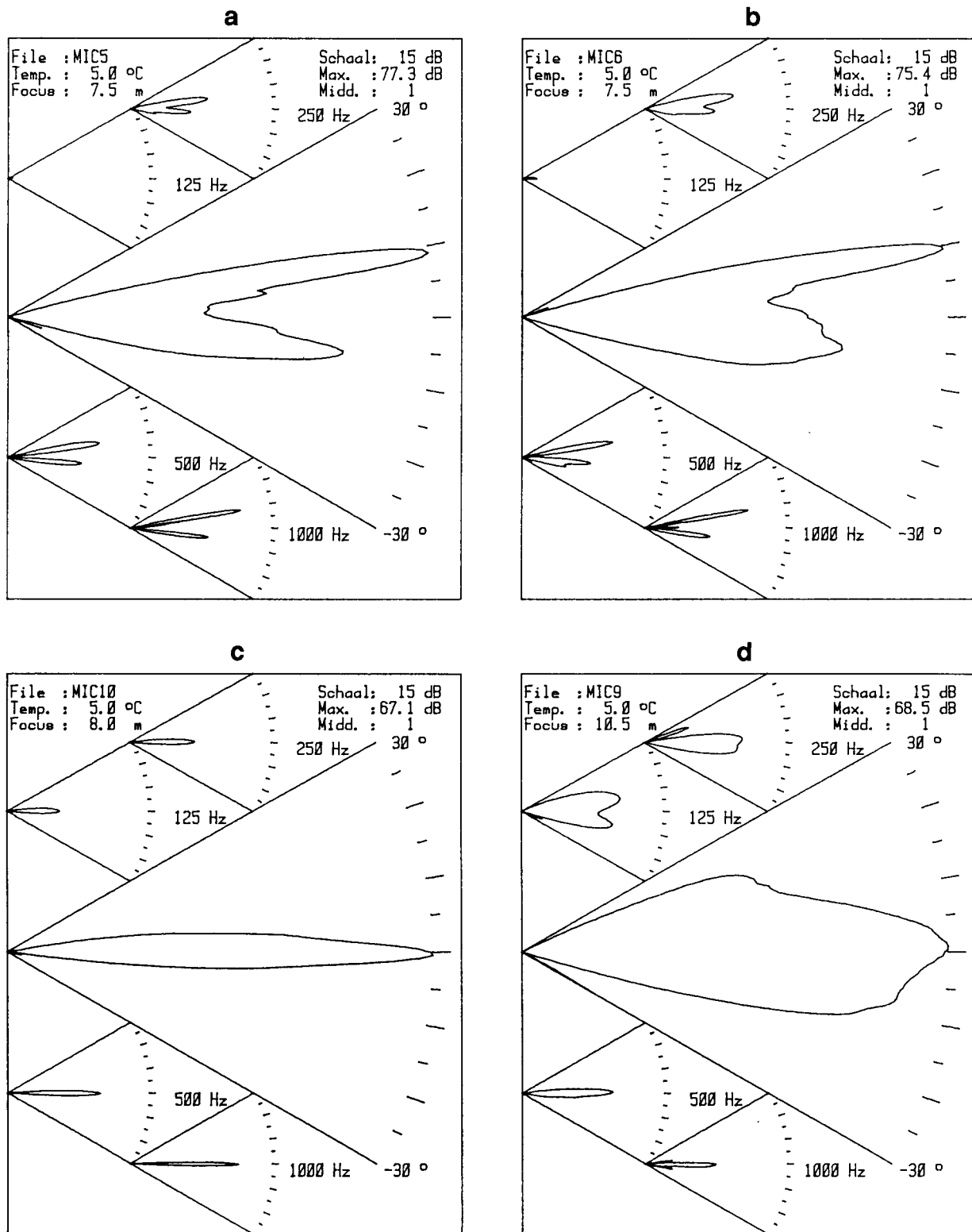
Figure 6.8: Polar diagrams of source height measurements above a brick-paved road. a. Stationary source, mounted on a truck at a height of 1.3 m and at a distance of 7.5 m from the antenna; b. The same source, but now with the truck passing at a distance of 7.5 m from the antenna with a speed of 50 km/h; c. Passing passenger car; d. Passing truck.

A point of great concern with the vertical antenna are the image sources caused by ground reflections. The image sources are correlated with the direct sources, and under those conditions the antenna can produce "ghost" sources in the image as a result of interference. A detailed discussion on these effects is presented in Section 5.3. Simulations showed that these effects are not severe if the sources are broadband.

Some measurement results are presented in figure 6.8. First we will discuss a point source, i.e. a loudspeaker, placed at a height of 1.3 m on a small truck. These measurements were carried out to check the measurement procedure. Figure 6.8a shows the polar diagram when the truck with the loudspeaker was placed at 7.5 m in front of the antenna with the truck engine turned off. Notice that in this polar presentation the angle direction has been changed in sign, so that positive angles correspond with positive source heights. In this case the source was seen at an angle of 10° from the antenna origin. Focussing was at a distance of 7.5 m and frontal incidence. The source and image source are resolved well. The source position is measured at 9°; so the angular deviations, caused by the frontal focussing, are only small in this direction. As the figure shows, the image source is more out of focus, as can be expected from theory (see § 2.8.4). The same measurement was repeated while the truck passed the antenna with a speed of 50 km/h (14.5 m/s), also at a distance of 7.5 m. The results are given in figure 6.8b. Note the strong resemblance to figure 6.8a. The only difference is some extra noise in the 0° direction, originating from the moving source and probably caused by tire-to-road noise of the truck (see below). From these test measurements it could be concluded that the antenna, placed vertically and equipped with appropriate time-gating, is suitable for measurements of the height of sources passing nearby.

We will conclude this paragraph by giving two measurement results on passing vehicles. Figure 6.8c shows a typical measurement on a passing motorcar. Only one source direction is found, which is on the road surface; the source and the image of the source are so close together that they cannot be resolved. Hence, the source height of a motorcar is extremely low. This can be appreciated by realizing that the noise is produced mainly by:

• the tire-to-road noise;

• the engine noise, shielded by the body, except at the bottom;

• the exhaust pipe, which is in a low position and produces only low frequency noise.

All motorcars measured show the same characteristics, although there are obvious differences in the spectra.

The situation is drastically different in case of trucks: the motor is placed higher and the body is more open. A typical result is shown in figure 6.8d. There the low frequency noise from the engine and the exhaust pipe are found to be between about 2.5° and 8°, which implies a height of 0.5 to 1.5 m. At higher frequencies, when the tire-to-road noise dominates, the situation is comparable with motorcars.

6.5   CONCLUSIONS

In this Chapter we have presented a number of practical applications of SYNTACAN. Originally, the instrument was designed for measuring of vast industrial areas at large distances. SYNTACAN has proven to function very well for these purposes and it is an attractive alternative for emission measurements and propagation modeling. Because of the large distances, the transfer functions are strongly influenced by meteorological conditions. As a consequence, great care has to be taken about speed and direction of the wind. Besides, resolution is also limited by the transverse coherence loss due to propagation over long distances. At smaller distances the system also is a very useful tool. Here interest is in the evaluation of annoying sound sources and the measurement of screening effects that are difficult to model. At small distances focussing is critical, and the results have to be interpreted with great care. Special care has to be taken of correlations between narrow band sources and reflections, as these can produce interference lobes in the polar diagrams.

We also discussed the measurement of non-stationary sound sources, i.e. aerodynamic sources on the rotorblades of wind turbines, and the acoustic source distribution of passing vehicles. Although the antenna was originally not constructed for these applications, it has been adapted to capture triggered time slices of the wavefield, so that sharp images of the moving sources can be obtained. The antenna has proven to be a valuable tool in these situations too, where conventional measurement techniques cannot be used.

CHAPTER 7

ANTENNA SIGNAL PROCESSING TECHNIQUES
IN RELATED DISCIPLINES

7.1 INTRODUCTION

In this final Chapter we will discuss some important antenna signal processing techniques which are being used in different disciplines, i.e. optical and radio-astronomy, sonar, radar and seismology. In these disciplines one has a common objective in finding direction, range, source or reflector strength, etc. of a number of emitters or reflectors. As we will see, there is a great similarity between these antenna techniques and the technique that we are using with SYNTACAN. This is caused largely by the similar nature of the wave propagation characteristics, which are basically given by the same wave equation. Of course, each discipline has its own characteristic approach that has led to particular solutions of the source (or reflector) identification problem, but as we will see, the use of modern computers has led to significant digital number crunching in all these disciplines. The availability of these facilities has stimulated the development of advanced multi-channel signal analyses procedures. Because of the similarity between the antenna techniques in these disciplines, a lot of cross-fertilization has taken place already. In this chapter we will discuss whether some of these techniques can also be applied to the identification problem of acoustic noise sources.

Much attention will be given to procedures with so-called super-resolution. Let us first define what we actually mean with this concept. In figure 7.1a, a basic beampattern in the k_x'-domain is depicted, with two resolution quantities: the peak-to-trough distance $\Delta k_R'$, defining the Rayleigh beamwidth, and the distance between the central lobe inflection points $\Delta k_r'$, defining the Ricker beamwidth (e.g. Berkhout [7]). In Section 2.7 we defined the antenna resolution as the -3 dB beamwidth, which is very near to the Ricker criterion. Figure 7.1b shows a number of closely spaced beampatterns with equal amplitudes, indicating that images which are closer than $\Delta k_r'$ cannot be distinguished by visual inspection. Although the beampattern can be changed by spatial windowing, the beamwidth will have a lower bound due to the finite aperture length, leading to the general resolution formula of Eq. (1.3). Procedures

which can resolve images that are closer than this criterion will be called super-resolution techniques. They involve in some way extrapolation along the antenna.
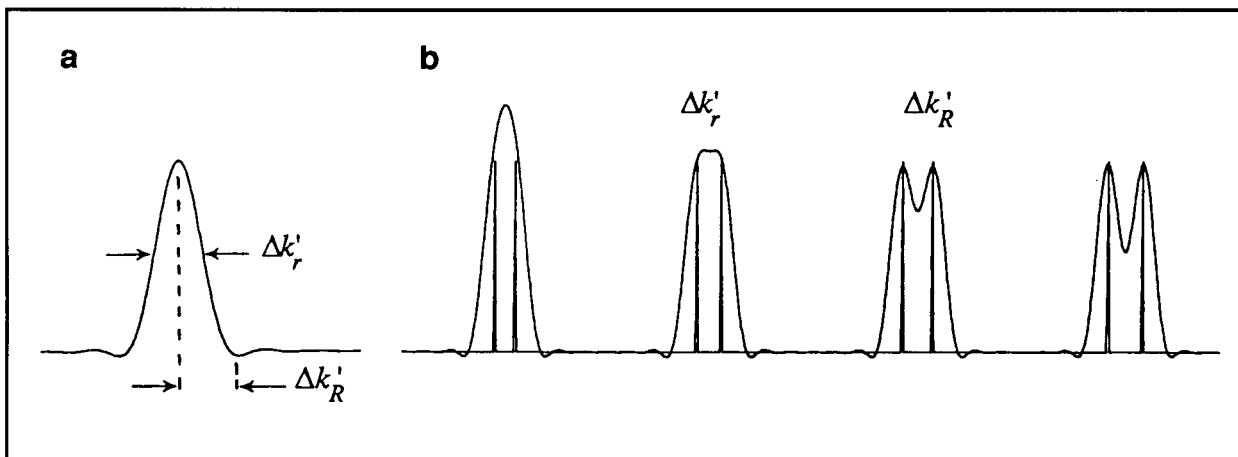

Figure 7.1: a. Basic beampattern, showing the Rayleigh beamwidth $\Delta k_R'$ and the Ricker beamwidth $\Delta k_r'$; b. Visual resolution for several beampattern separations.

7.2 OPTICAL ASTRONOMY

Most electro-magnetic waves that enter the earth's atmosphere are absorbed, scattered or reflected. There are only two frequency regions, called the *optical window* and the *radio window*, for which the atmosphere is transparent. The optical window comprises the wavelengths between 0.3 and 1 μm and some small windows between 1 and 10 μm. Observations of celestial objects have for a long time been restricted to the visual wavelengths. Since the invention of the telescope by Galilei in 1609, optical observations have been improved by a further development of these instruments, leading to brighter images and higher resolution.

Because of the very small wavelengths of visible light (0.4 – 0.8 μm), it is possible to obtain a high resolution even with small apertures. Theoretically, the resolution of these instruments is given by Eq. (1.3):

$$B = \lambda / D \quad , \tag{7.1}$$

where λ is the wavelength, D is the aperture diameter and B is the resolution in radians. The cosine factor of Eq. (1.3) has been dropped here, because of the paraxial imaging of a telescope. To give an example: Galilei's telescope has an aperture of only 25 mm, so the theoretical resolution of this instrument at a wavelength of 0.6 μm is 24×10^{-6} radians, or 5 arc seconds. According to Readhead [8], its actual resolution is only a factor of two worse. It must be noted that further enlargement of the aperture does not give the expected improvement in resolution. Also according to Readhead [8], the Palomar telescope has an aperture of 5 m, so a theoretical performance of 0.025 arc seconds could be expected, but the actual resolution is only 1 arc second. This large difference is caused by the fact that the propagation of starlight through

the atmosphere gives rise to a spatial decorrelation of the incoming wavefield, restricting the transverse coherence length of the waves to about 5 to 10 cm, thereby limiting the achievable resolution. So, at a first glance, the only benefit of these large terrestrial telescopes is the enormous gain in sensitivity. There are possibilities, however, to utilize these large apertures for a better resolution in spite of the transverse coherence loss. From inspection of the images of these large aperture telescopes it can be found that, although a point source gives a considerably extended image, this image has a structure, which depends on the statistical behavior of the atmospheric layer between the object and the aperture. This structure is not stationary, but changes as a function of time with variations of the atmospheric turbulence. Observations of the image at one moment, for instance by taking a photograph with a short exposure time, will show that the image contains a large number of so-called speckles, caused by the different turbulent regions in the transmission path, each acting as a disturbance on only a part of the image. It can also be observed that the speckle structures of two simultaneously observed objects are nearly the same, implying that the waves of two closely spaced sources have been disturbed by the same atmospheric turbulence. This property has led to the development of the so-called speckle-interferometry. An overview of this technique is given a.o. by Labeyrie [43]. The technique is based on the computation of the two-dimensional spatial auto-correlation function of the image and from this auto-correlation function the angular distance between double stars can be found, though it could never have been resolved from the image itself. The spatial auto-correlation function can be obtained with digital processing of the image, which must be digitized first. Note that it is essential for speckle interferometry that the disturbance function is identical for the two sources which have to be separated. This is true for astronomical observations with visible light for sources near zenith, having separations of less than 10 arc seconds, because then the same atmospheric column is passed through by the rays from both sources. The applicability of speckle interferometry for industrial noise source identification is very doubtful, because here the atmospheric column that is passed through by the rays will be different for sources which are only the antenna length apart.

7.3 RADIO ASTRONOMY

The radio window, which was already mentioned in Section 7.2, extends from about 30×10^6 to 30×10^9 Hz, corresponding with wavelengths from 10 m to 10 mm. Observations in this frequency region have proven to be very useful for our understanding of the universe.

A distinction can be made between broadband and narrow band radiating sources. The broadband signals are for instance caused by thermal and synchrotron radiation; the narrow band signals are caused by atomic and molecular emission of electro-magnetic energy. A very popular observation frequency is 1420 MHz ($\lambda = 0.21$ m), the electron spin flip (magnetic dipole) frequency of neutral hydrogen. The celestial radio sources can be further divided into

areas of distributed radiation from diffused media of, for instance, gas cloud nebula, sources with a modest angular extent like nearby radio galaxies, and point sources like quasars.

The radio signals are usually measured with a parabolic telescope that acts as a focussing mirror for plane waves to an aerial in its focus point. The aerial is connected to a high quality radio receiver. Usually the signals are down-converted in frequency and filtered. The output signal is then used for further post-processing. The simplest post processing is to measure its RMS value as a measure of the radiation strength of the observed object in the filtered frequency region.

It must be realized that the resolution of a single parabolic telescope is very poor, due to the long wavelength. Using Eq. (7.1) we find that the theoretical resolution of a reflector with a diameter of 25 m, operated at a wavelength of 0.21 m is only 0.5 degrees. Such a resolution was good enough in the beginning of radio astronomy after World War II, when the strongest radio sources were discovered, but since then, higher resolutions have become necessary. It is not possible to make parabolic reflectors much larger, due to problems with stability, deformation by gravitation, forces by wind, etc. Solutions have been found by constructing telescope arrays. Basically, these arrays work on the same principle as our SYNTACAN system, i.e. the output signals of the telescope receivers are cross-correlated and the cross-correlation functions are temporally and spatially Fourier transformed to decompose the wavefield into monochromatic waves from different directions. (See Section 2.6.) In radio astronomy one always needs a two-dimensional image, so the spatial correlation function is a function of 2 coordinates u and v:

$$R(u, v, \tau) = E\{s(u_o, v_o, t) \, s(u_o+u, v_o+v, t+\tau)\} \quad , \tag{7.2}$$

where $E\{\cdot\}$ denotes the expectation operator and s is the antenna signal, measured by one of the telescopes. For the two-dimensional Fourier transform from u, v to k_u, k_v, it is necessary that the u,v plane is sampled adequately. Because the radiation of the sources is continuous and statistically invariant, these functions can be measured over a long period of time, but as we will see in the next paragraph, a complete sampling of the u,v plane is never possible in radio astronomy.

A well known example of a Synthesis Radio Telescope is the Westerbork Synthetic Radio Telescope (WSRT), located in the eastern part of the Netherlands. It consists of 14 telescopes, placed on a straight line in east-west direction over a length of 2.8 km. The daily earth rotation gives a scan through the u,v plane that rotates 180° in 12 hours. A few of the telescopes can be moved on a rail, so the distances between the array elements can be changed, in order to obtain a dense sampling in the u,v plane. The sampling distance must be chosen in such a way that spatial aliasing is avoided within the spatial bandwidth of the individual receivers. The longest baseline of the Westerbork observatory is 2.8 km. This gives a theoretical resolution at a

wavelength of 0.21 m of 15 arc seconds; a value which is even worse than that of the Galilei telescope!

In the following paragraph we will discuss two procedures, the CLEAN and the Steer algorithm, which are successfully applied in radio astronomy.

7.3.1 The CLEAN method

The basic beampattern of a rotation synthesis radio telescope is not as nice as one might expect. The reason is that the sampling of the u, v plane is never ideal. For instance, the sampling of the baseline space is non-uniform, as it depends on the source declination, and a part of the circular scan may even be totally absent due to blocking by the earth. As a consequence, parts of the u, v plane are sampled badly and some parts have even to be replaced by zeros before Fourier transformation. Hence, the basic beampattern in the k_u, k_v plane is usually far from ideal and will have large sidelobes, which usually are called alias-lobes, as they are due to under-sampling. The alias-lobes of bright images are so strong that they can completely obscure weaker images and are therefore called *confusion noise*. Fortunately, the beampattern is usually the same for all source directions under consideration, all being within the beampattern of the individual telescopes and this property has led to a deconvolution technique, called CLEAN, which is widely used in radio astronomy.

We will now give a summary of the CLEAN method. It was originally published by Högbom [44] in 1974. A mathematical-statistical description of the method is given by Schwarz [45]. We will confine ourselves here to a one-dimensional description of the technique, extension to the two-dimensional case is straightforward, however.

The easiest way of description is in the k_u-domain. Let the sampling function along the u-axis be given by the window function $W(u)$, then the basic beampattern in the k_u-domain is given by its Fourier transform:

$$\tilde{W}(k_u) = \int W(u)\exp(jk_u u)du \quad .$$ (7.3)

$\tilde{W}(k_u)$ is called the *dirty beam* because it contains strong sidelobes. Let the real source strength as a function of k_u, called the brightness distribution, be given by $\tilde{S}(k_u)$. Assuming a constant dirty beam for all source directions under investigation, the *dirty map* $\tilde{D}(k_u)$ is obtained as

$$\tilde{D}(k_u) = \tilde{W}(k_u) * \tilde{S}(k_u) \quad .$$ (7.4)

In this equation $\tilde{D}(k_u)$ is measured, $\tilde{W}(k_u)$ is a known function and $\tilde{S}(k_u)$, the true brightness distribution or *true map*, has to be found. So Eq. (7.4) reflects a deconvolution problem.

CLEAN solves this problem by assuming that the brightness distribution is essentially empty and that it can be described as a sum of scaled delta-functions, each representing a point source:

$$\tilde{S}(k_u) = \sum_i A_i \delta(k_u - k_{ui}) \quad .$$

(7.5)

The A_i and k_{ui} are found in the following iterative procedure:

a. Start with a residual map $\tilde{D}_j(k_u)$, which equals the dirty map, and a brightness $\tilde{S}_j(k_u)$ that is empty:

$$\tilde{D}_j(k_u) = \tilde{D}(k_u)$$

and

$$\tilde{S}_j(k_u) = 0 \quad .$$

Here j is the loop counter, set to zero at this point.

b. Increment the loop counter j and search for the absolute maximum in the residual map, giving a value A_j at position k_{uj};

c. Compute a new estimate of the brightness by adding a fraction g of this maximum:

$$\tilde{S}_j(k_u) = \tilde{S}_{j-1}(k_u) + gA_j\delta(k_u - k_{uj}) \quad ;$$

d. Eliminate this fraction from the residual map:

$$\tilde{D}_j(k_u) = \tilde{D}_{j-1}(k_u) - gA_j\delta(k_u - k_{uj}) * \tilde{W}(k_u) \quad .$$

e. Test if the residuals $\tilde{D}_j(k_u)$ are sufficiently low. If not: repeat steps b-e, otherwise finish the iteration.

Schwarz [45] has shown theoretically that under some well defined conditions, the iteration converges for $0 < g < 2$. In practice a gain factor < 1 is always chosen, because it makes the procedure more stable for extended source areas. After the above iterative inversion procedure, the series of Dirac pulses $\tilde{S}_j(k_u)$ is an estimate of the true brightness distribution $\tilde{S}(k_u)$. This estimate is not unique, because the spike-model gives an interpolation and an extrapolation of the observed spectrum in the u-domain. For presentation purposes, the result $\tilde{S}_j(k_u)$ is usually convolved with a so-called *clean beam*, giving the result, called the *clean map*, an appearance that does not exceed the intrinsic resolution of the antenna array. The clean beam usually is some artificial beam with about the same mainlobe as the dirty beam, but without the sidelobes. This convolution step is essential, as during the CLEAN iterations measurement inaccuracies and noise may lead to some closely spaced spikes associated with only one point source, and these spikes will make one source to appear as a number of closely spaced sources. By convolution with a clean beam having a beamwidth in agreement with the array resolution, such a cluster is depicted again as one unresolved source.

7.3.2 Extended sources: the Steer algorithm

Application of the CLEAN algorithm in radio astronomy has shown that it performs very well if the model of sparse point sources is correct. However, in case of extended source areas, the clean map does not always converge to the desired smooth brightness distribution, but may contain "stripes" or "corrugations". These problems have a.o. been addressed by Cornwell [46] and Steer et al. [47] and are caused by the point source assumption. In each iteration, a point source response is subtracted from the residual map, and in a broad source area that causes sidelobes. The maxima and minima of these sidelobes are preferred locations for the positioning of point sources in the next iterations, leading to the stripes. These sidelobes contain energy in the unsampled u-region and the CLEAN algorithm cannot correct for that. Hence, due to an incorrect source model, the unsampled u-values will be estimated incorrectly.

If the extended source areas are not too wide, the instability can be avoided by lowering the gain factor of the CLEAN loop, but for wide source areas the number of iterations increases drastically and the stripes do not disappear.

The stability for extended source areas can be improved with a modification of the CLEAN algorithm, published by Steer et al. [47]. We will call this approach the Steer algorithm. The original CLEAN algorithm is based on the assumption of point sources and recovers these point sources spike by spike. The Steer algorithm anticipates on the extension of a source area by removing a whole mainlobe (or even more mainlobes with about the same amplitudes) in one iteration.

The Steer algorithm consists of the following steps:

a. Start with a residual map $\tilde{D}_j(k_u)$, which equals the dirty map and a brightness $\tilde{S}_j(k_u)$ that is empty:

$$\tilde{D}_j(k_u) = \tilde{D}(k_u)$$

and

$$\tilde{S}_j(k_u) = 0 \quad .$$

Here j is the loop counter, set to zero at this point.

b. Increment the loop counter j and search for the absolute maximum in the residual map, giving a value A_j.

c. Make a so-called *trim map* $\tilde{T}_j(k_u)$ of the dirty map, by setting to zero all points which are absolutely smaller than $T_c A_j$. The factor T_c is called the *trim contour*.

d. Convolve the trim map with the dirty beam and search for its absolute maximum, giving a value B_j.

e. Compute a new estimate of the brightness by adding a fraction $g(A_j/B_j)$ of the trim map:

$$\tilde{S}_j(k_u) = \tilde{S}_{j-1}(k_u) + g(A_j/B_j)\,\tilde{T}_j(k_u) \quad .$$

f. Eliminate this fraction from the residual map:

$$\tilde{D}_j(k_u) = \tilde{S}_{j-1}(k_u) - g(A_j/B_j)\tilde{T}_j(k_u) * \tilde{W}(k_u) \quad .$$

g. Test if the residuals $\tilde{D}_j(k_u)$ are sufficiently low. If not: repeat steps b-g, otherwise finish the iteration.

7.3.3   Application of CLEAN and Steer to SYNTACAN

We have tested the CLEAN and the Steer algorithm in a number of simulations to see if these procedures could be applied to SYNTACAN. All simulations have been carried out using a 128-point discrete Fourier transform representation as with SYNTACAN. To be consistent with the theory presented in this chapter we will use the variables u and k_u instead of ξ and k_x. We will now discuss the simulations:

a. Improvement of the angular resolution

It should be mentioned that CLEAN has not been developed for improvement of the angular resolution beyond the Rayleigh criterion. However, because of the spike model of Eq. (7.5) it is interesting to see if some improvement of resolution will be possible.

Figure 7.2a shows a true map of 3 point sources at positions 40, 43 and 60 Δk_u with relative energies of 1, $^1/4$ and 1 resp. In the SYNTACAN design $\Delta k_u \approx 1°$ at 1 kHz. In the simulation we took an antenna length of 31 $\Delta u = 4.65$ m, which is half the usual value. The dirty map of this simulation is given in figure 7.2b, showing the wide beam pattern and the sidelobes of the rectangular window function. In the SYNTACAN data processing the sidelobes are reduced with aperture tapering. The result is shown in figure 7.2c. Note that under these conditions the small source at $k_u = 43$ Δk_u is not resolved at all. The dirty map and the dirty beam of this simulation were used as input for the CLEAN algorithm and the clean map was computed with a gain factor $g = 1$, until the residuals were smaller than 1×10^{-6} (-60 dB). This occurred after 67 iterations and resulted in an accurate replica of the true map as shown in figure 7.2d. (In our simulations, the clean maps are not convolved with a clean beam as this presents more clearly the performance of the algorithms.) So, under these ideal circumstances, i.e. no noise and a true map of a small number of point sources, the CLEAN algorithm results in a very accurate restoration of the source angles and amplitudes.

This result suggests that the CLEAN algorithm can be used to achieve super-resolution, i.e. separation of sources which are closer than the Rayleigh resolution criterion. This is not true, as demonstrated in figure 7.3. The figure shows a true map of point sources with equal energy at
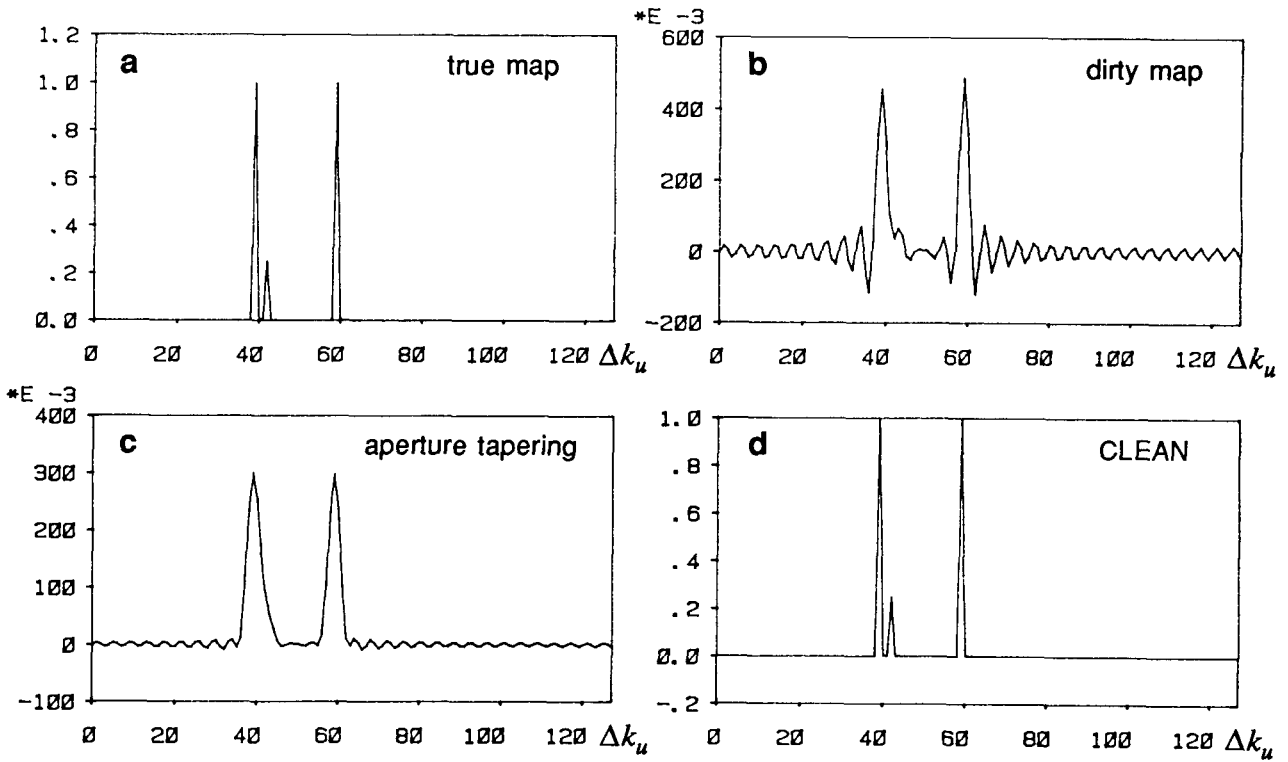
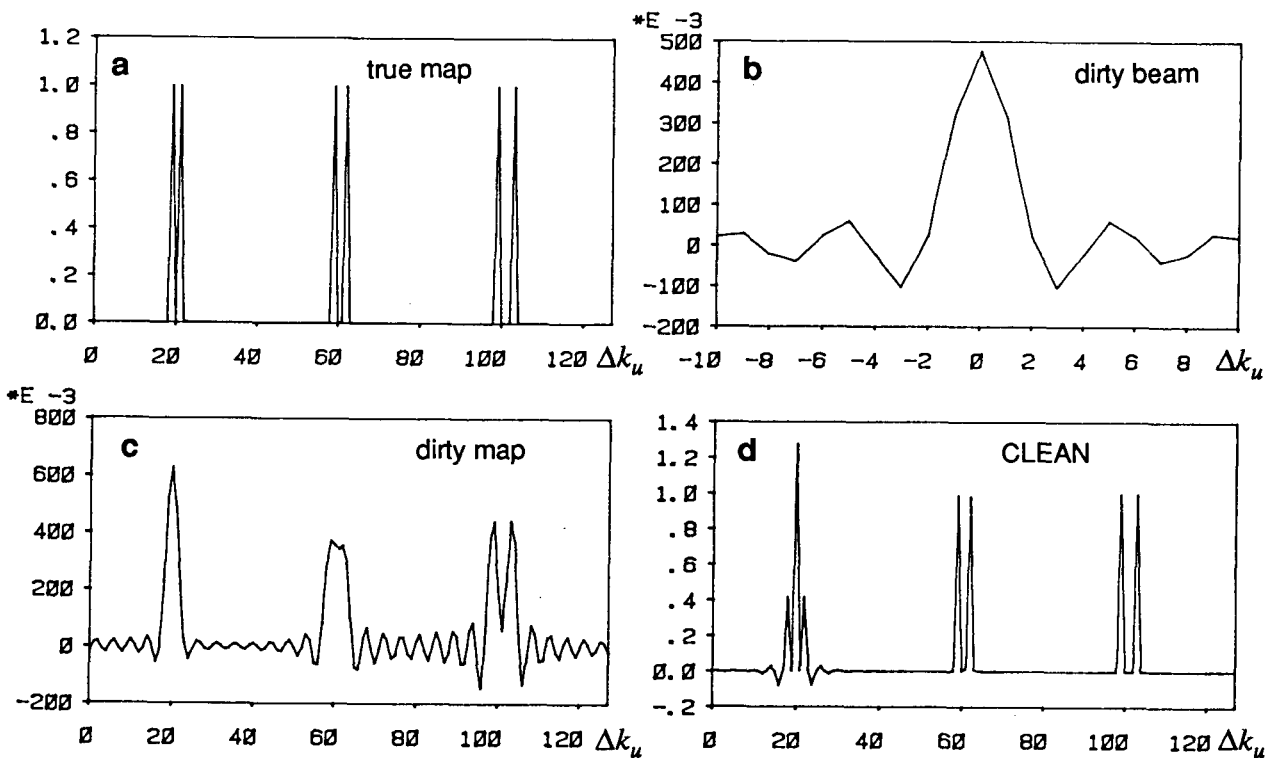Figure 7.2: Improvement of the angular resolution of point sources.

Figure 7.3: Simulation, showing that the maximum resolution of CLEAN is given by the Rayleigh criterion.

the positions (20, 22, 60, 63, 100, 104) Δk_u. This map was convolved with the same dirty beam as in figure 7.2. The central part of this beam is depicted in figure 7.3b. The Rayleigh resolution criterion is the distance between the main lobe maximum and the first minimum of the dirty beam and equals 3 Δk_u in this case. The clean map of this simulation shows that CLEAN cannot resolve the sources at 20 and 22 Δk_u, but gives accurate results for the other sources.

Hence, CLEAN is not able to give a real improvement of resolution, but it offers a result which allows a much better visual interpretation of the source positions and amplitudes than the conventional presentations, because the sidelobes are removed.

Resolution enhancement was also tested for a more complicated source distribution, depicted in figure 7.4a. Here two extended source areas were added. The same aperture window was used, giving the dirty map of figure 7.4b. In this case the CLEAN algorithm took 729 iterations ($g = 1$, residuals < -60 dB) to give the clean map of figure 7.4c. Note that the point sources are restored well, but that the extended sources are distorted due to a lack of bandwidth. The image could be smoothed by convolution with a clean beam, but this, of course, would reduce the resolution. Much better results were obtained with the Steer algorithm, shown in figure 7.4d. The result was obtained after only 31 iterations with $g = 1, T_c = 0.7$ and residuals < -60 dB. Note that the stripes have almost disappeared in the result, and that the point sources are also depicted with almost full accuracy.

b. Absent or malfunctioning microphone

This situation was simulated with an aperture window over all 64 points (0, 1, ..., 63)Δu. So the full antenna length was taken, where instead of leaving out the sample points (32, ..., 63)Δu, as discussed above, now the sample points (16, ..., 23)Δu are absent. Note that it is exactly for such a situation that CLEAN was developed, i.e. incompletely sampled visibility functions. This situation was tested with the same model as in figure 7.4. The results are given in figure 7.5. The CLEAN algorithm took 512 iterations ($g = 1$, residuals < -60 dB). Note the occurrence of the stripes in the large source area. The Steer algorithm was used with $g = 1$ and $T_c = 0.7$ and took only 38 iterations. The stripes have almost disappeared.

c. Compensation of transverse coherence loss

As discussed in Section 3.3, the transverse coherence loss plays an important role in outdoor noise propagation. We have simulated a situation of strong coherence loss, assuming that Eq. (3.38) is valid. So the window function equals

$$W(u, f) = \exp(-\beta f |u|) \ . \tag{7.6}$$

We performed the simulation with $\beta = 5 \times 10^{-4}, f = 1000$ Hz and the full antenna length of 63 Δu.
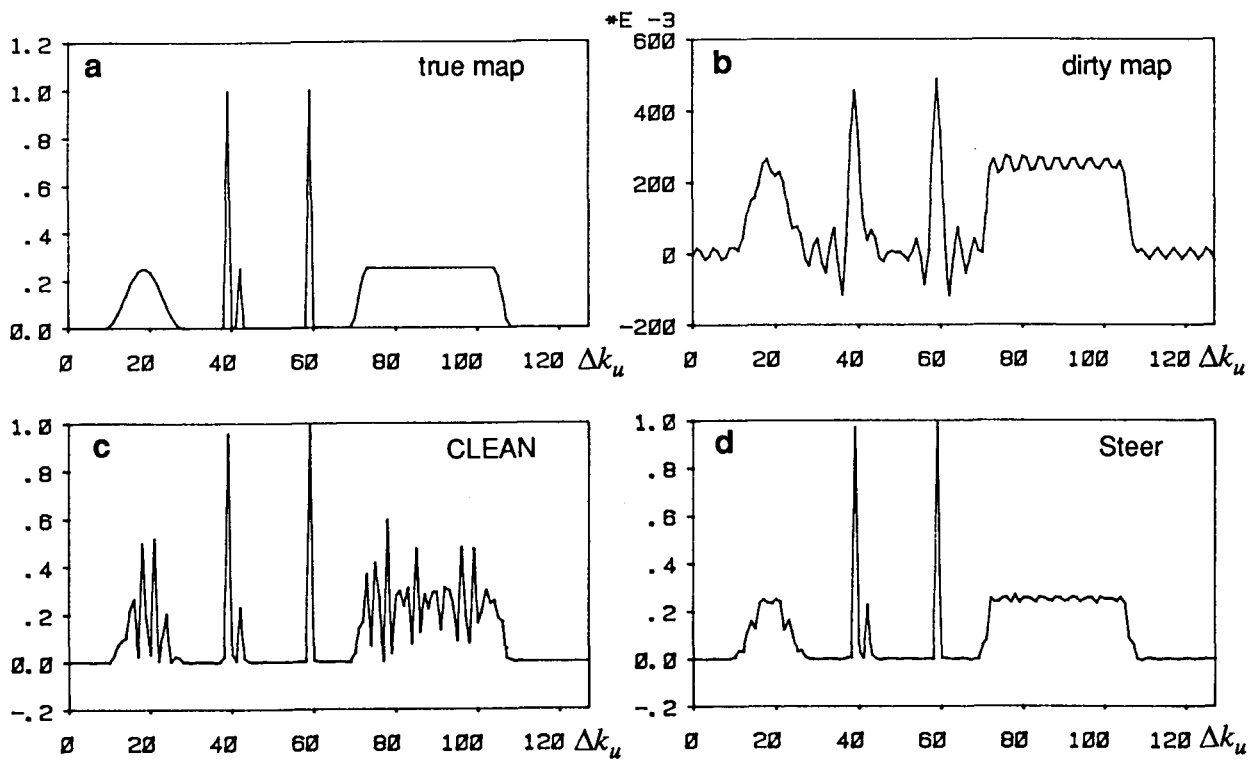
Figure 7.4: Improvement of the angular resolution of point sources and extended source areas.
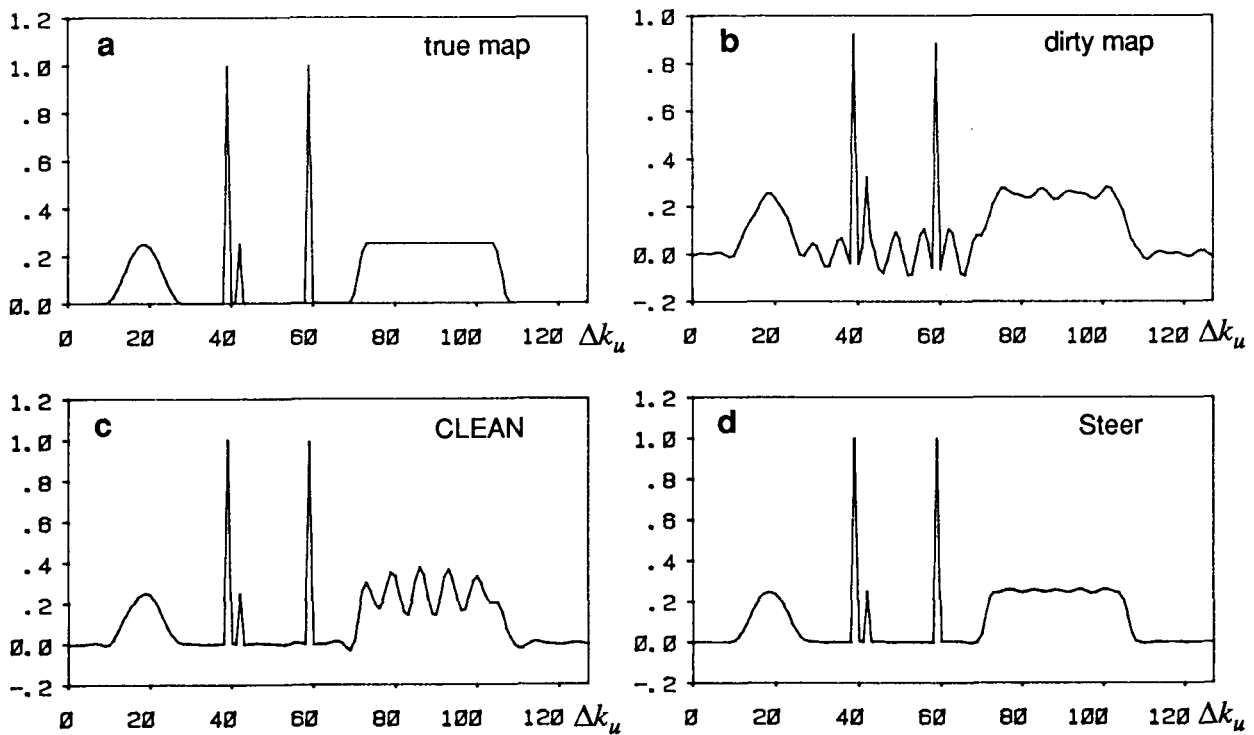
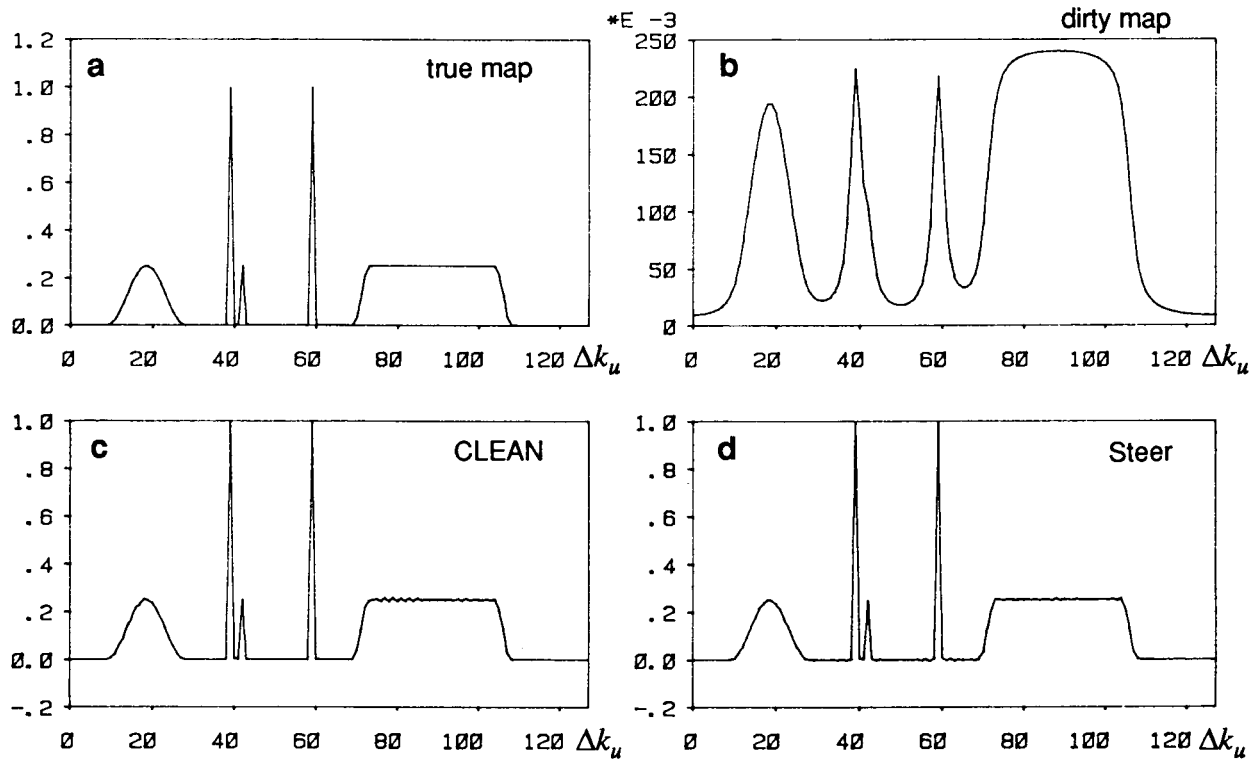Figure 7.5: Restoration of the source image when a microphone is absent.

Figure 7.6: Restoration of the source image in case of transverse coherence loss.

Figure 7.6 shows the results, again for the same source model as used before. Because of the strong attenuation of the signals in the dirty map for high u-values, a large number of iterations was necessary, even with the Steer algorithm, and the residuals could not be made smaller than -40 dB. The number of iterations was 890 with CLEAN and 165 with the Steer algorithm. Notice that here CLEAN also gives stable results for the extended source areas. It must be noted that in order to get a good deconvolved result, it is necessary to have a reliable estimate of the transverse coherence loss at the time of measurement.

This is illustrated in figure 7.7. We used the same dirty map as in figure 7.5, but the deconvolution was carried out with a dirty beam in accordance with Eq. (7.6), with $\beta = 4 \times 10^{-4}$ and 6×10^{-4} resp. Notice the deformation of the point source responses for incorrect transverse coherence loss. These results suggest that it must be possible to estimate the transverse coherence loss (or the dirty beam) by an iterative procedure in which the response of an isolated point source is optimized in the clean map.

Comparison of the figures 7.4, 7.5 and 7.6 shows that the CLEAN-algorithm acts quite differently under the various circumstances. The instability in figure 7.4 is caused by an incorrect extrapolation of the unsampled u-region ($u > 31$ Δu) and the instability in figure 7.5 is caused by an incorrect interpolation of the unsampled u-region (16, ... 23 Δu). In the simulation of figure 7.6 the whole u-region is sampled, which explains why no instability occurs here.
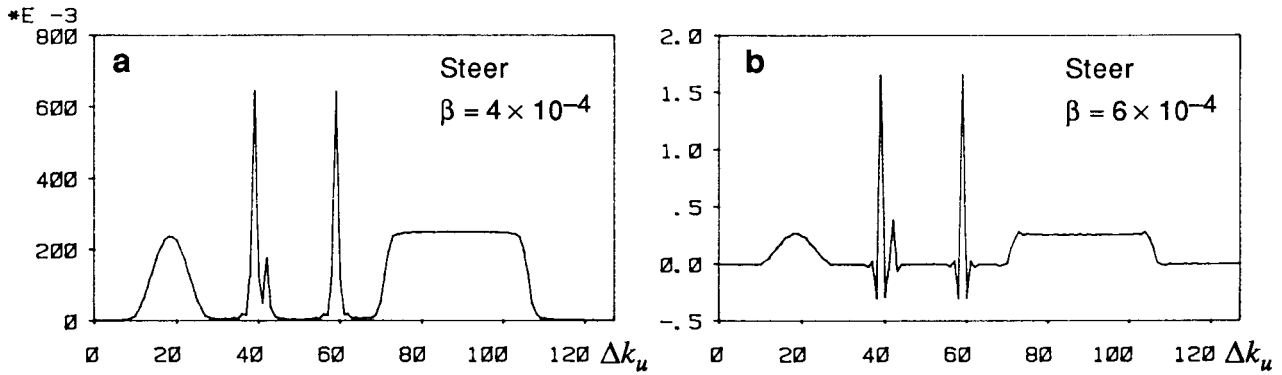
Figure 7.7: Effect of cleaning with incorrect coherence loss. The true coherence loss is given by $\beta = 5 \times 10^{-4}$.
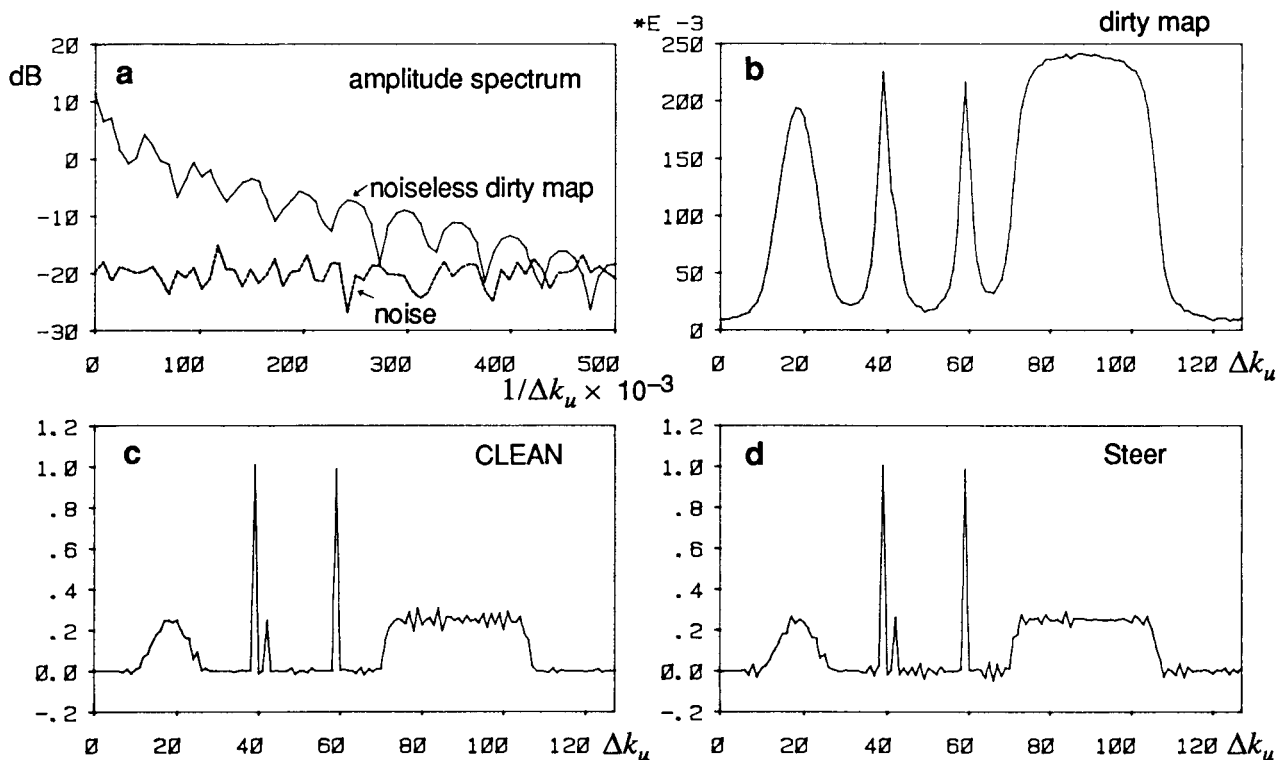

Figure 7.8: Effect of measurement noise in the dirty map by adding white Gaussian noise to the dirty map of figure 7.6.

A special point of concern is the signal to noise ratio, which must be high enough to compensate for the dirty beam. This is illustrated in figure 7.8. A simulation was carried out with the same source model and dirty beam as in figure 7.6, but now white Gaussian noise was added, to account for the uncertainties in the measured cross-spectrum. The amplitude spectra of the noiseless dirty map and the added noise are shown in figure 7.8a, and the disturbed dirty map in figure 7.8b. In our experiments with the CLEAN and Steer methods it was found that the most stable results were obtained by limiting the iterations to a residual level of −30 dB. This level was reached with CLEAN after 551 iterations and with the Steer algorithm after 68 iterations. The results are shown in figures 7.8c and d.

In conclusion it can be stated that the CLEAN and Steer procedures are very promising for SYNTACAN applications. We have a preference for the Steer-algorithm, not only for its higher stability but also because this algorithm is computationally very efficient, especially for extended source areas. As has become clear from the simulations, CLEAN (or Steer) does not give a super-resolution, but its advantage is that it presents results which are much easier to interpret than the conventional presentations.

Under practical measurement conditions, where transverse coherence loss occurs, the dirty beam will usually not be known. In those cases it is possible to estimate the dirty beam by optimizing the response of a known isolated point source. The CLEAN or Steer algorithms might be further optimized with a procedure in which the remaining residuals are minimized in each iteration step. Such an algorithm could be used for estimation of unknown parameters such as the transverse coherence loss, by searching for the parameters that give the fastest reduction of the residuals as a function of the number of iterations. Using such procedures, it might even be feasible to construct an expert system for automatic interpretation of the measurement results. This is very interesting as interpretation of the results takes up a considerable amount of time, especially when the measurements are distorted by propagation effects.

7.4 SONAR AND RADAR

These two disciplines are presented in one Section, as many of the signal processing techniques to be discussed here,can be applied to both sonar and radar. We will first give a short overview of the main objectives of both disciplines.

Sonar

The name SONAR is an acronym for "SOund NAvigation and Ranging". It is a technique similar to radar, but the electro-magnetic waves in air are replaced by acoustic waves in water. Sonar can be divided into two operationally different techniques, i.e. active and passive sonar.

Active sonar systems radiate acoustic energy into the medium with a *projector* (underwater loudspeaker) and observe the reflections from objects in the water with (arrays of) *hydrophones* (underwater microphones). The objects can range from fish to submarines. The received reflection signals are processed to find:

- **The distance of the reflector.** It can be found from the delay time between the radiated and the reflected waves, making use of the propagation speed of sound in water, (about 1500 m/s);
- **The direction of the reflector.** For this measure, good lateral resolution is necessary, so the hydrophone (array) must be large, compared with the wavelengths of the received sound in at least one dimension;

- **The speed of the reflector.** This can be found from the Doppler-shift between the radiated and reflected waves.

In passive, or listen-only sonar, hydrophone arrays are used to observe the immission from external sound sources. The received signals are processed to find:

- **The source distance.** The distance of the radiating objects can be estimated only from the curvature of the received wavefront, so range finding is restricted to the near field of the array;

- **The source direction.** Here we have the same situation as in active sonar, i.e. the hydrophone array must be long compared with the wavelengths in at least one dimension;

- **The source type.** Classification is done by spectral analysis of the time signals of the emitting sources.

Active sonar systems are used in commercial applications as fish location finding, navigation, and bottom mapping. They are also used in military applications such as target localization, weapons guidance and communications. Passive sonar systems are mainly used for applications such as target detection, localization and classification.

Propagation of sound through seawater is strongly influenced by:

- Reflections at the horizontal boundaries, i.e. the sea surface and the sea bed, which give rise to multipath reception and, at larger distances, to ducting. Ducting — or wave-guiding — can also be the result of depth-dependent propagation speeds due to differences in temperature and salinity. The non-stationarity of the multipath reception causes longitudinal and transverse coherence loss of the waves;

- The absorption of sound in seawater, which is strongly dependent on frequency and ranges from less than 10^{-3} dB/km below 100 Hz to more than 100 dB/km above 1 MHz.

The large absorption of underwater sound at high frequencies restricts the frequency range of sonar severely. Active sonar systems usually function in the frequency range from 2 kHz to 40 kHz with a practical limit to distances of 1 to 10 km. Passive sonar systems are limited to the frequency range of about 10 Hz to 2 kHz, but special interest is paid to the frequency band from 10 Hz to 300 Hz, as it contains most information from vessels (Diesel engines and propulsion noise). At these frequencies absorption is small and observations are possible at distances of several 100 km, provided that favorable propagation conditions occur.

Although active and passive sonar systems are operated in a different way, they have in common that, in order to get sufficient lateral resolution, use is made of large arrays of hydrophones. Especially in passive systems, where wavelengths are between 150 m at 10 Hz to 5 m at 300 Hz, these arrays have to be very long. They may be constructed as a towed array: a

long hose with a large number of hydrophones, immersed in the water and towed by a ship where the signal processing takes place.

Surveys of sonar techniques are given by Knight et al. [48], Baggeroer [49] and Owsly [50].

Radar

The word RADAR stands for RAdio Detection And Ranging. Radar systems are based on the emission of electro-magnetic waves and the reception of these waves after they have been reflected by objects. In this respect, there is a large similarity between radar and active sonar, so it is not surprising that many sonar techniques are also used in radar.

The main objectives of radar are finding the distance, direction and velocity of the reflector. Applications are found in military systems as well as in civilian systems for air traffic control, ship navigation, weather mapping and speed measurements of road traffic. An extensive description of radar techniques is given by Skolnik [51].

Basically, a radar system consists of a radio transmitter, an antenna system, a radio receiver and a post processing system. In many cases, the sending signal is a repetitive burst and the antenna system is switched between sending and receiving. In its simplest form the transmitted burst has a short duration and the traveltimes of the received reflections are a direct measure for the distance of the reflector. To obtain better signal to noise ratios, the modern radar systems use a modulated pulse as a sending signal. Because of their long duration, these signals contain much more energy than short pulses, but the received signals have to be deconvolved for the transmitted signal to obtain a high temporal resolution. This is usually performed with a matched filter technique.

According to Skolnik [51], the carrier frequencies of radar systems range from about 3 MHz to about 40 GHz, with wavelengths from about 100 m to about 7.5 mm. The long wavelengths (>1 m) are used for long distance ranging, including beyond horizon observations; the wavelengths between 1 m and 5 cm are used for aircraft surveillance, and the even shorter wavelengths for marine navigation and such military applications as weapon control.

In order to obtain a high spatial resolution, the antenna must have a small beamwidth in the receiving mode. At high frequencies, a small beamwidth can be obtained with a parabolic reflector. In this case the radar system can scan the surroundings by rotation of the antenna disc. In many cases, however, the reaction time of mechanically steered beams is unacceptably large. This has led to the development of radar antenna arrays where the beamsteering is carried out electronically.

7.4.1 The data model

Radar and active sonar techniques are always based on *modulation* of a carrier frequency during transmission and *detection* of this modulation during receiving. Such a signal can be represented as a real function of time:

$$u(t) = m(t) \cos [2\pi f_0 t + \psi(t)] \tag{7.7}$$

where f_0 = carrier frequency

$m(t)$ = amplitude modulation

$\psi(t)$ = phase modulation.

A separation between the carrier and the modulation signal is obtained by taking the analytical signal

$$u_H(t) = u(t) + jH\{u(t)\} \quad , \tag{7.8}$$

where $H\{\cdot\}$ is the Hilbert transform operator. If $m(t)$ and $\psi(t)$ are narrow-band in relation to the carrier frequency, the analytical signal can be written as

$$u_H(t) = m(t) \exp[j\psi(t)] \exp(j2\pi f_0 t) = s(t) \exp(j2\pi f_0 t) \tag{7.9}$$

where $s(t) = m(t) \exp[j\psi(t)]$ is called the *complex modulation* or *complex amplitude*, consisting of the *in-phase* and *quadrature* components $\text{Re}\{s(t)\} = m(t) \cos \psi(t)$ and $\text{Im}\{s(t)\} = m(t) \sin \psi(t)$ respectively. Note that $s(t)$ contains all amplitude and phase information of the signal. Hence, it forms the basis for all signal processing after reception and demodulation. The complex signal $s(t)$ can be obtained from the received signal $u(t)$ with synchronous detection. To show this, Eq. (7.7) can be rewritten as

$$u(t) = \text{Re}\{s(t)\} \cos 2\pi f_0 t - \text{Im}\{s(t)\} \sin 2\pi f_0 t \quad . \tag{7.10}$$

The synchronous detection basically means multiplying $u(t)$ by $2\cos 2\pi f_0 t$ and low-pass filtering to obtain $\text{Re}\{s(t)\}$ and multiplying $u(t)$ by $-2\sin 2\pi f_0 t$ and low-pass filtering to obtain $\text{Im}\{s(t)\}$.

The same description can be used for the received signals of a passive sonar system after appropriate bandpass filtering around a central frequency f_0.

In the following, we will describe the signals with their complex amplitudes $s(t)$. Hence, the detected signals of an M-sensor array can be written as M complex signals $s_1(t)$, $s_2(t)$, ... $s_M(t)$. These signals are considered to be quasi monochromatic. This can be accomplished by narrow band filtering. The set of all received signals at one moment can now be written as a vector $s(t_i)$, given by:

$$s(t_i)^T = (s_1(t_i), s_2(t_i), \ldots , s_M(t_i)) \quad , \tag{7.11}$$

where T denotes transposition. The vector $s(t_i)$ is called a snapshot of the received data.

To obtain a uniform description of the received signals in passive and active systems, we will consider the reflecting objects in active systems as emitters. Although this is actually not true, they can be viewed as secondary sources and this will help us in understanding the nature of the receiver signals. (The same procedure is often applied in seismology, see Section 7.5). Using the same terminology as Schmidt [52], the amplitude behavior of each emitter is described by its complex modulation at one reference point. Usually this reference point is chosen at one of the receivers. If the complex amplitude of the kth emitter at time t_i at the reference position is given by $g_k(t_i)$, then the complex amplitudes of all K emitters can be represented by the vector $\mathbf{g}$:

$$\mathbf{g}^T = (g_1, g_2, \ldots, g_K) \ . \tag{7.12}$$

In this expression, the time variable t_i has been dropped for convenience. The number of emitters K may be or may not be known in advance. The elements of $\mathbf{g}$ can be viewed as the detected signals of each emitter as measured by an omni-directional sensor at the reference position. The contributions of each emitter k to the actual sensor signals $\mathbf{s}$ will depend on the emitter location, given by its distance r_k, its azimuth angle α_k, its elevation angle β_k, the sensor geometry and the directivity of each sensor. This is expressed by the so-called *mode vector* $\mathbf{a}_k(r_k, \alpha_k, \beta_k)$. The elements of $\mathbf{a}_k$ give the contributions of an emitter with $g_k = 1$ at each of the sensors. The vector continuum $\mathbf{a}(r, \alpha, \beta)$ for all values of the parameters r, α and β is called the *array manifold*.

Using a matrix notation, the received signals can now be written according to the following model:

$$
\begin{bmatrix} s_1 \\ s_2 \\ \cdot \\ \cdot \\ \cdot \\ \cdot \\ s_M \end{bmatrix}
=
\begin{bmatrix} & & & \\ \mathbf{a}_1 & \mathbf{a}_2 & \cdots\cdots & \mathbf{a}_K \\ & & & \end{bmatrix}
\begin{bmatrix} g_1 \\ g_2 \\ \cdot \\ \cdot \\ \cdot \\ g_K \end{bmatrix}
+
\begin{bmatrix} n_1 \\ n_2 \\ \cdot \\ \cdot \\ \cdot \\ n_M \end{bmatrix}
$$

or

$$\mathbf{s} = \mathbf{A}\mathbf{g} + \mathbf{n} \ , \tag{7.13}$$

where $\mathbf{n}$ represents the receiver noise. Notice that in this formulation no restrictions have been made concerning the emitter and receiver positions. The receivers can also have angle-dependent sensitivities, as will be expressed by the elements of $\mathbf{A}$.

For a better understanding of the structure of the matrix **A**, let us assume that the K emitters are in the far field of a full linear array with sensor spacing Δx and omni-directional sensors. With the reference position at the first sensor, the column vectors of **A** are given by:

$$\mathbf{a}_k^T = \left(1, e^{-j\phi_k}, e^{-j2\phi_k}, \ldots\ldots, e^{-j(M-1)\phi_k}\right) \tag{7.14}$$

with $\phi_k = (2\pi/\lambda)\Delta x \sin \alpha_k$. This result follows directly from the theory presented in Section 2.5 and the data model of Eq. (7.13). If the sensor spacing Δx is small enough to avoid spatial aliasing, there will be a one-to-one relation between the mode vectors $\mathbf{a}_k$ and the corresponding angle of incidence α_k. This is expressed by saying that the array manifold is *unambiguous*. Hence, the matrix **A** in Eq. (7.13) can be considered as a direction matrix, because each vector $\mathbf{a}_k$ has a unique relation with one source direction, while the source strengths are related to the complex amplitudes g_k.

We continue our discussion on the general model of Eq. (7.13), where the sources may be at any distance from an antenna with arbitrary sensor geometry and directivity. If the sensor array has been configured correctly, there will be a one-to-one relation between the vectors $\mathbf{a}_k$ and the parameters r_k, α_k and β_k, although in many practical situations, when the sources are in the far field of the antenna, a distinction between different r-values cannot be made and only the source directions α_k and β_k can be calculated. Note that in active sonar and radar applications, the (secondary) source distances are obtained from traveltime information. In the following we will restrict ourselves to the case of far field sources of which only the azimuth directions and the source strengths have to be estimated, using an antenna with an unambiguous array manifold. In this case the array manifold $\mathbf{a}(\alpha)$ is a one-parameter function.

7.4.2 Conventional beamforming

In broadband applications, all array elements are time-delayed, summed and filtered, giving a high output for one direction and range (this can be infinity) and a much lower output for other directions. This technique has the benefit that processing takes place in real time, so the output signals are available continuously for listening (in sonar) and for further processing.

The same principle can be applied to the monochromatic complex amplitudes, where the time delays are replaced by phase adjustments. Let us consider a full linear array with sources at infinity. Using Eq. (7.14) to compute $\mathbf{a}(\alpha)$, an estimate of the immission power for a direction α is obtained by phase compensation of the sensor signals for that direction, summing these signals and dividing by their number M to preserve unity gain, followed by quadratic averaging. This is expressed by

$$P_{BF}(\alpha) = \mathrm{E}\left\{|\frac{1}{M}\mathbf{a}^*(\alpha)\mathbf{s}|^2\right\} = \frac{1}{M^2}\mathrm{E}\left\{\mathbf{a}^*(\alpha)\mathbf{s}\mathbf{s}^*\mathbf{a}(\alpha)\right\} = \frac{1}{M^2}\mathbf{a}^*(\alpha)\mathbf{S}\mathbf{a}(\alpha) \tag{7.15}$$

where **a*** is the complex conjugate transpose of **a** and $S = E\{ss*\}$ is the correlation matrix of the sensor signals.

Using the data model of Eq. (7.13) and making the assumption that the emitter signals **g** and the noise **n** are uncorrelated, **S** can be written as:

$$\mathbf{S} \quad = E\{ss*\} \quad = \mathbf{A}\,E\{gg*\}\,\mathbf{A}* + E\{nn*\} = \mathbf{AGA}* + \sigma_a^2\mathbf{N} \quad . \tag{7.16}$$

In this expression $\mathbf{G} = E\{gg*\}$ represents the correlation matrix of the emitter signals. If the source signals are uncorrelated, as is the case in passive sonar, **G** is diagonal, but in general **G** will only be restricted to be positive definite because of the correlations between the incident waveforms. In radar, the reflections usually are highly correlated. **N** represents the correlation matrix of the noise signals, scaled in such a way that tr **N** (trace of **N** = sum of the diagonal elements) $= M$. Hence, **N** defines the structure of the noise and σ_a^2 the average noise power. Note that in case of uncorrelated noise with equal power at each sensor, $\sigma_a^2\mathbf{N} = \sigma^2\mathbf{I}_M$, where σ^2 is the noise power and $\mathbf{I}_M$ is the $M \times M$ identity matrix.

Substitution of Eq. (7.16) into (7.15) gives

$$P_{BF}(\alpha) = \frac{1}{M^2}\,\mathbf{a}*(\alpha)\mathbf{AGA}*\,\mathbf{a}(\alpha) + \frac{1}{M^2}\,\mathbf{a}*(\alpha)\sigma_a^2\mathbf{N}\mathbf{a}(\alpha) \quad . \tag{7.17}$$

This result clearly shows that the output of the beamsteered array consists of two terms; a part caused by the emitters and a part caused by the additive noise.

As a first example, let us consider the simple case of a single source in the direction α_1, with immission power $E\{g_1*\,g_1\} = P_1$ and uncorrelated noise with power σ^2 at each sensor. In this situation, Eq. (7.17) reduces to

$$P_{BF}(\alpha) = \frac{1}{M^2}\,\mathbf{a}*(\alpha)\mathbf{a}(\alpha_1)P_1\mathbf{a}*(\alpha_1)\mathbf{a}(\alpha) + \frac{1}{M}\,\sigma^2 \quad ,$$

$$= \frac{P_1}{M^2}\,\left|\mathbf{a}*(\alpha)\mathbf{a}(\alpha_1)\right|^2 + \frac{1}{M}\sigma^2 \quad . \tag{7.18a}$$

Using Eq. (7.14), we find

$$\left|\mathbf{a}*(\alpha)\mathbf{a}(\alpha_1)\right|^2 = \left|\sum_{m=0}^{M-1}\exp(jm(\phi - \phi_1))\right|^2 = \left|\frac{\sin\frac{M}{2}(\phi - \phi_1)}{\sin\frac{1}{2}(\phi - \phi_1)}\right|^2 \quad , \tag{7.18b}$$

with $\phi = (2\pi/\lambda)\Delta x \sin\alpha$ and $\phi_1 = (2\pi/\lambda)\Delta x \sin\alpha_1$. Eq. (7.18b) has maxima with the value M^2 for $\phi - \phi_1 = 2\pi n$ (n = integer). When $\Delta x < 1/2\,\lambda$ this maximum will only occur if $\phi - \phi_1 = 0$, or $\alpha = \alpha_1$. In that case the array has no grating lobes or ambiguities.

If we choose $\alpha = \alpha_1$, we find from Eq. (7.18a):

$$P_{BF}(\alpha_1) = P_1 + \frac{1}{M}\sigma^2 \ . \tag{7.19}$$

Hence, in this simple case, the maximum of $P_{BF}(\alpha)$ will give the correct source direction and, as shown by Eq. (7.19), the measured source power is only biased by the noise.

As a second example, let us see what happens in case of two uncorrelated sources in the directions α_1 and α_2 with powers P_1 and P_2. Here too, we will assume uncorrelated noise with power σ^2 at each sensor. Now Eq. (7.17) becomes

$$P_{BF}(\alpha) = \frac{1}{M^2}\mathbf{a}^*(\alpha)\mathbf{a}(\alpha_1)P_1\mathbf{a}^*(\alpha_1)\mathbf{a}(\alpha) + \frac{1}{M^2}\mathbf{a}^*(\alpha)\mathbf{a}(\alpha_2)P_2\mathbf{a}^*(\alpha_2)\mathbf{a}(\alpha) + \frac{1}{M}\sigma^2 \ . \tag{7.20}$$

Beamsteering in the direction α_1 gives

$$P_{BF}(\alpha_1) = P_1 + \frac{1}{M^2}\mathbf{a}^*(\alpha_1)\mathbf{a}(\alpha_2)P_2\mathbf{a}^*(\alpha_2)\mathbf{a}(\alpha_1) + \frac{1}{M}\sigma^2 \ . \tag{7.21}$$

This result shows that beamsteering in the direction α_1 also gives a contribution of the source in the direction α_2, because $|\mathbf{a}^*(\alpha_1)\mathbf{a}(\alpha_2)|$ will generally not be zero. Only when $\mathbf{a}(\alpha_1)$ and $\mathbf{a}(\alpha_2)$ happen to be orthogonal, the second term in the right hand side of Eq. (7.21) will vanish. Notice that the behavior of $\mathbf{a}^*(\alpha)\mathbf{a}(\alpha_1)$ for different values of α can be seen as a formulation of the angular resolution problem of the beamsteering.

7.4.3 Adaptive beamforming

There has been extensive research in the field of adaptive beamforming. These techniques can be seen as a special kind of time-delay and sum beamforming, where the weighting factors of the summing procedure are chosen in such a way that:

a. The antenna has a high output in the observation direction (large main lobe);

b. Interfering noise sources are suppressed as much as possible (small side lobes).

In sonar applications, the interfering noise sources are sometimes very directional and may be caused, for instance, by nearby non-target vessels. In radar, the interference may be due to other radar installations. In its simplest form noise suppression is achieved by additional beamsteering in the direction of the interfering noise. The output of that beamsteering is then optimally scaled and subtracted from the output signal of the primary beamsteering. Notice the strong resemblance of this procedure with the CLEAN method, described in Section 7.3.

If the interfering noise field is complicated, the optimal beamforming process demands elaborate processing schemes, based on estimates of the correlation matrix of the sensor signals. One of these methods is Capon's Maximum Likelihood method, to be discussed in the next paragraph.

7.4.4 Capon's Maximum Likelihood Method

This method has been developed by Capon [53] for the Large Aperture Seismic Array (LASA) which was built for the purpose of discriminating between tremors and covert underground nuclear weapon tests. This technique has become popular in several disciplines, especially so in sonar and radar. The algorithm can be derived from different optimization criteria. The maximum likelihood derivation is — strictly speaking — only applicable for the estimation of the complex amplitudes of monochromatic point sources in a spatially extended noise field, also including instrumentation noise. The Capon algorithm can also be derived for narrow band random point sources and this approach will be followed here, because it is more appropriate for SYNTACAN applications. In this case the term maximum likelihood is actually a misnomer and it would be better to call it a minimum noise variance procedure. We will now give a short derivation of Capon's method, based on the minimum noise variance criterion.

Let us consider an array of sensors in the wavefield of a number of narrow band point sources, for which the data model of Eq. (7.13) is valid. In § 7.4.2 we discussed how a conventional beamformer combines the sensor signals s with a steering vector a to obtain an estimate of the immission power from one direction. In that case the steering vector only contains phase factors. The steering vector can be made more general — containing weighting coefficients with different amplitudes and phases — such that an optimization is obtained according to some criterion. Such a beamforming process is illustrated in figure 7.9. The output of this beamformer is given by:

$$P(\alpha) = E\left\{ |w^*(\alpha)s|^2 \right\} = w^*(\alpha)Sw(\alpha) \ . \tag{7.22}$$
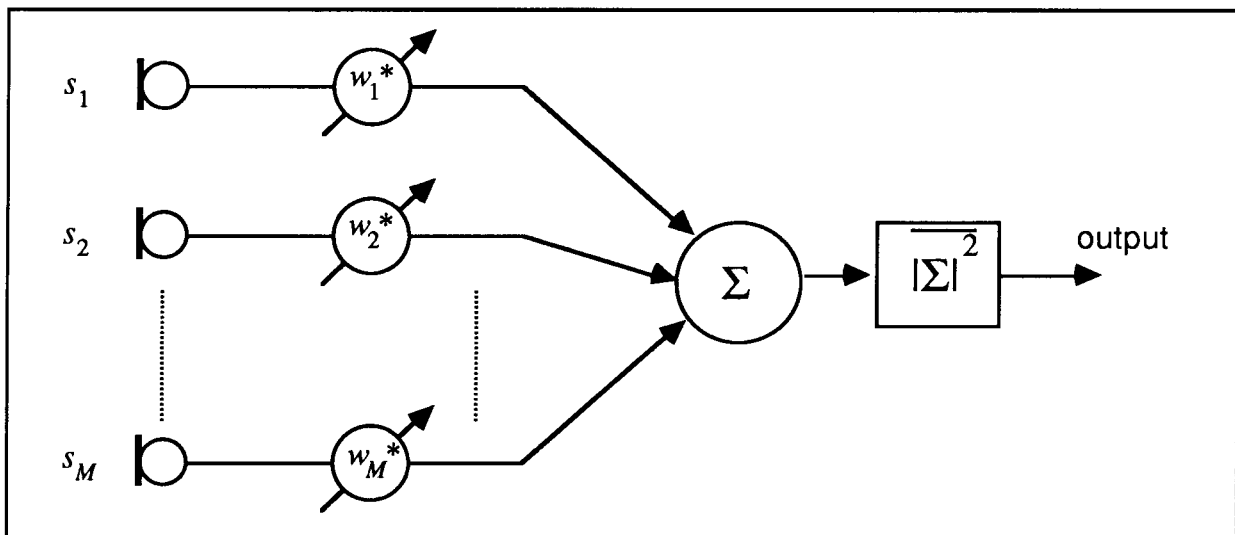

Figure 7.9: Principle of a general weight and sum beamformer.

In the Capon method, the optimal steering vector $\mathbf{w}^*$ is found by minimizing $P(\alpha)$ of Eq. (7.22) under the constraint that the beamformer has unity gain in the direction α, expressed by

$$\mathbf{w}^*(\alpha)\mathbf{a}(\alpha) = 1 \quad , \tag{7.23}$$

where $\mathbf{a}$ is the mode vector for the direction α, as defined in § 7.4.1. The minimization of Eq. (7.22) under the constraint of Eq.(7.23) is given by

$$\nabla_{\mathbf{w}} \{\mathbf{w}^*\mathbf{S}\mathbf{w} - \lambda\mathbf{w}^*\mathbf{a}\} = 2\mathbf{S}\mathbf{w} - \lambda\mathbf{a} = 0 \tag{7.24a}$$

where λ is a Lagrange multiplier, or

$$\mathbf{w} = \frac{\lambda}{2} \mathbf{S}^{-1}\mathbf{a} \quad . \tag{7.24b}$$

Combination of Eq. (7.23) and (7.24b) to solve for λ gives the optimal steering vector for the observation direction α:

$$\mathbf{w}(\alpha) = \frac{\mathbf{S}^{-1}\mathbf{a}(\alpha)}{\mathbf{a}^*(\alpha)\,\mathbf{S}^{-1}\mathbf{a}(\alpha)} \quad . \tag{7.25}$$

The minimized power (the output of the beamformer) is found by substitution of Eq. (7.25) into (7.22), giving the result

$$P_{\mathrm{C}}(\alpha) = \frac{1}{\mathbf{a}^*(\alpha)\,\mathbf{S}^{-1}\,\mathbf{a}(\alpha)} \quad . \tag{7.26}$$

For the application of Capon's method it is sufficient to calculate an estimate of the correlation matrix $\mathbf{S}$ and to compute $P_{\mathrm{C}}(\alpha)$ for a range of α-values, using Eq. (7.26). Note that the array sensors do not need to be at equidistant positions or even on a straight line, and that the mode vectors $\mathbf{a}$ can be calculated for all source positions; the Fraunhofer condition is not necessary.

The Capon method has been tested for the SYNTACAN array with a small number of simulations. The cross-spectrum of the antenna signals due to the simulated source distribution was computed in the ξ-domain, in the same way as in § 7.3.3 for the CLEAN simulations (there it was called the u-domain). This cross-spectrum gives the first row of the correlation matrix $\mathbf{S}$. The other rows can easily be calculated by making use of the Toeplitz structure of $\mathbf{S}$ (all diagonals have the same values) and of the Hermitian property of $\mathbf{S}$. Notice that in this way the correlation matrix of SYNTACAN is exactly the same as for a full linear array, with the restriction that this is only true in case of uncorrelated noise sources. The simulations were carried out for some of the same situations as used in § 7.3.3, to facilitate a comparison between CLEAN and the Capon method.
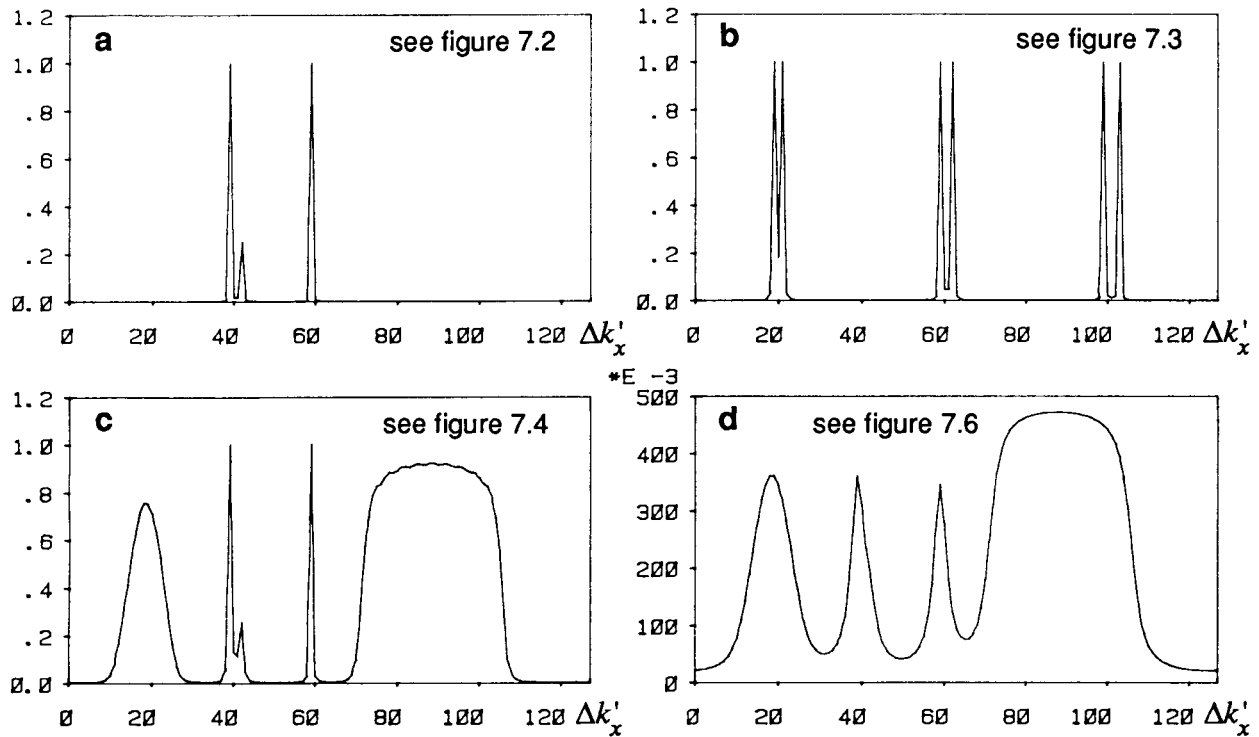
Figure 7.10: Simulation results of the Capon method; to be compared with the referenced figures.

Figure 7.10a shows the results of the same simulation as presented in figure 7.2: three point sources, measured with an antenna length of 31 $\Delta\xi$. Figure 7.10b should be compared with figure 7.3 and shows a resolution test. The results clearly show that the Capon method measures the correct source strengths and that it has an excellent resolution, which goes beyond the Rayleigh criterion. In figure 7.10c, the more complicated situation of point-sources and distributed sources is presented (see figure 7.4), again measured with an antenna length of 31 $\Delta\xi$. It shows two drawbacks of the method: the resolution of the closely spaced point sources has become worse due to the extended sources, and the method does not give correct estimates of the extended source areas: the estimates are much too high. In figure 7.10d the Capon results are given that should be compared with figure 7.6. Here the simulation is carried out for the full antenna length of 63 $\Delta\xi$, but the cross-spectrum is multiplied with a coherence loss according to Eq. (7.6) with $\beta = 5 \times 10^{-4}$. In this situation the Capon method does not give any improvement of resolution. This is not surprising, because the method does not take this condition into account. A correction would be possible using inverse filtering of the cross-spectrum with the correct coherence loss, before the method is applied. Note that this is only possible if the coherence loss is identical for all sources. In conclusion it must be stated that the Capon method is ideally suited for direction and source strength finding of point sources in a medium without coherence loss, but application to SYNTACAN is doubtful, because these conditions are seldom met in industrial noise source measurements.

7.4.5 Conventional 2-dimensional Fourier processing.

This processing scheme has been described in Section 2.5. It gives a decomposition of the wavefield in monochromatic plane waves from different angles of incidence. The processing is usually based directly on the received signals and not on the time-space correlation function (see Section 2.6). This seems surprising, as the latter technique gives the possibility of sparsed array processing where the number of sensors can be reduced for a given array length. However, under circumstances of bad signal to noise ratios, a full array gives a better performance for the detectability of targets. This has been discussed for sonar arrays by Earwicker [54]. Besides, full arrays are more flexible in maintenance and it is easier to switch between different procedures of array processing.

7.4.6 Parametric spectral estimation

The decomposition of the wavefield into plane waves from different directions is comparable to the classical estimation problem of temporal spectra, where the time variable t is replaced by the place coordinate x and the temporal frequency f by the spatial frequency k_x'. This has already been discussed in Section 2.5, where we found that in case of a number of far-field sources, the wavefield can be expressed in the k_x'-f domain as:

$$\tilde{S}(k_x',f) = \sum_n S_n(f)\, \delta\, (k_x' - f/c_n) \qquad (7.27)$$

with $c_n = c\ /\ \sin \alpha_n$, where $S_n(f)$ is the temporal spectrum of source n and α_n is the angle of incidence. This principle is illustrated in figure 7.11. Hence, if the sources are in the far field, the spatial spectrum gives direct estimates of the source directions and immission levels. To apply a spatial spectrum estimation technique, the sensor signals $s(x, t)$, where $x = 0$, Δx, ..., $(N-1)\Delta x$ are first Fourier transformed from the time domain to the temporal frequency domain, giving $S(x, f)$ for $x = 0$, Δx, ..., $(N-1)\Delta x$. The spatial spectrum estimation is then
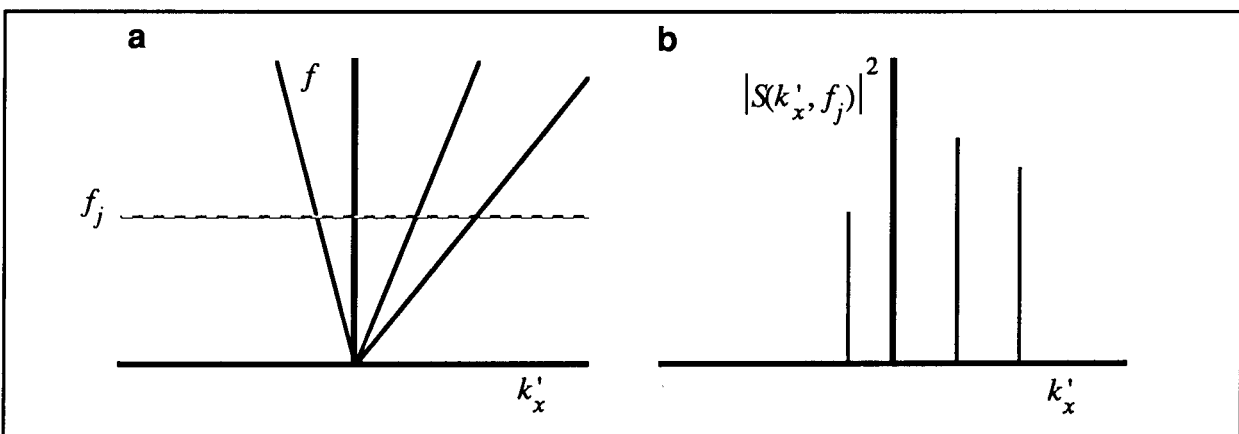

Figure 7.11: Source direction finding, viewed as a spectral estimation problem. a: source directions, mapped in the k_x'-f domain, b: spatial spectrum for one temporal frequency component f_j.

applied separately for each temporal frequency component f_j. Hence, the input for the spatial spectrum estimation procedures is given by the complex sensor signals $S_1, S_2,..., S_N$, where $S_i = S((i-1)\Delta x, f_j)$.

Spectrum estimation is usually obtained with Fourier processing, but if the observation length (here the aperture) is short, the resolution will be poor. Under such conditions parametric spectral estimation can give better, so-called super-resolution results. These techniques are summarized here, because they are under investigation in sonar and radar.

In conventional Fourier processing, the power spectrum is obtained from data, measured at a limited number of equally spaced positions (or time intervals). Although it is known that these samples should be extended beyond the measured aperture (or time window), the standard Fourier techniques do not give possibilities for that. Instead, zeros are assumed in the region not-measured. If the data is periodic over the observed interval, the Discrete Fourier Transform (DFT) gives exact answers, but usually this condition is not met and severe sidelobes are the result. These sidelobes can be reduced by aperture windowing at the price of mainlobe broadening. If the aperture length is long, these shortcomings are not severe and the decomposition into a harmonic set of frequencies gives a good sampling of the actual spectrum. However, if the aperture is short, it may be necessary to abandon the direct Fourier approach and to search for alternatives. At first sight one may argue that a dramatic improvement of the spectral resolution cannot be expected, because this would violate the general resolution principle, as for instance given by Eq. (1.3). We must however keep in mind that all parametric estimation techniques are based on an *assumed model* of the signals generated by the array sensors. This means that, instead of assuming zeros, the measurements are extrapolated outside the registration window. To give an example, if the model of the received data is a harmonic set of frequencies, then the DFT gives a least squares estimate of the complex amplitudes of these frequencies. If, however, the data can be described by a limited number of poles, an AR-model will give a much better resolution.

An overview of traditional and parametric spectral estimation procedures is given by Kay and Marple [55]. These are summarized in Table 7.1.

We will now give some comments on the techniques presented in Table 7.1 and will bring them into relation with the SYNTACAN system. The periodogram is based on a direct Fourier transform of the sensor signals S_i and is identical with a monochromatic delay and sum beamformer. This procedure is repeated for a number of realizations and the spatial amplitude spectrum is averaged to obtain a reliable estimate. The Blackman-Tukey (BT) approach first computes estimates of the auto-correlation function of the S_i-signals. This auto-correlation function is then Fourier transformed to find an estimate of the spatial spectrum. An important difference between both methods is that the spatial periodogram can only be computed with a full linear array, whereas the spatial BT-method can be applied on a sparsed array, as only a

Table 7.1

Summary of spectral estimation methods, according to Kay and Marple [54].

Name of technique	Model	Procedure
Periodogram	Sum of harmonically related sinusoids	FFT and averaging of power spectrum
Blackman-Tukey	Continuous spectrum	Fourier transform of auto-correlation function
AR Yule-Walker version	Auto-regressive process	Levinson recursion from auto-correlation function
AR Burg-algorithm	Auto-regressive process	Minimizes the prediction error, using the Levinson constraint
AR Marple-algorithm	Auto-regressive process	Minimizes the prediction error, without constraints
MA	Moving average process	Generalized BT-procedure
ARMA	Auto-regressive moving average process	Usually the AR and AM parameters are solved separately
Pisarenko Harmonic Decomposition (PHD)	Non-harmonic undamped sinusoids in white noise	Eigenvalue analysis of the auto-correlation matrix
Prony's extended method	Non-harmonic, exponentially damped sinusoids	Least squares fit of model
Prony's spectral line decomposition	Non-harmonic undamped sinusoids	Least squares fit of model
Capon Maximum Likelihood	Sinusoids in a continuous background spectrum	Optimal bandpass filter for each spectral component

contiguous set of sensor spacings is needed. Actually, SYNTACAN makes use of the BT-method, the necessary auto-correlation function being equivalent with the spatial cross-spectrum $\tilde{R}(\xi, f)$, as defined in Section 2.6.

The applicability of the parametric spectral estimation methods to SYNTACAN will strongly depend on the validity of the underlying signal model. Let us consider the case of a number of far-field point sources. Under ideal circumstances the spatial cross-spectrum of such a field is given by

$$\tilde{R}(\xi, f) = \sum_n \tilde{R}_n(f) \exp(-j2\pi f \xi / c_n) , \qquad (7.28)$$

which represents a number of sinusoids at $k_x = 2\pi f/c_n$. In principle, the cross-spectrum as measured over the antenna length X can be extended with AR-procedures. However, better results can be expected from models which are specially based on non-harmonic undamped sinusoids. It is shown by Kay and Marple [55] that the most accurate estimates are obtained with Prony's spectral line decomposition.

When transverse coherence loss occurs, due to turbulence in the propagation path, the spatial cross-spectrum is given by

$$\tilde{R}\ (\xi, f) = \sum_n \tilde{R}_n(f)\ \exp(-\beta_n|\xi\ |f)\ \exp(-j2\pi f\xi/c_n) \tag{7.29}$$

and this expression is in agreement with Prony's extended method. Note that this procedure allows for each source to have its own specific transverse coherence loss. This can be important if the sources are at different heights and distances.

7.4.7 The MUSIC algorithm

MUSIC stands for multiple signal classification. It is a method, developed by Schmidt [52], for the decomposition of the signal correlation matrix S into a *signal* and a *noise subspace*, which are spanned by the signal and the noise eigenvectors, respectively. We will use the data model of Eq. (7.13) and assume that the emitter signals g and the noise n are uncorrelated, so that S is given by Eq. (7.16).

Let us assume for this moment that the noise is uncorrelated and that all noise signals have the same power σ^2. In that case Eq. (7.16) gives

$$S = AGA^* + \sigma^2 I_M\ . \tag{7.30}$$

Because S is a Hermitian $M \times M$ matrix, it has M real and positive eigenvalues λ_i with corresponding orthonormal eigenvectors e_i, which satisfy the expression

$$Se_i = \lambda_i e_i\ ,\qquad\qquad \text{for } i = 1, ..., M. \tag{7.31}$$

Substitution of Eq. (7.30) into (7.31) gives

$$AGA^*e_i = (\lambda_i - \sigma^2)e_i\ ,\qquad\qquad \text{for } i = 1, ..., M. \tag{7.32}$$

If the number of incident waves K is smaller than the number of array elements M, AGA^* is singular with only K eigenvectors > 0. In addition, because G is positive definite, AGA^* is non-negative definite and has only non-negative eigenvalues. From inspection of Eq. (7.32) it follows that there are K eigenvalues $\lambda_1, ... , \lambda_K > \sigma^2$ and $M - K$ eigenvalues $\lambda_{K+1}, ..., \lambda_M = \lambda_{min} = \sigma^2$.

The situation is more complicated when the noise signals are correlated. In that case N will only be restricted to be positive definite. For this general situation Schmidt [52] makes use of

the generalized eigenvectors and eigenvalues of S in the metric of N, which means that the eigenvectors of S are expressed in a coordinate system based on the eigenvectors of N and must satisfy the expression:

$$Se_i = \lambda_i Ne_i \quad , \qquad\qquad \text{for } i = 1, ..., M. \qquad\qquad (7.33)$$

Substitution of Eq. (7.16) now gives

$$AGA^*e_i = (\lambda_i - \sigma_a^2)Ne_i \quad , \qquad\qquad \text{for } i = 1, ..., M. \qquad\qquad (7.34)$$

With the same arguments as presented above (AGA^* is singular and non-negative definite) it can be found that in the metric of N there are K eigenvalues $\lambda_1, ..., \lambda_K > \sigma_a^2$ and $M - K$ eigenvalues $\lambda_{K+1}, ..., \lambda_M = \lambda_{min} = \sigma_a^2$. Hence, Eq. (7.16) can be written as

$$S = AGA^* + \lambda_{min}N \quad . \qquad\qquad\qquad (7.35)$$

From Eq. (7.34) it can be seen that for the minimum eigenvectors $e_{K+1}, ..., e_M$, AGA^* $e_i = 0$ or $A^* e_i = 0$. This means that these eigenvectors are orthogonal to the space spanned by the columns of A, the mode vectors, or stated otherwise: the signal and noise subspaces are orthogonal. This also means that each mode vector a_k will be orthogonal to the subspace E_N, spanned by the noise eigenvectors $e_{K+1}, ..., e_M$. This property forms the basis of the MUSIC algorithm, where the minima of $|a(\alpha)^*E_N|^2$ are searched for by scanning all possible α-values. Note that for each α the corresponding $a(\alpha)$ is given by the array manifold, which can be computed from the array geometry and sensor directivities, or measured under laboratory conditions.

The MUSIC algorithm consists of the following steps:

1. Collect data and compute S.
2. Estimate the number of signals K (if unknown). As described by Schmidt, this can be performed with a χ^2 test.
3. Estimate the noise subspace matrix E_N, consisting of the $M - K$ eigenvectors $e_{K+1}, ..., e_M$.
4. Find the source positions from the minima of $|a^*E_N|^2$ or, as Schmidt defines in case of far field sources, search for peaks of

$$P_{MU}(\alpha) = \frac{1}{a^*(\alpha)\, E_N\, E_N^*\, a(\alpha)} \quad . \qquad\qquad\qquad (7.36)$$

5. Estimate the signal strengths and correlations G from Eq. (7.35) as:

$$G = (A^*N^{-1}A)^{-1}A^*(S - \lambda_{min}N)A(A^*N^{-1}A)^{-1} \quad . \qquad\qquad\qquad (7.37)$$

For the computation of the eigenstructure of S, the singular value decomposition (SVD) technique can be used, as given by Lanczos [57]. The K largest eigenvalues with associated eigenvectors define the signal subspace and the $M - K$ smallest eigenvalues are due to the noise. If the observation length would be infinitely long, the noise eigenvalues would all be exactly the same. In that case the number K can easily be found as the number of eigenvalues which are larger than λ_{min}. In practice, however, only an estimate of S will be available and a statistical test will be necessary as indicated in step 2 of the algorithm. The definition of P_{MU} as given by Eq. (7.36) is chosen in such a way that the source directions are indicated by peaks, just as with conventional beamforming. However, P_{MU} is not a measure for the source strengths, but only for the source directions. The source strengths must be computed with Eq. (7.37).

It is interesting to mention an essential difference between conventional beamforming and MUSIC. As demonstrated in § 7.4.2, the resolution of the conventional beamforming is limited by the fact that the different source mode vectors a_k are not orthogonal, and that property is essential because the maxima of $|a^*(\alpha)S|^2$ are used there as a measure of the source directions and immission strengths. This problem does not occur in the MUSIC algorithm, because here the minima of $|a^*(\alpha)E_N|^2$ are sought and E_N is orthogonal to all mode vectors a_k. Consequently, the direction finding and the source strength estimation of MUSIC for one direction are in principle not influenced by the presence of signals in other directions. This is an essential difference with conventional beamforming.

7.4.8   The KT-algorithm

We will now give a brief description of the algorithm, developed by Kumaresan and Tufts [58]. It can be seen as a variant of the MUSIC algorithm, as it also makes use of the eigenstructure of S. The most important difference is that the KT-method is restricted to the situation of far-field sources, detected by a full linear array, so the array manifold vectors have the form of Eq. (7.14).

The KT-algorithm searches for a vector d such that

$$a_i^* \, d = 0 \qquad \text{for } i = 1, \dots, K \ . \tag{7.38}$$

From the foregoing it will be clear that such a vector d must be a linear combination of the noise subspace vectors e_i for $i = M+1, \dots, K$. From the components of d, a polynomial $D(z)$ can be constructed, given by:

$$D(z) = \sum_{i=0}^{M-1} d_{i+1} z^{-i} \tag{7.39}$$

and this expression will have zeros at $z = \exp(-j\phi_i)$ for $i = 1, \dots, K$. From these roots the angles of incidence can be found.

Kumaresan and Tufts solve for that vector **d** which has the following constraints:

a. $d_1 = 1$;

b. $\sum_{i=1}^{M} |d_i|^2 = $ minimum.

The authors argue that this solution — as compared with the MUSIC algorithm — gives a more accurate estimate of the angles of arrival, even under bad signal to noise ratios, and that it has less tendency for "false sources" or spurious estimates.

Computer simulations by Kumaresan and Tufts demonstrate that the KT-algorithm performs better than the MUSIC algorithm, especially in cases of bad signal to noise ratios.

7.4.9 Conclusions

In this Section we have discussed the most important techniques which are used in or are in development for sonar and array processing. We have found that these array techniques are mainly concerned with target localization and classification under conditions of bad signal to noise ratios. This has led to the techniques known as adaptive beamforming. A favorable adaptive algorithm is the Capon Maximum Likelihood method, which anticipates on the structure of the noise field to obtain a high resolving power. Unfortunately, the procedure is only applicable to point sources in a medium without transverse coherence loss. For that reason the method is unattractive for our purposes, because these conditions are seldom met in industrial noise measurements.

Some of the parametric spectral estimation procedures — which are also suitable for spatial wavefield decomposition — look promising for application to the SYNTACAN data. Especially the extended Prony procedure might give good results, as this model is applicable to the data obtained from point sources in a turbulent atmosphere, where transverse coherence loss causes exponentially damped sinusoidal responses. Here again, it must be kept in mind that in many practical situations the industrial noise sources cannot be described as point sources, but must be considered as extended source areas. Under such conditions the parametric methods might completely fail, or at least reduce to the conventional spectral estimation procedures.

The MUSIC and KT-procedures could also be adapted to industrial noise source measurements, because the sound propagation from the sources to the antenna-microphones can be well described by Eq. (7.13). Because the acoustic signals usually have a wide temporal spectrum, narrow-band filtering will be necessary.

The MUSIC and KT-procedures have in principle been developed for full linear arrays, allowing for arbitrary cross-correlations between the emitters. Note that this is essential for radar and active sonar processing, because the emitters are in reality reflectors of the same

sending signal and, especially if the reflectors are close together — when there is a need for higher resolution — the transverse coherence loss will be small.

In our problem of industrial noise source measurements, we are primarily interested in the case where the noise sources are uncorrelated. This has resulted in the SYNTACAN design, based on sparsed array processing. This array will not be suitable for direct signal processing according to the MUSIC and KT algorithms. The KT algorithm explicitly demands that the array is fully linear and although the MUSIC algorithm does not demand this explicitly, the array manifold of SYNTACAN will be highly ambiguous. There might, however, be a possibility to apply the MUSIC or the KT procedures on the cross-spectra data of SYNTACAN, given by Eq. (2.105):

$$\tilde{R}(\xi, f) = \sum_n \tilde{R}_n(f) \, \exp(-j2\pi f \xi / c_n) \quad .$$

In that case the same procedure can be followed as in the simulations of the Capon method in § 7.4.4: $\tilde{R}(\xi, f)$ gives the first row of the correlation matrix S and the remaining elements are calculated by making use of the Toeplitz and Hermitian properties of S. This procedure is only valid when the noise sources are uncorrelated. The MUSIC and KT-algorithms show the same shortcomings as the Capon method: they are only applicable to point sources (the array manifold of extended sources will not be known a priori) and they cannot cope with transverse coherence loss.

7.5 SEISMOLOGY

In exploration seismology, information of the subsurface layers of the earth's crust is obtained by sending elastic waves into the medium and measuring the resulting reflections. From these reflections one tries to estimate the positions of the different layers and to find such physical parameters as lithology and pore fill. The results of these techniques are primarily used to find potential reservoirs of oil and natural gas.

In this Section we will give a brief description of the procedures used in exploration seismology and discuss a parametric technique which has been adapted to the SYNTACAN-system.

7.5.1 Measurements and signal processing procedures.

For seismic measurements, acoustic waves are sent into the earth's crust. If the surveys take place on land, the seismic sources either are *dynamite explosions* or *vibrators*, depending on the cultivation and local legislation. In marine surveys, use is made of airguns, which produce highly repeatable shock waves.

The reflected waves are measured on land by vibration pick-ups, called *geophones* and at sea by *hydrophones*. During a survey, measurements are taken for a large number of shot positions. For each shot position, simultaneous measurements are taken with a large number of receivers, placed in a one- or two-dimensional array.

A general overview of the most common seismic data acquisition and processing procedures is for instance given by Sheriff et al. [59] and, more specifically concerning the signal analysis, by Robinson and Treitel [60].

Seismic processing is based on the spatial and temporal recognition of the reflections from the boundaries of different earth layers. These reflections are caused by the differences in density and sound velocity of adjacent layers. Usually, the measured reflections are very weak, caused by the long propagation distances of several kilometers and by the absorption in the layers. Seismic signals usually contain energy in the frequency region between 2 and 200 Hz with a central region around 30 Hz. The sound velocities can be very different and are in the range from 500 to about 5000 m/s.

A severe problem of seismic data acquisition is the bad signal to noise ratio, not only because the received signals are weak, but also because there can be many disturbing vibrations that are also received by the geophones or the hydrophones. One of the biggest problems during land surveys is the reception of the surface wave of the source. This wave contains much energy and can travel so slowly that it arrives at the geophones together with the reflections of interest. These problems have led to acquisition and processing techniques, in which the signal to noise ratio is augmented as much as possible. Many of these techniques rely on the combination of the signals of several receivers and can thus be classified as array signal processing techniques.

We will now present a summary of the most commonly used techniques that are applied in seismics:

a. **Field array techniques.** In order to suppress the surface waves and to enhance the signal strengths of the "vertical" reflections, one places a group of geophones close together. Their output signals are summed, so the group of receivers act as a broadside array. This array has a high gain for the vertical reflections and gives a suppression of the surface waves and other disturbances, caused for instance by traffic. There is a general tendency to minimize the size of the field arrays and use them as "spatial anti-aliasing filters" only.

b. **Filtering.** The signal to noise ratio of the received signals can be further enhanced by temporal and spatial frequency filtering (band limitation).

c. **Deconvolution of the seismic wavelet.** The axial resolution is directly related to the time-resolution of the seismic traces. These traces consist basically of a series of pulses — caused by the reflections of the waves — convolved with the primary waveform, or *wavelet*. In this processing step the length of the wavelet is minimized with a deconvolution procedure.

d. **Calculation of zero-offset stacks.** For further processing of the reflections it is usually required to compute zero-offset traces. These are reflection patterns that would occur if sources and receivers coincide. The standard procedure to compute these zero-offset traces is based on the alignment and averaging of Common MidPoint (CMP) gathers. A CMP gather consists of traces where the source and receiver positions are symmetrical around one surface point, the *common midpoint*. For this procedure an estimate of an averaged wave propagation velocity for each reflector depth must be computed first. The stacking procedure not only simulates a zero-offset registration, but it also gives a considerable improvement of the signal to noise ratio. Notice that stacking is a kind of array beamforming.

e. **Migration.** The zero-offset traces are used to reconstruct the reflector positions. The post-stack migration technique is based on an *exploding reflector model,* where the reflections are replaced by imaginary sources which propagate to the surface with half the actual propagation speed. Using this model, the "source"-positions are computed with inverse wavefield extrapolation techniques. A profound treatment of this subject is given by Berkhout [26]. Migration can be viewed as a focussed array procedure for *inhomogeneous* media. This is an important difference with the antenna techniques, used in active sonar and radar, where the propagating medium is assumed to be homogeneous. Another important difference is the fact that seismic migration takes place in the near field of the sensors, while generally this is not the case in sonar and radar.

7.5.2 Trace inversion in seismics

As outlined in the preceding paragraph, one of the standard procedures in seismic signal processing is deconvolution of the seismic wavelet. If the wavelet, or primary pulse, is $w(t)$ and the reflectivity of the sublayers is $r(t)$, then the measured trace is given by

$$s(t) = w(t) * r(t) + n(t) \tag{7.40}$$

where $n(t)$ is additive noise. If $s(t)$ and $w(t)$ are known, and if one also has an estimate of the noise source power, the reflectivity function $r(t)$ can be obtained with inverse filtering procedures. A well known least squares inverse filtering procedure is given by Berkhout [7, 61] and can be written in the frequency domain as

$$F(f) = \frac{W^*(f)}{|W(f)|^2 + R_{nn}(f)/R_{rr}(f)} . \tag{7.41}$$

where $R_{nn}(f)$ and $R_{rr}(f)$ are the power spectra of the noise and the reflectivity, respectively. An estimate of the reflectivity is obtained as

$$\hat{r}(t) = f(t) * s(t) . \tag{7.42}$$

The resolution which can be obtained with this method is limited by the bandwidth of the wavelet and the power spectrum of the noise.

As was already mentioned in Section 7.4, if a parametric signal model is applied, so-called super-resolution can be obtained. This has been worked out for the seismic trace by Van Riel et al. [62]. The authors assume that the reflectivity can be written as

$$r(t) = \sum_{n=1}^{N} a_n \, \delta(t - \tau_n) \tag{7.43}$$

where a_n is the reflection strength and τ_n is the time lag of the nth reflector. A next step is, that the continuous time signals are replaced by sampled versions. Eq. (7.40) can then be written in matrix form as:

$$s = Wa + n \tag{7.44}$$

with $s^T = (s(0), s(\Delta t), \dots, s((M-1)\Delta t)$

$a^T = (a_1, a_2, \dots, a_N)$

$n^T = (n(0), n(\Delta t), \dots, n((M-1)\Delta t))$

and W is a matrix with elements

$$w_{mn} = w[(m-1)\Delta t - \tau_n] \qquad \text{for } m = 1, \dots, M; \, n = 1, \dots, N.$$

Eq. (7.44) gives a set of M equations from which the N reflection coefficients $a_1, \dots, a_N$ and the N time lags $\tau_1, \dots, \tau_N$ have to be solved. Notice that Eq. (7.44) is linear in the reflection coefficients a_i, but non-linear in the time lags τ_i. The proposed method makes use of a matrix inversion technique, which can be used to solve a linear set of equations. The non-linearity of the τ-parameters is avoided by a linearization of Eq. (7.44) around an initial model, leading to the approximation

$$s = W_0 \, a + X_0(\tau - \tau_0) + n \; . \tag{7.45}$$

W_0 is the operator W for $\tau = \tau_0$ and X_0 is a matrix with elements

$$x_{mn} = \left. \frac{\partial s_m}{\partial \tau_n} \right|_{a_0, \tau_0} \qquad \text{for } m = 1, \dots, M \, ; \, n = 1, \dots, N \; , \tag{7.46}$$

where a_0 and τ_0 are the parameters of the initial model. Eq. (7.45) can be solved iteratively for a and τ by using the estimates of τ to update the model, hoping that this approach converges to a stable solution.

We will now discuss how a solution of a can be found from Eq. (7.44) under the assumption that τ is known. Inspection of Eq. (7.44) suggests a solution of the form

$$\hat{a} = W^{-1} s \; , \tag{7.47}$$

where W^{-1} is the inverse of W and $\hat{a}$ is an estimate of a. However, this solution will only exist in the *well-determined* case, when the number of linear equations M equals the number of unknowns N, with as a further restriction that there is no linear dependence between the equations. In many cases $M > N$, which can lead to *over-determination* of the system, giving a *well-posed* problem for a statistical inversion procedure, but because $w(t)$ is a band limited operator, there will be dependence between the equations and this can make the problem *ill-posed*. These problems can be solved with the Singular Value Decomposition (SVD) of W, as given by Lanczos [57]:

$$W = U \Lambda V^* . \tag{7.48}$$

The columns of the $M \times N$ matrix U are the first N orthonormal eigenvectors of WW^* (the remaining eigenvalues are zero), the columns of the $N \times N$ matrix V are the N orthonormal eigenvectors of W^*W and Λ is an $N \times N$ diagonal matrix, containing the square roots of the eigenvalues of W^*W, called the singular values. The singular values and associated eigenvectors are organized in descending order. The *natural inverse* H of W is now obtained as:

$$H = V \Lambda^{-1} U^* , \tag{7.49}$$

leading to an estimate of the reflection coefficients, given by:

$$\hat{a} = Hs = a + V \Lambda^{-1} U^* n . \tag{7.50}$$

Notice from Eq. (7.49) that the natural inverse will only exist if none of the eigenvalues of Λ equals zero, so the rank of W must be N. Also notice from Eq. (7.50) that small eigenvalues of Λ can lead to an unacceptable large variance of $\hat{a}$.

From these observations it can be concluded that the problem is *well posed* if there are N large eigenvalues. In that case the noise will have little influence and $\hat{a} \approx a$. However, the problem is *ill-posed* if there are one or more small eigenvalues. As Eq. (7.50) shows, this can lead to considerable noise enhancement. The problem can even be unresolvable if one or more of the eigenvalues are zero.

In the case of ill-posed problems, a compromise can be found which will give the best resolution and the least variance under the given conditions. We will discuss three procedures which can be used for ill-posed problems (e.g. Van Riel [63], Menke [64], Bard [65], Jackson [66]). The optimalizations depend on the structure of the noise covariance matrix $C_n = cov(n, n)$, and the parameter covariance matrix $C_a = cov(a, a)$. These matrices may or may not be known in advance. If they are, making use of their properties can lead to results with better resolution and lower variance. The characteristics of the first two procedures to be discussed, can be described easier if the noise and the parameters are white processes, or otherwise stated: if $C_n = \sigma_n^2 I_M$ and $C_a = \sigma_a^2 I_N$. As this is generally not the case, we will perform a principle axis transformation to a coordinate system in which the noise covariance matrix equals I_M and

the parameter covariance matrix equals I_N. This normalization is obtained by multiplying Eq. (7.44) with $C_n^{-1/2}$ and writing it as:

$$C_n^{-1/2} s = C_n^{-1/2} W C_a^{1/2} C_a^{-1/2} a + C_n^{-1/2} n \qquad (7.51)$$

or

$$s_1 = W_1 a_1 + n_1 \qquad (7.52)$$

with $s_1 = C_n^{-1/2} s$; $W_1 = C_n^{-1/2} W C_a^{1/2}$; $a_1 = C_a^{-1/2} a$ and $n_1 = C_n^{-1/2} n$.

The SVD of W_1 is given by

$$W_1 = U_1 \Lambda_1 V_1^* \qquad (7.53)$$

and the natural inverse is obtained as

$$H_1 = V_1 \Lambda_1^{-1} U_1^* \quad . \qquad (7.54)$$

We are now ready to discuss the three stabilization procedures.

1. The general natural inverse. For this procedure the normalized description of Eq. (7.52) is needed. The stabilization is obtained by using only the N_c largest singular values of W_1, resulting in

$$H_c = V_c \Lambda_c^{-1} U_c^* \quad , \qquad (7.55)$$

and leading to the estimate of a_1:

$$\hat{a}_c = H_c s_1 = V_c V_c^* a_1 + V_c \Lambda_c^{-1} U_c^* n_1 \quad . \qquad (7.56)$$

N_c is called the cutoff point. It must be chosen such that a good compromise is found between the loss in resolution and the smaller variance because of the deletion of the smallest eigenvalues of Λ. It is shown by Van Riel [63] that $\hat{a}_g$ is the least mean squares estimate of this class of stabilization, when N_c is chosen such that all eigenvalues < 1 are discarded.

2. The diagonal stabilized inverse or ridge estimator. The instability of H_1, due to the smallest eigenvalues of Λ_1 is reduced here by replacing Λ_1^{-1} in Eq. (7.54) by

$$\Lambda_{st}^{-1} = \Lambda_1 (\Lambda_1^2 + c^2 I_N)^{-1} \quad , \qquad (7.57)$$

which means that the inverse eigenvalues $\lambda_1^{-1}(n)$ are replaced by

$$\lambda_{st}^{-1}(n) = \frac{\lambda_1(n)}{\lambda_1^2(n) + c^2} \quad . \tag{7.58}$$

Note the resemblance between this expression and the inverse filter of Eq. (7.41). It can be shown that in the normalized coordinate system, the least mean squares estimate of this class of stabilization is obtained with $c^2 = 1$ and that this estimate has the least total mean squares error of *all* linear estimators.

3. **The Bayesian approach.** This procedure can be viewed as a generalization of the ridge estimator. Using Bayes' rule of probability density functions (e.g. Jackson [66]), optimal use is made of the covariance matrices C_a and C_n and also of *a priori* values of the parameters that are sought. Application of this theory under the assumption of Gaussian statistics leads to the estimation $\hat{a}_b$:

$$\hat{a}_b = (W^* C_n^{-1} W + C_a^{-1})^{-1} (W^* C_n^{-1} s + C_a^{-1} a') \quad , \tag{7.59}$$

where the elements of a' are the a priori parameter values.

One might conclude that of these three methods, the best results can be expected from the Bayesian approach, as it makes use of a priori information of the parameters and the other methods do not. However, this a priori information can also be used in the first two methods by rewriting the model of Eq. (7.52) as

$$s_1 = W_1 (a_1' + \Delta a_1) + n_1 \tag{7.60}$$

and solving for Δa_1. Defined in that way, methods 2 and 3 turn out to be exactly equivalent.
Note that the general natural inverse and the ridge estimator also assume knowledge of C_a and C_n, as these quantities are required for the principle axis transformations to obtain the normalized form of Eq. (7.52). In many cases such detailed information is not available. The stabilization can then be applied by assuming for instance that the noise and the reflectivity are white Gaussian processes.

The general natural inverse has been worked out for the seismic trace inversion by Van Riel et al. [62]. In the following we will refer to this procedure as *the SVD-method*. If the problem is well-posed, the cutoff point $N_c = N$ (the number of unknown parameters) and the method is equivalent with the natural inverse of Eq. (7.49). In that case all parameters are well resolved. If the problem is ill-posed, due to small eigenvalues and the presence of noise, the smallest eigenvalues are deleted before inversion, leading to the estimate of Eq. (7.56). Note that this stabilization decreases the variance, but some of the resolution will be lost, as expressed by the resolution matrix P:

$$\mathbf{P} = \mathbf{H_c W} = \mathbf{V_c V_c^*}$$ (7.61)

which will be $\neq \mathbf{I_N}$ when $N_c < N$.

An important part of all parametric inversion methods is the verification of the model. For that purpose, a data mismatch vector $\mathbf{d}$ is defined, given by

$$\mathbf{d} = \mathbf{W\hat{a}} - \mathbf{s} \ .$$ (7.62)

If the model is not correct and the resolution is good, the data mismatch vector will clearly show the time lags where important reflections have been neglected, so that the model can be updated.

7.5.3 Applicability of the SVD method to SYNTACAN.

We will now discuss how the SVD-method can be adapted to the SYNTACAN system to acquire a better resolution for closely spaced sources. We will consider the case of a number of uncorrelated noise sources which can be described as monopoles in the far-field of our antenna, so that the Fraunhofer approximation is valid. We will assume that the propagation gives rise to a transverse coherence loss, which can be different for each noise source. Then the antenna response in the k_x'-f domain can be written for one frequency component f_i as (see § 3.3.3):

$$\tilde{R}'(k_x', f_i) = \sum_n \tilde{R}_n(f_i) \, \tilde{W}_n(k_x' - f_i / c_n)$$ (7.63a)

with

$$\tilde{W}_n(k_x') = \tilde{W}(k_x') * \tilde{\gamma}_n(k_x') \ ,$$ (7.63b)

where $\tilde{W}(k_x')$ is the basic beam pattern of the antenna and $\tilde{\gamma}_n(k_x')$ is the Fourier transform of the transverse coherence loss of source n. For simplicity, we will assume here that the source directions and the transverse coherence loss are known, so Eq. (7.63) has only to be solved for the unknown source spectra $\tilde{R}_n(f_i)$. This can be done through parametric inversion with the SVD method by rewriting Eq. (7.63) as the following linear matrix equation:

$$\mathbf{y} = \mathbf{W x} + \mathbf{g}$$ (7.64)

with
$$\mathbf{y}^T = (\tilde{R}'(k_0', f_i), \tilde{R}'(k_0' + \Delta k_x', f_i), \dots , \tilde{R}'(k_0' + (M-1)\Delta k_x', f_i)),$$
     where k_0' is the minimum value of k_x' of interest;
$$\mathbf{x}^T = (\tilde{R}_1(f_i), \tilde{R}_2(f_i), \dots , \tilde{R}_N(f_i));$$
$$\mathbf{g}^T = (G_1(f_i), G_2(f_i), \dots , G_M(f_i))$$
and $\mathbf{W}$ is a matrix, describing the *forward problem*, with elements

$$w_{mn} = \tilde{W}_n(k_0' + (m-1)\Delta k_x' - f_i/c_n) \ .$$

Equation (7.64) shows that the antenna response **y** is linearly related to the source powers **x**. Deviations from the ideal relationship are accounted for by the vector **g**, consisting of measurement noise and deviations from the applied model. Note that Eq. (7.64) has the same structure as Eq. (7.44), which means that the SVD method can be directly applied to Eq. (7.64), leading to the result

$$\overset{\wedge}{\mathbf{x}} = \mathbf{Hy} = \mathbf{V}_c \, \mathbf{V}_c^* \, \mathbf{x} + \mathbf{V}_c \, \Lambda_c^{-1} \, \mathbf{U}_c^* \, \mathbf{g} \quad . \tag{7.65}$$

We have investigated the applicability of this method for SYNTACAN and the results have been presented by Bakker [67] and by Boone et al. [68]. We will now discuss two simulation examples of the method.

As a first example, we consider 5 monochromatic monopoles, radiating at 1029 Hz and situated at a distance of 1000 m from the antenna, with angles of incidence and immission powers as indicated in table 7.2. It is assumed that there is no coherence loss ($\beta = 0$).

Table 7.2

Source directions and immission powers of 5 simulated monopole sources
for testing of the SVD-method.

angle in °	level in dB
−5	0
0	0
3	0
3.2	−3
7	0

The polar diagram of this simulation is given in figure 7.12a. This example has been chosen such that the sources at 3° and 3.2° are so close together that they are within the resolution of SYNTACAN, and can thus not be separated by the normal analysis software. The immission levels have been calculated with the angular integration method and the results are presented in table 7.3, showing that this method is correct within 0.5 dB, but of course the sources at 3° and 3.2° cannot be resolved.

To test the SVD-method, we first show the results of an initial model, where we assume that there are only sources at −5°, 0°, 3° and 7°. This model is based on the idea that, when sources are so close together that they fall within the resolution of the antenna, they can be modelled as one source. The SVD was computed under the assumption of white Gaussian noise with a level of −20 dB relative to the average immission power. Figure 7.13 gives a plot of the singular values of this model, indicating that the problem is well-posed. Application of this model, where the simulation data is first correctly "focussed at infinity" leads to the results of table 7.4. Notice that a very accurate estimation of the true immission levels is achieved. Figure 7.12b shows a polar presentation of the data mismatch of this model as defined by Eq. (7.62).

a

File :MOD3   Schaal: 15 dB
Temp. : 20.0 °C   Max. : 1.8 dB
Focus : 1000 m   Midd. : 1
                              -30 °

1000 Hz   30 °

b

File :MIS   Schaal: 15 dB
Temp. : 20.0 °C   Max. :-9.3 dB
                    Midd. : 1
                              -30 °

1000 Hz   30 °

c

File :MIS   Schaal: 15 dB
Temp. : 20.0 °C   Max. :-12. dB
                    Midd. : 1
                              -30 °

1000 Hz   30 °

d

File :SUP   Schaal: 15 dB
Temp. : 20.0 °C   Max. : .3 dB
                    Midd. : 1
                              -30 °
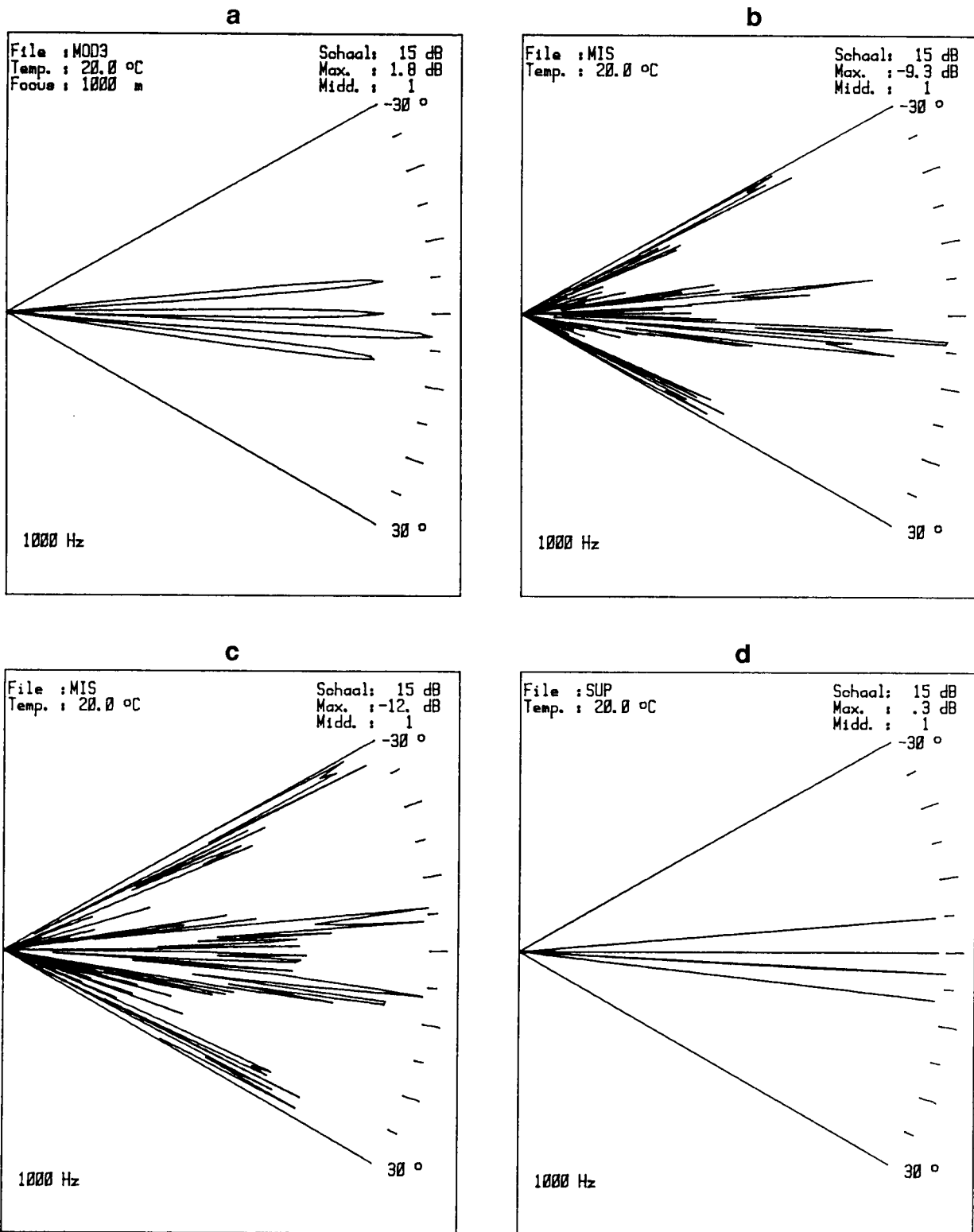
1000 Hz   30 °

Figure 7.12: Polar diagrams of the simulation of table 7.2, to test the performance of the SVD-method. a: conventional result; b: data mismatch of the initial model; c: data mismatch of correct model; d: super-resolution plot.

Table 7.3

Immission levels obtained with conventional SYNTACAN processing

integration range in °	true level in dB	estimated level in dB
−7 to −3 −2 to 1.5 1.5 to 5 5 to 9	0.0 0.0 1.8 0.0	0.0 0.5 1.4 0.0

Table 7.4

Immission levels obtained with the SVD-method, using an initial model of 4 sources

model angle in °	true level in dB	estimated level in dB
−5 0 3 (and 3.2) 7	0.0 0.0 1.8 0.0	0.0 0.0 1.7 0.0

Table 7.5

Immission levels obtained with the SVD-method, using the correct model of 5 sources

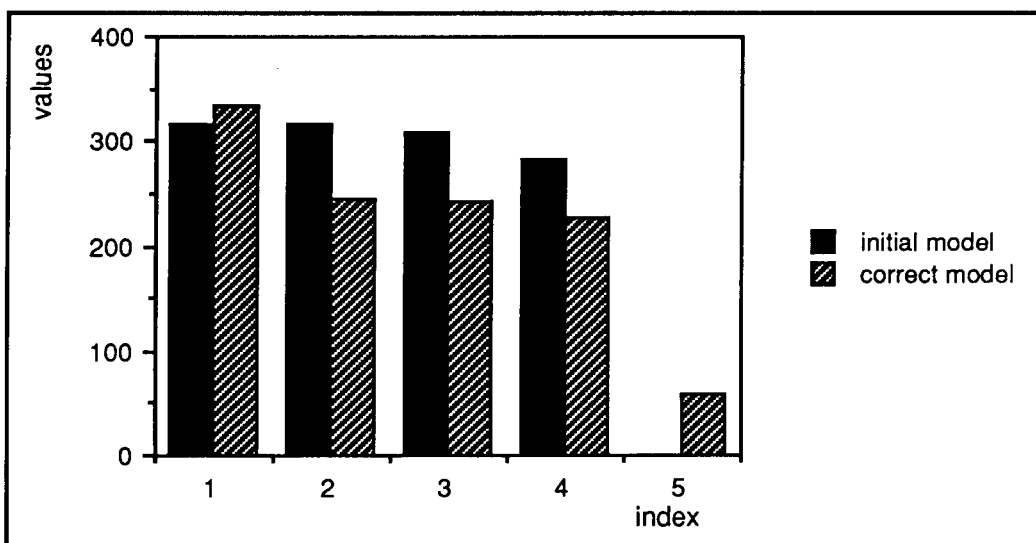| model angle in °	true level in dB	estimated level in dB
−5 0 3 3.2 7	0.0 0.0 0.0 −3.0 0.0	0.0 0.1 0.4 −3.9 0.1

Figure 7.13: Singular values of the two models of the first example.

Because the model is very near to the true model, the data mismatch is already low, but there is a clear peak in the direction of the missing source. The SVD was also computed for the correct model, where the source direction of 3.2° was included, also for a signal to noise ratio of 20 dB. The singular values are also given in figure 7.13. Notice that the two closely spaced source directions give rise to a relatively small singular value. Application of this model gives the data mismatch as given in figure 7.12c. The resulting data mismatch shows the imperfections of the implementation of the method. They are due to the applied focussing procedure, which is only exact at frontal incidence. This focussing is good enough for the conventional signal processing, but is no longer satisfactory for this super-resolution procedure. The results of this almost correct model are given in table 7.5 and in the super-resolution plot of figure 7.12d. Note that the two sources at 3° and 3.2° are so close together that they cannot be distinguished in the polar diagram! Also notice from table 7.5, that the method shows a deviation of 0.9 dB for the source at 3.2°. This must be due to the imperfect focussing.

The second example has been chosen such that there are a large number of closely spaced sources. Here, we also modelled monochromatic sources, radiating at 1029 Hz and situated at a distance of 1000 m from the antenna in a medium without coherence loss ($\beta = 0$). The SVD-method was applied under the assumption of white Gaussian noise with a signal to noise ratio of 20 dB. Table 7.6 shows the angles of incidence, the true immission powers and a summary of the SVD-results. The singular values of the model are given in figure 7.14. The smallest singular value is 10, so if the model is correct, the sources can be resolved completely with a small variance. Inspection of table 7.6 shows that for $N_c = 12$ there are considerable deviations from the true immission values for the closely spaced sources at 5° and 5.2°. As we discussed earlier, this is caused by the imperfect focussing. The deviations can be reduced by deletion of the smallest singular value, giving the results in table 7.6 for $N_c = 11$. However, the deletion of the smallest singular value has resulted in a loss of resolution. This is expressed by the resolution matrix **P** as defined by Eq. (7.61).

The resolution matrix of this model with $N_c = 11$ is presented in a graphical format in figure 7.15. It clearly shows that the deletion of the smallest singular value has resulted in "cross-talk" between the estimated source powers at 4.7°, 5° and 5.2°. Table 7.7 shows the immission levels obtained with conventional processing. Here those sources that did not produce separate mainlobes had to be combined. Notice that the levels of these "clusters" are measured very accurately by SYNTACAN. The polar diagrams of this model for conventional and SVD processing are given in figure 7.16.

Table 7.6

Immission levels obtained with the SVD-method with two different cutoff points.

index	source direction in °	true immission power [dB]	SVD with $N_c = 12$ [dB]	SVD with $N_c = 11$ [dB]
1	−10	3	3.2	3.2
2	− 8	2	1.8	1.8
3	− 5	6	6.1	6.1
4	0	0	−0.1	−0.1
5	1	0	0.0	0.0
6	2	0	−0.1	−0.1
7	4.7	4	4.2	4.6
8	5	4	5.1	4.2
9	5.2	4	2.2	3.1
10	7	2	2.6	2.6
11	7.5	2	1.5	1.6
12	10	0	0.3	0.3

Table 7.7

Immission levels obtained with conventional SYNTACAN processing

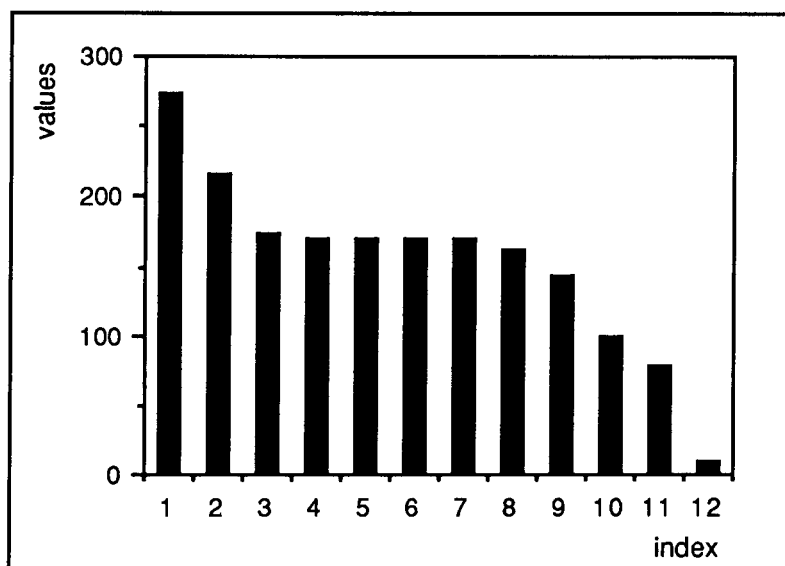| integration range in °	true level in dB	estimated level in dB
−12 to −9	3.0	3.0
− 9 to −6.5	2.0	1.6
− 6.5 to −2.5	6.0	6.1
− 2.5 to 3	4.8	4.6
3 to 6	8.8	8.4
6 to 9	5.0	5.9
9 to 12	0.0	−0.2

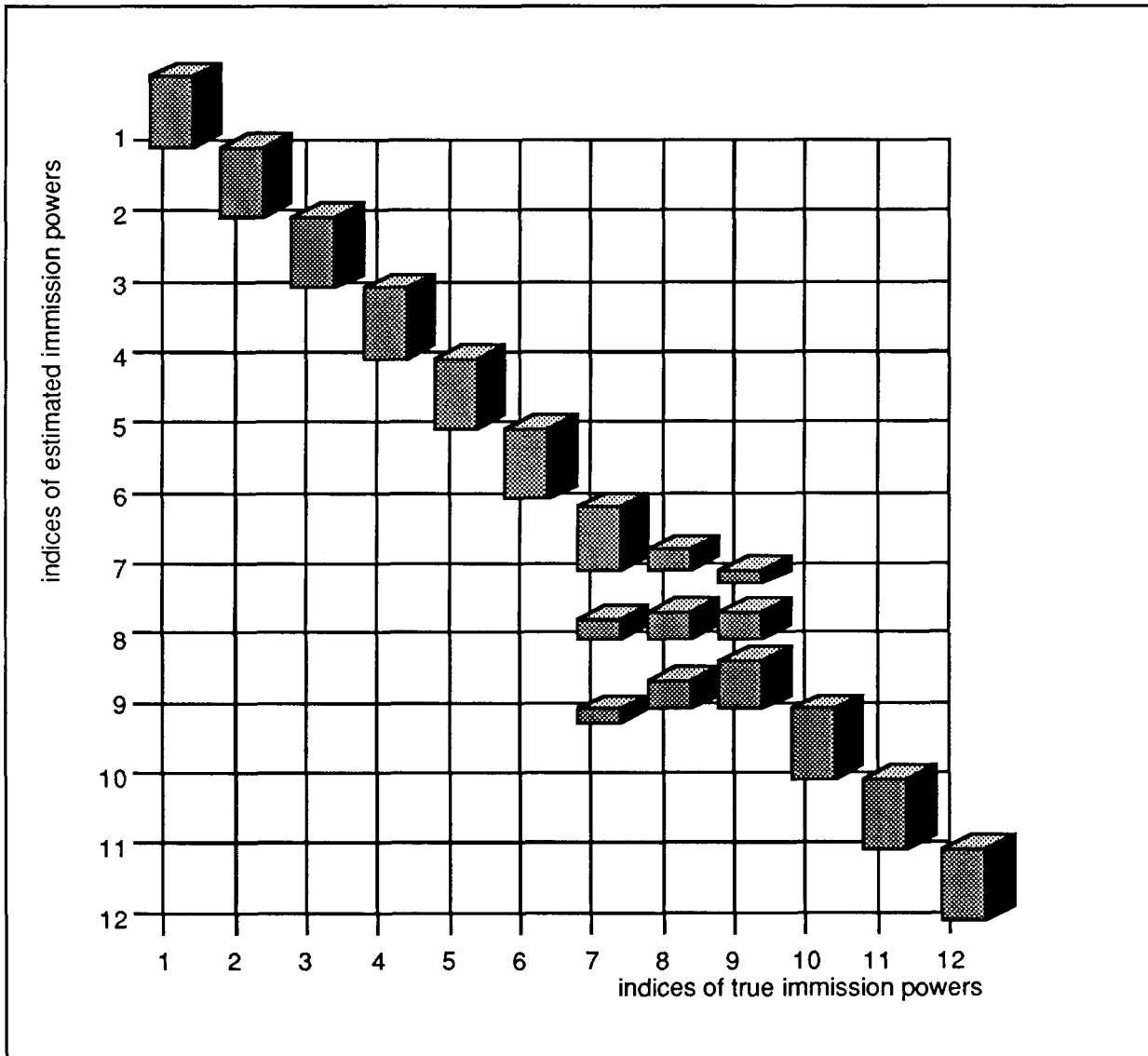Figure 7.14: Singular values of the model of the second example.

Figure 7.15: Graphical presentation of the resolution matrix of the model of table 7.6 with $N_c = 11$.

In conclusion it can be stated that the SVD-method can be applied successfully on the SYNTACAN-data. One must however keep in mind that distinguishing between closely spaced sources demands exact knowledge of the propagation characteristics of each source to the antenna as was demonstrated in the examples by the effect of imperfect focussing. Regarding this, a point of special concern is the transverse coherence loss, which diminishes the resolving power, not only of the conventional processing, but also of the SVD-method. Application of the SVD-method in practical situations demands that the coherence loss is also estimated. Note that this can be done, if the parameters β_n are made part of the estimation problem. It must however be kept in mind that increasing of the number of parameters will decrease the potential resolution enhancement of the procedure.
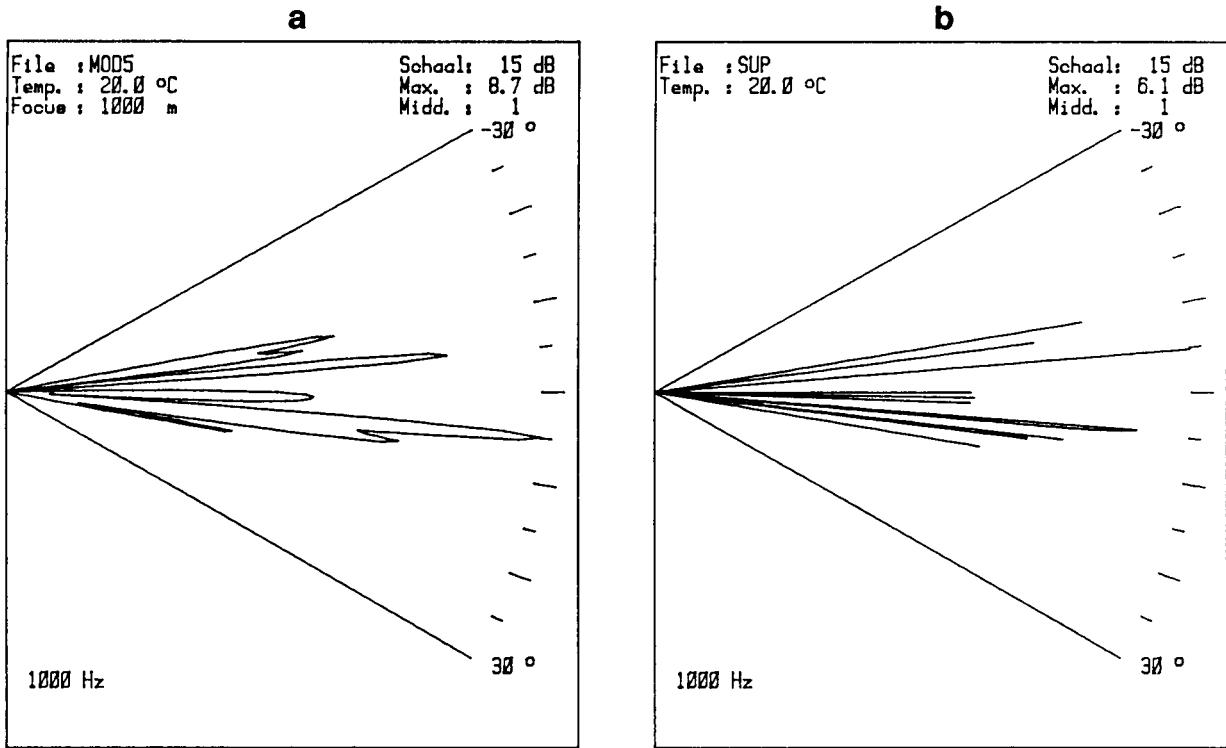
Figure 7.16: Polar diagrams of the simulation of table 7.6. a. conventional result; b. super-resolution plot.

7.6   CONCLUSIONS

In this Chapter we have discussed a number of signal processing techniques which have been developed for optical and radio-astronomy, sonar, radar and seismology. We have shown that many of these techniques are closely related to the acoustic noise source identification problem for which the SYNTACAN system has been developed. A summary of these techniques is given in table 7.8.

To compare the different resolution enhancement procedures, let us consider our general imaging problem for far field sources, where for clarity we will omit the parameter f in the formulas:

$$\tilde{R}(\xi) = \left[\sum_n \tilde{R}_n(\xi) \gamma_n(\xi) \right] W_a(\xi) \tag{7.66a}$$

or, with a Fourier-transform from ξ to k_x':

$$\tilde{R}'(k_x') = \left[\sum_n \tilde{R}_n'(k_x') * \tilde{\gamma}_n(k_x') \right] * \tilde{W}_a(k_x') \quad . \tag{7.66b}$$

In the last expression, $\tilde{R}_n'(k_x')$ represents the angular distribution of one source according to the relation $k_x' = f/c \sin \alpha$, where α is the angle of incidence.

Table 7.8

Summary of the signal processing techniques, developed for related disciplines.

name	discipline	procedure	source type	transfer char. *)	source inform.	super-resol.
speckle interfero-metry	optical astronomy	spatial correlation of image	extended + point sources	sp. stat.	no	no
CLEAN	radio astronomy	iterative curve fitting	point sources	coh. loss	no	no
Steer	radio astronomy	modified CLEAN	extended + point sources	coh. loss	no	no
Capon	sonar, radar	adaptive beamforming	point sources	undist.	no	yes
Prony's extended method	sonar, radar	parametric spectral estimation	point sources	exp.	yes	yes
MUSIC	sonar, radar	signal and noise sub-space decomposition	point sources	undist.	yes	yes
KT	sonar, radar	modified MUSIC	point sources	undist.	yes	yes
wavelet deconvo-lution	seismology	least squares inversion	extended + point sources	coh. loss	no	no
SVD	seismology	parameter estimation by generalized matrix inversion	point sources **)	coh. loss **)	yes	yes

*)   sp. stat.   = spatial stationarity over short observation times

   coh. loss   = transverse coherence loss allowed if known

   exp.   = exponential coherence loss; the β_n's are estimated by the method

   undist.   = undisturbed medium only (no transverse coherence loss)

**)   other implementations are possible

Our imaging problem consists of estimating the functions $\tilde{R}_n'(k_x')$, after $\tilde{R}(\xi)$ has been measured for a range of ξ-values. In the classical approach of SYNTACAN, only $\tilde{R}'(k_x')$ is computed. This means that the true distribution functions remain convolved with $\tilde{\gamma}_n$, due to the coherence loss, and with $\tilde{W}_a$ due to the finite antenna length. Before continuing with a discussion of the resolution enhancement techniques, let us formulate the important situation of far field point sources , where we find

$$\tilde{R}(\xi) = \left[\sum_n \tilde{R}_n \exp(-j2\pi f\xi/c_n)\, \gamma_n(\xi) \right] W_a(\xi)$$

(7.67a)

and

$$\tilde{R}'(k_x') = \left[\sum_n \tilde{R}_n \delta(k_x' - f/c_n) * \tilde{\gamma}_n(k_x') \right] * \tilde{W}_a(k_x')$$

(7.67b)

with $c_n = c\,/\sin\,\alpha_n$; α_n is the direction of source n and f represents the frequency component under consideration.

We are now ready to compare the techniques of this Chapter and to bring them in relation to Eq. (7.66) and (7.67). We will restrict ourselves in all cases to a one-dimensional aperture, as applicable to SYNTACAN.

Speckle interferometry. This procedure is used in optical astronomy to restore the resolution of a telescope when the images are disturbed by atmospheric turbulence. It is based on the computation of the auto-correlation function of $\tilde{R}'(k_x')$. The exposure time to obtain $\tilde{R}'(k_x')$ is made so short that the atmosphere may be viewed as a frozen medium. In this case the γ_n's will only have phase distortion and no amplitude distortion, so the auto-correlation function of $\tilde{\gamma}_n$ will be a spike. Besides, the $\tilde{\gamma}_n$'s of closely spaced sources will be equal, because the atmosphere is only a small disturbing layer and the raypaths of these sources will be disturbed by the same turbulences. Consequently, the auto-correlation function of $\tilde{R}'(k_x')$ will only be disturbed by the auto-correlation function of $\tilde{W}_a$ and not by the auto-correlation function of $\tilde{\gamma}_n$. The spatial auto-correlation function gives sufficient information to measure the extension of one source or the angular distance between two sources. Notice that this procedure does not give super-resolution. It only compensates the effects of the transverse coherence loss. For industrial noise source identification speckle interferometry is not applicable because there the disturbances occur along the whole transmission path and are different for each source.

CLEAN. This procedure is based on the model of Eq. (7.67b), where all $\tilde{\gamma}_n * \tilde{W}_a$ are known. In practical implementations it is usually assumed that all γ_n's are equal. It is an iterative curve fitting procedure for finding the amplitudes $\tilde{R}_n$ on a full grid with spacing $\Delta k_x'$. As such, CLEAN can be viewed as a deconvolution procedure. Because of the spike model, the procedure gives no bandwidth limitations in the result, but instead gives an extrapolation of the observation bandwidth. From this, one may inadvertently conclude that CLEAN is a super-resolution technique, but we have clearly shown in Section 7.3 that this is not true; if the source directions are closer than the Rayleigh criterion, the procedure fails. For that reason one often convolves the results with a clean beam, in accordance with the beamwidth of the antenna.

Steer. This is a modification of CLEAN to stabilize the results for extended source areas. Here the model of Eq. (7.66b) is applicable. It is assumed that the $\tilde{\gamma}_n * \tilde{W}_a$ are known. The stabilization of the Steer-algorithm gives an automatic bandwidth limitation for extended sources, but isolated point sources still produce spikes. The resolution properties are also given by the Rayleigh criterion.

Prony's extended method. This is one of the procedures of parametric spectrum estimation. It is applicable to the point source model of Eq. (7.62a), where γ_n may be different for each source, but it must be of the form $\gamma_n = \exp[-\beta_n|\xi|f]$, which is in accordance with our general model of the transverse coherence loss. After measuring $\tilde{R}(\xi)$ over the aperture length, the parameters $\tilde{R}_n$, β_n and c_n are estimated from the model. This is one of the procedures with super-resolution capabilities. The super-resolution is obtained here by the use of a model with a *small* number of sources. The number of sources needs to be known a priori, or it must be estimated with a special procedure.

Capon's method. This adaptive beamforming algorithm is applicable to point sources in a continuous noise field, making use of the correlation matrix of the sensor signals. This suggests that the general model of Eq. (7.67a) is valid. This is not true, however, because the method does not give a correct estimate of extended sources. Hence, the correct model is given by Eq. (7.66a) with added noise. The Capon method does not allow for transverse coherence loss. If the signal to noise ratio is high and the number of point sources is small, this procedure gives super-resolution, even without additional source information. The method is applicable to the sparsed SYNTACAN array under the condition of uncorrelated sources.

MUSIC. This procedure is based on the model of Eq. (7.13):

$$s = Ag + n \tag{7.68}$$

where s is a vector of sensor signals, the column vectors of A give the transfer characteristics of each source to the array elements relative to a fixed reference position, g is a vector of immission signals of the sources at the reference position, and n represents additive measurement noise. MUSIC has been developed for sonar and radar applications, where the s, g and n signals represent complex amplitudes of a synchronous detection system. The MUSIC procedure makes use of the sensor signals s, the transfer characteristics of all possible source directions, and an estimate of the number of sources, for finding the source directions and, subsequently, the correlation properties of the source signals g. The MUSIC-algorithm allows for unequal sensor element spacing, but in general the procedure is only applicable to full arrays because the array manifold has to be unambiguous. MUSIC is interesting because of its super-resolution capabilities, but it is limited to point sources in a medium without coherence loss. The method is applicable to the sparsed SYNTACAN array under the condition of uncorrelated sources.

KT. This is a modification of the MUSIC algorithm. In general, the KT-algorithm is restricted to full linear arrays and far field sources in a non-disturbed medium. This condition is met by Eq. (7.67a) with $\gamma_n = 1$ (no coherence loss). The method is applicable to the SYNTACAN array under the same conditions as for MUSIC.

Wavelet deconvolution. This procedure is applicable to the models of Eq. (7.66) and (7.67). The effects of γ_n and W_a are minimized by convolving $\tilde{R}'(k_x')$ with a band-limited so-called inverse filter having a bandwidth determined by $\gamma_n W_a$ and the noise properties. All γ_n's and W_a must be known in advance. Because of the band-limited filter operation and computation of the results on a full grid, the resolution will be according to the Rayleigh (or Ricker) criterion.

SVD. Use is made of a linear model, based on the matrix equation

$$\mathbf{s} = \mathbf{Wa} + \mathbf{n} \qquad (7.69)$$

where $\mathbf{s}$ is a vector of measurement signals, $\mathbf{W}$ is a matrix with known model parameters, $\mathbf{a}$ is a vector of unknown parameters to be solved and $\mathbf{n}$ is a vector of additive measurement noise. The SVD-method is directly applicable to the model of Eq. (7.67b), where $\mathbf{s}$ corresponds with the discretized measured values of $\tilde{R}'(k_x')$, $\mathbf{W}$ contains the known transfer characteristics and $\mathbf{a}$ contains the unknown $\tilde{R}_n'$'s. Notice that with this implementation, the source directions, all $\tilde{\gamma}_n$'s and $\tilde{W}_a$ must be known in advance. It is also possible to estimate, for instance, unknown source directions and coherence loss parameters β_n. In that case a (linearized) model must be set up, where these unknowns are made a part of $\mathbf{a}$.

Inspection of table 7.8 shows that only those methods which make use of source information (the number of sources or their positions) are capable of super-resolution, the exception being the Capon method. Super-resolution can only be obtained by an excessive reduction of the number of unknown parameters that have to be solved in relation to the number of parameters of a *full grid* method where $\tilde{R}'(k_x')$ has to be computed for each sampled value of k_x'. The Capon method seems to be able to do this automatically; it can be seen as an AR-procedure with automatic selection of the number of parameters. It must, however, be mentioned that super-resolution can only be obtained if a very precise knowledge of the underlying model is available. This is illustrated in the simulation results of the SVD method where we found that even small deviations from the true model (due to imperfections in the focussing) can lead to considerable errors in the estimated immission levels of closely spaced sources. In many cases the precise propagation characteristics of the sources are *not* known. Hence, one must be very careful with the parametric procedures under super-resolution conditions.

The applicability of the discussed signal enhancement techniques to SYNTACAN strongly depends on the available source and model information. Regarding this, we must mention that SYNTACAN has been developed for those conditions where such precise information usually is not known. In that case only the standard signal processing of SYNTACAN can be used. If the propagation characteristics of the sources, as expressed by the parameters γ_n and W_a are known, procedures like CLEAN or wavelet deconvolution can be used to optimize the beam patterns. If super-resolution is required, most procedures require additional source information, i.e. the number of sources and their positions. Procedures like the SVD-method can then be used to estimate the source powers and to improve the initial estimates of the source positions and the coherence loss parameters β_n. Super-resolution procedures can only be successful if the problem is well-posed; the model must be (almost) correct, the number of unknown parameters must be small and the signal to noise ratio must be high.

Of all discussed procedures, the Steer-algorithm is the most attractive for general purpose deconvolution of the antenna pattern. This method is easy to implement and gives reliable results, also for extended source areas. If there are only point sources, it is better to use the original CLEAN algorithm. We mentioned the possibility to optimize the CLEAN or Steer algorithms with a procedure in which unknown parameters such as the transverse coherence loss are estimated by minimizing the remaining residuals in each iteration step.

We finally want to mention a possible modification of the CLEAN algorithm for those situations where the source positions are known and only the immission levels have to be found. The modification is that in step *b* of the CLEAN algorithm (see Section 7.3), the absolute maxima are only sought at the known source directions. Notice that it can be allowed that each source has its own dirty beam, which must be known in advance, or must be computed from the model. We expect that in this way super-resolution performance of the CLEAN algorithm is very well possible. Here also, care has to be taken that the model is correct, and results with small variances can only be expected if the signal to noise ratio is such that the problem is well-posed.

REFERENCES

1. "Inwerkingtreding hoofdstukken IV en V Wet Geluidhinder (industrielawaai) m.i.v. 1 september 1982", Nederlandse Staatscourant, 25 augustus 1982.

2. H.E.A. Brackenhoff, P. Buis and A. von Meier, "Handleiding meten en rekenen industrielawaai", ICG-rapport IL-HR-13-01.

3. L.L. Beranek, "Acoustics", Chapter 6, Mc Graw-Hill, New York, (1954).

4. F.J. Fahy, "Measurement of acoustic intensity using the cross-spectral density of two-microphone signals", J. Acoust. Soc. Am., 62, 1057 (1977).

5. J.S. Bendat and A.G. Piersol, "Random data: analysis and measurement procedures", Wiley-Interscience, New York, (1971).

6. K. Verhulst, "Het toepassen van kruiscorrelatie bij metingen in de buitenlucht", ICG-project IL 16, TPD (1977).

7. A.J. Berkhout, "Seismic Resolution", Geophysical Press, London-Amsterdam, (1984).

8. A.C.S. Readhead, "Radio Astronomy by Very-Long-Baseline Interferometry", Scientific American, June 1982.

9. J. Billingsley and R. Kinns, "The acoustic Telescope", J. of Sound and Vibration, 48 (4), 485 (1976).

10. M.J. Fisher, M. Harper-Bourne and S.A.L. Glegg, "Jet Engine noise source localization: The polar correlation technique", J. of Sound and Vibration, 51 (1), 23 (1977).

11. B. Escudié, J. Larcher, P. Ningre, "Etat des recherches sur la propagation aléatoire du son dans l'atmosphère", Revue d'Acoustique, 51, 224 (1979).

12. Brochure "Laboratoire mobile d'imagerie sonore", by Métravib and Electricité de France.

13. Journées d'étude sur la recherche et l'identification des sources sonores, Lyon-Bron, 18/19 October 1979.

14. P. Ningre, "Etude critique de divers modèles statistiques de propagation aléatoire du son dans l'atmosphère", Thése présentée a l'Institut National Polytechnique de Grenoble (1978).

15. E. Bergsma, "Invloed van het weer op de geluidsbrondetectie met een microfoonarray", afstudeerverslag vakgroep Akoestiek, TH-Delft (1979).

16. E. Hoyer, "Onderzoek naar de transversale coherentiefunktie in het buitenlucht medium", kandidaatsverslag vakgroep Akoestiek, TH-Delft (1980).

17. A.D. Pierce, "Acoustics: An introduction to its physical principles and applications", Mc Graw-Hill, New York (1981).

18. P. Ugincius, "Ray acoustics and Fermat's principle in a moving inhomogeneous medium", J. Acoust. Soc. Am., 51, 1759 (1972).

19. Lord Rayleigh, "The theory of sound", Vol. 2, p. 132, Mac Millan and Co Ltd, London (1929).

20. E.T. Kornhauser, "Ray theory for moving fluids", J. Acoust. Soc. Am., **25**, 945 (1953).

21. C.H.E. Warren, "A note on the refraction of sound in a moving gas", J. Sound Vib., **1**, 175 (1964).

22. R.J. Thompson, "Ray theory for an inhomogeneous moving medium", J. Acoust. Soc. Am., **51**, 1675 (1972).

23. R.W. Herschy, editor, "Hydrometry, principles and practices", p. 300, John Wiley & Sons (1978).

24. A.H. Nuttall, G.C. Carter and E.M. Montavon, "Estimation of the two-dimensional spectrum of the space-time noise field of a sparse line array", J. Acoust. Soc. Am., **55**, 1034 (1974).

25. F.J. Harris, "On the Use of Windows for Harmonic Analysis with the Discrete Fourier Transform", Proceedings of the IEEE, **66**, 51 (1978).

26. A.J. Berkhout, "Seismic Migration, Imaging of acoustic energy by wave field extrapolation, A: Theoretical aspects", Elsevier Scientific Publishing Company, Amsterdam (1982).

27. K. Attenborough, S.I. Hayek and J.M. Lawther, "Propagation of Sound above a Porous Half-space", J. Acoust. Soc. Am., **68**,1493 (1980).

28. P. Koers, "A calculation method for the propagation of outdoor sound over several kinds of barriers on an inhomogeneous ground", afstudeerverslag vakgroep Akoestiek, TH-Delft (1983).

29. B.A. de Jong, "The influence of wind and temperature gradients on outdoor sound propagation", thesis TH-Delft (1983).

30. V.I. Tatarskii, "The Effects of the Turbulent Atmosphere on Wave Propagation", Keter, Jerusalem (1971).

31. A. Ishimaru, "Wave Propagation and Scattering in Random Media", Volume 2, Academic Press, New York (1978).

32. T. Hidaka, K. Kageyama and S. Masuda, "Fluctuation of spherical wave propagation over a ground through atmospheric turbulence", J. Acoust. Soc. Jpn (E), **6**, 247 (1985).

33. L.P.M. Hertsig, "De invloed van het transmissiemedium op de richting-afhankelijke detektie van bronnen in de buitenlucht", afstudeerverslag vakgroep Akoestiek, TH-Delft (1981).

34. G.A. Daigle, J.E. Piercy and T.F.W. Embleton, "Line-of-sight propagation through atmospheric turbulence near the ground", J. Acoust. Soc. Am., **74**, 1505 (1983).

35. J. Leech, "On the representation of 1, 2, ... n by differences", J. London Math. Soc, **31**, 160 (1955).

36. R. Sinnema, "Onderzoekingen aan een richtmicrofoon", intern rapport vakgroep Akoestiek, TH-Delft (1979).

37. L.F. van der Wal, "Interpolatie door middel van konvolutie met een eindig n-punts filter", intern rapport vakgroep Akoestiek, TH-Delft.

38. H.E.A. Brackenhoff, "Toepassingsmogelijkheden van de Syntakan in het kader van het industrielawaai-beleid", VROM-rapport GF-HR-01-01 (1985).

39. M. van Overbeek and M.M. Boone, "Evaluatie-rapport Syntakan, optimalisatie en testmetingen", VROM-rapport GF-DR-01-02 (1985).

40. L. Gomes and B.J. Vickery, "On the prediction of extreme wind speeds from the parent distribution", J. Industr. Aerodyn. **2**, 21 (1977).

41. J.A. Bakker, "Bronhoogtebepaling bij voertuigen", I1-verslag, vakgroep Akoestiek, TH-Delft (1983).

42. M. van Overbeek, "Bronlocalisatie bij passerende voertuigen", reported to VROM (1984).

43. A. Labeyrie, "High resolution techniques in optical astronomy", Progress in Optics (ed. Wolf), Vol XIV, 47 (1976).

44. J.A. Högbom, Astron. Astrophys. Suppl. **15**, 417 (1974).

45. U.J. Schwarz, "Mathematical-statistical Description of the Iterative Beam Removing Technique (Method CLEAN)", Astron. Astrophys. **65**, 345 (1978).

46. T.J. Cornwell, "A method of stabilizing the clean algorithm", Astron. Astrophys. **121**, 281 (1983).

47. D.G. Steer, P.E. Dewdney and M.R. Ito, "Enhancements to the deconvolution algorithm CLEAN", Astron Astrophys. **137**, 159 (1984).

48. W.C. Knight, R.G. Pridham and S.M. Kay, "Digital Signal Processing for Sonar", Proc. IEEE, **69**, 1451 (1981).

49. A.B. Baggeroer, "Applications of digital signal processing: sonar signal processing", (ed. Opphenheim), Prentice-Hall Inc. (1978).

50. N.L. Owsley, "Array signal processing: sonar array processing", (ed. Haykin), Prentice-Hall Inc. (1985).

51. M.I. Skolnik, "Radar Handbook", McGraw-Hill, New York (1970).

52. R.O. Schmidt, "A signal subspace approach to multiple emitter location and spectral estimation", PhD Dissertation Stanford University (1982).

53. J. Capon, "High-resolution frequency-wavenumber spectrum analysis", Proc. IEEE, **57**, 1408 (1969).

54. M.J. Earwicker, "Signal-to-noise ratio gain of sparse array processors", J. Acoust. Soc. Am., **68**, 1129 (1980).

55. S.M. Kay and S.L. Marple, "Spectrum Analysis – A modern Perspective", Proc. IEEE, **69**, 1380 (1981).

56. J.P. Burg, "The relationship between maximum entropy and maximum likelihood spectra", Geophys., **37**, 375 (1972).

57. C. Lanczos, "Linear differential operators", D. van Nostrand Co. (1961).

58. R. Kumaresan and D.W. Tufts, "Estimating of the angles of arrival of multiple plane waves", IEEE Trans. AES Vol. 19, no. 1, 134 (1983).

59. R.E. Sheriff and L.P. Geldart, "Exploration seismology, volume 1 and 2, Cambridge University Press, Cambridge (1982).

60. E.A. Robinson and S. Treitel, "Geophysical signal analysis", Prentice-Hall, Inc., Englewood Cliffs, NJ (1980).

61. A.J. Berkhout, "Least-squares inverse filtering and wavelet deconvolution", Geophysics, **42**, no. 7, 1369 (1977).

62. P. van Riel and A.J. Berkhout, "Resolution in seismic trace inversion by parameter estimation", Geophysics, **50**, no. 9, 1440 (1985).

63. P. van Riel, "Seismic trace inversion", afstudeerverslag vakgroep Akoestiek, TH-Delft (1982).

64. W. Menke, "Geophysical data analysis: discrete inverse theory", Academic Press Inc., Orlando (Fl.) (1984).

65. Y. Bard, "Nonlinear Parameter Estimation", Academic Press, Inc. New York (1974).

66. D.D. Jackson, "A Bayesian approach to nonlinear inversion", J. of Geophysical Research, **90**, p. 581 (1985).

67. J. Bakker, "Superresolutie met SYNTAKAN door parametrische inversie", afstudeerverslag vakgroep Akoestiek, TH-Delft (1985).

68. M.M. Boone, P. van Riel and A.J. Berkhout, "Super-resolution of a synthetic acoustic antenna by parametric inversion", Proceedings of 12th ICA, G4-4 (1986).

SUMMARY

This thesis describes the design and development of the SYNThetic ACoustic ANtenna SYNTACAN. The instrument is intended for highly directional sound measurements with an average resolving power of 1.5°. The system comprises the frequency range from 89 to 1413 Hz (4 octave bands); it has a resolution of 1/12 octave. Its main application is the measurement of sound immissions from individual sources on industrial areas. The design of SYNTACAN has been kept flexible enough, however, for using the instrument in other situations where directional sound measurements are required.

An important part of the antenna design was the reduction of the number of microphones as much as possible. This has been reached with a *sparsed array,* consisting of "only" 32 microphones, positioned in a row over a length of nearly 80 m. The measurement principle is based on the correlation of the microphone signals. Due to the sparsing, the obtained correlation functions are only correct in case of uncorrelated noise sources. The influence of correlations between noise sources is discussed extensively. Using a two-dimensional Fourier technique, the soundfield is decomposed into the frequency-dependent contributions from different directions; a technique which gives directly the directions of plane wave sources. In practice, a plane wave approximation along the antenna (Fraunhofer approximation) is often not permitted. For that reason attention is given to the focussing which is necessary to make the system suitable for spherical waves of sources at a close distance.

Outdoors, wave propagation is disturbed by wind and temperature effects. The theory of acoustic wave propagation in a moving medium and the influence on the antenna performance are discussed. It is found that a stationary cross-wind component causes an error in the measured source direction; in practice this error never exceeds 1°. Effects of more importance are caused by the turbulence due to wind and temperature differences. This leads to decorrelation of the microphone signals, known as *transverse coherence loss.* This limits the resolving power of the antenna to about 2° for sources at distances of more than 500 m.

The applicability of SYNTACAN is illustrated with a large number of test measurements concerning resolution, focussing, correlations, screening and coherence loss. Results from practice are shown too, such as measurements of sound immissions from large industries, sound radiation from rotor blades of wind turbines, and the estimation of the source height of passing vehicles.

Much similarity is observed between the imaging technique of SYNTACAN and techniques in use in optical and radio-astronomy, sonar, radar and seismology. In the last Chapter these techniques and their applicability to SYNTACAN are discussed. Important points are the influence of the finite length of the antenna and the disturbance of the wave propagation by turbulences in the medium, causing finite beampatterns and thus unsharp source images.

Interesting quantitative interpretation techniques are based on the CLEAN-algorithms used in radio astronomy. Simulations have shown that the CLEAN algorithms are well applicable to SYNTACAN.

In addition, attention is given to so-called *super-resolution* techniques. Specifically, the Capon-method and the MUSIC-algorithm from sonar and radar, and the SVD-method from seismology are discussed. The SVD-method has been investigated for SYNTACAN under the assumption of known source positions, where only the immission levels had to be estimated. Results show that the method is attractive, but that super-resolution can only be obtained if the propagation is accurately known.

SAMENVATTING

ONTWERP EN ONTWIKKELING
VAN EEN SYNTHETISCHE AKOESTISCHE ANTENNE
VOOR STERK RICHTINGGEVOELIGE GELUIDMETINGEN

Dit proefschrift behandelt het ontwerp en de ontwikkeling van de SYNThetische AKoestische ANtenne SYNTAKAN, waarmee het mogelijk is om sterk richtinggevoelige geluidmetingen uit te voeren met een scheidend vermogen van gemiddeld 1,5°. Het systeem bestrijkt het frequentie-gebied van 89 tot 1413 Hz (4 octaafbanden) en heeft een spectrale resolutie van $1/12$ octaaf. Het belangrijkste toepassingsgebied is het meten van geluidimmissies rond industrieterreinen: hierbij kunnen de bijdragen van de verschillende bronnen worden onderscheiden. De opzet van SYNTAKAN is echter zo algemeen dat het systeem ook kan worden gebruikt in andere situaties waarin richtinggevoelige geluidmetingen nodig zijn.

Een belangrijk onderdeel van het antenne-ontwerp is de beperking geweest van het benodigde aantal microfoons. Hiervoor is een *sparsed array* ontwikkeld, bestaande uit "slechts" 32 microfoons die op een rij worden geplaatst over een lengte van bijna 80 m. Het meetprincipe is gebaseerd op de correlatie van de microfoonsignalen en is als gevolg van de *sparsing* alleen toepasbaar op onderling ongecorreleerde geluidbronnen. De invloed van corre-laties tussen de verschillende bronnen wordt uitgebreid besproken. Door middel van een twee-dimensionale Fouriertechniek wordt het geluidveld ontleed in de frequentie-afhankelijke bijdra-gen uit de verschillende richtingen; een techniek die direct de richtingen van vlakke golf bronnen geeft. In de praktijk is een vlakke golf benadering over de antenne-lengte (Fraunhofer benade-ring) vaak niet toelaatbaar. Er wordt daarom uitvoerig aandacht geschonken aan de focussering die noodzakelijk is om de methode ook geschikt te maken voor de sferische golven van bronnen op korte afstand.

In de buitenlucht treden verstoringen op in de golfvoortplanting die vooral door wind- en temperatuureffecten worden veroorzaakt. De theorie van de akoestische golfvoortplanting in een bewegend medium en de gevolgen hiervan voor de antenne worden behandeld. Het blijkt dat een aanwezige stationaire dwarswindcomponent een misaanwijzing van de bronrichting tot gevolg heeft, die in de praktijk echter nooit groter is dan 1°. Veel belangrijker effecten worden veroorzaakt door de turbulentie ten gevolge van windstromingen en temperatuurverschillen. Hierdoor treedt decorrelatie van de microfoonsignalen op, wat bekend staat als *transversaal coherentie-verlies*. Ten gevolge hiervan wordt het scheidend vermogen van de antenne beperkt tot circa 2° voor bronnen op meer dan 500 m afstand.

De toepasbaarheid van SYNTAKAN wordt geïllustreerd aan de hand van een groot aantal test-metingen, die betrekking hebben op resolutie, focussering, ijking, correlaties, afscherming en

coherentie-verlies. Ook worden de resultaten van een aantal praktijkmetingen besproken, die verkregen zijn in uiteenlopende situaties, zoals metingen van de geluidimmissie van grote industrieën, de geluidafstraling van rotorbladen van windturbines en de bronhoogte bepaling van voorbijrijdende voertuigen.

Er blijkt grote overeenkomst te bestaan tussen de afbeeldingstechniek van SYNTAKAN en de technieken die worden toegepast in de optische en radio-astronomie, sonar, radar en seismiek. In het laatste hoofdstuk worden deze technieken en hun toepasbaarheid voor SYNTAKAN besproken. Centraal hierbij staan de invloed van de eindige afmeting van de antenne en de verstoring van de golfvoortplanting door turbulenties in het medium, waardoor de bronnen met een eindige bundelbreedte — en dus enigszins onscherp — worden afgebeeld.

Interessant zijn vooral kwantitatieve interpretatie technieken, gebaseerd op de zogenaamde CLEAN-algoritmes, die worden toegepast in de radio-astronomie. Simulaties geven aan dat de CLEAN-algoritmes goed toepasbaar zijn voor SYNTAKAN.

Ook interessant zijn de zogenaamde *super-resolutie* technieken. Besproken worden onder andere de Capon-methode en het MUSIC-algoritme uit de sonar en radar technieken en de SVD-methode uit de seismiek. De SVD-methode is voor SYNTAKAN onderzocht voor het geval dat de bronposities gegeven zijn en alleen de immissie-niveaus moeten worden bepaald. De resultaten geven aan dat deze methode goed bruikbaar is, maar dat super-resolutie alleen kan worden bereikt wanneer de overdracht nauwkeurig bekend is.

CURRICULUM VITAE

van Rinus Boone

2 februari 1947	: geboren te Colijnsplaat (gemeente Kortgene) in Zeeland
1953 – 1959	: lager onderwijs in Colijnsplaat
1959 – 1965	: middelbare schoolopleiding
1965	: eindexamen op het openbare Lyceum te Goes (diploma HBS-B)
1965 – 1972	: studie voor natuurkundig ingenieur aan de Technische Hogeschool Delft, 4e- en 5e-jaarswerk in de werkgroep Akoestiek en Bouwfysica, o.l.v. prof.dr.ir. C.W. Kosten en lector ir. D.W. van Wulfften Palthe op het gebied van luidheidsonderzoek
20 juni 1972	: doctoraal examen
1972 – 1974	: vervulling militaire dienstplicht
1974 – heden	: wetenschappelijk medewerker, resp. hoofdmedewerker, resp. universitair docent in de onderzoekgroep Akoestiek van de Technische Universiteit Delft.